ALMA MATER STUDIORUM
UNIVERSITÀ DI BOLOGNA

DOTTORATO DI RICERCA IN

FISICA

Ciclo 38

Settore Concorsuale: 02/A2 – Fisica teorica delle interazioni fondamentali

Settore Scientifico Disciplinare: FIS/02 – Fisica Teorica, Modelli e Metodi Matematici

FROM THE EARLY UNIVERSE TO COSMIC ACCELERATORS: MESSENGERS BEYOND LIGHT

Presentata da: Jacopo Nava

Coordinatore Dottorato

Alessandro Gabrielli

Supervisore

Filippo Sala

Co-Supervisore

Silvia Pascoli

Esame finale anno 2025

Abstract

The quest to uncover physics Beyond the Standard Model (BSM) faces two fundamental experimental limitations: the energy reach of terrestrial colliders, limited to the TeV scale by current accelerator technology, and the depth of cosmological observations, which typically probes only up to the epoch of the cosmic microwave background. Yet, the universe itself provides laboratories at energies and epochs far beyond human made experiments. In this thesis, I explore how emerging cosmic messengers, gravitational waves (GWs) and high-energy neutrinos, offer unprecedented opportunities to probe new physics in otherwise inaccessible regimes.

In particular, I investigate how these probes can shed light on some of the most profound open questions in fundamental physics: the origin of the matter-antimatter asymmetry, the nature of dark matter (DM), and the origin of neutrino masses. GWs, whose direct detection became reality less than a decade ago, have rapidly evolved into a powerful observational tool. Recent evidence for a stochastic GW background by the pulsar timing arrays underscores their potential to reveal phenomena from the very early Universe. Next generation detectors, such as LISA and the Einstein Telescope, have the potential to probe even earlier epochs and to test a plethora of new physics scenarios. Among these, a particularly intriguing possibility that I discuss is that a stochastic GW signal may originate from a first-order phase transition in the early universe, potentially connected to the generation of the baryon asymmetry.

Similarly, the past decade has witnessed the first detections of astrophysical high-energy neutrinos made by IceCube, opening a new observational window on both cosmic accelerators and possible dark sectors. New generation neutrino observatories, such as IceCube-Gen2 and KM3NeT, will offer improved sensitivity and larger datasets, enabling more stringent tests of BSM scenarios. At the same time, they will enhance our understanding of astrophysical sources. These two goals, probing new physics and characterizing cosmic sources, are inherently intertwined, requiring a complementary, multi-messenger approach. Among potential astrophysical sources, blazars have emerged as key candidates for high-energy neutrino emission. In this context, I explore the possibility that the observed neutrino flux from blazars may originate from DM–proton interactions in the dense environments surrounding them.

Throughout this work, I emphasize the complementarity of gravitational waves and neutrino observations with traditional probes, including high-energy and high-intensity laboratory tests, direct DM detection and cosmology. I highlight how their unique properties enable them to test BSM scenarios at energy scales and epochs inaccessible to other current experiments. As both fields are undergoing rapid experimental advances, the results presented here aim to contribute to the growing effort of leveraging multi-messenger astrophysics as a strategic frontier in the search for new physics.

Acknowledgments

I would like first of all to express my deepest gratitude to my supervisor, Filippo Sala, for his constant support throughout these years. His active involvement, sharp ideas, physical intuition and his tireless energy in both physics discussions and motivation have been fundamental to my growth as a researcher and to make this journey never boring.

I am sincerely thankful to my co-supervisor, Silvia Pascoli, for her insightful guidance and for offering me the invaluable opportunity to spend many months in visit at Fermilab, an experience that greatly enriched my scientific journey and personal life.

I also want to thank Gordan Krnjaic for his openness to discussions on a wide range of topics during my visit, and for the many inputs that helped broaden my perspective.

Thanks also to all the people of the Fermilab village for the warm welcome when I arrived and for all the fun that we had together.

A special acknowledgment goes to the people I had the opportunity and the pleasure to collaborate with during these years, especially Alessandro Granelli, Andrea Giovanni de Marchi and Maximilian Dichtl. Without their collaboration and friendship, not only would this journey have been much harder, but it would have lacked much of the enjoyment and shared enthusiasm that made it worth it.

I am very grateful to my office mates during these years, Filippo, Polina, Jaime, Simone, and Elina, for their support, the countless conversations we shared over these years, and also for your patience during my inevitable moments of madness along the way!

To the PhD students of 101, my first office at Unibo and lasting gathering point, thank you for all the lunches together and the countless table-tennis matches.

Finally, I owe my deepest gratitude to my family, for always believing in me, even through the challenging moments I faced along the way. Their unwavering support has been the foundation that sustained me throughout this journey.

Associated Publications

The work presented in this thesis has led to the following publications and preprints:

1. "Baryogenesis and Leptogenesis from Supercooled Confinement", M.Dichtl, J.Nava, S.Pascoli, F.Sala, JHEP 02 (2024) 059, [1]

2. "Relic Neutrino Background from Cosmic-Ray Reservoirs", A.Granelli, A.G. De Marchi, J.Nava, F.Sala, Phys.Rev.D 111 (2025) 2, 023023 [2]

3. "Did IceCube discover Dark Matter around Blazars?", A.Granelli, A.G. De Marchi, J.Nava, F.Sala, Phys.Rev.D 112 (2025) 4, 043042 [3]

4. "Diffuse astrophysical neutrinos from dark matter around blazars", A.Granelli, A.G. De Marchi, J.Nava, F.Sala, [4]

5. "Boosted dark matter versus dark matter-induced neutrinos from single and stacked blazars", A.Granelli, A.G. De Marchi, J.Nava, F.Sala, [5]

6. "Nanohertz gravitational waves from the baryon dark matter coincidence", A. Musumeci, J.Nava, S.Pascoli, F.Sala, in preparation, [6]

where [1, 6] and [2, 3, 4, 5] constitute the main body text of Sections 3.2, 3.3 and Chapter 4 respectively, with some introductory details and refinements. Before starting my PhD, I have published the following works of research not presented in this thesis:

1. "Observable flavor violation from spontaneous lepton number breaking", P.Escribano, M.Hirsch, J.Nava, A.Vicente, JHEP 01 (2022) 098, [7].

2. "Dark Matter in the Scotogenic model with spontaneous lepton number breaking", V.De Romeri, J.Nava, M.Puerta, A.Vicente, Phys.Rev.D 107 (2023) 9, 095019, [8].

During my PhD, during my research stay at Fermilab, I have also carried out the following project not included in this thesis

- "Exploring the Cosmological Triangle in Search for Axion-Like Particles from a Reactor", D.Kim, G.Krnjaic, J.Nava and NEON Collaboration, Phys.Rev.Lett. 134 (2025) 20, 201002, [9]

The author is also a member of the DUNE collaboration, although this thesis does not directly include results related to the experiment.

Contents

Motivation and Purpose

The Standard Model of particle physics describes the interactions among the fundamental constituents of matter, and its theoretical predictions have been in astonishing agreement with experimental data so far. Nevertheless, it cannot represent the ultimate *Theory of Everything*. Indeed, despite its remarkable success in describing particle interactions up to the TeV scale, the Standard Model is widely understood to be an effective theory, valid only below a certain energy cutoff. In particular, it does not incorporate gravity, and its structure is expected to break down near the Planck scale, where quantum gravitational effects become important. This theoretical limitation underscores the need for a more fundamental framework that unifies the Standard Model with gravity. Moreover, even well below this cutoff, the Standard Model fails to account for several key observations. One of the most immediate and experimentally established shortcomings is the existence of neutrino masses. In the Standard Model, neutrinos are introduced as massless fermions, yet the existence of neutrino oscillations imply that they need to have a non vanishing mass. This fact requires an extension of the Standard Model field content or symmetries.

A second major puzzle is the nature of dark matter. Astrophysical and cosmological observations, from galactic rotation curves and gravitational lensing to studies on large scale structure formation and on the cosmic microwave background, provide compelling evidence for a non-luminous, non-baryonic component of matter that makes up about 27% of the universe's energy density. Still, the Standard Model offers no viable dark matter candidate, strongly suggesting the existence of new particles and interactions.

Finally, the observed matter-antimatter asymmetry of the universe remains a mistery. While the Standard Model contains sources of CP violation and baryon number violation, they are insufficient to account for the magnitude of the baryon asymmetry generated in the early universe. Explaining this asymmetry requires new dynamics in the early universe, which could also intersect with the physics of neutrino masses and phase transitions.

It is also worth noting that these problems may not require entirely independent solutions. Several theoretical frameworks propose unified explanations that simultaneously address two or more of these open questions. Examples include models where dark matter is involved in baryogenesis through matter–dark matter oscillations, or radiative neutrino mass generation mechanisms in which neutrino masses and dark matter originate from the same dynamics.

One of the major challenges in the search for physics beyond the Standard Model lies in the uncertainty surrounding the energy scale at which new phenomena emerge. While collider experiments, such as the LHC, have pushed our direct exploration up to the TeV scale, their progress in the coming decade is likely to be incremental and technically demanding. In this context, alternative approaches become increasingly valuable, particularly those that can access scales and epochs far beyond the reach of terrestrial experiments.

Among these, gravitational waves and high-energy neutrinos stand out as promising messengers of new physics. Gravitational waves offer a unique opportunity to probe the early universe, including processes such as first-order phase transitions associated with symmetry breaking and baryogenesis. Excitingly, recent results from pulsar timing arrays have reported hints of a stochastic signal around the nanohertz frequency that could be the first detection of a gravitational wave background. While its origin remains under investigation, these observations strengthen the case for pursuing new physics signatures through the gravitational wave sky. Future space based interferometers like LISA, as well as next generation ground based detectors such as Einstein Telescope, could be sensitive to stochastic gravitational wave backgrounds from these primordial events.

On the other hand, high-energy neutrinos can serve as probes of violent astrophysical environments where new physics may be at play, for instance, in regions with dark matter acceleration or cosmic-ray interactions with hidden sectors. Importantly, both gravitational wave and neutrino astronomy are rapidly evolving fields, with groundbreaking observations already achieved by collaborations such as LIGO/Virgo/KAGRA for gravitational waves, and IceCube and KM3NeT for neutrinos. These developments mark the beginning of a new era in particle physics and cosmology, in which non-electromagnetic messengers offer complementary and potentially groundbreaking insights into the fundamental laws of nature.

What makes these messengers particularly powerful is their broad relevance across distinct areas of fundamental physics. The same gravitational wave or neutrino signal can simultaneously carry information about dark matter, baryogenesis, or neutrino mass generation, depending on the underlying dynamics. This convergence motivates a unified approach in which observational signatures are studied not in isolation, but as probes of multiple interconnected problems. In this thesis, we adopt such a strategy, exploring how gravitational waves and high-energy neutrinos can test a range of BSM dynamics and scenarios addressing these deep open questions.

The thesis is structured in four main chapters. In Chapter 1 the following open issues of the Standard Model are discussed: the matter-antimatter asymmetry, the origin of neutrino masses and the nature of dark matter. In Chapter 2 we introduce the messengers beyond light, gravitational waves and high-energy neutrinos, with emphasis on their relevance to the cosmology of the early universe and extreme astrophysical environments. In Chapter 3 we discuss in detail first-order phase transitions and the associated stochastic gravitational wave spectrum, in particular in the context of supercooled phase transitions. We build concrete models for the generation of the baryon asymmetry and we show that our framework could be testable through gravity waves at LISA and the Einstein Telescope. We also propose a low scale baryogenesis model, addressing also DM abundance, that relies on a supercooled phase transition below the GeV scale, in order to address the gravitational wave signal recently observed by the pulsar timing arrays. In Chapter 4 we discuss some implications of the observations of high-energy astrophysical neutrinos on Beyond the Standard Model physics. We study the possibility that the neutrino observed in 2017 by IceCube associated to the blazar TXS 0506+056, as well the diffuse astrophysical neutrino flux detected in the past decade at IceCube could be the result of the interaction of dark matter around blazars with high-energy protons that are accelerated in the blazar environment. We also suggest that high-energy neutrinos could probe the only component of dark matter which is predicted by the Standard Model, namely the relic neutrino background. We conclude by summarizing the main results of this thesis and outlining future directions for addressing the open questions of the Standard Model, emphasizing the growing role of non-electromagnetic messengers such as gravitational waves and high-energy neutrinos in unveiling new physics.

Chapter 1

Open Issues of the Standard Model

1.1 Generation of the Baryon Asymmetry

Matter-Antimatter asymmetry of our Universe

The existence of antimatter is a fundamental prediction of relativistic quantum mechanics. In 1928, Dirac's formulation of the electron's wave equation implied the existence of a particle with identical mass and spin but opposite electric charge, the positron [10]. This prediction was confirmed a few years later, in 1932, when Anderson observed positron tracks in a cloud chamber [11]. Today, antimatter is an integral part of the Standard Model (SM): every fermion has an associated antiparticle, with the possible exception of neutrinos due to the ongoing debate on their Dirac/Majorana nature. The CPT theorem implies an exact symmetry between particles and antiparticles in their intrinsic properties such as mass and lifetime. Despite this fundamental symmetry, the observable Universe exhibits a striking imbalance, dominated almost entirely by matter rather than antimatter. Indeed, cosmic ray observations, gamma-ray constraints, and the absence of antimatter regions up to the scale of galaxy clusters [12, 13] all point to the conclusion that the observable Universe has a net cosmological matter-antimatter asymmetry.

Measurements of the Cosmic Microwave Background (CMB) [14] and Big Bang Nucleosynthesis (BBN) [15] yield a precise value for the baryon-to-photon ratio,

$$\eta_B \equiv \frac{n_B - n_{\bar{B}}}{n_\gamma} \simeq 6.1 \times 10^{-10}\,, \tag{1.1}$$

where n_B, $n_{\bar{B}}$ and n_γ are the number densities of baryons, antibaryons and photons, respectively, indicating a tiny but significant excess of baryons over antibaryons. As the photon number density n_γ can change due to processes such as electron-positron annihilation, it is more convenient to express the baryon asymmetry of the Universe (BAU) in terms of the baryon-to-entropy ratio, which remains constant as long as baryon number violating processes are inactive. The baryon-to-entropy ratio is defined as

$$Y_{\text{BAU}} \equiv \frac{n_B - n_{\bar{B}}}{s} = \eta_B \frac{45\,\xi(3)}{\pi^4 g_{*s}} \simeq \frac{\eta_B}{7.04} \simeq 8.6 \times 10^{-11}\,, \tag{1.2}$$

where $g_{*s} = 3.75$ is the effective number of relativistic degrees of freedom after recombination. Explaining this value of the observed BAU is theoretically challenging. Indeed, if one assumes no initial baryon asymmetry, then baryon-antibaryon annihilations would have occurred as the temperature dropped below the baryon mass, Boltzmann suppressing their abundance [16]. The remaining relic densities of both baryons and antibaryons would be negligible, of order $\sim 10^{-20} n_\gamma$, far below the value required by BBN and CMB data. Moreover, the absence of strong diffuse gamma-ray signals from annihilations, as well as the consistency of BBN and CMB physics, rules out this symmetric freeze-out scenario by many orders of magnitude.

Taken together, these considerations imply that the observed matter-antimatter asymmetry must have a dynamical origin. It is extremely unlikely that such a small imbalance was set as an initial condition, particularly in the context of inflationary cosmology, which tends to erase any pre-existing asymmetry [17]. Therefore, the baryon asymmetry must have been generated through physical processes in the early Universe, after inflation and before BBN. This leads to the concept of *baryogenesis*, a dynamical mechanism by which a net baryon number is created out of an initially symmetric state.

The theoretical foundation for baryogenesis was established by Sakharov, who identified three necessary conditions for generating a baryon asymmetry in the early Universe. These conditions, which we review in the next section, provide the essential ingredients for any successful model which can account forn the generation of the BAU.

1.1.1 The Sakharov conditions

In 1967, Sakharov presented three necessary conditions that must be simultaneously fulfilled in order to generate the observed BAU [18]. These conditions are: i) the violation of the baryon number, ii) violation of C and CP symmetries, and iii) the presence of an out-of-equilibrium phase. Let us analyze each of these requirements in some detail, see [19] for a similar discussion. We begin by defining the total baryon number operator in terms of the quark fields $q(x)$ at spacetime point $x = (t, \vec{x})$:

$$\hat{B}_{\text{tot}}(t) \equiv \frac{1}{3} \sum_q \int d^3x \, q^\dagger(x) q(x), \, . \tag{1.3}$$

This operator therefore counts the number of baryons in a given volume at the time t.

- The first condition is obvious. If the baryon number $\hat{B}_{\text{tot}}$ is strictly conserved, then the operator commutes with the Hamiltonian $\hat{H}$

$$[\hat{H}, \hat{B}_{\text{tot}}] = 0, \tag{1.4}$$

  and therefore its expectation value $\langle \hat{B}_{\text{tot}}(t) \rangle$ is constant in time. Consequently, no net baryon number can be generated dynamically from an initially baryon-symmetric state.

- Using the transformation properties of spinor fields under discrete symmetries, one can show:

$$\hat{P} \hat{B}_{\text{tot}}(t) \hat{P}^{-1} = \hat{B}_{\text{tot}}(t), \tag{1.5}$$

$$\hat{C} \hat{B}_{\text{tot}}(t) \hat{C}^{-1} = -\hat{B}_{\text{tot}}(t), \tag{1.6}$$

  and therefore,

$$(\hat{C}\hat{P}) \hat{B}_{\text{tot}}(t) (\hat{C}\hat{P})^{-1} = -\hat{B}_{\text{tot}}(t). \tag{1.7}$$

Now consider the quantum expectation value of baryon number at time t, computed using the density matrix $\rho(t)$:

$$\langle \hat{B}_{\text{tot}}(t) \rangle = \text{Tr}[\rho(t) \hat{B}_{\text{tot}}(t)], \tag{1.8}$$

with $\rho(t) = e^{i\hat{H}t} \rho(0) e^{-i\hat{H}t}$. Assuming that the theory is invariant under charge conjugation $\hat{C}$, i.e., $[\hat{C}, \hat{H}] = 0$, and that the initial state is C-symmetric, namely $\hat{C}\rho(0)\hat{C}^{-1} = \rho(0)$, is then $\hat{C}$-invariance is preserved at all times, $\hat{C}\rho(t)\hat{C}^{-1} = \rho(t)$.

The expectation value of $\hat{B}_{\text{tot}}(t)$ can be computed as :

$$\begin{aligned} \langle \hat{B}_{\text{tot}}(t) \rangle &= \text{Tr}[\rho(t) \hat{B}_{\text{tot}}(t)] && (1.9) \\ &= \text{Tr}[\hat{C}\rho(t)\hat{C}^{-1} \hat{C}\hat{B}_{\text{tot}}(t)\hat{C}^{-1}] && (1.10) \\ &= \text{Tr}[\rho(t)(-\hat{B}_{\text{tot}}(t))] = -\langle \hat{B}_{\text{tot}}(t) \rangle. && (1.11) \end{aligned}$$

Therefore $\langle \hat{B}_{\text{tot}}(t) \rangle = 0$ and hence no baryon asymmery is generated. A similar argument holds if the theory is CP symmetric (i.e., $[\hat{C}\hat{P}, \hat{H}] = 0$) and $\rho(0)$ is CP-invariant. In both cases, the system cannot evolve to produce a net baryon number from an initially symmetric state.

- The third Sakharov condition requires that baryon-generating interactions occur out of thermal equilibrium. This necessity can be seen from the fact that, in equilibrium, the density matrix ρ is time-independent and commutes with the Hamiltonian:

$$[\rho, \hat{H}] = 0. \tag{1.12}$$

As a result, the expectation value of any observable, including the total baryon number $\hat{B}_{\text{tot}}$, is conserved. Moreover, in equilibrium the system respects CPT symmetry. Since $\hat{\theta} \equiv CPT$ satisfies

$$\hat{\theta}\hat{B}_{\text{tot}}\hat{\theta}^{-1} = -\hat{B}_{\text{tot}}, \qquad \hat{\theta}\rho\hat{\theta}^{-1} = \rho, \tag{1.13}$$

it follows immediately that

$$\langle \hat{B}_{\text{tot}} \rangle = \text{Tr}[\rho \hat{B}_{\text{tot}}] = \text{Tr}[\rho(-\hat{B}_{\text{tot}})] = -\langle \hat{B}_{\text{tot}} \rangle \Rightarrow \langle \hat{B}_{\text{tot}} \rangle = 0. \tag{1.14}$$

Baryogenesis within the Standard Model

Let us now examine whether the SM satisfies the above Sakharov conditions. In the SM there are four global *accidental* $U(1)$ symmetries, meaning that they are not fundamental symmetries but result from gauge invariance, renormalizability and the particle content of the theory. These are the baryon number B and the lepton family numbers, L_e, L_μ, L_τ (clearly the total lepton number $L = L_e + L_\mu + L_\tau$ is conserved as well). Though conserved at the classical level, the baryon and lepton number are anomalous, namely their conservation is broken at the quantum level. The baryonic and leptonic currents, specifically J^μ_B and J^μ_L, are not conserved at the non-perturbative level but they satisfy the following equation [20]

$$\partial_\mu J^\mu_B = \partial_\mu J^\mu_L = -\frac{n_f}{32\pi^2} \left(g^2 W^a_{\mu\nu} \tilde{W}^{\mu\nu,a} - g'^2 B_{\mu\nu} \tilde{B}^{\mu\nu} \right) , \tag{1.15}$$

where $g(g')$, $W_{\mu\nu}(B_{\mu\nu})$ and $\hat{W}_{\mu\nu}(\hat{B}_{\mu\nu})$ denote the gauge coupling, the field strength tensor and its dual of the SM $SU(2)_L(U_1(Y))$ gauge groups; n_f is the number of fermionic families, that is $n_f = 3$ in the SM. It thus follows that in the SM $B - L$ is conserved while $B + L$ is violated.

In the SM, baryon number violation (BNV) arises from the chiral anomaly and is mediated by non-perturbative $\mathrm{SU}(2)_L$ gauge field configurations. These are characterized by the *Chern-Simons number* N_{CS}, a topological quantity defined on spatial slices:

$$N_{\mathrm{CS}}(t) = \frac{g^2}{32\pi^2} \int d^3x \, \epsilon^{ijk} \left(W_i^a \partial_j W_k^a + \frac{g}{3} \epsilon^{abc} W_i^a W_j^b W_k^c \right) . \tag{1.16}$$

These vacuum configurations, distinguished by different integer values of N_{CS}, are classically degenerate but topologically distinct. Transition between topologically distinct vacua induce a change ΔN_{CS}, which leads to baryon and lepton number violation (LNV) through the anomaly:

$$\Delta B = \Delta L = n_f \, \Delta N_{\mathrm{CS}}, \qquad \Delta(B - L) = 0. \tag{1.17}$$

At zero temperature, such transitions are mediated by instantons, which are finite-action solutions to the Euclidean equations of motion for the gauge fields, describing tunneling events between topologically distinct vacua, with an exponentially suppressed rate $\Gamma_{\mathrm{inst}} \sim e^{-4\pi/\alpha_W} \approx 10^{-170}$ [21, 22], where $\alpha_W \equiv g^2/(4\pi)$. However, at finite temperature, thermal fluctuations can induce transitions over the potential barrier between the degenerate vacua. These transitions are mediated by the electroweak sphalerons [23], which are the field configurations at the maxima of the energy barriers and are characterised by half-integer Chern-Simons number. The rate per unit volume of these transitions depends strongly on the temperature. At low temperatures $T \leq T_{\mathrm{EW}}$, that is in the electroweak broken phase, the sphaleron rate is exponentially suppressed:

$$\Gamma_{\mathrm{sph}}^{(T \leq T_{\mathrm{EW}})} \sim A(T) \, e^{-E_{\mathrm{sph}}(T)/T}, \tag{1.18}$$

where $A(T) \sim T^4$ and $E_{\mathrm{sph}}(T) \sim \frac{4\pi v(T)}{g}$ is the temperature-dependent sphaleron energy, with $v(T)$ the Higgs VEV. At high temperatures $T \geq T_{\mathrm{EW}}$, namely in the symmetric phase, the rate becomes unsuppressed and is estimated as [24]:

$$\Gamma_{\mathrm{sph}}^{(T \geq T_{\mathrm{EW}})} \sim \kappa \, \alpha_W^5 T^4, \tag{1.19}$$

where $\kappa \sim 20$ is a constant determined by lattice simulations [25]. To determine whether sphalerons are in thermal equilibrium, we compare Γ_{sph} to the Hubble expansion rate $H(T)$, which in the radiation-dominated era is given by

$$H^2(T) = \frac{\rho_{\mathrm{rad}}}{3{M_{\mathrm{Pl}}}^2} \, , \quad \rho_{\mathrm{rad}}(T) = \frac{g_* \pi^2}{30} T^4 \, , \tag{1.20}$$

where g_* is the effective number of relativistic degrees of freedom and $M_{\mathrm{Pl}} \simeq 2.4 \times 10^{18}$ GeV the reduced Planck mass. The condition for equilibrium, $\Gamma_{\mathrm{sph}}/T^3 > H$, then implies that electroweak BNV is in thermal equilibrium in the temperature range:

$$T_{\mathrm{sph}} \leq T \leq 10^{12} \text{ GeV} \, , \tag{1.21}$$

with $T_{\mathrm{sph}} \simeq 130$ GeV [24]. In this range of temperatures, $B + L$ is effectively violated, while $B - L$ remains conserved. As long as the EW sphalerons are in thermal equilibrium, one can derive relations between the chemical potential of the various particles composing the plasma and, correspondingly, between the numbers B, L and $B - L$, [26]:

$$B = c_s(B - L)\,, \qquad\qquad L = (c_s - 1)(B - L)\,, \tag{1.22}$$

where c_s is the sphaleron coefficient, which is given by

$$c_s = \begin{cases} \dfrac{8n_f + 4n_H}{22n_f + 13n_H} & T \gtrsim T_{\rm EW}, \\ \dfrac{8n_f + 4(n_H + 2)}{24n_f + 13(n_H + 2)} & T \lesssim T_{\rm EW}\,, \end{cases} \tag{1.23}$$

where $T_{\rm EW} \simeq 160$ GeV the temperature of the electroweak crossover [24] and n_H the number of Higgs doublets of the theory. As in the SM $n_H = 1$, it follows that $c_s = 28/79$ for $T \geq T_{\rm EW}$ and $c_s = 12/37$ for $T \leq T_{\rm EW}$. The expressions in Eq. (1.22) imply that, as long as $B+L$ violating process are in thermal equilibrium, a pre-existing baryon asymmetry can be reprocessed by the EW sphalerons into a lepton asymmetry and vice-versa, in the presence of a net $B-L$ initial asymmetry. Therefore, if a $B-L$ asymmetry is generated at $T > T_{\rm EW}$, it is reprocessed into B and L asymmetries by EW sphalerons, as long as $T > T_{\rm sph}$ and effectively "frozen in" below $T_{\rm sph}$. This is the key idea of leptogenesis, where the $B-L$ asymmetry is first produced in the lepton sector and is then transferred to the baryon sector.

Regarding the other Sakharov's conditions, C is maximally violated in the SM by the weak interactions. Moreover, CP is violated in the quark sector by the physical phase of the CKM matrix [27]. However, it was shown in Refs. [28, 29] that CP-violating effects in the SM are far too small to account for the observed BAU. A straightforward way to quantify CP violation in a basis-independent way is through the construction of reparametrisation invariant combinations of the quark mass matrices. The leading CP-violating quantity can be written as

$${\rm Im}\left[{\rm Det}\left[M_u M_u^\dagger, M_d M_d^\dagger\right]\right] \simeq -2J\, m_t^4 m_b^4 m_c^2 m_s^2,$$

where M_u and M_d are the up and down type quark mass matrices, m_i the quark masses and J is the Jarlskog invariant [30], defined as

$$J \equiv {\rm Im}\,[V_{us}V_{cb}V_{ub}^* V_{cs}^*] \simeq 2 \times 10^{-5}\,,$$

with V_{ij} the elements of the CKM matrix. To assess the cosmological relevance of this CP violating invariant quantity, one can construct a dimensionless ratio by normalising to a temperature scale relevant for baryogenesis. Taking $T = T_{\rm sph} \approx 130$ GeV the temperature at which the sphaleron processes freeze out, we can define the following dimensionless quantity:

$$Y_{\rm SM} \sim \frac{J\, m_t^4 m_b^4 m_c^2 m_s^2}{T_{\rm sph}^{12}} \sim 10^{-19} \ll Y_{\rm BAU}\,. \tag{1.24}$$

This result implies that there should be other sources of CP violation beyond the CKM phase to produce the observed matter-antimatter asymmetry.

In addition to the weakness of CP violation, the SM also fails to provide the necessary departure from thermal equilibrium. A first-order electroweak phase transition (EWPT) would create bubbles of broken electroweak symmetry in a symmetric background, driving the system out of equilibrium. However, for the measured value of the Higgs mass $m_H = 125$ GeV, the EWPT in the SM is known to be a smooth crossover [31, 32], and thus fails to provide a significant deviation from thermal equilibrium.

Together, the absence of $B - L$ violating interactions, the extreme suppression of CP violation and the absence of a strongly first-order phase transition imply that the SM alone cannot account for the observed BAU. These limitations of the SM provide a compelling motivation for BSM physics that includes new sources of CP violation, a mechanism for generating a net $B - L$ asymmetry and dynamics capable of inducing a strong departure from thermal equilibrium.

1.1.2 Mechanisms for the generation of the baryon asymmetry

Several theoretical frameworks have been proposed to explain the origin of the BAU, each of them relying on BSM physics to satisfy the Sakharov conditions.

One of the earliest proposals came in the context of Grand Unified Theories (GUT), which aim to unify the electroweak and the strong interactions by embedding the SM particles into the fundamental representations of larger gauge groups, e.g. $SU(5)$ or $SO(10)$ [33]. As quarks and leptons are unified into the same multiplets, the appearance of BNV processes becomes natural. This mechanism, known as *GUT Baryogenesis* is driven by the out of equilibrium decays of heavy bosons X present in the GUT, whose mass is comparable to the GUT scale, $M_X \sim 10^{16}$ GeV [34, 35]. However, these models are strongly constrained by bounds on the proton lifetime [36] and from inflation. Indeed, the former puts a lower bound on the mass of the decaying boson, and therefore on the reheating temperature of the Universe after inflation. Simple inflation models do not give such a high reheating temperature, which might also produce unwanted heavy relics [37]. Finally, in the simplest $SU(5)$ based GUTs, $B + L$ is violated but $B - L$ is not. Consequently, EW sphalerons would wash-out any baryon asymmetry produced at the GUT scale (see [38] for a review).

An alternative high-scale mechanism for generating the baryon asymmetry is the *Affleck–Dine* baryogenesis [39], originally proposed in the context of supersymmetric (SUSY) theories. In this framework, scalar fields carrying baryon or lepton number, typically flat directions of the scalar potential in SUSY extensions of the SM, develop large vacuum expectation values during inflation. These scalar condensates later evolve and rotate in field space, effectively generating a net baryon or lepton number through CP-violating phases in the potential. As the universe expands, the condensate eventually decays into SM particles, transferring its asymmetry to the thermal plasma. A nice feature of this mechanism is that it can lead to an asymmetry in any combination of B and L. However, its predictions are sensitive to the details of the scalar potential, SUSY breaking, and reheating, and often require careful model building to ensure consistency with cosmology and avoid overproduction of unwanted relics (see [40]).

Leptogenesis [41] is a compelling mechanism for generating the BAU, intimately linked to the origin of neutrino masses via the seesaw mechanism [42, 43]. In this framework, heavy right-handed neutrinos, singlet under the SM gauge group, are introduced and coupled to the lepton doublets and the Higgs field via Yukawa interactions. Their Majorana masses explicitly violate lepton number, and their out-of-equilibrium decays can generate a lepton asymmetry through the complex Yukawa couplings. This lepton asymmetry is then partially converted into a baryon asymmetry by the electroweak sphalerons.
A particularly attractive feature of leptogenesis is its natural embedding in the seesaw mechanism, which simultaneously explains the smallness of neutrino masses observed in oscillation experiments. However, the canonical scenario of thermal leptogenesis typically requires the lightest right-handed neutrino to have a mass above 10^9 GeV [44], placing it well beyond

the reach of current experiments. Nevertheless, alternative realizations such as resonant leptogenesis [45], where two or more right-handed neutrinos are nearly degenerate in mass, can enhance CP violation and lower the scale of leptogenesis to the TeV range or below, offering potential prospects for experimental tests via lepton flavor violation, neutrinoless double beta decay, or collider signatures. For a comprehensive review of this framework see [46, 47].

Electroweak baryogenesis (EWBG) offers a compelling framework to explain the observed BAU via new physics at the electroweak scale [23, 48]. In this scenario, a departure from thermal equilibrium is provided by the EWPT itself, which is set to be first-order, during which bubbles of broken electroweak symmetry nucleate and expand in a symmetric phase background. CP violating interactions between particles in the plasma and the advancing bubble walls generate a CP asymmetry in left-handed fermions, which is converted into a baryon asymmetry by the EW sphalerons active in the symmetric phase. The generated baryon number is subsequently swept into the broken phase, where sphalerons are suppressed, preventing washout.

As discussed in the previous section, the SM fails to support EWBG due to two key shortcomings: i) the EWPT is a smooth crossover for the observed Higgs mass; ii) the only source of CP violation, the CKM phase, is too small, appearing only at high order in the Yukawa expansion. Viable models of EWBG therefore require extensions of the Higgs sector and new CP violating sources, as realized in two-Higgs-doublet models, SUSY, or composite Higgs frameworks. These models are highly testable: indeed, they may lead to electric dipole moments (EDMs) near current experimental limits [49], collider signatures, and, in particular, gravitational wave signals from first-order phase transitions that could be observed by future detectors such as LISA [50, 51]. While traditional EWBG relies on subsonic bubble walls, recent proposals have explored mechanisms that allow for relativistic walls and novel particle production effects [52, 53, 54], potentially broadening the class of viable models and their gravitational wave phenomenology.

While many baryogenesis models operate at high temperatures, often well above the electroweak scale, it is in principle possible to generate the baryon asymmetry at much lower scales, even around 1–100 MeV. Such scenarios naturally emerge in frameworks with low reheating temperatures, as predicted in certain SUSY models [55] or axion DM models with suppressed isocurvature perturbations [56]. Recent low-scale baryogenesis proposals have revived and improved upon early ideas from the 1980s, addressing challenges such as washout by late-decaying particles and EDM constraints, see [57] for a review on the topic, here we will mention a few interesting examples four our purpose.

One scenario, known as *Mesogenesis* [58, 59], exploits CP violating processes in SM meson systems, such as $B^0_{d,s}$ mixing or charged meson decays, which occur after quark hadronization at low temperatures. The baryon number can be transferred to a dark sector state carrying $B = -1$, enabling an overall baryon symmetric universe. These models are experimentally testable through CP violation in meson systems, exotic decays into invisible particles, and collider peak searches.

Another intriguing baryogenesis framework seeks to explain the observed abundances of both baryonic matter and DM through a common origin, as motivated by the fact that their cosmological energy densities differ by only an order-one factor, with $\rho_{\rm DM}/\rho_B \sim 5$. A well-known example is the class of *asymmetric dark matter* (ADM) models, see [60], where a shared asymmetry in a conserved global charge (such as $B-L$) is split between the visible and dark sectors. This leads to a DM density naturally comparable to that of baryons if the DM mass is of a few GeV. Two broad classes of ADM models exist. In *cogenesis* [61], the visible and dark sector asymmetries are generated simultaneously from a common out-of-equilibrium process, such as the decay of a heavy particle. In contrast, *darkogenesis* [62, 63] refers to scenarios in which the asymmetry is first generated in the dark sector, and subsequently transferred to the visible sector. This causal structure offers a dynamical explanation for the baryon asymmetry as a consequence of dark sector dynamics. Both approaches are especially attractive as they predict correlated cosmological and laboratory signatures, motivating new searches for exotic baryon-violating processes, dark sector particles, and indirect signatures such as altered cosmic abundances or novel collider decays.

Interestingly, the possibility of a strongly first-order phase transition occurring at MeV-scale temperatures also opens the door to connections with the stochastic gravitational wave background hinted at by recent Pulsar Timing Array (PTA) observations [64]. If confirmed, such signals could point to cosmological dynamics in the very temperature range relevant for low-scale baryogenesis, making this class of models particularly timely and intriguing. We will present a darkogenesis model connected to the scale of the PTA signal in Section 3.3.

1.2 The origin of neutrino masses

1.2.1 From neutrino oscillations to New Physics

Neutrinos are the most enigmatic particles in the SM. First postulated by Wolfgang Pauli in 1930 as a solution to the apparent violation of energy and momentum conservation in β-decay [65], neutrinos were experimentally discovered in 1956 by Reines and Cowan using a nuclear reactor as a source of electron antineutrinos [66]. Since then, neutrinos have been detected from a wide variety of astrophysical and terrestrial sources, see Section 2.1 for details.

A pivotal moment in neutrino physics came with the observation of the so-called *solar neutrino problem*. The Homestake experiment found in the 1960s that the flux of solar neutrinos was significantly lower than the theoretical predictions [67]. This discrepancy persisted across other solar neutrino detectors and was ultimately resolved by the phenomenon of neutrino oscillations.

The idea that neutrinos could change flavor as they propagate, initially proposed by Pontecorvo [68, 69], was experimentally confirmed by the Super-Kamiokande collaboration in 1998 through the observation of atmospheric neutrino oscillations [70]. Further confirmation came from solar neutrino measurements by SNO [71] and reactor neutrino experiments like KamLAND [72].

1.2.2 Flavor Mixing and the PMNS Matrix

In the SM, neutrinos appear in three flavor states ν_e, ν_μ, ν_τ, each associated with a charged lepton. However, neutrino oscillation implies that these flavor states are not the eigenstates of the free Hamiltonian, but rather coherent mixtures of mass eigenstates ν_1, ν_2, ν_3. From neutrino oscillation data it follows that at least two neutrinos must have non-zero masses. This mixing is described by the 3×3 unitary Pontecorvo-Maki-Nakagawa-Sakata (PMNS) matrix U [73]:

$$|\nu_\alpha\rangle = \sum_{i=1}^{3} U_{\alpha i} |\nu_i\rangle \,. \tag{1.25}$$

The PMNS matrix can be parameterized in terms of three mixing angles $\theta_{12}, \theta_{23}, \theta_{13}$ and up to three CP-violating phases. For Dirac neutrinos, only one CP phase δ_{CP} is physical, while for Majorana neutrinos two additional Majorana phases η_1 and η_2 appear. The standard parametrization is given by [74]

$$U_{\mathrm{PMNS}} = \begin{pmatrix} c_{12}c_{13} & s_{12}c_{13} & s_{13}e^{-i\delta_{\mathrm{CP}}} \\ -s_{12}c_{23} - c_{12}s_{23}s_{13}e^{i\delta_{\mathrm{CP}}} & c_{12}c_{23} - s_{12}s_{23}s_{13}e^{i\delta_{\mathrm{CP}}} & s_{23}c_{13} \\ s_{12}s_{23} - c_{12}c_{23}s_{13}e^{i\delta_{\mathrm{CP}}} & -c_{12}s_{23} - s_{12}c_{23}s_{13}e^{i\delta_{\mathrm{CP}}} & c_{23}c_{13} \end{pmatrix} \cdot \begin{pmatrix} 1 & 0 & 0 \\ 0 & e^{i\eta_1} & 0 \\ 0 & 0 & e^{i\eta_2} \end{pmatrix}, \tag{1.26}$$

where $c_{ij} = \cos\theta_{ij}$, $s_{ij} = \sin\theta_{ij}$. The charged current interaction in the mass basis is then given by

$$\mathcal{L}_{\mathrm{CC}} = -\frac{g}{\sqrt{2}} \bar{\ell}_\alpha \gamma^\mu P_L U_{\alpha i} \nu_i W_\mu^- + \mathrm{h.c.} \tag{1.27}$$

1.2.3 Neutrino Oscillations in Vacuum

In vacuum, the transition probability that a neutrino of flavor α will be detected as a neutrino of flavor β after travelling a distance L with energy E is given by:

$$\begin{aligned} P(\nu_\alpha \to \nu_\beta) = \delta_{\alpha\beta} - 4\sum_{i>j} \mathrm{Re}\left[U^*_{\alpha i}U_{\beta i}U_{\alpha j}U^*_{\beta j}\right] \sin^2\left(\frac{\Delta m^2_{ij}L}{4E}\right) \\ +2\sum_{i>j} \mathrm{Im}\left[U^*_{\alpha i}U_{\beta i}U_{\alpha j}U^*_{\beta j}\right] \sin\left(\frac{\Delta m^2_{ij}L}{2E}\right), \end{aligned} \tag{1.28}$$

where $\Delta m^2_{ij} = m^2_i - m^2_j$ are the neutrino mass squared differences and the expression for the antineutrinos are obtained by simply taking the conjugate of the corresponding PMNS matrix elements. This equation illustrates that neutrino oscillations are sensitive to mass squared differences and mixing angles, but not to the absolute value of the mass eigenvalues or to the Majorana phases. We can also see explicitly from Eq. (1.28) that the phase δ_{CP} induces CP violation, as in general $P(\nu_\alpha \to \nu_\beta) \neq \bar{P}(\bar{\nu}_\alpha \to \bar{\nu}_\beta)$.

1.2.4 Experimental Status

The absolute mass scale of neutrinos remains unknown and cannot be accessed through oscillation experiments, which are sensitive only to mass squared differences, see Eq.(1.28). Direct bounds are instead obtained from β-decay experiments such as KATRIN [75], which currently provides an upper bound of $m_\nu < 0.45$ eV (90% C.L.), and from cosmological data [76], which constrain the sum of neutrino masses to be $\sum m_\nu \lesssim 0.07$-0.16 eV depending on the cosmological model and dataset used.

A closely related question in neutrino physics is the *mass ordering*, that is, whether the mass eigenstate ν_3, which has the smallest electron flavor content, is heavier (normal ordering, NO) or lighter (inverted ordering, IO) than the other two. In the NO, the masses satisfy $m_1 < m_2 < m_3$, while in the IO $m_3 < m_1 < m_2$. The labels ν_1, ν_2, and ν_3 are fixed by their flavor composition, with the electron neutrino mixing element $|U_{ei}|^2$ decreasing from ν_1 to ν_3. Current global fits of oscillation data slightly favor the NO, though the statistical significance remains below the 3σ level. Upcoming experiments such as JUNO [77], DUNE [78], and Hyper-Kamiokande [79] are expected to provide a definitive resolution to this question.

The parameters governing neutrino oscillations have been determined with increasing precision over time. Solar, atmospheric, reactor, and accelerator experiments have all contributed to the current picture. In particular, reactor neutrino experiments like Double Chooz [80] and KamLAND [81] have precisely measured θ_{13} and Δm^2_{21}, while long-baseline accelerator experiments such as T2K [82] have provided important constraints on θ_{23} and δ_{CP}.

The CP-violating phase δ_{CP} remains poorly constrained, but current data provide intriguing hints of CP violation in the leptonic sector. In particular, long-baseline (LBL) experiments such as T2K and NOνA have reported a preference for values of δ_{CP} close to $3\pi/2$, which would correspond to maximal CP violation. However, these results are subject to statistical and systematic uncertainties, and there exist some tensions between the datasets of different experiments [83, 84]. Despite these suggestive indications, global fits to all available neutrino oscillation data cannot yet exclude CP-conserving values of δ_{CP}

(i.e., 0 or π) at a statistically significant level. Future LBL experiments such as DUNE and Hyper-Kamiokande are expected to clarify this picture with much greater sensitivity.

Thanks to the synergy of reactor, solar, atmospheric, and accelerator experiments, we now have precise measurements of the three mixing angles and two mass squared differences. Global fits (e.g., NuFit 6.0 [85]) compute the following best-fit values for these parameters, which we report in Table 1.1:

Parameter	**Best Fit $\pm$ 1σ**	**3σ Range**
Δm^2_{21} $[10^{-5}\ \text{eV}^2]$	$7.49^{+0.19}_{-0.19}$	$6.92 - 8.05$
Δm^2_{31} (NO) $[10^{-3}\ \text{eV}^2]$	$2.51^{+0.02}_{-0.02}$	$2.45 - 2.58$
Δm^2_{31} (IO) $[10^{-3}\ \text{eV}^2]$	$2.48^{+0.02}_{-0.02}$	$2.42 - 2.54$
$\sin^2\theta_{12}$	0.308 ± 0.11	$0.275 - 0.345$
$\sin^2\theta_{23}$ (NO)	$0.47^{+0.02}_{-0.01}$	$0.435 - 0.585$
$\sin^2\theta_{23}$ (IO)	$0.55^{+0.01}_{-0.01}$	$0.440 - 0.584$
$\sin^2\theta_{13}$ (NO)	$0.02215^{+0.0006}_{-0.0006}$	$0.02030 - 0.02388$
$\sin^2\theta_{13}$ (IO)	$0.02231^{+0.0006}_{-0.0006}$	$0.02060 - 0.02409$
$\delta_{\text{CP}}/(^\circ)$ (NO)	212^{+26}_{-41}	$124 - 364$
$\delta_{\text{CP}}/(^\circ)$ (IO)	274^{+22}_{-25}	$201 - 335$

Table 1.1: Best-fit values and 3σ ranges of neutrino oscillation parameters for Normal Ordering (NO) and Inverted Ordering (IO). Values taken from the global fit [85]. If not specified, results hold for both mass hierarchies.

1.2.5 Dirac vs Majorana Nature

The observation that neutrinos possess non-zero masses raises a fundamental question about their nature: are they Dirac or Majorana particles? This distinction is closely tied to the conservation of the total lepton number. If neutrinos are Dirac fermions, total lepton number is conserved. In contrast, Majorana neutrinos violate total lepton number by two units, as they are their own antiparticles.

A clear phenomenological difference between these two possibilities arises in the structure of the PMNS matrix. While Dirac phases can be reabsorbed through field redefinitions, the Majorana phases η_1 and η_2 remain physical in the Majorana case and can influence LNV processes, even though they have no impact on neutrino oscillations.

The most promising avenue to experimentally probe the Majorana nature of neutrinos is the search for *neutrinoless double beta decay* ($0\nu\beta\beta$), a hypothetical nuclear process in which a nucleus undergoes double beta decay without emitting neutrinos. Observation of this process would unambiguously signal LNV and confirm that neutrinos are Majorana particles.

Assuming that the decay is mediated by light neutrinos, its half-life is [86]

$$T_{1/2}^{-1} = G(Q,Z)\ g_A^4\ M^2\ \frac{|m_{\beta\beta}|^2}{m_e^2}, \tag{1.29}$$

where $G(Q,Z)$ is the phase-space integral, which depends on the atomic number Z of the decaying nucleus and on the Q-value of the reaction; $g_A \simeq 1.27$ [87] is the axial-vector

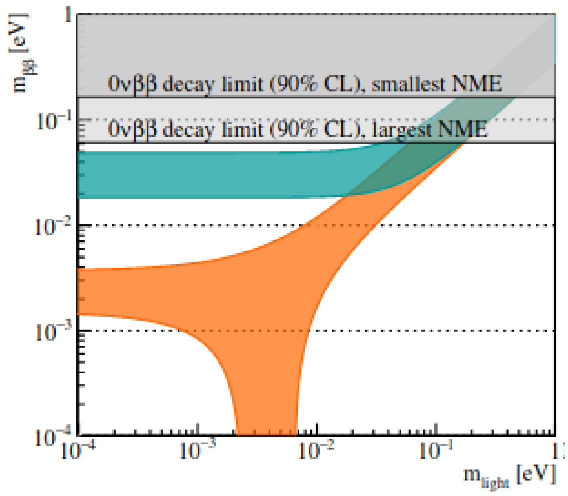

Figure 1.1: Maximally allowed parameter space for $|m_{\beta\beta}|$ as a function of the lightst neutrino mass, assuming central value of neutrino oscillation parameters. The orange and green areas show the parameter space allowed assuming NO and IO, respectively. The shaded areas indicate the regions already excluded by $0\nu\beta\beta$ searches. Figure taken from Ref. [89].

coupling; M is the nuclear matrix element, which accounts for all the hadronic current effects inside the nucleus; $m_{\beta\beta}$ is the effective Majorana mass, normalized for convenience by the electron mass m_e. The quantity $G(Q, Z)$ is typically of order $(10^{-14}\text{-}10^{-15})$ yr^{-1} for common isotopes such as ^{76}Ge and ^{136}Xe [88]. The nuclear matrix element M is dimensionless and typically ranges from 1 to 5 depending on the nuclear model adopted [89]. Finally, the effective Majorana mass $m_{\beta\beta}$ is given by

$$|m_{\beta\beta}|^2 = \left|m_1|U_{e1}|^2 + m_2|U_{e2}|^2 e^{i\eta_1} + m_3|U_{e3}|^2 e^{i\eta_2}\right|^2,$$

which depends on the neutrino masses, the mixing angles and the Majorana phases. Theoretical predictions for $|m_{\beta\beta}|$ depend significantly on the neutrino mass ordering, see Figure 1.1:

- In the **IO**, $|m_{\beta\beta}|$ has a lower bound given by $|m_{\beta\beta}| \leq 18.4 \pm 1.3$ meV, whose uncertainty is dominated by the uncertainty on the solar mixing angle θ_{12}.

- In the **NO**, destructive interference may allow $|m_{\beta\beta}|$ to vanish.

So far, no confirmed $0\nu\beta\beta$ event has ever been observed in any of the numerous dedicated experiments. Current and future $0\nu\beta\beta$ experiments aim to reach sensitivities that can probe the IO region [89]. A positive signal would confirm the Majorana nature of neutrinos, while a null result would begin to constrain or rule out the IO scenario, depending on the uncertainties in the nuclear matrix elements involved.

The interplay of future neutrino oscillation measurements, cosmological observations, and searches for rare processes such as $0\nu\beta\beta$ decay will be essential to fully characterize neutrino properties and their implications for physics beyond the SM.

1.2.6 Neutrino masses and mixings

The discovery of neutrino oscillations has firmly established that neutrinos have non-zero masses, thereby requiring an extension of the SM. However, the nature of these masses, whether they are of Dirac or Majorana type, remains unknown. This question is not only central to understanding the fundamental properties of neutrinos, but also intimately linked to LNV and to the structure of possible UV completions of the SM.

From the theoretical standpoint, the distinction between Dirac and Majorana neutrinos hinges on the conservation or violation of lepton number. In the Dirac case, one introduces right-handed neutrinos ν_R, which are singlets under the SM gauge group. This allow introducing a Yukawa interaction with the SM Higgs doublet H and the left-handed neutrinos ν_L, analogous to the interactions responsible for the masses of charged leptons and quarks:

$$\mathcal{L}_Y = -y_\nu \, \overline{L}\tilde{H}\nu_R + \text{h.c.}, \tag{1.30}$$

where L is the lepton doublet and $\tilde{H} = i\sigma_2 H^*$. After EWSB a Dirac mass term is generated as

$$\mathcal{L}_D = -m_D \, \overline{\nu_L}\nu_R + \text{h.c.}, \tag{1.31}$$

with $m_D = y_\nu v/\sqrt{2}$. In this case, lepton number is conserved, with the assignment $L(\nu) = 1$, $L(\bar{\nu}) = -1$, and the neutrino behaves like any other Dirac fermion. However, the smallness of the observed neutrino masses would imply Yukawa couplings $y_\nu \sim \mathcal{O}(10^{-12})$, much smaller than those of all the other fermions in the SM.

In contrast, if one introduces a right-handed neutrino ν_R as a gauge singlet, its SM-neutral nature allows the construction of a Majorana mass term $\frac{1}{2}M_R \, \overline{\nu_R^c}\nu_R$. This term is not forbidden by any SM gauge symmetry, making it a technically natural extension. In this framework, the smallness of the light neutrino masses arises not from tiny Yukawa couplings, but from the suppression due to the large Majorana mass scale M_R. Thus, the Majorana scenario provides a more appealing and economical explanation, both from a symmetry perspective and in terms of naturalness.

However, in the minimal SM, where no right-handed neutrino is present, one cannot write a mass term for neutrinos at the renormalizable level. The left-handed neutrino ν_L, being part of an $SU(2)_L$ doublet, cannot form a gauge-invariant Majorana mass term without introducing additional fields or violating gauge symmetry. Consequently, any attempt to generate neutrino masses and violate lepton number must occur through higher-dimensional operators.

The key theoretical tool to describe the generation of Majorana neutrino masses at low energies is the *Weinberg operator* [90], a dimension-5 effective operator that violates lepton number by two units and represents the leading contribution to neutrino masses in an effective field theory expansion:

$$\mathcal{O}_5 = \frac{C_5^{\alpha\beta}}{\Lambda}(\bar{L}^c_\alpha H)(H^T L_\beta) + \text{h.c.} \tag{1.32}$$

Here, L is the SM lepton doublet, with α and β flavor indices, H the Higgs doublet, Λ the scale of new physics, and C_5 a dimensionless flavor matrix. After electroweak symmetry breaking, this operator yields a Majorana mass for neutrinos:

$$(m_\nu)_{\alpha\beta} = \frac{C_5^{\alpha\beta} v^2}{\Lambda}, \tag{1.33}$$

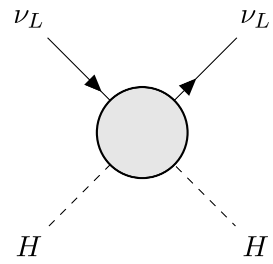

Figure 1.2: Representation of the Weinberg operator O_5 defined in Eq. (1.33). Being of $\mathcal{D} = 5$ it must be generated by some BSM physics above the EW scale.

where $v \approx 246\,\text{GeV}$ is the Higgs vacuum expectation value. The observed tiny masses of the neutrinos are naturally explained for $\Lambda \sim 10^{14}\,\text{GeV}$, assuming $C_5 \sim \mathcal{O}(1)$.

The Weinberg operator is not fundamental as it is not renormalizable but can be UV completed in several ways. In particular, there are three possible 4-dimensional operators allowed by the SM gauge group that can generate the Weinberg operator at tree-level [91]. These are classified on the basis of the type of the heavy mediator which is integrated out in the low-energy theory. It can be either a fermion singlets N [42], $SU(2)_L$ triplet scalars Δ [92, 93], or $SU(2)_L$ triplet fermions Σ [94]. We refer to these specific realizations as the type-I seesaw for the singlet fermion, type-II seesaw for the triplet scalar and type-III seesaw for the triplet fermion. In addition to tree-level realizations, there are radiative neutrino mass models, see [95] for a review, where the smallness of neutrino masses is justified by the fact that they appear at the loop level, compared to those of the other SM fermions. We will briefly review the phenomenology of these neutrino mass mechanisms in this section.

1.2.7 The Seesaw Mechanism

The *seesaw mechanism* is the current high-energy theory paradigm for the generation of the neutrino masses. The attractiveness of this framework stems from several key features. First, it is minimal, requiring only the addition of a single new field to the SM. Second, it provides a natural explanation for the smallness of neutrino masses. Third, it allows for leptogenesis at high energies, thanks to LNV interactions, offering a possible origin for the observed BAU, something that would not occur if neutrinos were purely Dirac particles. Then, the theory is renormalizable at high energies, containing a finite set of parameters that, in principle, can be fully constrained by low-energy measurements. Finally, this setup can be elegantly embedded into larger unified frameworks such as $\text{SU}(2)_L \times \text{SU}(2)_R$ or SO(10), linking neutrino physics to more unified theories of fundamental interactions.

- **Type-I seesaw** [42]:

  The type-I seesaw mechanism extends the SM by introducing $n \geq 2$ copies of right-handed, SM singlet, neutrino fields N_R, sharing the same quantum numbers as the previously defined ν_R, but are now allowed to possess large Majorana masses M_R. The most general renormalizable Lagrangian involving these fields is given by

$$\mathcal{L}_{\text{SS1}} = \mathcal{L}_{\text{SM}} + i\overline{N_R}\partial\!\!\!/ N_R - \left(\overline{L}Y_\nu \tilde{H} N_R + \frac{1}{2}\overline{N_R^c} M_R N_R + \text{h.c.}\right), \tag{1.34}$$

where Y_ν is a general $n \times 3$ Yukawa coupling matrix, and M_R is a symmetric $n \times n$ Majorana mass matrix.

After electroweak symmetry breaking, the neutral lepton mass terms can be written in the basis (ν_L, N_R^c) as

$$-\mathcal{L}_\nu = \frac{1}{2}\begin{pmatrix}\overline{\nu_L} & \overline{N_R^c}\end{pmatrix}\begin{pmatrix}0 & m_D^T \\ m_D & M_R\end{pmatrix}\begin{pmatrix}\nu_L^c \\ N_R\end{pmatrix} + \text{h.c.}, \tag{1.35}$$

where the Dirac mass matrix is $m_D = Y_\nu \frac{v}{\sqrt{2}}$. Assuming the hierarchy $m_D \ll M_R$, the effective mass matrix for the light neutrinos is given by

$$m_\nu \approx -m_D^T M_R^{-1} m_D. \tag{1.36}$$

This naturally explains the smallness of neutrino masses if the right-handed neutrinos have large masses, typically around 10^{14} GeV for $Y_\nu \sim \mathcal{O}(1)$. While the large scale of M_R makes the testability of this model challenging, the type-I seesaw still provides an elegant and minimal mechanism for generating neutrino masses.

- **Type-II seesaw** [92]: The type-II seesaw mechanism extends the Standard Model by introducing a scalar $\mathrm{SU}(2)_L$ triplet Δ with hypercharge $Y = 1$, which can be written as

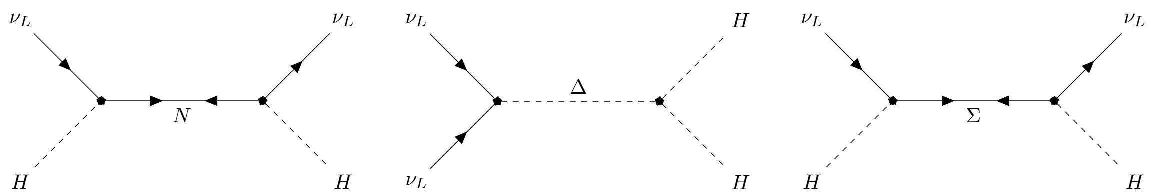

Figure 1.3: Diagramatic representation of neutrino mass generation via the seesaw mechanism : (left) type-I via fermion singlet N, (center) type-II via scalar triplet Δ, and (right) type-III via fermion triplet Σ.

$$\Delta = \frac{\sigma_i}{\sqrt{2}}\Delta_i = \begin{pmatrix}\frac{\Delta^+}{\sqrt{2}} & \Delta^{++} \\ \Delta^0 & -\frac{\Delta^+}{\sqrt{2}}\end{pmatrix}.$$

The relevant Yukawa interaction coupling the triplet to the lepton doublets is

$$\mathcal{L}_Y = -Y_\Delta \overline{L^c} i\sigma_2 \Delta L + \text{h.c.},$$

where Y_Δ is a symmetric matrix in flavor space. The scalar potential contains a crucial trilinear term

$$V \supset \mu H^T i\sigma_2 \Delta^\dagger H + \text{h.c.}, \tag{1.37}$$

where μ is a dimensionful parameter that explicitly breaks lepton number by two units. This term induces a small vacuum expectation value for the neutral triplet component after electroweak symmetry breaking, $v_\Delta \approx \frac{\mu v^2}{\sqrt{2} m_\Delta^2}$, being m_Δ the mass of the triplet scalar. The neutrino mass matrix is then generated as

$$m_\nu = \sqrt{2}\, Y_\Delta v_\Delta, \tag{1.38}$$

showing the direct connection between the neutrino mass scale and the induced triplet VEV. Indeed, m_Δ does not to be close to the GUT scale as in the type-I Seesaw, since μ is technically small, as it breaks lepton number. The scalar triplet Δ in the type-II seesaw is typically heavy, with its vacuum expectation value constrained to lie within the range

$$\mathcal{O}(10^{-2}\ \text{eV}) \lesssim v_\Delta \lesssim \mathcal{O}(1\ \text{GeV}),$$

where the lower bound ensures perturbative Yukawa couplings and the upper bound arises from electroweak precision measurements [96]. Moreover, if m_Δ lies near the TeV scale or below, these new scalars can produce rich phenomenological signatures, particularly at collider experiments. The doubly-charged scalars $\Delta^{\pm\pm}$ offer especially distinctive signals, such as same-sign dilepton events, which provide a promising avenue for experimental tests. Recent studies have extensively analyzed the constraints and discovery prospects of the type-II seesaw scalars in various experimental contexts [97].

- **Type-III seesaw** [94]:

  In the type-III seesaw mechanism, the SM is extended by at least two $\mathrm{SU}(2)_L$ fermion triplets with zero hypercharge, denoted as $\Sigma = (\Sigma^+, \Sigma^0, \Sigma^-)$. These are vector-like fermions with a Majorana mass term and couple to the SM lepton doublets via Yukawa interactions. The relevant part of the Lagrangian is:

$$\mathcal{L} \supset \mathrm{Tr}\left[\overline{\Sigma} i \not{D} \Sigma\right] - \frac{1}{2}\mathrm{Tr}\left[\overline{\Sigma^c} M_\Sigma \Sigma\right] - \sqrt{2}\, Y_\Sigma^{\alpha i}\, \overline{L_\alpha} \Sigma^i \tilde{H} + \text{h.c.}, \tag{1.39}$$

  where L_α is the SM lepton doublet of generation α and i runs over the triplet components. After electroweak symmetry breaking, this leads to the neutrino mass matrix in the basis (ν_L, Σ^0):

$$\mathcal{M} = \begin{pmatrix} 0 & m_D \\ m_D^T & M_\Sigma \end{pmatrix}, \quad \text{with } m_D = \frac{Y_\Sigma v}{\sqrt{2}}. \tag{1.40}$$

  Assuming $m_D \ll M_\Sigma$, the heavy triplets can be integrated out, yielding an effective mass for the light neutrinos:

$$m_\nu = -m_D M_\Sigma^{-1} m_D^T = -\frac{v^2}{2} Y_\Sigma M_\Sigma^{-1} Y_\Sigma^T. \tag{1.41}$$

  While the neutrino mass matrix has the same structure of the type-I seesaw, this mechanism features a richer phenomenology. Indeed, as the triplets are charged under $\mathrm{SU}(2)_L$, they can be produced via electroweak interactions, making the type-III seesaw potentially testable at colliders. Moreover they mix with the SM charged leptons with the NP states through the Yukawa Y_Σ. As a result, direct searches impose stringent lower bounds on the mass of the triplet, which should be larger than the TeV scale [98].

Besides tree level realizations of the Weinberg operator, radiative models provide an appealing alternative to tree-level seesaw mechanisms by generating neutrino masses at loop level. The loop suppression naturally explains the smallness of neutrino masses without requiring extremely high-scale physics or tiny Yukawa couplings. These models [99, 100, 101] often involve new particles at or below the TeV scale, making them testable at current or near-future experiments. A particularly attractive feature is the possibility of connecting neutrino mass generation to the DM problem: in many radiative models, the same symmetry that forbids a tree-level mass term also stabilizes a viable DM candidate. A well known example is the Scotogenic model [102], where neutrino masses are generated via a one-loop diagram involving a scalar doublet and singlet fermions, all odd under a $\mathbb{Z}_2$ symmetry. This symmetry not only enables radiative neutrino masses but also ensures the stability of the lightest new particle, which can serve as a DM candidate. Thus, radiative models offer a minimal and economical framework to simultaneously address two of the most pressing open questions in particle physics.

1.3 The search for Dark Matter

The aim of this section is to provide a structured overview of the theoretical and experimental landscape related to the dark matter puzzle. We begin by reviewing the observational evidences for dark matter from astrophysical and cosmological probes. We then discuss the main strategies to detect dark matter, highlighting both the prospects and current limitations of each approach. Particular attention is given to the thermal freeze-out mechanism and the so-called "WIMP miracle," which has historically guided much of the experimental effort. We also discuss more recent developments that extend the DM mass range below the GeV scale, as well as alternative candidates beyond the WIMP paradigm. This organization is designed to guide the reader from established empirical facts to theoretical frameworks and current frontiers in dark matter research, setting the stage for the more model specific discussions in Sec. 3.3 and Sec. 4.1.

1.3.1 Evidences for Dark Matter

Astrophysical and cosmological observations strongly point towards the existence of a massive, weakly-interacting component of our Universe. These observations are only sensitive to the gravitational interaction of this component, which is therefore refered to as Dark Matter (DM). Due to its elusive nature and far reaching implications, the study of DM stands at the intersection of cosmology, astrophysics, and particle physics, making it one of the most active and interdisciplinary areas of research in modern science. The current concordance model of cosmology, known as the ΛCDM model, provides a remarkably successful framework for describing the large-scale structure and evolution of the Universe. In this model, the energy content of the Universe today is dominated by three main components: *dark energy* Λ, responsible for the accelerated expansion of the Universe; *cold* DM (CDM), a neutral, non-relativistic, pressureless form of matter that clusters gravitationally and drives structure formation; and ordinary baryonic matter. Together with a nearly scale-invariant spectrum of primordial perturbations and the assumption of a spatially flat Universe, the ΛCDM model has proven to be in excellent agreement with a wide array of observations, from the CMB to galaxy surveys and large-scale structure. DM plays a central role within this framework, acting as the gravitational potential source for the formation of galaxies and clusters. In the remainder of this section, we summarize the key astrophysical and cosmological observations that support the existence of this dark component.

Astrophysical Evidences for DM

One of the earliest and most direct evidence for DM arises from the study of galactic rotation curves of spiral galaxies. For a star of mass m in uniform circular motion at a distance r from the galactic center, Newton's second law yields the circular velocity v_c as

$$v_c^2(r) = \frac{GM(r)}{r}, \qquad \text{with} \quad M(r) = 4\pi \int_0^r r'^2 \rho(r')\, dr', \tag{1.42}$$

where $\rho(r)$ is the radial mass density of the galaxy and $M(r)$ the total enclosed mass. In a galaxy where the visible matter is concentrated within a finite radius (typically $\sim$ 10–20 kpc), one expects the circular velocity to decay as $v_c(r) \propto 1/\sqrt{r}$ beyond this radius. However, astronomical observations, first performed by Rubin and Ford in the 1970s [103], reveal that $v_c(r)$ remains approximately constant even far beyond the visible edge of galaxies. This observation points to the presence of an extended mass distribution not accounted for by luminous matter. The flatness of the rotation curves suggests a halo of matter that does not emit or absorb light, and which extends beyond the galactic disk, up to 100–200 kpc and following a density profile $\rho(r) \propto 1/r^2$, such that $M(r) \propto r$ at large r. We show in Figure 1.4 (left panel), the rotation curve of the galaxy NGC 6503, with the contribution of visible matter and DM.

In 1933, Zwicky measured the velocity dispersion σ_v of galaxies in the Coma cluster [104] and, using the virial theorem, inferred a total cluster mass much larger than that deduced from visible matter:

$$\sigma_v^2 = \frac{3GM}{5R}, \tag{1.43}$$

where R is the cluster radius and M its total mass. The observed dispersion velocity, $\sigma_v \sim 100$ km/s, far exceeded the value expected from the luminous mass, pointing again to a substantial dark component. While galactic rotation curves provide compelling evidence for DM on galactic scales, complementary techniques have been developed to probe its presence at the scale of galaxy clusters. In particular, X-ray observations of the hot intracluster medium offer an independent method to infer the total mass of clusters, providing further support for the existence of a dominant non-luminous component. Indeed, hot intracluster gas emits X-rays via bremsstrahlung and inverse Compton scattering, and its temperature and density profile can be related to the total cluster mass under hydrostatic equilibrium:

$$M(r) = -\frac{k_B T_{\rm gas} r}{G\mu_{\rm gas}}\left(\frac{d\ln n_{\rm gas}}{d\ln r} + \frac{d\ln T_{\rm gas}}{d\ln r}\right), \tag{1.44}$$

where $T_{\rm gas}$ and $n_{\rm gas}$ are the temperature and number density of the gas, and $\mu_{\rm gas}$ is the mean molecular weight. Observations show that the visible matter (galaxies and hot gas) accounts for only a fraction of the total inferred mass [105]. Similar signatures have been observed in other merging clusters, such as MACS J0025.4-1222 [106] and the Virgo cluster [107], establishing the presence of DM in a wide class of systems.

Gravitational lensing provides a further, independent evidence for DM. When light from a background galaxy passes near a massive cluster, its path is bent, leading to distorted images. In the weak lensing regime, such distortions yield the projected mass distribution. A striking example is the Bullet Cluster, a merger of two galaxy clusters. Weak lensing maps show that the dominant mass components are not associated with the X-ray-emitting gas but rather with regions containing little baryonic matter, thus providing strong evidence for the existence of collisionless DM [108] (see right panel of Figure 1.4).

Cosmological evidences for DM

The most convincing and precise evidence for DM comes from the largest possible scale, namely the observable Universe. The basic point, qualitatively, is that our Universe would not have acquired the features that we observe today if not for the critical role played by DM. Without it, galaxies would not be distributed in their current web-like structure, and the anisotropies in the CMB would not exhibit the precise features that we measure. In this sense, DM acts as an indispensable catalyst for the formation of cosmic structures.

This becomes evident when considering early Universe cosmology. Tiny fluctuations in the primordial plasma, imprinted as temperature anisotropies in the CMB, evolved over billions of years into the large-scale structure of the Universe. These fluctuations required gravitational amplification, which was primarily driven by the DM component, as baryonic

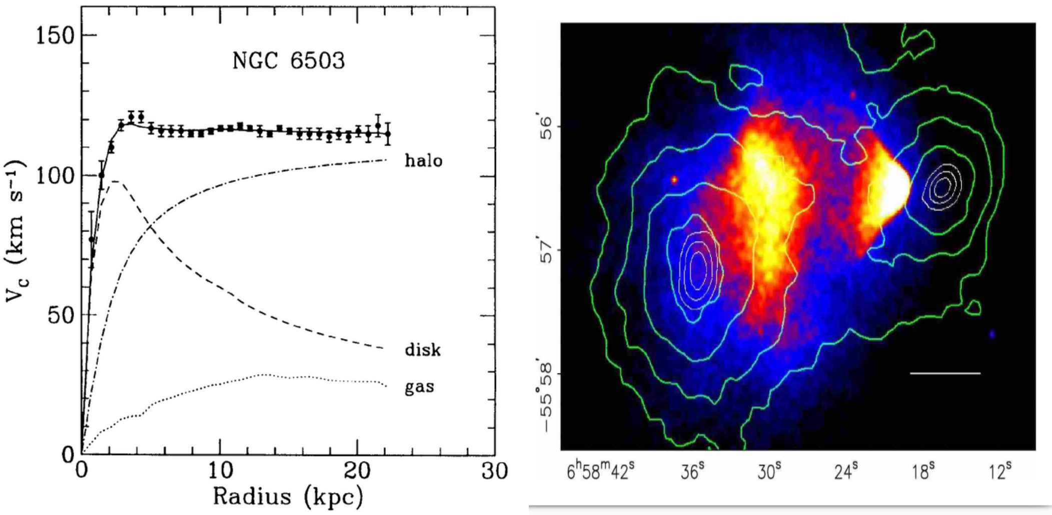

Figure 1.4: **Astrophysical evidences of DM:** The rotation curve of Galaxy NGC 6503 [109] (left). Bullet cluster: colored map representing the X-ray image of the hot baryonic gas. See the displacement from the distribution of the total mass reconstructed through weak lensing, shown in green. Figure taken from [108].

matter alone was too tightly coupled to radiation before recombination. As such, cosmological observables, especially the CMB spectrum, baryon acoustic oscillations (BAO), large-scale structure (LSS), and Lyman-α forest data, offer some of the most powerful and precise constraints on the abundance and nature of DM.

Among these, the CMB provides a particularly robust probe. During recombination, photons decoupled from matter and formed a nearly uniform blackbody radiation with small anisotropies at the level of 10^{-5}. These anisotropies can be parametrized via the following expansion at a specific position in the sky (θ, ϕ):

$$T(\theta, \phi) = T_0 + \sum_{\ell=0}^{\infty} \sum_{m=-\ell}^{\ell} a_{\ell m} Y_{\ell m}(\theta, \phi)\,, \tag{1.45}$$

where $T_0 = 2.7255 \pm 0.0006$ K the average CMB temperature[110], $Y_{\ell m}(\theta, \phi)$ the spherical harmonics and their angular power spectrum $C_\ell = \langle |a_{\ell m}|^2 \rangle$ encodes information on cosmological parameters.

The position and height of the acoustic peaks in the CMB angular power spectrum are highly sensitive to the matter content of the Universe. Fitting the flat ΛCDM model to the PLANCK data constrains the physical baryon and DM densities to be $\Omega_b h^2 = 0.0224 \pm 0.0001$ and $\Omega_{\rm DM} h^2 = 0.119 \pm 0.001$, respectively [14].

The CMB also confirms the need for DM at the time of recombination: without it, BAO would be overdamped and inconsistent with observations. Indeed, the evolution of the Universe from the nearly homogeneous state observed in the CMB to the complex web of galaxies and clusters seen today cannot be explained by baryonic matter alone. A non-luminous and non-relativistic component that interacts gravitationally is required to drive the growth of structures and to reproduce the observed distribution of matter across cosmic time.

The observed large-scale distribution of matter in the Universe is well described by the *matter power spectrum*, which quantifies the variance of matter density fluctuations across different length scales. In Fourier space, the power spectrum $P(k)$ is defined as:

$$\langle\delta(\vec{k})\delta^*(\vec{k}')\rangle = (2\pi)^3\delta^{(3)}(\vec{k}-\vec{k}')P(k), \tag{1.46}$$

where $\delta(\vec{k})$ is the Fourier transform of the matter overdensity field $\delta(\vec{x}) = \frac{\rho(\vec{x})-\bar{\rho}}{\bar{\rho}}$, and $\vec{k}$ is the comoving wavenumber, inversely related to spatial scale.

The power spectrum serves as a powerful unifying tool in cosmology, connecting early Universe physics with present day structure. Its shape and amplitude encode the imprint of primordial perturbations, often assumed to arise from inflation, and their evolution under gravitational instability in a Universe dominated by DM.

A key feature of the matter power spectrum is the imprint of BAO. These originate from the same acoustic waves in the photon–baryon plasma that give rise to the peaks in the CMB spectrum. Before recombination, photons and baryons were tightly coupled, forming a relativistic fluid that supported sound waves. As the Universe expanded and cooled, neutral hydrogen formed and photons decoupled, leaving a characteristic scale in the matter distribution: the sound horizon at the drag epoch.

This scale acts as a standard ruler in the late-time Universe, appearing as a distinct feature in the two-point correlation function of galaxies and as periodic "wiggles" in the matter power spectrum. The BAO scale has been precisely measured in galaxy surveys such as BOSS and eBOSS [111, 112], providing independent constraints on the expansion history, spatial curvature, and matter content of the Universe. In particular, BAO data consistently support a Universe with CDM, as purely baryonic models would predict a significantly different pattern of clustering [111].

At smaller scales ($k \gtrsim h\,\mathrm{Mpc}^{-1}$), the matter power spectrum can be probed by the *Lyman-α forest*. The forest consists of a series of absorption lines in the spectra of distant quasars, caused by neutral hydrogen clouds in the intergalactic medium (IGM). The pattern and distribution of these lines trace the underlying density field and are sensitive to the shape and amplitude of the matter power spectrum at scales of ~ 1 Mpc. Lyman-α data constrain not only the total amount of DM but also its properties, such as its thermal history and free-streaming length. For instance, they place lower bounds on the mass of warm DM candidates, since such particles would erase small-scale structure. Observations from SDSS and XQ-100 have been used to exclude thermal relic warm DM with masses below a few keV [113]. These observations are sensitive to the suppression of power at small scales that would occur in scenarios with warm or hot DM, due to their free-streaming effect erasing small-scale structures. Current Lyman-α data are consistent with CDM, lending further support to the standard ΛCDM paradigm.

Together, these cosmological observables, namely CMB anisotropies, large-scale structure, BAO, and the Lyman-α forest, points to a consistent and precise picture of the Universe as dominated by cold, collisionless DM. Each of these probes tests different epochs and scales of cosmic evolution, and yet they all converge on the need for a DM component with properties well captured by the ΛCDM paradigm. The success of this model across such diverse datasets is one of the strongest indirect arguments for the existence of DM, even though its fundamental nature remains unknown.

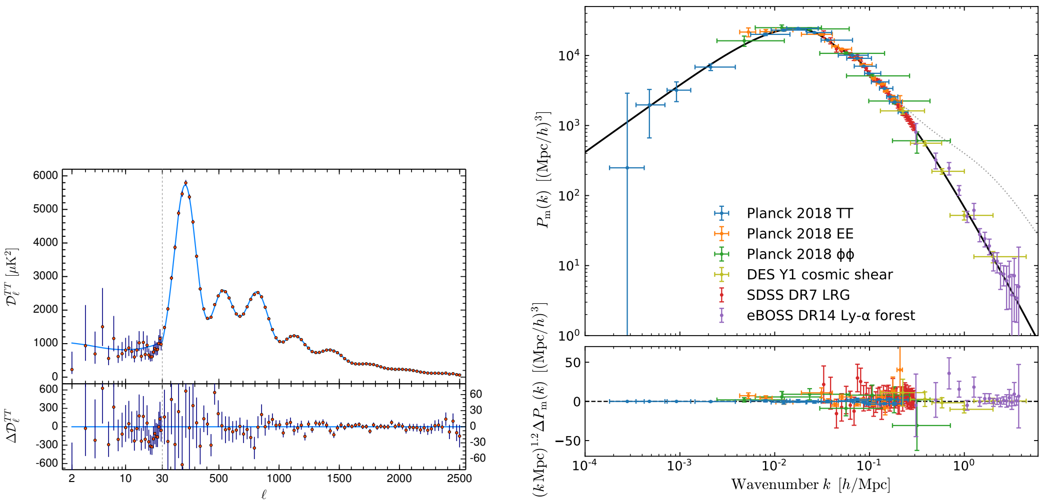

Figure 1.5: **Cosmological evidences of DM:** PLANCK measurements of the variance of the CMB temperature anisotropies across a range of angular scales (red) together with a 6-parameter fit to the flat ΛCDM model (blue) [14] (left panel). Measurements of the linear matter power spectrum via CMB, galaxy clustering, Lyman-α forest and weak lensing data, Figure from [114] (right panel).

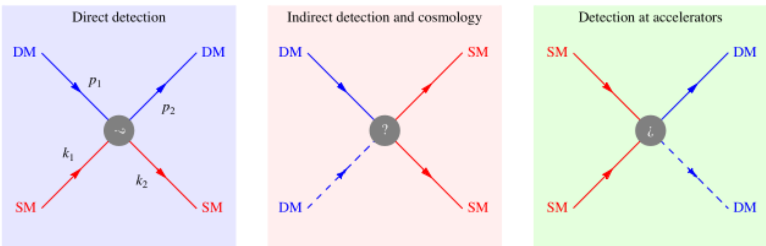

Figure 1.6: Main DM search strategies: direct detection, indirect detection and production of particle at accelerators. Figure taken from [115].

1.3.2 Detection strategies

Having established the need for DM through a variety of astrophysical and cosmological observations, the next fundamental question is how to detect it directly. Under the assumption that DM consists of elementary particles that interact, albeit very weakly, with SM particles, a broad experimental program has been developed to search for such interactions. These efforts are commonly categorized into three main strategies: *direct detection*, which aims to measure the recoil of nuclei from rare DM scattering events in terrestrial detectors; *indirect detection*, which seeks the by-products of DM annihilation or decay (such as photons, neutrinos, or charged cosmic rays); and *collider production*, where DM particles may be created in high-energy collisions, such as those at the LHC, and inferred through missing energy signatures. Each of these approaches probes complementary regions of the DM parameter space and, together, form a comprehensive framework for exploring the particle nature of DM.

Direct Detection

Direct detection (DD) of DM aims to measure the rare collisions between DM particles and atomic nuclei in underground detectors. In 1985, Goodman and Witten proposed that DM particles inhabiting the Galactic halo might be detected through nuclear recoils induced by their elastic scattering off the nuclei [116]. Since then, this has become a cornerstone of experimental DM searches.

The differential nuclear recoil rate, as a function of the recoil energy E_r, is given by:

$$\frac{dR}{dE_r}(E_r, t) = \frac{\rho_\odot}{m_N m_{\rm DM}} \int_{v_{\rm min}}^{v_{\rm esc}} d^3\vec{v}\, v\, f(\vec{v} + \vec{v}\oplus(t)) \frac{d\sigma}{dE_r}(E_r, v)\,, \tag{1.47}$$

where m_N is the target nucleus mass, $m_{\rm DM}$ the DM mass, $\rho_\odot \simeq 0.4$ GeV/cm^3 the local DM density and $d\sigma/dE_r$ the differential scattering cross section. The function $f(\vec{v}+\vec{v}\oplus(t))$ is the velocity distribution of DM particles in the Earth frame, typically modeled as a truncated Maxwell-Boltzmann distribution. The quantity $v_{\rm min} = \sqrt{\frac{m_N E_r}{2\mu_{\chi N}^2}}$ is the minimum velocity required to produce a recoil of energy E_r, being $\mu_{\chi N} = \frac{m_N m_{\rm DM}}{m_N + m_{\rm DM}}$ the reduced mass of the DM-nucleus system; finally $v_{\rm esc}$ is the escape velocity from the MW gravitational potential.

Due to the Earth's orbit around the Sun and the Sun's motion around the Galactic center, the Earth's velocity in the Galactic frame varies throughout the year, producing an annual modulation in the event rate. The expected modulation amplitude is $\sim 5\%$. The DAMA Collaboration claims to have detected this expected seasonal variation in the measured event rate [117]. However, the DAMA observation is puzzling in reason of the absence of any statistical significant excess above the background in other DD experiments [118, 119].

To translate the theoretical predictions of DM scattering into experimental constraints on the cross section, one computes the expected number of recoil events in a detector using Eq. (1.47) and the appropriate differential cross section, spin-independent (SI) or spin-dependent (SD). The total number of events is given by:

$$N_{\rm events} = \int_{E_{\rm min}}^{E_{\rm max}} dE_r\, \epsilon(E_r) \frac{dR}{dE_r}(E_r), \tag{1.48}$$

where $\epsilon(E_r)$ is the detector efficiency and $[E_{\rm min}, E_{\rm max}]$ is the detector's recoil energy range sensitivity.

This DM induced signal is then compared with the observed data or a well-modeled background spectrum. In the absence of an excess above background, statistical methods are used to derive upper bounds on the DM-nucleon cross section.

For SI interactions, DM couples coherently to all nucleons, leading to an enhanced cross section proportional to A^2, where A is the atomic mass number. The differential SI cross section is given by [115]:

$$\frac{d\sigma_{\rm SI}}{dE_r} = \frac{m_A A^2 \sigma_{\rm SI}}{2\mu_{\chi N}^2 v^2} F^2(q), \tag{1.49}$$

where $\sigma_{\rm SI}$ is the DM-nucleon SI cross section, $\mu_{\chi N}$ the reduced mass of the DM-nucleon system, and $F(q)$ the nuclear form factor, with $q = \sqrt{2m_A E_r}$ the momentum transfer. In the non-relativistic limit $q \to 0$ and $F(q) \to 1$; the SI interaction is coherently enhanced. The total SI cross section is then given by:

$$\sigma_{\rm SI}^A = \sigma_{\rm SI}^N \frac{\mu_{\chi A}^2}{\mu_{\chi N}^2} A^2, \tag{1.50}$$

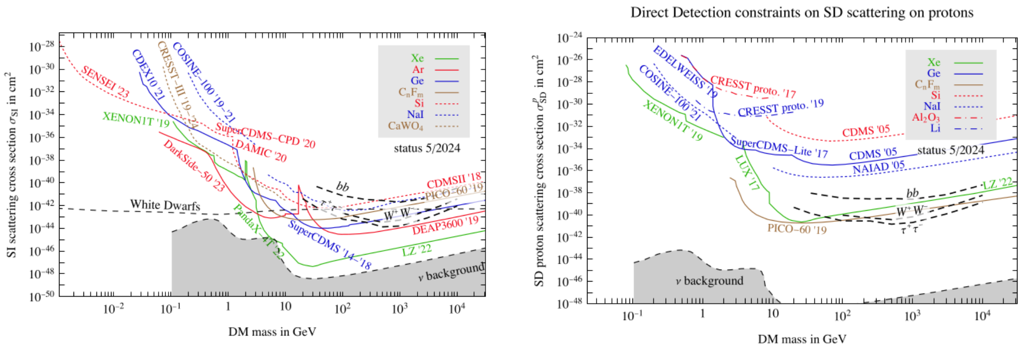

Figure 1.7: Bounds on the spin-independent (SI) DM-nucleon scattering cross-section (left panel) and spin-indpendent (SD) DM-proton cross-section (right panel) from DM direct detection. Also shown is the irreducible neutrino backround in grey. The sub-GeV mass region is discussed in further detail in Section 1.3.5. Figure taken from [115].

where $\sigma_{\rm SI}^N$ is the SI cross section for scattering off a single nucleon.

In contrast, spin-dependent (SD) interactions arise from the coupling of the DM spin to the nuclear spin. The SD differential cross section is more involved and sensitive to nuclear structure and can be written as:

$$\frac{d\sigma_{\rm SD}}{dE_r} = \frac{m_A}{2v^2}\frac{J_{\rm DM}(J_{\rm DM}+1)}{(2J_A+1)}\sum_{\tau,\tau'} c_\tau c_{\tau'} W^{\tau\tau'}(q), \tag{1.51}$$

where $J_{\rm DM}$ and J_A are the spins of the DM particle and nucleus, respectively, and $W^{\tau\tau'}(q)$ are nuclear response functions [115]. The c_τ coefficients encode the DM couplings to proton and neutron spin content.

In the non-relativistic limit, the SD cross section can be approximated by:

$$\frac{d\sigma_{\rm SD}}{dE_r} = \frac{m_A \sigma_{\rm SD} S(q)}{2\mu_{\chi N}^2 v^2}, \tag{1.52}$$

where $S(q)$ encapsulates the SD nuclear form factors. Unlike SI interactions, there is no A^2 enhancement, making SD detection more challenging.

Figure 1.7 shows current constraints on $\sigma_{\rm SI}$ and $\sigma_{\rm SD}$ as a function of $m_{\rm DM}$ from various experiments. The most stringent bounds for $m_{\rm DM} \geq 10$ GeV come from liquid xenon experiments like XENON1T [119], XENONnT [120], LZ [121] and PandaX [122].

At low DM masses ($m_{\rm DM} \lesssim 10$ GeV), the limits weaken due to insufficient recoil energy. Techniques like probing electronic recoils or utilizing the Migdal effect [123] have been proposed to address this. These approaches have gained significant traction in recent years as promising avenues for sub-GeV DM detection, see Sec. 1.3.5 for more details and [124] for a review.

As experimental sensitivities improve, they approach the so-called *neutrino fog* [125], that is the background arising from solar, atmospheric, and diffuse supernova neutrinos, which mimic the DM induced signal and will ultimately limit the reach of DD experiments unless new techniques for background discrimination are developed.

Indirect Detection

Indirect detection of DM aims to identify the annihilation or decay products of DM particles in the form of gamma rays, antimatter, or neutrinos. These products may show up as anomalies in the cosmic ray spectrum; to this purpose the most promising sources to investigate are those with high DM densities, such as the Galactic center (GC), dwarf spheroidal galaxies, and galaxy clusters. Leptonic channels are expected to produce hard spectra of $e^{\pm}$ and neutrinos, while hadronic channels to produce mesons such as π^0 (which decay into gamma rays) and charged pions (which produce $e^{\pm}$ and neutrinos). Gamma rays may also result from secondary processes such as inverse Compton scattering and synchrotron radiation. A distinctive monochromatic gamma-ray line or a high-energy solar neutrino signal would serve as a "smoking gun" for DM, though such signatures are rare and difficult to separate from astrophysical backgrounds.

The GC is considered a promising target for DM searches because of its proximity to the Earth and the fact that the DM density is expected to be higher towards the centre of the MW. The 511 keV gamma-ray line observed from the GC is a prominent and long-standing signal in the indirect detection of DM. Detected initially by balloon-borne instruments and later confirmed by INTEGRAL/SPI, this line results from electron-positron annihilation at rest [126]. The spatial distribution is approximately spherically symmetric around the Galactic bulge, which is unexpected from standard astrophysical sources such as supernovae or X-ray binaries alone. Several DM models have been proposed to explain the origin of these positrons, typically involving MeV-scale DM particles annihilating or decaying into e^+e^- pairs [127, 128, 129]. Constraints from the CMB and diffuse gamma-ray backgrounds, however, significantly limit the allowed parameter space [130]. Additionally, the lack of a similar signal in the Galactic disk complicates the DM interpretation. Astrophysical explanations, including positrons from pulsars, neutron star mergers [131], and supernovae, remain viable but are not yet definitive, see [132] for a review. Future high-resolution gamma-ray observations may clarify the origin and test exotic particle physics explanations.

Another potential DM indirect signature associated to the GC is the GeV gamma-ray excess, first identified in data from the Fermi-LAT telescope, see [133] for a review. This excess peaks at around 1-3 GeV, and it appears spatially correlated with the inner 10 degrees of the MW. The morphology of the GC excess is roughly spherically symmetric and centered on the GC, consistent with predictions from annihilating DM with masses in the range of 30-70 GeV, particularly via $b\bar{b}$ final states [134, 135]. The spectrum and spatial distribution have prompted intense debate regarding its origin. While DM annihilation remains a viable explanation, especially within models that respect existing constraints from other indirect and DD channels, astrophysical sources such as a population of unresolved millisecond pulsars may also account for the signal [136]. Machine learning and statistical analyses of the photon count maps have yielded evidence for point-source-like structure, favoring the pulsar hypothesis. However, uncertainties in the Galactic diffuse emission models and pulsar population synthesis leave room for DM interpretations. Continued Fermi observations and future missions with better angular resolution are critical for resolving this ambiguity.

Neutrinos are ideal probes due to their weak interactions and straight line propagation. Neutrino telescopes like IceCube, ANTARES, and Super-Kamiokande search for muons produced by neutrino interactions in the vicinity of the detectors. WIMPs can be captured and accumulate in massive celestial bodies such as the Sun or Earth, where they may annihilate and produce high-energy neutrinos (1 GeV to 10 TeV) [137, 138, 139]. These are distinguish-able from the lower-energy solar neutrinos arising from nuclear fusion. Non-observation of such signals places constraints on the WIMP-nucleon scattering cross section.

In the antimatter sector, the positron excess measured by PAMELA in 2008 [140] marked a turning point in indirect DM detection efforts. PAMELA observed a significant rise in the positron fraction above ~ 10 GeV, in contrast with expectations from secondary production in cosmic-ray interactions, suggesting the possibility of new primary sources. This trend was later confirmed and extended to higher energies by Fermi-LAT and AMS-02, with AMS-02 measuring the excess up to several hundred GeV with high precision. While DM annihilation or decay could explain this feature, particularly with leptophilic final states and enhanced annihilation cross sections, a population of nearby pulsars remains a compelling astrophysical alternative. Simultaneously, AMS-02 reported a mild excess in the antiproton-to-proton ratio around $\sim$ 10-20 GeV, potentially consistent with DM annihilation to hadronic channels such as $b\bar{b}$ [141]. However, uncertainties in the cosmic-ray propagation models and secondary production cross sections limit the robustness of this interpretation. Overall, antiproton measurements are broadly consistent with astrophysical backgrounds and place stringent constraints on hadronic annihilation channels. Finally, antinuclei, in particular antideuteron and antihelium, being even rarer and with extremely low astrophysical backgrounds at low kinetic energies, offer a promising probe. Upcoming or ongoing experiments like AMS-02 and GAPS are expected to reach the sensitivity required to test DM models predicting antideuteron production [142].

Collider Searches

Another promising avenue for DM detection involves producing DM particles directly in high-energy collisions at particle accelerators. The most powerful example to date is the LHC, where beams of protons are accelerated in opposite directions and made to collide at center-of-mass energies up to 13 TeV. If DM particles can be generated in such collisions, they would traverse the detector without interacting, resulting in events with apparent missing transverse momentum. Such events are often accompanied by a visible SM particle, giving rise to mono-jet, mono-photon, or mono-Z signatures. These events allow for triggering and reconstruction, enabling a search for deviations from SM predictions.

In most models, DM is stable and electrically neutral, meaning it must be produced in pairs to conserve momentum and other quantum numbers. This implies a minimum partonic collision energy $\sqrt{s} > 2m_{\mathrm{DM}}$ is required. Theoretical interpretations of collider searches are inherently model-dependent. Minimal approaches include DM production via an off-shell Z or Higgs boson, while more elaborate frameworks embed DM within broader extensions of the SM. SUSY models, for instance, predict the existence of a stable lightest SUSY particle (LSP), often a neutralino, which can be a viable DM candidate [143]. At the LHC, colored SUSY particles like squarks or gluinos may be produced with large cross sections and undergo cascade decays, ending in the LSP and yielding events with multiple jets, leptons, and significant missing energy.

Despite extensive searches across a wide range of final states and simplified model assumptions, no statistically significant excess compatible with DM production has been observed at the LHC [144]. These null results have been used to place stringent constraints on the masses and couplings of DM candidates and their mediator particles. In the SUSY context, for example, searches for long decay chains such as $pp \to \tilde{g}\tilde{g}, \quad \tilde{g} \to q\bar{q}\tilde{\chi}^0 \to q\bar{q}\ell\bar{\nu}\tilde{\chi}_1^0$ have been extensively studied. If such chains existed with sufficient production rates and kinematic accessibility, they would allow for simultaneous insights into DM, SUSY breaking, and even Higgs naturalness. The absence of such events in $\sim 140\ \text{fb}^{-1}$ of LHC data places strong lower bounds on sparticle masses, often pushing them above 1 TeV.

Beyond SUSY, other scenarios involve colored co-annihilation partners that are nearly degenerate with the DM particle. These can lead to soft visible final states, challenging current detector capabilities. Nevertheless, the strong production cross sections of these partners make them attractive targets for hadron colliders. Additionally, exotic possibilities such as long-lived particles, dark bound states, or decay signals delayed beyond the collider run time offer non-traditional but intriguing signatures. Future colliders, with higher luminosities or energies, may enhance sensitivity to such elusive signals.

It is important to note, however, that a collider signature alone cannot unambiguously identify a particle as cosmological DM. For this, complementary confirmation is required via direct or indirect detection methods that probe astrophysical DM. Nevertheless, collider searches form a vital part of the broader experimental DM program, offering a unique window into weak-scale interactions and exotic extensions of the SM.

1.3.3 Cosmological constraints: BBN and the CMB

Cosmological observables, particularly BBN and the CMB, provide robust and model independent constraints on DM properties. These early Universe probes are sensitive to the expansion rate, particle content, and energy injection history of the Universe, and thus serve as essential complements to laboratory searches.

BBN refers to the formation of light nuclei (such as D, ^{3}He, ^{4}He, and ^{7}Li) when the Universe had cooled to $T \sim$ MeV. The predicted abundances are highly sensitive to the Hubble rate at that time, which in turn depends on the total energy density, including any contribution from new relativistic species. Light DM candidates that are in equilibrium during or after BBN can alter the neutron to proton ratio, inject entropy, and affect the number of effective relativistic degrees of freedom, N_{eff}. Moreover, decays of DM or other unstable relics into electromagnetic or hadronic final states after BBN can cause significant photodisintegration of light nuclei. High-energy photons produced in such decays initiate electromagnetic cascades that eventually lead to a non-thermal photon spectrum capable of breaking up previously formed nuclei [145, 146]. Observations of primordial element abundances therefore constrain such scenarios, see [147] for a review.

The CMB also constrains DM properties in several ways. First, the anisotropies in the CMB power spectrum are sensitive to N_{eff}, placing bounds on light or interacting DM species that were relativistic at recombination [14]. Second, DM annihilation or decay around the time of recombination can inject energy into the photon-baryon plasma, altering the ionization history and damping the acoustic peaks of the CMB. These effects have been used to place limits on the annihilation cross section of light WIMPs and decaying dark matter models [148].

Overall, BBN and CMB measurements provide stringent constraints on light or feebly interacting DM, ruling out large regions of parameter space independently of assumptions about local density or astrophysical backgrounds. These cosmological probes are especially valuable for testing scenarios beyond the standard WIMP paradigm, such as sub-GeV thermal relics, hidden sector models, or decaying dark matter.

1.3.4 The WIMP miracle

As we have discussed in the previous sections, the existence of DM is firmly established by astrophysical and cosmological observations, yet its particle nature remains unknown. To account for its present day abundance, some mechanisms must have produced DM in the early Universe. A particularly well motivated scenario is that DM was once in thermal equilibrium with the SM plasma and later froze out as the Universe expanded and cooled. We will now show that this thermal freeze-out mechanism [16] naturally leads to the observed relic density for particles with masses and interaction strengths around the electroweak scale.

We consider the scenario where DM is made of spin 1/2 particles, with mass $m_{\rm DM}$ and $g_{\rm DM}$ internal degrees of freedom, in thermal contact at early times with the SM plasma through $2 \to 2$ scattering and annihilation processes:

$$\mathrm{DM} + \mathrm{DM} \leftrightarrow \mathrm{SM} + \mathrm{SM}, \tag{1.53}$$

$$\mathrm{DM} + \mathrm{SM} \leftrightarrow \mathrm{DM} + \mathrm{SM}, \tag{1.54}$$

without specifying the underlying interaction model. The number density n of DM particles evolves according to the Boltzmann equation:

$$\dot{n} + 3Hn = \langle \sigma v \rangle (n_{\rm eq}^2 - n^2), \tag{1.55}$$

where $\langle \sigma v \rangle$ is the DM thermally averaged annihilation cross section times relative velocity and $n_{\rm eq}$ its chemical equilibrium number density.

Defining the comoving number density $Y \equiv \frac{n}{s}$, where s is the entropy density of the plasma, and noting that $\dot{s} = -3Hs$ in an adiabatically expanding Universe, we obtain:

$$\dot{Y} = s\langle \sigma v \rangle \left(Y_{\rm eq}^2 - Y^2 \right). \tag{1.56}$$

Introducing the dimensionless variable $x = \frac{m_{\rm DM}}{T}$, Eq. (1.56) can be rewritten as

$$\frac{dY}{dx} = -\frac{\lambda(x)}{x^2} \left(Y^2 - Y_{\rm eq}^2 \right), \tag{1.57}$$

with

$$\lambda(x) = \sqrt{\frac{\pi}{45}} m_{\rm DM} M_{\rm Pl} \frac{g_*^{1/2}(x) \langle \sigma v \rangle}{x^2}. \tag{1.58}$$

In the relativistic limit $T \gg m_{\rm DM}$ ($x \ll 1$), the equilibrium abundance is:

$$Y_{\rm eq}(T \gg m_{\rm DM}) = \frac{45\zeta(3)}{2\pi^4} \frac{g_{\rm DM}}{g_s(T)} \times \begin{cases} 1 & \text{fermion,} \\ \frac{3}{4} & \text{boson,} \end{cases} \tag{1.59}$$

whereas in the non-relativistic regime $T \ll m_{\rm DM}$ ($x \gg 1$), it is exponentially suppressed:

$$Y_{\rm eq}(T \ll m_{\rm DM}) = \frac{45}{4\pi^{7/2}} \frac{g_{\rm DM}}{g_s(T)} x^{3/2} e^{-x}. \tag{1.60}$$

Freeze-out occurs approximately when the DM interaction rate $\Gamma = n\langle \sigma v \rangle$ falls below the expansion rate of the Universe:

$$\Gamma_{\rm eq} = \langle \sigma v \rangle n_{\rm eq} \simeq H. \tag{1.61}$$

After freeze-out, $Y(x)$ asymptotically approaches a constant value, determining the present relic abundance:

$$\Omega_{\mathrm{DM},0} = \frac{m_{\mathrm{DM}} Y_0 s_0}{\rho_c}, \tag{1.62}$$

where $s_0 \simeq 2.69 \times 10^3\ \mathrm{cm}^{-3}$ is the present day entropy density [74], and $\rho_c = 3H_0^2 M_{\mathrm{Pl}}^2$ the critical energy density of the Universe, being $H_0 \simeq (67.4 \pm 0.5)$km/s/Mpc the Hubble parameter today as measured by PLANCK [14] and $M_{\mathrm{Pl}} \simeq 2.4 \times 10^{18}$ GeV the reduced Planck mass. We focus on cold relics, namely particles that are non-relativistic at the time of freeze-out, since they naturally arise in WIMP scenarios and are favored by structure formation, which requires DM to be sufficiently cold to seed the observed large-scale structure in the Universe. For cold relics, the freeze-out typically occurs at $x_f \sim 20$ [149] and the freeze-out condition yields:

$$x_f e^{-x_f} = \frac{1}{\sqrt{g_\rho(x_f)}} \sqrt{\frac{45}{2\pi^7}} \frac{1}{g_{\mathrm{DM}} m_{\mathrm{DM}} M_{\mathrm{Pl}} \langle \sigma v \rangle}. \tag{1.63}$$

The final DM abundance is approximately given by [150]:

$$\Omega_{\mathrm{DM},0} h^2 \approx \frac{0.1\ \mathrm{pb}}{\langle \sigma v \rangle}, \tag{1.64}$$

and by matching it with the observed value, $\Omega_{\mathrm{DM},0} h^2 \simeq 0.12$, it follows that $\langle \sigma v \rangle \approx 3 \times 10^{-26} \mathrm{cm}^3/s$.

This result is only weakly dependent on the DM mass m_{DM}, entering primarily through the freeze-out parameter x_f. A more precise computation shows that x_f has a logarithmic dependence on m_{DM} and on the number of relativistic degrees of freedom at freeze-out, and thus introduces only mild corrections to the relic abundance.

Remarkably, the required annihilation cross section to reproduce the observed DM density is of the same order as the typical cross sections mediated by weak interactions at the EW scale. Indeed, for $m_{\mathrm{DM}} \simeq 100$ GeV and interaction strength $\alpha_{\mathrm{weak}} \sim 10^{-2}$, a naive dimensional estimate gives

$$\langle \sigma v \rangle \sim \frac{\alpha_{\mathrm{weak}}^2}{m_{\mathrm{DM}}^2} \sim 10^{-26}\ \mathrm{cm}^3/\mathrm{s}, \tag{1.65}$$

which coincides with the value needed for thermal freeze-out. This numerical coincidence, sometimes referred to as the "WIMP miracle", provides strong motivation for considering DM candidates at the EW scale. Independently, new physics at or near the TeV scale is theoretically motivated by natural solutions to the hierarchy problem of the Fermi scale [143]. The fact that the same scale simultaneously explains both the stability of the EW scale and the observed DM abundance adds strong appeal to the WIMP paradigm.

1.3.5 Hunting sub-GeV Dark Matter

The possibility that DM consists of particles lighter than a few GeV has received significant attention recently, motivated by the absence of signals from WIMPs in the current standard DD experiments [151, 120, 121]. Sub-GeV DM is a theoretically motivated framework (e.g. asymmetric DM) [152, 153]. However, detecting such light DM particles is particularly challenging, as their kinetic energy transfer to nuclei falls below the $\mathcal{O}$(keV) threshold of conventional detectors.

To address this challenge, a number of DD experiments traditionally targeting WIMPs through nuclear recoils have been pushing their sensitivity to smaller energy depositions and lighter DM candidates. These include CRESST-III, DarkSide, NEWS-G, SENSEI, and SuperCDMS [154, 155, 156, 157, 151].

In the case of hadrophilic sub GeV DM, which couples dominantly to nucleons, the momentum exchange becomes comparable or smaller than the inverse atomic size, and target nuclei can no longer be treated as free particles. In this regime, the scattering of sub GeV DM can excite collective nuclear modes, such as phonons in crystal lattices [158]. Depending on the DM mass and momentum transfer, the relevant processes include acoustic and optical phonon excitations, as well as multi-phonon regimes.

Another promising detection strategy is through the Migdal effect [123, 159], where the nuclear recoil from DM scattering perturbs the atomic electron cloud, leading to ionization. This inelastic process allows detectors to register an electron recoil signal even when the nuclear recoil alone would fall below detection thresholds. The Migdal effect can thus significantly enhance the sensitivity of conventional detectors to sub GeV DM. However, a dedicated search using neutron scattering in liquid xenon yielded a puzzling null result where a signal was expected [160]. This outcome could indicate either an overestimation of the theoretical rate, or that electromagnetic interactions of neutrons complicate the detection of this effect.

In addition, DM coupling to electrons provides another well-motivated search strategy for DM in the sub MeV mass range, for which the mass of the target (the electron) is closer to the mass of DM and so the energy transfer is efficient. Experimental concepts based on atomic ionization [161], and scintillators [162] have been developed to exploit these interactions, where the relatively low electron binding energies enable detection of small energy depositions.

On the phenomenological side, additional strategies have also emerged to broaden the reach of detection efforts. One promising approach involves *cosmic ray-boosted* DM [163, 164], where high-energy cosmic rays scatter off DM particles in the MW halo, transferring enough kinetic energy to allow sub GeV DM to produce observable signals in terrestrial standard DD and neutrino experiments [165]. The existence of an upscattered DM component relies only on the assumption of a non-vanishing DM-nucleus scattering cross section, a condition no more restrictive than those typically assumed in any DD search. In this thesis we investigate a similar scenario, known as *Blazar boosted DM*, first proposed in [166], in which sub-GeV DM is boosted by high-energy protons inside the jets of active galactic nuclei, potentially producing observable signals at neutrino detectors. The details and phenomenological implications of this mechanism will be discussed in Section 4.1.

1.3.6 Other DM candidates

Aside from the well-studied WIMP and sub GeV paradigms, the landscape of DM candidates is remarkably diverse, encompassing a range of models with distinct theoretical motivations and cosmological production mechanisms, see Figure 1.8 for an illustrative map. These candidates span an enormous range of masses—over 90 orders of magnitude—from ultra-light bosons with masses $\sim 10^{-22}\,\mathrm{eV}$ (as in fuzzy DM) to macroscopic primordial black holes with masses up to several solar masses. In what follows, we briefly discuss a few representative candidates beyond the thermal relic paradigm. Importantly, many of these scenarios are not ad hoc constructions tailored to explain DM alone; rather, they emerge as natural byproducts

Figure 1.8: Conceptual map of the most studied DM candidates and theories. Figure taken from Ref. [167].

of broader theoretical frameworks. For example, axions are introduced to resolve the strong CP problem, sterile neutrinos arise in the context of neutrino mass generation, PBHs may form in connection with inflationary dynamics, and SUSY particles are motivated by the hierarchy problem and gauge coupling unification. Each of these candidates features distinct production mechanisms and phenomenology:

- **Axions and axion-like particles (ALPs)** are pseudo-Nambu–Goldstone bosons associated with spontaneously broken global symmetries. The QCD axion, proposed to solve the strong CP problem via the Peccei–Quinn mechanism [168], is produced non-thermally through vacuum misalignment. Its relic abundance depends on the symmetry-breaking scale and initial field configuration. More generally, ALPs arise in various extensions of the SM, including string-theory constructions, and can populate a wide parameter space of interest to laboratory and astrophysical searches.

- **Sterile neutrinos** are gauge singlet fermions that naturally extend the SM and participate in the seesaw mechanism to generate active neutrino masses. In the early universe, they can be produced through oscillations with active neutrinos via the Dodelson–Widrow mechanism [169], with the resulting abundance and momentum distribution sensitive to mixing angles and lepton asymmetry. Sterile neutrinos with masses in the keV range are viable warm DM candidates and are constrained by structure formation as well as X-ray searches stemming from their radiative decay channels.

- **SUSY candidates**, such as the lightest neutralino in the Minimal Supersymmetric Standard Model (MSSM), are among the most studied particle DM models [143]. If R-parity is conserved, the LSP is stable and can be thermally produced in the early universe. While neutralinos often behave as WIMPs, SUSY frameworks also allow for non-thermal relics such as gravitinos or axinos, depending on the SUSY-breaking mechanism. These candidates naturally arise in theories addressing the hierarchy problem and unification of gauge couplings.

- **Primordial black holes (PBHs)** represent a non-particle DM candidate formed through the direct gravitational collapse of overdensities in the early universe. These overdensities may originate from inflationary fluctuations, cosmic string loops, or first-order phase transitions. PBHs bypass the need for new fundamental particles and are subject to a broad range of astrophysical constraints, including gravitational lensing, CMB distortions, and gravitational wave detections. Despite strong limits, viable windows remain, especially in sublunar and intermediate mass ranges, see [170] for a review on PBH searches.

Altogether, these non-standard candidates underscore the richness of DM theory space and the deep connections between DM physics and other unresolved questions in cosmology and particle physics.

The open issues of the SM, ranging from the nature of DM and the origin of neutrino masses to the generation of the BAU, definitely require some BSM physics, in order to be addressed. While traditional electromagnetic observations have greatly shaped our understanding of the cosmos, addressing these fundamental problems increasingly calls for complementary messengers. Gravitational waves and high-energy neutrinos, capable of traversing dense and distant environments with minimal interaction, offer unique and powerful probes of BSM phenomena. In particular, gravitational waves provide a window into the earliest epochs of the universe, well before the formation of the CMB, allowing us to investigate processes occurring at energy scales and times inaccessible to electromagnetic observations. Complementarily, high-energy neutrinos can reveal extreme astrophysical environments and particle interactions beyond current terrestrial experiments. Together, these novel messengers promise to unlock new insights into the early universe, the nature of DM and exotic processes otherwise hidden from conventional observations.

Chapter 2

Messengers beyond Light

Building upon the challenges outlined in the previous chapter, such as the nature of DM, the origin of neutrino masses, and the generation of the BAU, it is clear that new observational tools are needed to probe BSM physics. Gravitational waves and high-energy neutrinos have emerged as complementary messengers that can traverse regions opaque to electromagnetic signals, providing unparalleled access to exotic astrophysical phenomena and early Universe processes. In this chapter, we explore how these messengers open new windows into BSM physics, offering promising avenues for discovery.

2.1 High-Energy Neutrinos as probes of New Physics

The landscape of neutrino sources

Neutrinos span an extraordinary range of energies, covering approximately 20 orders of magnitude, from the meV scale predicted by ΛCDM for the relic neutrino background (RνB) to the PeV neutrinos detected by IceCube and KM3NeT [171, 172]. Their weak interactions allow them to propagate largely unimpeded over cosmological distances, making them valuable messengers of both astrophysical phenomena and potential BSM physics. Below, we briefly overview the major known astrophysical and terrestrial sources of neutrinos, ranging from relics from the early universe to the most energetic astrophysical accelerators. We show in Figure 2.1 the energy and the flux at Earth of various neutrino populations, which proves the huge amount of sources that can be probed by neutrino physics (see [173] for a review on the topic). We now summarize the most relevant features of each component shown in Figure 2.1:

- **Relic neutrino background (RνB)**. A remnant of the Big Bang, the RνB consists of relic neutrinos which decoupled from the SM plasma at a temperature of $T \sim 1\,\mathrm{MeV}$, due to the freeze-out of the weak interactions. These neutrinos today have a temperature of $T_\nu = (4/11)^{1/3} T_0 \simeq 1.95\,\mathrm{K}$, hence sub meV kinetic energy. Although never directly detected, their existence is a robust prediction of the ΛCDM model and indirectly supported by measurements of the CMB and BBN via N_{eff}. Notably, they are the only sub-component of DM that is predicted by the ΛCDM model. Nevertheless, the detection of RνB is challenging due to the very tiny interaction cross-sections of relic neutrinos and it remains a key goal for future experiments, such as PTOLEMY [174], which aim to detect relic neutrinos through inverse β decay at sub-eV energies. In particular, up-scattering of RνB neutrinos by ultrahigh-energy cosmic rays (UHECRs) trapped in galaxy clusters may generate a detectable neutrino flux at high energies [2]. This mechanism, and its observational prospects with present and upcoming neutrino telescopes, will be discussed in detail in Section 4.2.

- **Solar Neutrinos.** Solar neutrinos are produced in the core of the Sun as a result of nuclear fusion processes powering the star. The dominant source is the proton-proton (pp) chain, which includes several neutrino-producing reactions such as the $pp \to d + e^+ + \nu_e$ reaction producing a continuous neutrino spectrum up to about 420 keV, and the electron capture on ^{7}Be, which emits neutrinos at 0.862 MeV (90% branching ratio) and 0.384 MeV (10% branching ratio). Additionally, neutrinos from ^{8}B beta decay have a broad energy spectrum extending up to about 15 MeV. A smaller contribution arises from the CNO cycle neutrinos, with energies generally between 1 and 2 MeV, recently observed by Borexino [175]. Solar neutrinos were first detected in the pioneering Homestake experiment [67], which used a chlorine based radiochemical detector and was sensitive primarily to ^{8}B neutrinos. This experiment revealed a significant deficit relative to theoretical predictions, known as the solar neutrino problem. This puzzle was eventually resolved by the discovery of neutrino flavor oscillations, confirmed by measurements at SNO [71], which showed that neutrinos oscillate as they propagate to the Earth.

- **Reactor Neutrinos.** Neutrinos produced in nuclear reactors originate primarily from the beta decays of neutron-rich fission fragments generated during the fission of heavy nuclei (such as ^{235}U or ^{239}Pu). These decays emit a large flux of electron antineutrinos ($\bar{\nu}_e$) with typical energies in the range of a few MeV. Reactor experiments such as Daya Bay, Double Chooz, and KamLAND have played a pivotal role in measuring mixing angles like θ_{13} [80, 81] and probing short-baseline anomalies potentially hinting at sterile neutrinos.

- **Geoneutrinos.** Emitted by radioactive decays of elements like ^{238}U and ^{232}Th within the Earth's interior, geoneutrinos provide a unique probe of Earth's composition and radiogenic heat production. Although faint, they have been observed by KamLAND and Borexino [176, 177].

- **Diffuse Supernova Neutrino Background (DSNB).** The DSNB is the integrated flux of neutrinos from all past core-collapse supernovae events through the history of the Universe, see [178] for a review. It is therefore expected to be isotropic and to dominate the flux in the energy range $E_\nu \sim$ 10–50 MeV. Although not yet detected (evidence of a 2.3σ excess in Super-K data compatible with the DSNB signal have been released by the collaboration [179] in 2024), the DSNB lies within reach of upcoming detectors like JUNO , Hyper-Kamiokande, and DUNE [180, 181, 182], and could provide insights into the cosmic star formation rate and supernova neutrino physics.

- **Atmospheric Neutrinos.** Produced by the decay of secondary mesons (primarily pions and kaons) created when cosmic rays interact with Earth's atmosphere, atmospheric neutrinos span a wide energy range from sub-GeV up to $\sim$100 TeV. They played a fundamental role in the discovery of neutrino oscillations [70] and continue to serve as a calibration source and a background in high-energy neutrino experiments.

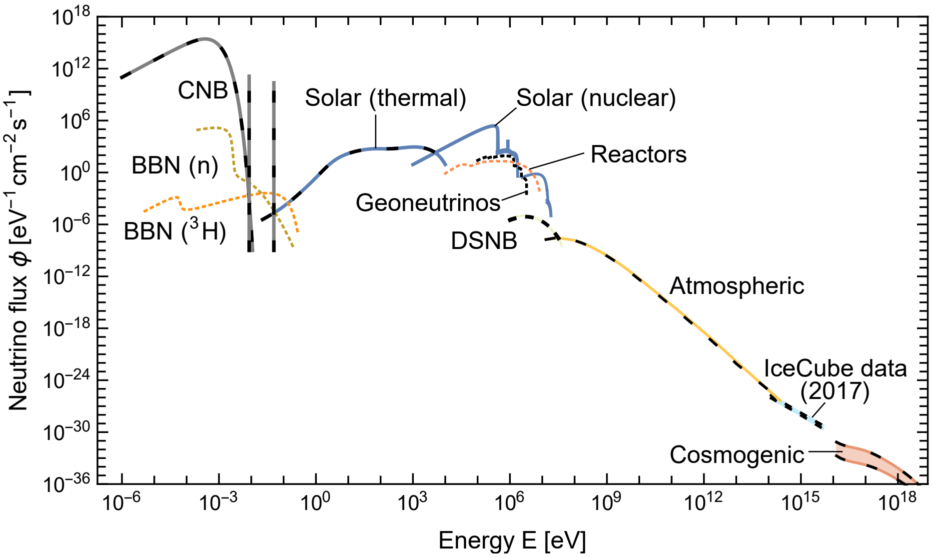

Figure 2.1: Neutrino sources and corresponding energies and fluxes on Earth, taken from Ref. [173], see the main text for details on each source.

- **Astrophysical Neutrinos.** First discovered by IceCube in 2013 [183], high-energy astrophysical neutrinos are believed to originate from cosmic accelerators such as active galactic nuclei (AGN), blazars, gamma-ray bursts (GRBs), and starburst galaxies. They exhibit a spectrum roughly compatible with an unbroken power-law $d\phi/dE \propto E^{-\gamma}$ with $\gamma \sim 2.1$–2.5, extending from tens of TeV to a few PeV. The association of a high-energy neutrino with the blazar TXS 0506+056 [184] marked a milestone in multi-messenger astrophysics. Given their relevance for the work presented in this thesis, we will expand on astrophysical neutrinos in Sec. 2.1.4.

- **Cosmogenic Neutrinos.** This high-energy neutrino population originates from the propagation of extragalactic CRs in the Universe, which can produce neutrinos via photo-meson interactions of the CRs with the CMB photons: $p+\gamma_{\rm CMB} \to \Delta^+ \to n+\pi^+$ and the extragalactic background light (EBL). Cosmogenic neutrinos have not been detected yet and IceCube have set upper limit on their flux [185]. Their predicted flux at Earth relies on astrophysical models involving production and propagation of the UHECR and photon background fields [186], hence their detection would shed light on the extreme astrophysical environments producing them.

Understanding the full landscape of neutrino sources is crucial not only for astrophysics but also for searches of new physics. High-energy neutrinos, in particular, are sensitive probes of exotic interactions and cosmic environments inaccessible to other messengers.

2.1.1 Detection of high energy neutrinos

Neutrinos, due to their weak interactions, offer an unobstructed view of the most extreme and distant regions of the universe. This exciting feature turns neutrino observatories into powerful tools for probing high-energy astrophysical environments and searching for signs of new physics. In this section, we briefly describe the current landscape of high-energy neutrino detectors, emphasizing their role as messengers of phenomena that could point towards BSM physics.

The IceCube Neutrino Observatory, located at the South Pole, marked a milestone in neutrino astrophysics by detecting a diffuse flux of high-energy neutrinos of astrophysical origin [183, 187]. IceCube identifies neutrino interactions via the Cherenkov light produced by secondary charged particles in the Antarctic ice. Although its detection technique is well established, what renders IceCube particularly relevant for fundamental physics is its ability to observe neutrinos in the TeV–PeV energy range, far beyond the reach of particle colliders. One of the most relevant observation made by IceCube was the detection at the 3σ level of a $E_\nu \sim 290$ TeV neutrino (IC-170922A) in spatial coincidence with the flaring blazar TXS 0506+056 [184]. This observation provided the first compelling evidence of a specific extragalactic source of high-energy neutrinos and highlighted the potential of IceCube to pinpoint cosmic accelerators. Beyond its astrophysical relevance, such detections open the door to BSM scenarios, including exotic neutrino interactions, decaying or annihilating DM near astrophysical accelerators, and Lorentz violating effects over cosmological baselines. Moreover, IceCube has provided stringent limits on many neutrino observables, such as non-standard neutrino interactions [188] and sterile neutrino mixing [189]. Its data have also been used to test models of quantum gravity, extra dimensions, and violations of the equivalence principle [190]. Therefore, due to the long propagation distances and extreme energies probed, IceCube is a currently unparalleled laboratory for testing extreme astrophyical environements and some of the fundamental properties of neutrinos. The forthcoming expansion of IceCube, known as IceCube-Gen2 [191], aims to increase the detector volume by an order of magnitude.

KM3NeT is a neutrino telescope under construction in the Mediterranean Sea. It consists of two main components: ARCA, optimized for high-energy astrophysical neutrinos, and ORCA, aimed at studying lower-energy atmospheric neutrinos and determining the neutrino mass ordering [192]. Its location allows it to observe the Southern sky via upward-going neutrinos, providing excellent coverage of the GC and densely populated regions by blazars and other potential neutrino sources. Its angular resolution for track-like events enhances the ability to correlate neutrino events with their astrophysical origins, which is crucial for identifying potential signatures of BSM physics related phenomena occurring in dense environments. A landmark achievement of KM3NeT came in early 2023, when it detected a neutrino-induced muon with an estimated energy of ~ 120 PeV, corresponding to a parent neutrino energy of approximately ~ 220 PeV [193]. This event, labeled `KM3-230213A`, represents the highest-energy neutrino observed to date. The event produced Cherenkov light across nearly one-third of the detector's optical modules, strongly suggesting an extragalactic origin. Still, its origin has not been clarified so far, with possible explanation including blazars and cosmogenic neutrinos, as well as its tension with IceCube data [194]. As the statistics of UHE neutrino detections grow, KM3NeT will play a key role in disentangling their origin, be it cosmogenic neutrinos, astrophysical accelerators, or BSM processes. Its synergy with IceCube and other observatories will be essential in confirming whether such extreme events are rare fluctuations of an isotropic flux or hint at a new class of sources. Several other existing and proposed detectors complement this effort. The ANITA balloon experiment has set strong limits on UHE neutrinos through radio detection of neutrino-induced air showers in Antarctica [195]. Similarly, the Baikal-GVD, deployed in Russia, is an underwater Cherenkov detector currently operational and expanding its capabilities [196].

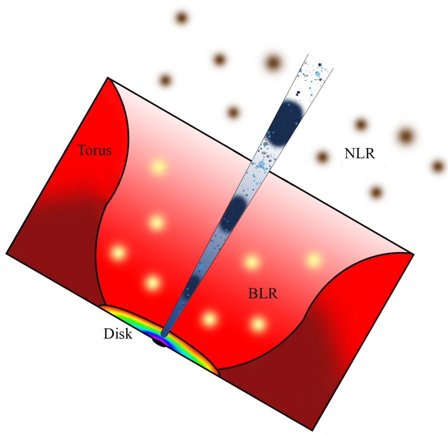

Figure 2.2: Representation of the central regions of a radio-loud AGN, figure from Ref. [204].

Other proposed radio-detection arrays like RNO-G [197] and GRAND [198], aim to extend the reach to even higher energies. These instruments will also test scenarios involving Lorentz invariance violation and new long-range forces. Other projects that have been proposed are P-ONE, a deep-sea Cherenkov detector planned off the coast of British Columbia, Canada [199], and TRIDENT, a large-scale underwater detector (8 km^3), which would be located in the South China Sea [200]. Taken together, the global network of high-energy neutrino detectors is set to become a vital component of multi-messenger astrophysics. Beyond identifying cosmic neutrino sources, these facilities offer a unique and growing avenue for probing fundamental physics at energy and distance scales inaccessible to any other means.

2.1.2 Blazars as high-energy neutrino sources

AGNs are among the most luminous persistent sources in the universe, powered by accretion of matter onto supermassive black holes (SMBHs) at the centers of galaxies. In the case that they show a pair of back-to-back relativistic jets, one of which closely aligned with our line of sight (LOS), we refer to them as *blazars* [201, 202]. This alignment leads to Doppler-boosted emission across a wide range of frequencies, making blazars observable from radio wavelengths up to TeV gamma rays.

They are characterized by a non-thermal, broadband spectral energy distribution (SED), which typically exhibits a characteristic double-peak structure. The low-energy component, peaking between the infrared and X-ray bands, is well understood as synchrotron radiation emitted by relativistic electrons spiraling in the magnetic fields of the jet. The origin of the high-energy component, which peaks at gamma-ray energies, is still a subject of debate and may involve both leptonic and hadronic processes [202].

A schematic representation of a blazar is shown in Figure 2.2. At the center lies a SMBH surrounded by an accretion disk, which emits thermal radiation primarily in the optical and UV. This radiation ionizes nearby clouds of gas, producing strong emission lines from the broad line region (BLR) [?], located on sub-parsec scales, and from the narrow line region (NLR), located farther out at scales of hundreds of parsecs [203]. A dusty torus surrounds the disk and BLR, obscuring certain lines of sight. Relativistic jets emerge perpendicular to the accretion disk, dominating the observed emission.

Blazars can be classified into two primary categories based on their optical spectral features. Flat-Spectrum Radio Quasars (FSRQs) exhibit strong and broad emission lines, whereas BL Lacertae objects (BL Lacs) display weak or no emission lines [205]. An alternative and complementary classification relies on the location of the synchrotron peak frequency $\nu^S_{\rm peak}$ in their SED. Sources are referred to as Low Synchrotron Peaked (LSP) or Intermediate Synchrotron Peaked (ISP) when $\nu^S_{\rm peak} < 10^{15}$ Hz, and as High Synchrotron Peaked (HSP) blazars when $\nu^S_{\rm peak} > 10^{15}$ Hz. This classification reflects differences in the energy of the electrons within the jets and has implications for both photon and potential neutrino emission mechanisms. This classification provides insight into the maximum energy reached by electrons in the jet and serves as a proxy for particle acceleration capabilities.

Several models have been proposed to explain the origin of the high-energy peak in the blazar SED. In leptonic models, gamma rays arise from inverse Compton scattering of soft photons off the same population of electrons responsible for the synchrotron emission. Hadronic models, on the other hand, posit the presence of highly energetic protons co-accelerated with electrons in the jet. These protons can interact with ambient photons or with matter, leading to the production of pions. The decay of charged pions produces high-energy neutrinos, while neutral pions decay into gamma rays. These scenarios are typically referred to as *lepto-hadronic models*, since both leptonic and hadronic contributions to the emission are considered (see [204] for a review of blazar jet models). Distinguishing between leptonic and hadronic models is challenging based solely on electromagnetic observations. However, the detection of high-energy neutrinos would provide a smoking gun for hadronic processes and could help resolve this ambiguity. Blazars have long been considered potential sources of high-energy astrophysical neutrinos. In hadronic scenarios, neutrinos are produced predominantly through the decay of charged pions created in $p\gamma$ or pp interactions [206]. A key ingredient of these models is the presence of relativistic protons accelerated in the jet, an assumption that is theoretically well-motivated in diffusive shock or magnetic reconnection scenarios, although direct observational evidence remains indirect and primarily inferred from the potential neutrino production.

The first association at the 3σ level between a high-energy neutrino and a blazar was reported by IceCube in 2017, involving a $\sim$290 TeV neutrino coincident with a flaring episode of the blazar TXS 0506+056 [184]. This observation marked a turning point in neutrino astronomy and lends support to the lepto-hadronic hypothesis, particularly for scenarios where the neutrino and photon emission regions coincide.

However, follow-up studies revealed tensions within standard single-zone lepto-hadronic models of the source. These models assume that both leptonic and hadronic emissions originate from a compact, homogeneous region in the jet. While they can reproduce the observed SED during the flaring state, they typically underpredict the neutrino flux by up to two orders of magnitude [207, 208], as illustrated in Figure 2.3. This discrepancy may suggest that the simplifying assumptions of the single-zone approximation, such as uniformity of the magnetic field, particle distributions, and photon targets, are overly restrictive. Multi-zone models, or time-dependent dynamics [209, 210] could improve the fit but at the cost of introducing significant model complexity and parameter degeneracy.

Alternatively, this tension could be interpreted as a sign of physics beyond the Standard Model, possibly involving dark matter interactions in the vicinity of the blazar jet. We will explore this possibility in detail in Section 4.1.

While gamma rays are also produced upon the same pp, $p\gamma$ interactions producing neutrinos in the blazar environment, their detectability is limited by the interactions with the

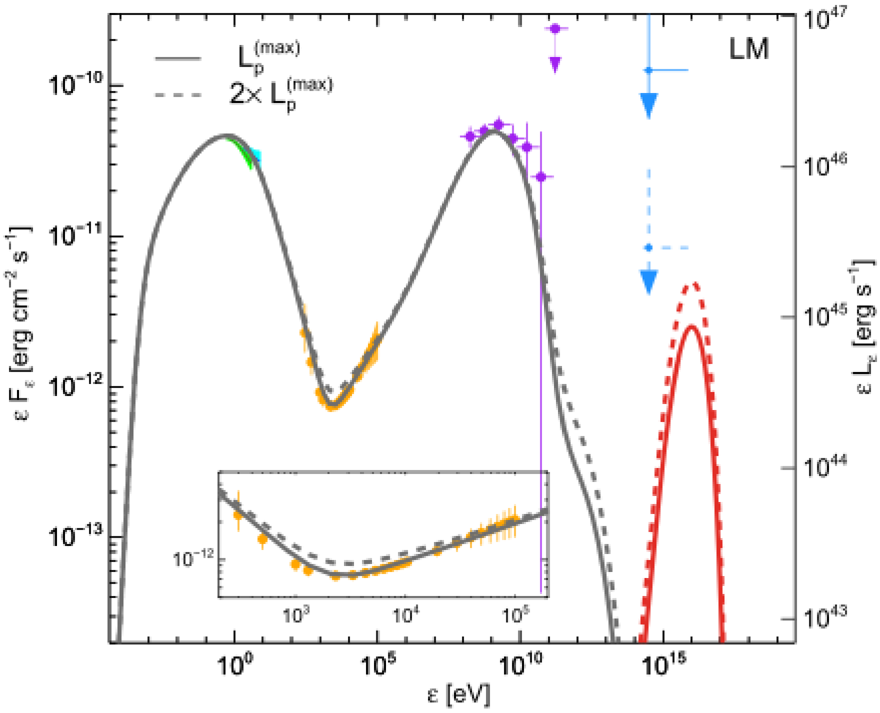

Figure 2.3: Lepto-hadronic model for the blazar TXS 0506+056 during the 2017 flare. Two SED scenarios, gray lines, are plotted against the observed photon flux (Fermi-Lat (violet), NuStar (yellow) and X-shooter (green)): one with proton luminosity $L_p^{(\max)} \approx 2\times10^{50}$ erg s^{-1} (solid), and the other set to twice this value (dashed). The corresponding all-flavor neutrino fluxes in solid red (dashed red). All-flavor neutrino flux upper limits for producing an event similar to IceCube-170922A are shown in blue for 0.5 years (solid blue) and 7.5 years (dashed blue). Figure taken from Ref. [207].

EBL or absorption within the source itself [208]. Indeed, the expected correlation between gamma-ray and neutrino fluxes is not straightforward, and a source may emit detectable neutrinos without a corresponding gamma-ray signature. One particularly intriguing event is the 2014–2015 neutrino flare from the blazar TXS 0506+056, identified through archival IceCube data [211]. Unlike the well-known 2017 event, which was accompanied by a coincident gamma-ray flare, this earlier neutrino outburst showed no clear enhancement in the gamma-ray flux. Such a mismatch between the neutrino and gamma-ray signals poses a challenge to standard lepto-hadronic models, where photo-hadronic interactions are expected to produce both charged pions (decaying into neutrinos) and neutral pions (decaying into high-energy gamma rays).

2.1.3 Ultra-High-Energy Cosmic Rays and the Role of Galaxy Clusters

While the detection of high-energy neutrinos offers a unique probe of astrophysical environments and fundamental physics, their production is intimately tied to the properties of ultra-high-energy cosmic rays (UHECRs) and their interactions with ambient matter and radiation fields. Observationally, the study of UHECRs relies on large-scale air shower observatories capable of detecting the extensive air showers produced when UHECRs interact with the Earth's atmosphere. The two leading experiments in this field are the Pierre Auger Observatory (PAO) in Argentina and the Telescope Array (TA) in Utah, USA. Both combine surface detector arrays with fluorescence telescopes to reconstruct the energy, arrival direction, and composition of primary cosmic rays. These experiments have provided high statistics measurements of the CR energy spectrum, anisotropies, and composition. Complementing these observatories, the Large High Altitude Air Shower Observatory (LHAASO), located in China, is rapidly emerging as a major facility in the field of CR and gamma-ray astrophysics.

The origin of UHECRs, particles with energies exceeding 10^{18} eV, remains a central open question in astroparticle physics. While galactic CRs are believed to originate from diffusive shock acceleration in supernova remnants [212, 213], this mechanism struggles to account for CR particles with energies above the so called *knee* at $E_{\rm knee} \sim 3$ PeV. Below the knee, the CR spectrum follows a power-law approximately given by $\frac{d\phi}{dE} \propto E^{-\gamma}$ with $\gamma \sim 2.7$, steepening to $\gamma \sim 3.1$ above it. Above the knee, the CR spectrum also exhibits several additional features that hint at transitions in both source populations and propagation effects, see Figure 2.4 for a global view of the measured CR spectrum. One such feature is the *second knee* around 100 PeV, associated with the steepening of the heavy galactic component, notably iron and other high-Z nuclei, which marks the exhaustion of the galactic CR sources acceleration capability. The spectral index of the total flux softens further to $\gamma \sim 3.3$. At the same time, a hardening of the light component is observed around 100 PeV, which is commonly interpreted as the emergence of a light, extragalactic component [214]. The most prominent spectral feature, the *ankle* at $E_{\rm ankle} \sim 5 \times 10^{18}$ eV, is understood [215] as a transition between two distinct extragalactic source populations, where at $E_{\rm ankle}$ the dominant component changes from light to heavy nuclei. This trend is supported by the lack of cosmogenic neutrinos, which would be more prevalent if UHECRs were dominantly protons [216]. At the highest energies, above $E_{\rm cut} \sim 5 \times 10^{19}$ eV, a suppression in the flux is observed. This could be attributed either to energy losses during propagation, like the GZK effect [217], where protons interact with the CMB, or to an intrinsic maximum acceleration energy at the sources.

In the UHECRs landscape, galaxy clusters stand out as compelling environments, acting as "CR-reservoirs" over cosmological timescales. Indeed, galaxy clusters are known to host magnetic fields of order $B \sim \mathcal{O}(\text{few})\ \mu$G [218], extending over Mpc scales. The Hillas condition [219], $E^{\max} = ZeBR$, where $E^{\max}$ the maximal energy of the accelerated particle, Z its charge, B the size of the magnetic field, and R the confinement size, dictates that clusters can confine particles up to ultra-high energies. For a μG field and a cluster radius of ~ 1 Mpc, clusters can trap particles with energies up to $\sim Z \times 10^{19}$ eV [186]. This makes them particularly relevant for the population of UHECRs observed above the ankle.

This motivates a detailed study of galaxy cluster environments in cosmic-ray physics, particularly for interpreting mixed-composition observations and modeling the secondary messengers arising from cosmic-ray interactions within these structures. Due to the long trapping times of UHECRs in the $\sim \mu$G magnetic fields of clusters, secondary particle production, including neutrinos and gamma rays, is significantly enhanced compared to propagation in intergalactic space. A concrete application of this effect is found in our study of the RνB upscattering, see Section 4.2, where clusters act as CR reservoirs, boosting a flux of upscattered relic neutrinos potentially detectable at present and future neutrino telescopes. This provides a unique particle-physics probe connected to the astrophysical processes governing cosmic-ray propagation and confinement within galaxy clusters.

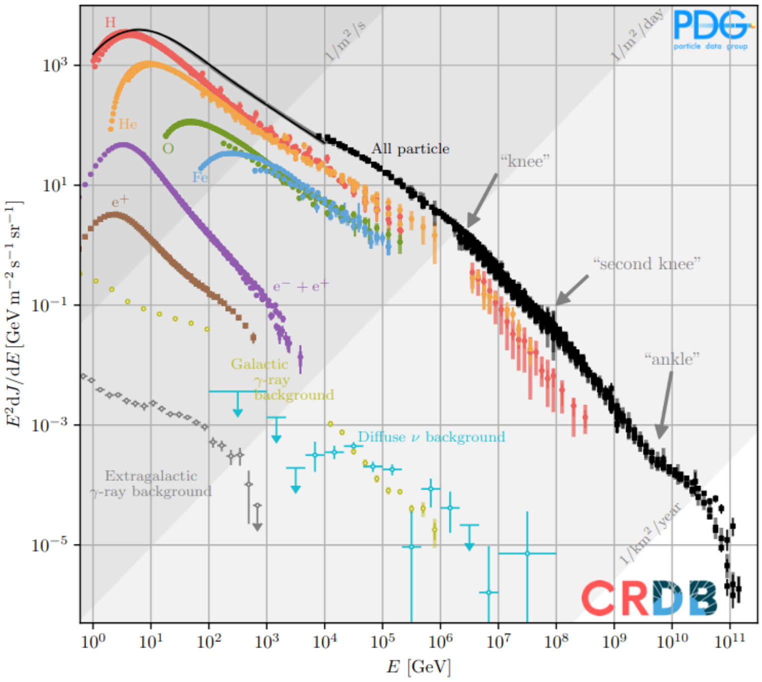

Figure 2.4: A global view of the CR spectrum at Earth. Figure taken from [74].

2.1.4 The diffuse astrophysical neutrino flux

The discovery of a diffuse flux of high-energy astrophysical neutrinos by the IceCube Neutrino Observatory in 2013 marked a milestone in multi-messenger astrophysics [187, 183]. This flux, spanning energies from tens of TeV to several PeV, appears nearly isotropic across the sky, suggesting an extragalactic origin. The spectral shape of the observed diffuse flux is best described by an unbroken power-law, $d\phi/dE \propto E^{-\gamma}$ with $\gamma \sim 2.1$–2.5, although this can vary slightly depending on the event selection and analysis technique [220]. The flux normalization and spectral index imply that the neutrinos are most likely produced in hadronic processes such as pp or $p\gamma$ interactions occurring in astrophysical accelerators, sources capable of accelerating protons to energies exceeding the PeV scale. Despite over a decade of observations, the individual sources contributing to this flux remain almost entirely unresolved, posing one of the most pressing open questions in astroparticle physics.

A critical test for any proposed source population is whether its sky distribution correlates with that of IceCube's neutrinos. In the case of blazars, several studies have investigated this connection. Notably, refs. [221, 222] report a significant correlation between IceCube's sky map and the distribution of blazars in the southern sky at neutrino energies $E_\nu \gtrsim 100$ TeV, and a smaller yet notable correlation in the northern sky for $E_\nu \lesssim 100$ TeV, consistent with expectations from structured, energy-dependent emission scenarios. On the other hand, a more recent analysis using updated data [223] finds no statistically significant correlation, though it remains unclear whether this holds for the highest-energy events, which are particularly relevant for many blazar-based models.

To overcome the limitations of neutrino-only searches, multi-messenger approaches have become crucial. These analyses seek to correlate neutrino detections with electromagnetic observations across the spectrum, particularly from gamma-ray telescopes like Fermi-LAT. A recent IceCube stacking search [224] involving a large catalog of $\mathcal{O}(2000)$ blazars finds no evidence for a neutrino excess, disfavouring a blazar origin for the observed astrophysical neutrinos. However, this analysis assumes a single power-law neutrino spectrum for all sources, an assumption that may not apply to more complex, energy-dependent scenarios predicted by many blazar models. Thus, while standard searches yield no conclusive detection, they may not yet be optimized to test the full range of predictions from physically motivated blazar mechanisms. Overall, these mixed results highlight the need for future searches to incorporate more realistic spectral and spatial features when probing correlations between high-energy neutrinos and blazars.

While this work focuses on blazars as promising sources of high-energy neutrinos, it is important to acknowledge that several other astrophysical source classes have been proposed as potential contributors to the diffuse neutrino flux observed by IceCube. These include core-collapse supernovae [225], gamma-ray bursts [226], starburst galaxies [227], AGN beyond blazars such as radio galaxies and Seyfert galaxies [228]. Each of these populations offers plausible environments for cosmic-ray acceleration and hadronic interactions leading to neutrino production. For instance, starburst galaxies exhibit high cosmic-ray densities and intense star formation, certain types of AGN, such as non-jetted Seyfert galaxies, may harbor dense environments conducive to efficient neutrino production and gamma-ray bursts colud be viable sources due to their extreme brightness. However, despite cross-correlation analyses, none of these classes has yet been identified as the dominant contributor to the observed neutrino flux, leaving open the possibility that multiple populations or a still unknown class of sources account for the observed signal.

The coming decade promises significant advances in sensitivity to the diffuse astrophysical neutrino flux across a broad energy range, see Figure 2.5 for a plot showing the projected sensitivities of present and future experiments. Next-generation instruments such as IceCube-Gen2, RNO-G, PUEO, and GRAND will dramatically improve detection capabilities through increased exposure, novel detection methods, and expanded energy coverage. These experiments will enhance the precision of spectral measurements, enable deeper searches for anisotropies or clustering, and strengthen multi-messenger correlations. Sensitivities are projected to improve by more than an order of magnitude at the highest energies, opening the possibility of resolving the composition of the diffuse flux and identifying the dominant source classes.

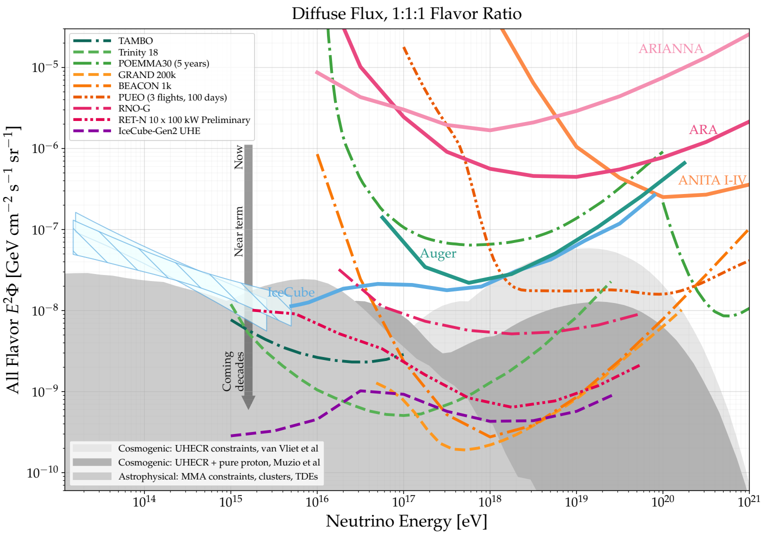

Figure 2.5: The expected all-flavor differential 90% C.L. neutrino flux sensitivities for a variety of experiments. The measurements and sensitivities are compared with cosmogenic and astrophysical neutrino models. The blue bands show the astrophysical neutrino flux measured by IceCube [220]. Solid lines show experimental upper limits at higher energies from the Pierre Auger Observatory [229], ARA [230], ARIANNA [231], ANITA I–IV [195], and IceCube [232]. Dashed lines represent the sensitivities of planned experiments: GRAND [198], BEACON [233], TAMBO [234], Trinity [235], RET-N [236], POEMMA30 [237], RNO-G [238] and PUEO [239]. Figure taken from Ref. [240].

2.2 Gravitational waves as cosmic messengers

2.2.1 Introduction

The first direct detection of gravitational waves (GWs) performed by the LIGO and Virgo collaborations in 2015 [241] (GW150914) marked the beginning of a new era in observational astronomy and fundamental physics. The observed signal, resulting from the merger of a binary black hole (BBH) system, provided the first direct evidence of strong field general relativity and established GW interferometry as a powerful tool for probing the Universe. Since then, the LIGO-Virgo-KAGRA (LVK) collaboration has announced more than 90 confirmed GW events [242], including mergers of BBHs, binary neutron stars (BNS), and neutron star–black hole (NSBH) systems. These events provide an unprecedented opportunity to study compact object populations, stellar evolution, and nuclear matter under extreme conditions.

While individually resolved events have dominated the GW landscape at frequencies accessible to ground based detectors (~ 10–10^3 Hz), theoretical models predict the existence of a *stochastic gravitational wave background* (SGWB). This background is generated by the superposition of many unresolved sources and is expected to contain contributions from astrophysical and possibly cosmological origins. On the astrophysical side, this includes compact binary coalescences involving binary BBH, BNS, and binary white dwarfs (BWD). These signals originate from sources beyond the sensitivity horizon of detectors and accumulate over cosmic time.

Unlike electromagnetic radiation, GWs interact very weakly with matter and propagate essentially freely across cosmic history. This decoupling occurs already at the moment of their production, due to the weakness of gravity: on general grounds, one can estimate their interaction rate with the primordial plasma as [243]

$$\Gamma(T) = n\,\sigma\,v \simeq G_N^2 T^5, \tag{2.1}$$

where $n \sim T^3$ is the number density of particles, $\sigma \sim G_N$ is the cross section for $g + SM \to SM + SM$ processes, where g the graviton, $v \sim 1$ and $G_N = 1/M_{\rm Pl}^2$ the Newton's constant. Comparing this rate to the Hubble rate during radiation domination, $H(T) \sim T^2/M_{\rm Pl}$, one finds

$$\frac{\Gamma(T)}{H(T)} \sim \frac{G_N T^3}{T^2/M_{\rm Pl}} \sim \frac{T}{M_{\rm Pl}} \ll 1, \tag{2.2}$$

for any temperature well below the Planck scale. Therefore, they carry unique information on cosmic epochs unreachable by any other messenger. A cosmological SGWB could originate from a range of processes in the early Universe, including first-order phase transitions, inflationary quantum fluctuations and cosmic strings (see [243] for a review about cosmological SGWBs). Recently, strong evidence for a SGWB at the nanohertz frequencies was reported by multiple pulsar timing array (PTA) collaborations, NANOGrav [244], EPTA [245], PPTA [246], and CPTA [247].

While these results are consistent across different experiments and suggest the presence of a common process affecting PTA residuals, the source of the signal is still under investigation. Several interpretations have been proposed, ranging from the standard astrophysical interpretation in terms of SMBH binaries (SMBHBs) coalescence to more exotic cosmological scenarios, see Section 2.2.4 for more details.

Let us now briefly review how GWs are described in both astrophysical and cosmological contexts.

GWs are described as transverse-traceless (TT) tensor perturbations h_{ij} of the flat Friedmann-Robertson-Walker metric:

$$ds^2 = -dt^2 + a^2(t)\,(\delta_{ij} + h_{ij})\,dx^i dx^j, \tag{2.3}$$

where the tensor h_{ij} satisfies the TT gauge conditions:

$$\partial^i h_{ij} = 0, \quad h_i^i = 0. \tag{2.4}$$

These conditions eliminate unphysical degrees of freedom and leave only the two propagating degrees of freedom of GWs. In Fourier space, the linearized Einstein equations yield the evolution equation:

$$\ddot{h}_{ij}(\vec{k},t) + 3H\dot{h}_{ij}(\vec{k},t) + \frac{k^2}{a^2} h_{ij}(\vec{k},t) = 16\pi G\,\Pi_{ij}^{\rm TT}(\vec{k},t), \tag{2.5}$$

where $\Pi_{ij}^{\rm TT}$ is the TT part of the anisotropic stress tensor and the source of GWs. The present day energy density $\rho_{\rm GW}$ of the SGWB is typically expressed per logarithmic frequency interval relative to the critical energy density of the Universe ρ_c as:

$$\Omega_{\rm GW}(f) = \frac{1}{\rho_c}\frac{d\rho_{\rm GW}}{d\log f}\,. \tag{2.6}$$

The energy density $\rho_{\rm GW}$ can be computed from the energy-momentum tensor $t_{\mu\nu}^{\rm GW}$, obtained by expanding Einstein's equations to second order in the metric perturbations. In the TT gauge, the leading contribution to the energy density is given by the t_{00} component as [248]:

$$\rho_{\rm GW} = t_{00}^{\rm GW} = \frac{1}{32\pi G} \left\langle \dot{h}_{ij} \dot{h}^{ij} \right\rangle , \tag{2.7}$$

where angle brackets indicate averaging over several wavelengths or modes.

To relate the SGWB energy density at the time of production to the present one, we note that GWs redshift like radiation. Therefore, the present day energy density parameter can be written in terms of its value at generation as:

$$\Omega_{\rm GW,0}(f) = \Omega^*_{\rm GW}(f_*) \left(\frac{a_*}{a_0}\right)^4 \left(\frac{H_*}{H_0}\right)^2 \simeq 1.65 \times 10^{-5}\, \Omega^*_{\rm GW}(f_*) \,, \tag{2.8}$$

where a_* and H_* are the scale factor and Hubble rate at the time of GW production and we have assumed the SGWB to have been generated during the radiation dominated era, as motivated by several cosmological scenarios. The factor $(a_*/a_0)^4$ accounts for the redshift of the GW energy density, which scales like radiation, while the factor $(H_*/H_0)^2$ arises from the ratio of the critical energy densities at generation and today.

Astrophysical sources, such as compact binary mergers (stellar mass black BHs and NSs) and inspiraling SMBHBs, are expected to contribute to the SGWB across a wide range of frequencies. For instance, SMBHBs should dominate the ($f \sim 10^{-9} - 10^{-7}\,$Hz) regime, targeted by the PTAs. Meanwhile, stellar mass compact binaries contribute primarily in the ($f \sim 10^{-3} - 10^{3}\,$Hz) range, observable by present and future detectors like LISA and LVK. These stochastic signals encode the integrated astrophysical history of star formation, binary evolution, and galaxy assembly.

Cosmological sources, including inflationary tensor modes, cosmic strings, and first-order phase transitions, can generate GWs across an even wider frequency range, depending on the characteristic energy scale T_* and the Hubble rate H_* at the time of the SWGB production. The present day frequency f_0 of a SGWB from a cosmological origin is related to that at production f_* by:

$$f_0 = \frac{f_* a_*}{a_0} \,. \tag{2.9}$$

Assuming that the GWs were produced during radiation dominated era at a characteristic physical scale $f_* \sim H_*$, corresponding to the Hubble rate at that time, this becomes:

$$f_0 \sim \frac{H_* a_*}{a_0} \simeq 1.6 \times 10^{-5}\ {\rm Hz} \left(\frac{T_*}{100\ {\rm GeV}}\right) \left(\frac{g_*}{100}\right)^{1/6} \,. \tag{2.10}$$

An important consequence of this equation is that it allows us to relate the frequency of GWs observed today to the temperature in the early Universe when they were produced. Therefore, for any given GW detection experiment, each sensitive to a specific frequency band, we can identify the corresponding epoch in the early Universe during which a source must have been active to produce a detectable signal. This correspondence is illustrated in Figure 2.6 for LIGO, LISA and PTAs.

In what follows, we first examine astrophysical contributions to the SGWB, followed by a discussion of early Universe cosmological sources.

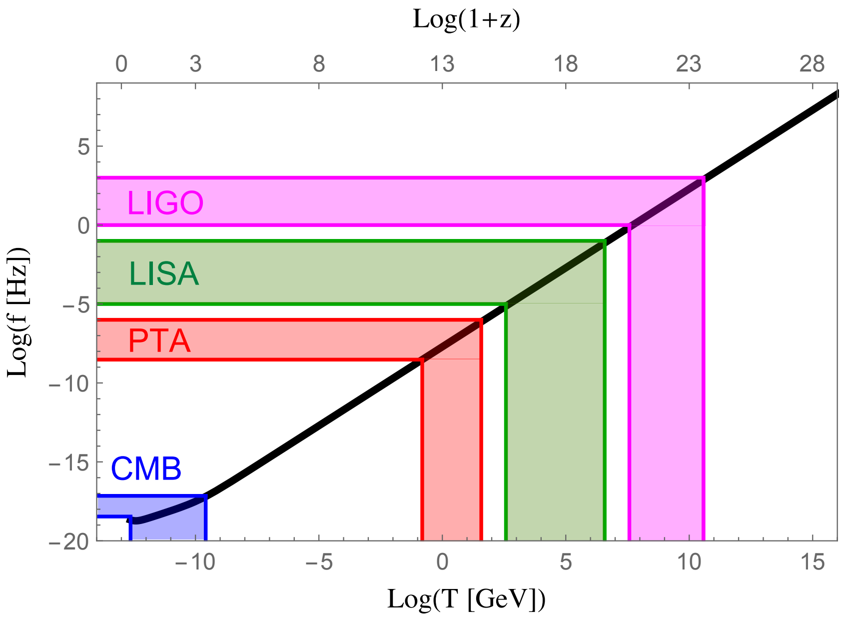

Figure 2.6: The present day GW frequency of Eq. (2.10) as a function of the temperature T at production. Shaded regions denote the frequency ranges detectable by several GW experiments, from right to left LIGO, LISA, PTA and the CMB. Figure taken from [243].

2.2.2 Astrophysical Sources of Gravitational Waves

The SGWB generated by an astrophysical population of inspiraling compact binaries exhibits a characteristic power-law spectrum in the inspiral phase. The GW energy density per logarithmic frequency interval typically scales as [249]:

$$\Omega_{\rm GW}(f) \propto f^{2/3}, \tag{2.11}$$

in a frequency range $[f_{\rm min}, f_{\rm max}]$ determined by the dynamics of the system and the endpoint of the inspiral phase.

A widely used expression for the contribution to the SGWB from a population of inspiraling binaries, with masses m_1, m_2 is given by (see e.g. [249]):

$$\Omega_{\rm GW}(f) = 1.3 \times 10^{-17} \left(\frac{\mathcal{M}}{M_\odot}\right)^{5/3} \left(\frac{f}{10^{-3}\,\rm Hz}\right)^{2/3} \left(\frac{N_0}{\rm Mpc^{-3}}\right) \left\langle \frac{(1+z)^{-1/3}}{0.74} \right\rangle, \tag{2.12}$$

where $\mathcal{M} = (m_1 m_2)^{3/5}/(m_1 + m_1)^{1/5}$ is the chirp mass of the binary system, N_0 the local comoving number density of binaries, and the average accounts for redshift effects. The minimum frequency contributing to the energy loss in GWs, $f_{\rm min}$, is typically set by the separation theat the binary had at formation or at the onset of the inspiral phase. Since very wide binaries take longer than the age of the Universe to merge, a typical choice is to include only systems that merge within this time. Each source population is also characterized by a proper UV frequency cutoff $f_{\rm max}$: for BBH and BNS, the maximum frequency corresponds to the frequency at the innermost stable circular orbit (ISCO), given by:

$$f_{\rm ISCO}^{\rm max} = \frac{1}{6\sqrt{6}\pi}\frac{c^3}{G(m_1+m_2)} \simeq 4.4\times 10^3 \text{ Hz}\left(\frac{M_\odot}{m_1+m_2}\right) , \tag{2.13}$$

while for BWD, the inspiral ends when the stars come into contact. The corresponding frequency is then given by:

$$f_{\rm BWD}^{\rm max} = \frac{1}{\pi}\sqrt{\frac{G(m_1+m_2)}{(r_1+r_2)^3}} \tag{2.14}$$

where the stellar radii r_i can be approximated using [250]:

$$r_i = 0.01 R_\odot \sqrt{\left(\frac{m_i}{m_{\rm Ch}}\right)^{-2/3} - \left(\frac{m_i}{m_{\rm Ch}}\right)^{2/3}} , \tag{2.15}$$

being $m_{\rm Ch} \approx 1.44 M_\odot$ the Chandrasekhar mass. Therefore, SMBHBs, with typical total masses ranging from $M \sim 10^6 - 10^{10} M_\odot$ have very low merger frequencies due to their enormous size, falling in the nanohertz range, roughly $f_{\rm merger} \sim 10^{-9} - 10^{-7}$ Hz, and are best probed by PTAs. BWD, which are much less massive ($M \sim 1 M_\odot$), emit in the millihertz band. Despite their low mass, their finite radii limit how close they can orbit before contact, setting a typical maximum frequency in the range (given by Eqs. 2.14, 2.15) $f_{\max} \sim 10^{-3} - 10^{-2}$ Hz, which lies within the sensitivity of space-based detectors like LISA. Finally, BNS and BBH, with masses between $\sim 1 - 100 M_\odot$, merge at much higher frequencies, $f_{\rm merger} \sim 10 - 10^3$ Hz, making them detectable by ground based interferometers such as LIGO, Virgo, and KAGRA. Therefore, while all these sources share a characteristic inspiral phase spectrum scaling as $\Omega_{\rm GW}(f) \propto f^{2/3}$, the frequency band over which each population dominates is controlled by their mass-dependent merger frequencies and the population properties.

Understanding the frequency range and shape of the SGWB from astrophysical sources is not only essential for characterizing their signal, but also crucial in the context of GW detection. Advanced ground based detectors such as LIGO and Virgo are approaching sensitivities in their current (O4) and upcoming (O5) observational runs that could allow detection of the SGWB from BBH and possibly BNS. This astrophysical foreground plays a dual role in the search for signals from new physics in the early Universe. On one hand, it acts as a background that must be accurately modeled and subtracted to uncover a potential cosmological signal originating from processes such as first-order phase transitions, cosmic strings, or inflationary relics. On the other hand, the astrophysical background is a rich source of information in itself, encoding details about the population, evolution, and merger history of compact objects, offering insights into stellar evolution, binary formation channels, and the cosmic star formation rate.

The detectability of a SGWB is quantified through the signal-to-noise ratio (SNR), which compares the GW signal to the noise spectral density $S_n(f)$ of a detector, which includes the relevant noise contributions from the detector itself as well as those from unresolved backgrounds. The energy density of the SGWB is characterized by $\Omega_{\rm GW}(f)$, while the detector sensitivity is defined by the equivalent SGWB energy density $\Omega_{\rm sens}(f)$ that mimics the noise level:

$$h^2\Omega_{\rm sens}(f) = \frac{2\pi^2}{3H_0^2} f^3 S_n(f) \, . \tag{2.16}$$

The expected SNR for a SGWB after an observation time T is given by:

$$\mathrm{SNR} = \sqrt{T}\left[\int_{f_{\min}}^{f_{\max}} \left(\frac{\Omega_{\mathrm{GW}}(f)}{\Omega_{\mathrm{sens}}(f)}\right)^2 df\right]^{1/2} . \tag{2.17}$$

To facilitate comparison with theoretical models, one often assumes a power-law spectrum for the SGWB:

$$\Omega_{\mathrm{GW}}(f) = \Omega_\beta \left(\frac{f}{f_{\mathrm{ref}}}\right)^\beta . \tag{2.18}$$

For chosen values of SNR and T, this yields an envelope of curves, the *power-law integrated* (PLI) sensitivity curves, which define the minimum amplitude required for detection [251]:

$$\Omega_{\mathrm{PLI}}(f) = \max_\beta \left[f^\beta \left(\frac{\mathrm{SNR}}{\sqrt{T}} \left(\int_{f_{\min}}^{f_{\max}} \frac{f^{2\beta}}{\Omega^2_{\mathrm{sens}}(f)} df \right)^{-1/2} \right) \right] . \tag{2.19}$$

We show in Figure 2.7 astrophysical foregrounds such as SMBHBs, BWDs, BNSs and BBHs are shown alongside the PLI curves for different detectors (computed for SNR=10), illustrating both the frequency ranges of dominant contributions and the sensitivity reach of current and future instruments. We remind here that the SNR formalism introduced here is independent of the GW signal under study and applies to both astrophysical and cosmological sources of the SGWB, which we will discuss below.

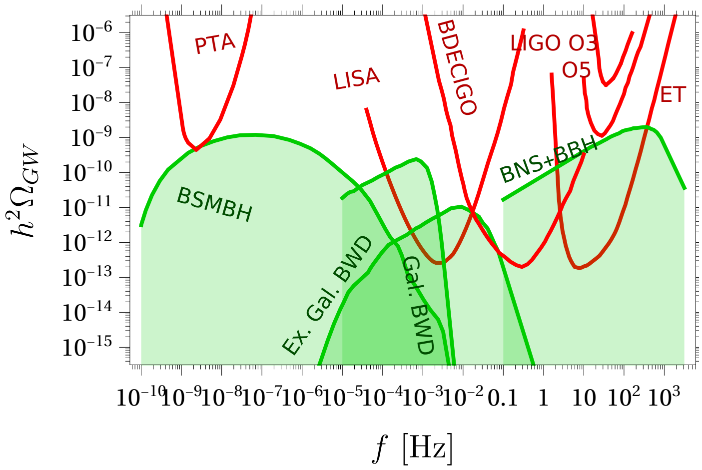

Figure 2.7: Estimated astrophysical foregrounds from binary super-massive black holes [250], galactic white-dwarf binaries [252], extragalactic white-dwarf binaries [253], binary black holes and neutron stars [254], shown as green shaded regions. We also show in red the PLI sensitivity curves for the Einstein Telescope (ET) [255], LIGO-VIRGO O3, LIGO-VIRGO Design A+ sensitivity (O5) [254], LISA [256], BDECIGO [257] and PTA [258]. Figure produced for this thesis.

2.2.3 Cosmological Sources of Gravitational Waves

In addition to astrophysical origins, GWs can arise from processes in the early Universe, offering a unique window into physics at energy scales far beyond the reach of terrestrial experiments.

- **First-Order Phase Transitions**: First-order phase transitions (FOPTs) in the early Universe are a well-motivated source of a SGWB. Such transitions proceed via the nucleation and expansion of true vacuum bubbles within a surrounding false vacuum. GWs are primarily sourced by three mechanisms, occurring upon bubble percolation: the collision of bubble walls (scalar field contribution), the propagation of sound waves in the plasma, and magnetohydrodynamic turbulence. A general estimate of the GW energy density produced can be obtained by analyzing the scaling of the tensor anisotropic stress Π. Assuming that the process sourcing GWs has a typical duration $\Delta t \sim \beta^{-1}$, shorter than the Hubble time (i.e., $\beta/H_* \gg 1$), one can estimate from Eq. (2.5)

$$\dot{h}_{ij} \sim \frac{16\pi G}{\beta}\Pi_{ij}^{\mathrm{TT}}, \tag{2.20}$$

and that the anisotropic stress is of order $\Pi \sim \kappa\rho_{\mathrm{vac}}$, the GW energy density at the time of production reads

$$\frac{\rho_{\mathrm{GW}}^*}{\rho_{\mathrm{tot}}^*} \sim \left(\frac{H_*}{\beta}\right)^2 \left(\frac{\Pi}{\rho_{\mathrm{tot}}^*}\right)^2 \sim \left(\frac{H_*}{\beta}\right)^2 \left(\frac{\kappa\alpha}{1+\alpha}\right)^2, \tag{2.21}$$

where $\alpha \equiv \rho_{\mathrm{vac}}/\rho_{\mathrm{rad}}$ characterizes the strength of the transition and κ quantifies the fraction of vacuum energy that is converted into the GW source, namely scalar field and sound wave contributions.

The present day GW energy density spectrum can then be estimated as

$$h^2\Omega_{\mathrm{GW}}(f) \sim 1.6 \times 10^{-5} \left(\frac{H_*}{\beta}\right)^2 \left(\frac{\kappa\alpha}{1+\alpha}\right)^2 \left(\frac{100}{g_*(T_*)}\right)^{1/3}, \tag{2.22}$$

where the additional factors with respect to Eq. (2.21) account for the redshift and entropy conservation. This result highlights that a strong signal is generated by sources with significant energy density ($\alpha \gtrsim \mathcal{O}(0.1)$) and a relatively long duration ($\beta/H_* \lesssim 100$). Such conditions are realized in strong, supercooled, FOPTs, and this scaling is broadly applicable across different types of GW sources including bubble collisions, sound waves, and turbulence. We will discuss in more detail each of these contributions in Section 3.1.3.

- **Inflation**: During inflation, quantum fluctuations of the metric tensor h_{ij} are inevitably generated alongside scalar perturbations, leading to a cosmological SGWB. The inflationary tensor power spectrum is expected to be nearly scale-invariant, as it originates from quantum fluctuations in a quasi-de Sitter background. For single-field slow-roll inflation, the tensor power spectrum at horizon crossing is given by [243]:

$$\Delta_t^2(k) = \frac{2}{\pi^2}\frac{H_k^2}{M_{\mathrm{Pl}}^2}, \tag{2.23}$$

where H_k the Hubble rate when the mode with comoving wavenumber k exits the horizon during inflation, and is related to the scalar power spectrum via the tensor-to-scalar ratio:

$$r(k) \equiv \frac{\Delta_t^2(k)}{\Delta_s^2(k)} = \frac{16H_k^2}{\pi^2 M_{\mathrm{Pl}}^2 \Delta_s^2(k)}, \tag{2.24}$$

with $\Delta_s^2(k) \simeq 2.1 \times 10^{-9}$ measured by the CMB. Using the constraint $r \lesssim 0.056$ from Planck [259], one can derive an upper bound on the energy scale of inflation and, consequently, on the amplitude of the associated SGWB.

The present day GW energy density per logarithmic frequency interval is given by [243]:

$$\Omega_{\rm GW}(f) \equiv \frac{1}{\rho_c}\frac{d\rho_{\rm GW}}{d\ln f} \simeq \frac{1}{12}\left(\frac{k}{a_0 H_0}\right)^2 \Delta_t^2(k) T^2(k), \tag{2.25}$$

where $T(k)$ is the transfer function accounting for the evolution after horizon re-entry. For modes re-entering during radiation domination the spectrum is nearly flat:

$$\Omega_{\rm GW}(f) \simeq 5 \times 10^{-16}\left(\frac{H_k}{H_{\rm max}}\right), \tag{2.26}$$

where $H_{\rm max} \sim 6 \times 10^{13}$ GeV is the maximum Hubble rate allowed by the CMB. This nearly scale-invariant plateau extends over the wide frequency range accessible to current and planned GW detectors, however it sits well below their projected sensitivity. It is important to stress that these predictions assume the standard single-field slow-roll framework. Alternative models, including multi-field scenarios, spectator fields, or non-standard vacua, can alter both the amplitude and spectral shape of the resulting GW background (see [243] for a review).

- **Topological Defects**: Networks of cosmic strings or domain walls formed during symmetry-breaking events may produce GWs through loop decay or annihilation events, generating a background over a broad frequency range. Cosmic strings are topological defects that may have formed during symmetry-breaking PTs in the early Universe, predicted in a variety of high-energy physics scenarios such as GUT, SUSY, and string theory [260, 261].

  Unlike domain walls or monopoles, cosmic strings do not overclose the Universe and instead reach a "scaling" regime, where the string network consists of a few Hubble-length long strings per horizon volume. Energy is lost primarily via the formation of closed loops that oscillate and radiate GWs, making them testable across a range of experiments from PTAs to ground based interferometers.

  The GW energy density spectrum emitted from cosmic strings can be written approximately as [262]:

$$\Omega_{\rm GW}(f) \equiv \frac{1}{\rho_c}\frac{d\rho_{\rm GW}}{d\ln f} \simeq \Omega_\gamma \sqrt{G\mu} \simeq 4.2 \times 10^{-5}\sqrt{G\mu}\,, \tag{2.27}$$

  where $G\mu$ is the dimensionless string tension, with G the Newton constant and μ the energy per unit length of the string.

  This expression gives a rough estimate for the amplitude of the flat part of the GW spectrum generated by a scaling string network. In realistic models, the full spectrum exhibits structure depending on the emission history and microphysics of the loops. Typically, it is approximately scale-invariant across a broad frequency range during the radiation-dominated era, while decaying in the matter-dominated era [262]. A complete description includes the contribution of higher harmonics and integrates over the evolution of the loop distribution.

Current limits from acoustic peaks in CMB data give $G\mu \lesssim 10^{-7}$, which have been improved by PTA searches, requiring $G\mu \lesssim 10^{-11}$ [263]. Further progress is expected in the near future from intermediate frequency observatories, such as LISA, DECIGO and BBO.

Detection of a cosmic string GW signal would open a direct observational window into ultra-high-energy physics far beyond the reach of terrestrial experiments, potentially revealing new insights into the nature of symmetry breaking and fundamental interactions in the early Universe.

Beyond the mechanisms described above, additional cosmological sources may contribute to the SGWB. These include preheating after inflation, during which explosive particle production can lead to significant GW emission [264]; anisotropic stresses from neutrino decoupling or other free-streaming relativistic species; and models involving extra dimensions or modified gravity, which can imprint distinctive spectral features. Although often more model-dependent, these cosmological sources illustrate the potential of GWs as probes of fundamental physics and the thermal history of the Universe. As detector sensitivities improve, these alternative scenarios may offer complementary channels for discovering BSM physics.

2.2.4 The PTA Signal as a hint for Dark Sectors?

The 2023 results from PTAs experiments [244] revealed a common spectrum stochastic GW signal in the nanohertz range, consistent with expectations for a SGWB. Two compelling explanations have emerged for this signal: a population of SMBHBs and a FOPT in the early Universe. The SMBHBs scenario attributes the signal to GWs emitted during the late inspiral of binary SMBHs formed during galaxy mergers. While standard astrophysical models assuming purely gravitational radiation-driven circular orbits can account for the amplitude and shape of the PTA signal, they require binaries to reach sub-parsec separations, in order for GW emission to be efficient [265]. This enters the realm of the *final parsec problem* [266], a longstanding open issue in astrophysics related to whether environmental interactions (e.g., gas dynamics, stellar scattering) are sufficient to overcome stalling and allow binaries to coalesce efficiently to sub-parsec separation. More optimistic scenarios, which incorporate eccentricity and environmental effects, provide better agreement with the PTA data, but uncertainties remain significant.

Alternatively, a FOPT in the early Universe provides a viable and perhaps more intriguing explanation. A frequentist analysis comparing the two hypotheses, performed by [267] shows a mild statistical preference ($\sim 2-3\sigma$) for the FOPT scenario over the SMBHBs coalescence hypothesis, see Figure 2.8. Crucially, only supercooled PTs with $\alpha \geq 0.3$, at the 100 MeV–GeV scale and with moderately small inverse durations, i.e. $\beta/H_* \lesssim 100$, are compatible with the observed spectrum. These features naturally arise in scenarios involving hidden dark sector, characterized by BSM physics below the electroweak scale [268, 269]. In this context, the SGWB detected by PTAs could represent the first indirect evidence of new, feebly interacting fields beyond the SM, thereby offering a novel probe of dark sectors and their cosmological dynamics. Discriminating between the astrophysical and cosmological interpretations will require future PTA data, particularly the detection of a spectral peak that would strongly favor a FOPT origin over the typically scale-free power-law spectrum expected from SMBH binaries.

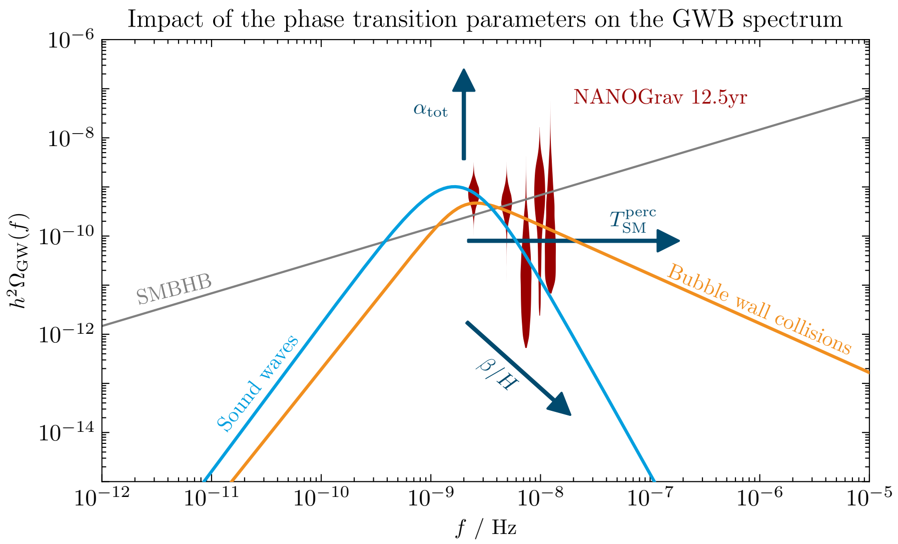

Figure 2.8: Plot showing the NANOGrav 12.5 year "violins" (red) [64], their standard explanation through a power-law spectrum from the inspiral of supermassive black hole binaries (SMBHBs) and two example GW spectra from cosmological FOPTS. A characteristic bubble wall collision spectrum is shown in orange, while a sound wave-induced spectrum is shown in blue. Blue arrows indicate the shifts in the signal corresponding to increasing the phase transition parameters α_{tot}, $T_{\mathrm{perc}}^{\mathrm{SM}}$, or β/H. Figure taken from [268].

2.2.5 Outlook: Future Gravitational Wave Observatories

The coming decades promise a dramatic expansion in GW sensitivity across all frequency bands, with several observatories either under construction or in advanced planning stages. These instruments will enable a deeper exploration of the Universe's astrophysical and cosmological history, probing phenomena ranging from stellar remnants to BSM physics.

- The *Laser Interferometer Space Antenna* (LISA) [270] is a space-based GW observatory developed by the European Space Agency (ESA) with NASA participation, currently scheduled for launch in the mid-2030s. Operating in the millihertz ($\sim 10^{-3}$ Hz) frequency band, LISA will be sensitive to sources inaccessible to ground based detectors, including mergers of SMBHBs, stellar mass BBH and both galactic and extra-galactic white BWD. Crucially, LISA can also probe cosmological sources such as GWs from FOPTs, cosmic strings, and possibly stochastic backgrounds from inflation or other early Universe processes. Its three-spacecraft configuration, with 2.5 million kilometer arm lengths, will orbit the Sun in a trailing Earth-like orbit. DECIGO, proposed by the Japanese space agency) with a conceptual launch in the late 2030s or early 2040s, aims to reach even higher sensitivity in the decihertz band [257]. This frequency range is especially well-suited for probing electroweak-scale FOPTs, making DECIGO an ideal instrument to search for SGWB originating from scenarios such as strongly supercooled PTs or early BSM dynamics. Their combined frequency range (from millihertz to decihertz) corresponds to GWs produced by FOPTs occurring at temperatures of approximately 10^2–10^4 GeV, making them especially suited to probe electroweak-scale baryogenesis scenarios, dark sector symmetry breaking, or other BSM dynamics in the

TeV regime.

- Einstein Telescope (ET) and Cosmic Explorer (CE) are next-generation ground based interferometric GW observatories targeting the 1-10000 Hz band. The *Einstein Telescope* (ET), proposed in Europe with potential sites in Italy and/or the Netherlands, aims to begin construction by the 2030s and operate underground to reduce seismic noise [271]. The *Cosmic Explorer* (CE) is a US led project that envisions detectors with 40-kilometer arms, an order of magnitude longer than current LIGO facilities [272]. Both observatories will significantly improve strain sensitivity, by about an order of magnitude, over current detectors, extending the detection horizon for BBH and binary neutron star BNS mergers to redshifts $z > 10$. These facilities will enable precision measurements of BH and NHS populations across cosmic time, tests of GR in the strong-field regime, and new constraints on the nuclear equation of state.

Therefore, the next decade promises a profound transformation in our ability to observe and interpret the Universe through GWs. With detectors spanning over ten orders of magnitude in frequency, from nanohertz PTAs, to millihertz range space missions like LISA, and up to high-frequency terrestrial observatories such as the ET and CE, we are building an observational network capable of capturing the GW landscape in its full richness. This spectral complementarity is more than technical diversity: it is a roadmap to a deeper, time-resolved understanding of cosmic history. PTAs will continue to probe the low-frequency domain, where signals from SMBHBs and stochastic backgrounds from the early Universe around the MeV scale reside. LISA will bridge the low and mid frequency regimes, uniquely sensitive to intermediate BH masses, BWD, and cosmological sources such as FOPTs around the electroweak scale. Meanwhile, next-generation ground based detectors will push sensitivity to unprecedented depths, expanding our reach to the earliest and most distant stellar mass BH and NS mergers. As this global network comes online, GW astronomy will evolve from a tool for detecting single extreme astrophysical events to a precision probe of fundamental physics. We will test GR in its most extreme regime, chart the formation history of BHs in the early Universe, and possibly uncover signatures of BSM physics through their imprints in the gravitational wave background. Therefore, GWs, once a theoretical curiosity, are rapidly becoming a cornerstone of cosmology and multi-messenger astrophysics. We stand at the threshold of a golden era, in which ripples in spacetime will hopefully unveil the deepest mysteries of our Universe.

Chapter 3

Gravitational Waves as probes for BSM physics in the early Universe

3.1 First order PTs and Gravitational Waves

Cosmological PTs are believed to have played a crucial role in the thermal history of the early universe, with possible implications for the structure and composition of matter and radiation observed today. Within the SM, both the EW and QCD transitions are known to be smooth crossovers [31, 273] and therefore do not produce significant cosmological relics. However, in many well motivated extensions of the SM, these transitions can become first order. A FOPT proceeds via the nucleation and expansion of bubbles of a new vacuum phase within a metastable background, releasing latent heat and driving the out-of-equilibrium phase. Such FOPTs are not just theoretical curiosities, indeed they play central roles in several key open questions in particle physics and cosmology. They can provide the necessary out-of-equilibrium phase for baryogenesis [23, 274] and also offer mechanisms for DM production [275, 53, 54], particularly in scenarios involving new strongly-coupled or confining sectors. Moreover, FOPTs can generate a SGWB [276], potentially within the reach of current or upcoming interferometers such as PTAs, DECIGO, LISA, Ligo-Virgo-Kagra and ET. Depending on their dynamics, these transitions may also yield other cosmological relics such as PBHs [277, 278, 279], topological defects [260, 280], or intergalactic magnetic fields [281].

Of particular interest are *supercooled* PTs, for which bubble nucleation occurs significantly below the critical temperature. In such cases, the universe could temporarily become vacuum-energy dominated, leading to a stage of inflation before bubble percolation completes. Supercooled transitions are typically very strong, leading to ultra-relativistic bubble walls and enhanced production of GWs, making them a promising target for GW astronomy [282, 283]. At the same time, the delay in completion can dilute pre-existing relics, impacting the predictions for baryon asymmetry and DM abundances [275]. In this work, we focus on supercooled FOPTs, exploring their GW signatures and the conditions under which they could be probed by future detectors.

3.1.1 Tunneling rate and nucleation temperature

In the presence of finite-temperature corrections the effective potential can manifest a barrier separating the false vacuum, $\phi_f = 0$ and the true vacuum $\phi_t = v$. Below the critical

temperature T_c the potential energy in the true minimum becomes lower than the potential energy in the false vacuum, which therefore becomes metastable.
The decay rate from the false vacuum to the true vacuum is given by [284], [285]

$$\Gamma(T) \equiv \max\left[T^4\left(\frac{S_3/T}{2\pi}\right)^{3/2}\exp(-S_3/T)\,,\quad R_0^{-4}\left(\frac{S_4}{2\pi}\right)^2\exp(-S_4)\right]\,, \tag{3.1}$$

where S_3 and S_4 are the 3 and 4 dimensional Euclidean actions of the symmetric $O(3)$ and $O(4)$ tunneling solutions. The former is thermally induced while the later is purely quantum. The S_3 and S_4 bounce actions read

$$S_3 = 4\pi\int dr\,r^2\left[\frac{1}{2}\phi'(r)^2+V(\phi(r))\right],\quad S_4 = 2\pi^2\int dr\,r^3\left[\frac{1}{2}\phi'(r)^2+V(\phi(r))\right], \tag{3.2}$$

where $V(\phi)$ is the finite temperature potential, $\phi(r)$ is the field configuration which interpolates between the two asymptotic vacua and the prime denotes differentiation with respect to the radial Euclidean coordinate r. Extremization of the action leads to the Euclidean equation of motion

$$\phi''(r)+\frac{d-1}{r}\phi'(r)=\frac{dV(\phi)}{d\phi}, \tag{3.3}$$

with the boundary conditions

$$\phi'(0)=0 \qquad \lim_{r\to\infty}\phi(r)=0\,. \tag{3.4}$$

We can consider the PT to occur around the nucleation temperature $T_{\rm nuc}$, when the number of bubbles nucleated per Hubble volume and per Hubble time is of order 1 [284]

$$N(T_{\rm nuc}) = \int_{T_{\rm nuc}}^{T_c}\frac{\Gamma(T)}{H(T)^4}\frac{dT}{T}=1, \tag{3.5}$$

that is approximately when

$$\Gamma(T_{\rm nuc})\simeq H(T_{\rm nuc})^4\ . \tag{3.6}$$

This condition can be rewritten as

$$\frac{S_3(T_{\rm nuc})}{T_{\rm nuc}}\simeq 146-2\,{\rm Log}\left(\frac{g_*(T_{\rm nuc})}{100}\right)-4\,{\rm Log}\left(\frac{T_{\rm nuc}}{100\,{\rm GeV}}\right)\,, \tag{3.7}$$

using the expression for the Hubble rate during radiation domination. Therefore, nucleation is expected to occur for $S_3/T\sim\mathcal{O}\,(150)$ for PTs around the GeV scale. It was proved in [284] that there is always a solution to Eqs. (3.3) and (3.4) by means of an undershoot/overshoot argument. If the initial position of the particle is too close to ϕ_t, it will have enough energy to move over ϕ_f with non-zero velocity: hence an overshoot configuration and a divergent solution. Conversely, if the initial position of the particle is too close to the false vacuum, the particle will not have enough energy to reach the true vacuum because of the friction term: we have an undershoot configuration and the solution will be oscillatory. Therefore, by continuity, there must be an intermediate initial position for which the particle comes to rest at the false vacuum, resulting in a finite action solution.

Analytical approximations of the bounce action

While numerical techniques such as shooting methods are often employed to solve the bounce equations, analytical approximations exist in two important regimes: the thin-wall and thick-wall limits, [286]. These provide simplified but insightful estimates of the Euclidean action associated with bubble formation.

In the thick-wall limit, which is relevant for supercooled phase transitions where the potential barrier is small compared to the vacuum energy difference, the bounce action can be approximated analytically. By approximating the bubble profile by a field excursion $\delta\phi = \phi_*$ occurring over a characteristic wall thickness $\delta R \sim R$, the S_3 bounce action, Eq (3.2), can be estimated as

$$S_3 \approx 4\pi \left(\frac{R}{2}\phi_*^2 + \frac{R^3}{3}V(\phi_*) \right), \tag{3.8}$$

where the first term represents the gradient energy and the second the potential energy inside the bubble. Extremizing this expression with respect to the bubble radius R by solving $\frac{\delta S_3}{\delta R} = 0$ yields the critical radius and bounce action [286]

$$R_c^2 = \frac{\phi_*^2}{-2V(\phi_*)}, \quad S_3 \simeq \frac{4\pi}{3}\frac{\phi_*^3}{\sqrt{-2V(\phi_*)}}. \tag{3.9}$$

Similarly, the zero temperature $O(4)$ symmetric bounce action in the thick-wall limit reads

$$R_c^2 = \frac{\phi_*^2}{-V(\phi_*)}, \quad S_4 \simeq \frac{\pi^2\phi_*^4}{-2V(\phi_*)}. \tag{3.10}$$

In thermal potentials relevant for supercooled transitions, the critical radius typically scales as $R_c \sim 1/T$, so the ratio

$$\frac{S_4}{S_3/T} \sim R_c T \tag{3.11}$$

is roughly constant with temperature, implying the relative dominance of thermal versus quantum tunneling is not strongly temperature dependent within this approximations. Although thin-wall approximations exist, they are less applicable for strongly supercooled PTs, where the thick-wall limit gives a better analytic description.

3.1.2 Bubble wall velocities: Runaway and Terminal regime

Understanding the dynamics of bubble wall expansion is crucial for characterizing the physical outcomes of a cosmological PT. In particular, the velocity of the expanding bubble wall determines how the vacuum energy released during the transition is partitioned between the bubble wall itself and the surrounding plasma. This has direct consequences for the strength and the shape of the GW signal, as we will discuss in Sec. 3.1.3.

In the thin-wall approximation, the bubble wall is modeled as a surface of negligible thickness separating regions of true and false vacuum. Under this assumption, one can write a relativistic Lagrangian for a spherically symmetric bubble of radius R as [284, 287]:

$$\mathcal{L} = -4\pi\sigma R^2\sqrt{1-\dot{R}^2} + \frac{4\pi}{3}R^3 p, \tag{3.12}$$

where σ is the free energy per unit area (tension) of the wall and p is the net pressure acting on the wall. This pressure can be decomposed into a driving component $\Delta V = V_f - V_t = c_{\rm vac} f^4$, being $c_{\rm vac} \simeq \mathcal{O}(0.01)$ a model dependent parameter and f the VEV of the order parameter in the true vacuum, and a frictional component $\Delta\mathcal{P}$, due to the interaction of the bubble wall with the ambient plasma. In the absence of friction, then, one has $p = \Delta V$.

From this Lagrangian, the total energy of a bubble is obtained as:

$$E = 4\pi\gamma\sigma R^2 - \frac{4\pi}{3}R^3 p\,, \tag{3.13}$$

with $\gamma = 1/\sqrt{1-\dot{R}^2}$, the Lorentz boost factor of the wall. The critical radius R_c, which gives the minimum bubble nucleation radius is obtained by extremizing the energy, yielding:

$$R_c = \frac{2\sigma}{\Delta V}. \tag{3.14}$$

Assuming that the bubble nucleates at $R_0 \approx R_c$, its subsequent evolution is governed by the Euler-Lagrange equation [288]:

$$\ddot{R} + \frac{2(1-\dot{R}^2)}{R} = \frac{(1-\dot{R}^2)^{3/2}}{\sigma}\Delta V, \tag{3.15}$$

which can be rewritten in terms of γ as:

$$\frac{d\gamma}{dR} + \frac{2\gamma}{R} = \frac{\Delta V}{\sigma}. \tag{3.16}$$

Solving this with initial condition $\gamma(R_0) = 1$ yields:

$$\gamma(R) = \frac{R}{3R_0} + \frac{R_0^2}{3R^2} \approx \frac{R}{3R_0} \tag{3.17}$$

as the bubble expands, indicating that the wall accelerates rapidly in the early stages of expansion. This solution assumes negligible interaction between nearby particle while they cross the wall. It therefore describes the so called *runaway* regime, where plasma interactions are weak and cannot stop the wall from accelerating indefinitely. Although the scaling $\gamma(R) \propto R$ is typically derived within the thin-wall approximation, it reflects generic features of bubble expansion under constant pressure and negligible friction. As such, this behavior is expected to persist qualitatively in the thick-wall regime relevant for strongly supercooled transitions.

The wall Lorentz factor in the absence friction, evaluated at the collision radius $R_{\rm coll}$, is then given by [53]:

$$\gamma_{\rm run} \simeq \frac{R_{\rm coll}}{3R_0} \simeq 1.7\frac{10}{\beta/H}\left(\frac{0.01}{c_{\rm vac}}\right)^2 \frac{M_{\rm Pl}}{f}\frac{T_{\rm nuc}}{f}\,, \tag{3.18}$$

where β/H characterizes the inverse duration of the PT and we used $R_0 \approx T_{\rm nuc}^{-1}$ for the bubble radius at nucleation and $R_{\rm coll} = \pi^{1/3}/\beta$ [289].

Thus far, we have assumed negligible friction, allowing the wall to accelerate freely. However, plasma interactions generally induce a frictional pressure $\Delta\mathcal{P}$ that can counteract the vacuum force, yielding

$$p = \Delta V - \Delta\mathcal{P}, \tag{3.19}$$

where the leading-order (LO) contribution $\mathcal{P}_{\rm LO}$ to the stopping pressure $\Delta\mathcal{P}$ is due to the massless particles in the broken phase getting a mass squared $\Delta m^2 \propto f^2$ while crossing the bubble wall, and it is given by [290]:

$$\Delta P_{\rm LO} = \sum_a g_a c_a \frac{\Delta m^2 T_{\rm nuc}^2}{24}\,, \tag{3.20}$$

being g_a is the number of the internal degrees of freedom and $c_a = 1(1/2)$ for bosons (fermions). If $\Delta V > \mathcal{P}_{\rm LO}$ the bubbles will keep accelerating to larger values of γ until either they collide in the runaway regime, or reach a *terminal velocity* regime, due to the next-to-leading order ($\mathcal{P}_{\rm NLO}$) contribution to the friction given by soft radiation [291]. Indeed, the latter is proportional to γ and is enhanced by large logarithms, which have been resummed in [292], giving:

$$\gamma\Delta\mathcal{P}_{\rm NLO} \approx g_{\rm eff}\, g^2\, \gamma\, m_V\, T^3_{\rm nuc}\, \frac{m_V}{\mu}\,, \tag{3.21}$$

with g the gauge coupling, $g_{\rm eff}$ a weighted sum of the radiating gauge of freedom times their charges, m_V the gauge boson mass in the broken phase and μ an IR cutoff (see Sec. 3.2.2 and [53] for a discussion about the stopping pressure in the case of strongly-coupled PTs). Therefore, friction stops the growth of γ when the net pressure vanishes, which occurs at:

$$\gamma_{\rm eq} = \frac{\Delta V - \Delta\mathcal{P}_{\rm LO}}{\Delta\mathcal{P}_{\rm NLO}}. \tag{3.22}$$

If $\gamma_{\rm eq} < \gamma_{\rm run}$, then the wall reaches a terminal velocity and transitions to a constant-speed regime. The corresponding radius at which this terminal velocity is reached is:

$$R_{\rm eq} = 3\gamma_{\rm eq} R_0. \tag{3.23}$$

To assess whether the transition is runaway or not, it is useful to define the following dimensionless quantities:

$$\alpha \equiv \frac{\Delta V(T) - T\frac{\partial\Delta V}{\partial T}}{\rho_{\rm rad}} \approx \frac{\Delta V}{\rho_{\rm rad}}, \quad \alpha_\infty \equiv \frac{\Delta P_{\rm LO}}{\rho_R}, \quad \alpha_{\rm eq} \equiv \frac{\Delta P_{\rm NLO}}{\rho_R}, \tag{3.24}$$

Our treatment, which neglects interaction between particles during the time when they enter the bubble, is justified for $\alpha > \alpha_\infty$, and the terminal velocity regime is reached when $\gamma = \gamma_{\rm eq} = (\alpha - \alpha_\infty)/\alpha_{\rm eq}$.

Finally, the fraction of the vacuum energy converted into bubble wall energy depends sensitively on the dynamics. In the absence of friction (i.e., in the runaway case), nearly all vacuum energy goes into the wall. However, once the terminal velocity is reached, further vacuum energy release contributes instead to heating and bulk motion of the plasma. The fraction of vacuum energy stored in the kinetic energy of the wall at percolation is given by [287]:

$$\kappa_{\rm wall} \equiv \frac{E_{\rm wall}}{E_V} = \begin{cases} 1 - \frac{\alpha_\infty}{\alpha}, & \gamma_{\rm run} \le \gamma_{\rm eq} \quad \text{(Runaway)}, \\ \frac{\gamma_{\rm eq}}{\gamma_{\rm run}}\left[1 - \frac{\alpha_\infty}{\alpha}\left(\frac{\gamma_{\rm eq}}{\gamma_{\rm run}}\right)^2\right], & \gamma_{\rm run} > \gamma_{\rm eq} \quad \text{(Terminal velocity)}\,, \end{cases} \tag{3.25}$$

while the remaining fraction of the vacuum energy $\kappa_{\rm fluid} = 1 - \kappa_{\rm wall}$ goes into kinetic and thermal energy of the plasma.

This analysis highlights the importance of wall velocity regimes. Whether a bubble wall runs away or saturates to a terminal speed directly affects both the efficiency of vacuum energy transfer to GW production and the feasibility of baryogenesis mechanisms. In Section 3.2 we will explore a specific model where either of the regimes could be realized, depending on parameter choices such as ΔV, particle content, and transition temperature.

3.1.3 Gravitational Waves from First Order PTs

FOPTs in the early Universe can generate a SGWB through violent processes associated with the collision of bubbles of the new phase. An accurate computation of the GW signal upon FOPTs is crucial to probe BSM physics through current and upcoming GW detectors. Our knowledge of the GW signal produced upon a FOPT is mostly based on scalar field and hydrodinamical simulations, see [276, 243] for reviews. The GW signal from a FOPT is governed primarily by the following parameters characterizing the PT dynamics and energy budget:

- **PT Strength** α: This parameter quantifies the latent heat released during the transition normalized by the radiation energy density,

$$\alpha(T) \equiv \left. \frac{\Delta V(T) - T\frac{\partial \Delta V}{\partial T}}{\rho_{\rm rad}} \right|_{T_{\rm nuc}} , \tag{3.26}$$

  which has to be evaluated at the nucleation temperature $T_{\rm nuc}$. A strongly supercooled PT ($T_{\rm nuc} \ll T_{\rm crit}$) leads to large $\alpha \gg 1$, since $\rho_{\rm rad} \propto T^4$ while ΔV stays roughly constant.

- **PT duration** β/H: This parameter characterizes the time scale of the transition relative to the Hubble time,

$$\beta/H \equiv \left. \frac{d}{dT}\left(\frac{S}{T}\right) \right|_{T_{\rm nuc}} , \tag{3.27}$$

  where S is the Euclidean action of the critical bubble, either S_3 or S_4. β/H determines how fast bubbles nucleate and the typical bubble size at collision, given by $R_{\rm coll} = \pi^{1/3}/\beta$ [289].

- **Reheating temperature** $T_{\rm RH}$: After the transition completes, the latent heat reheats the plasma, restoring radiation domination, and by applying energy conservation, neglecting the energy lost in the GW signal and assuming fast thermalization of the decay products, one obtains [293]

$$T_{\rm RH} \approx (1+\alpha)^{1/4} T_{\rm nuc} \,. \tag{3.28}$$

- **Bubble wall velocity** v_w: The final relevant parameter is the bubble wall velocity at collision v_w, in the rest frame of the plasma. Accurately computing the value of v_w is in general highly non-trivial, as it requires detailed modeling of the plasma dynamics and the microscopic interactions between the bubble wall and the thermal bath. Various theoretical approaches and approximations exist in the literature depending on the strength of the PT and the field content of the model [294, 295].

Three main mechanisms generate GWs during a FOPT: i) bubble collisions; ii) sound waves and iii) turbulence in the plasma produced upon bubble collisions. The total energy density emitted in GW $\Omega_{\rm gw}$ is then given by the sum of these terms

$$\Omega_{\rm gw} = \Omega_\varphi + \Omega_{\rm sw} + \Omega_{\rm turb} \tag{3.29}$$

We will briefly review each contribution in more detail.

- **Scalar field contribution:** The collisions of bubble walls release energy stored in the scalar field gradients at the bubble boundaries. This contribution has been first modeled by the envelope approximation, which assumes that the shear stresses are localized in thin shells in which the collided portions of the bubbles have been removed, accumulating energy from the kinetic energy of the bubble wall. The scalar field contribution is expected to be the dominant component of the GW energy density budget only for very relativistic bubbles, i.e. in the runaway regime. The GW energy density spectrum for the scalar field is approximated in the envelope approximation by [296]

$$h^2\Omega_\varphi(f) = 1.67\times10^{-5}\left(\frac{100}{g_*}\right)^{1/3}\left(\frac{1}{\beta/H}\right)^2\left(\frac{\kappa_{\text{wall}}\,\alpha}{1+\alpha}\right)^2\left(\frac{0.11v_w^3}{0.42+v_w^2}\right), \tag{3.30}$$

where the spectral shape function of the GW radiation from bubble collisions can be parametrized as

$$S_{\text{env}}(f) = \frac{3.8\,(f/f_{\text{env}})^{2.8}}{1+2.8\,(f/f_{\text{env}})^{3.8}}, \tag{3.31}$$

where $S_{\text{env}}(f)$ describes the spectral shape via a broken power-law and f_{env} is the peak frequency. Hence, from the numerical approximation the spectrum scales as f^{-1} in the UV and as $f^{2.8}$ in the IR, although causality requires the slope to be f^3 for frequencies below the inverse Hubble scale at the time of GW production [297].

The peak frequency from bubble collisions is related to the characteristic time scale of the PT, β^{-1}, and can be estimated at the time of production (t_*) as

$$\frac{f_*}{\beta} = \frac{0.62}{1.8-0.1v_w+v_w^2}, \tag{3.32}$$

where v_w is the bubble wall velocity.

This frequency is redshifted to today as [298]

$$f_{\text{env}} = 1.65\times10^{-5}\text{Hz}\left(\frac{f_*}{\beta}\right)(\beta/H)\left(\frac{T_*}{100\,\text{GeV}}\right)\left(\frac{g_*}{100}\right)^{1/6}. \tag{3.33}$$

Recent developments have qualitatively and quantitatively challenged the validity of the envelope approximation, particularly regarding the spectral slopes both in the IR and in the UV. In particular, lattice simulations [299, 300] have shown that the IR and UV slopes depend on the wall profile and that the IR slope is softened due to the long-lasting free propagation of anisotropic stress-energy shells after collisions, an effect that is not captured by the envelope approximation. These findings are in qualitative agreement with analytical studies based on the bulk flow model developed [301], which also predict IR enhancement due to post-collision dynamics. Notably, thick-walled bubbles show stronger IR enhancement, while thin-walled configurations can lead to dissipation through repeated wall bounces. Therefore, results indicate that the envelope approximation may not only be quantitatively inaccurate, but also qualitatively incomplete.

- **Sound waves contribution:** The contribution from sound waves to the GW spectrum arises from the bulk motion of the plasma induced by expanding bubbles during a

FOPT. This motion generates long-lasting acoustic waves, typically on the order of the Hubble time, which efficiently source GWs. The contributions from sound waves typically dominates the GW spectrum when the bubble wall reaches a terminal velocity v_w. The GW energy density spectrum from sound waves, following the numerical fit performed by [276], is given by

$$h^2\Omega_{\rm sw}(f) = 2.65\times 10^{-6}\left(\frac{H_*}{\beta}\right)\left(\frac{\kappa_v\alpha}{1+\alpha}\right)^2\left(\frac{100}{g_*}\right)^{1/3} v_w\, S_{\rm sw}(f), \tag{3.34}$$

where κ_v is the efficiency with which latent heat is converted into bulk fluid motion, given by [287]

$$\kappa_v = \kappa_{\rm fluid}\times\frac{\alpha}{0.73+0.083\sqrt{\alpha}+\alpha} \tag{3.35}$$

and the spectral shape function $S_{\rm sw}(f)$ is modeled as a broken power law, given by

$$S_{\rm sw}(f) = \left(\frac{f}{f_{\rm sw}}\right)^3\left(\frac{7}{4+3(f/f_{\rm sw})^2}\right)^{7/2}, \tag{3.36}$$

with a peak frequency $f_{\rm sw}$ estimated by

$$f_{\rm sw} = 1.9\times 10^{-5}\ {\rm Hz}\left(\frac{1}{v_w}\right)\left(\frac{\beta}{H_*}\right)\left(\frac{T_*}{100\ {\rm GeV}}\right)\left(\frac{g_*}{100}\right)^{-1/6}. \tag{3.37}$$

By comparing Eq. (3.34) with Eq. (3.30) one can see that due to the long-lasting nature of sound waves, their signal is enhanced with respect to that associated to bubble collision by a β/H factor, making them the dominant contribution to the SGWB spectrum in the case of a FOPT which is not strongly supercooled. Moreover, we point out that simulations of sound waves have been only successfully performed for moderate supercooling ($\alpha \le 1$), while the typical regime of runaway bubbles features $\alpha \gg 1$ and the contribution of sound waves in this regime is not well understood [298, 302]. In this regime it has been argued that derivatives of the envelope approximation such as the so-called bulk flow model [301] are more realistic in modeling the GW signal [302].

- **Turbulent contribution:** In addition to sound waves, percolation during a FOPT can also induce magnetohydrodynamic (MHD) turbulence in the plasma. This turbulence acts as a long-lasting source of GWs, potentially contributing significantly to the GW spectrum. Assuming Kolmogorov-type turbulence, the contribution from turbulence can be modeled as [297]

$$h^2\Omega_{\rm turb}(f) = 3.35\times 10^{-4}\left(\frac{H_*}{\beta}\right)\left(\frac{\kappa_{\rm turb}\,\alpha}{1+\alpha}\right)^{3/2}\left(\frac{100}{g_*}\right)^{1/3} v_w\, S_{\rm turb}(f), \tag{3.38}$$

where $\kappa_{\rm turb} \le 5-10\%$ is the efficiency factor [303] with which latent heat is converted into MHD turbulence.

The spectral shape of the turbulence contribution is given by

$$S_{\rm turb}(f) = \frac{(f/f_{\rm turb})^3}{[1+(f/f_{\rm turb})]^{11/3}\left(1+\frac{8\pi f}{h_*}\right)}. \tag{3.39}$$

The characteristic frequency associated with this contribution is given by

$$f_{\rm turb} = 2.7 \times 10^{-5}\ \text{Hz} \left(\frac{1}{v_w}\right) \left(\frac{\beta}{H_*}\right) \left(\frac{T_*}{100\ \text{GeV}}\right) \left(\frac{g_*}{100}\right)^{-1/6}. \tag{3.40}$$

As emphasized in Ref. [298], the GW signal from turbulence is subject to significant theoretical uncertainties. These arise from the difficulty of accurately modelling the onset, duration, and decay of turbulence in a relativistic plasma. In particular, the precise amount of kinetic energy converted into vortical motion remains uncertain, as well as its dependence on the amount of supercooling α. Different treatments of the turbulence decorrelation time and the autocorrelation function of the anisotropic stresses can lead to very different predictions for the GW spectrum. Moreover, numerical simulations of GW production from MHD turbulence are still in early stages and have yet to converge on a universal spectral shape or normalization. As a result, although the turbulent contribution may enhance the total GW signal, especially in the presence of strong transitions, its amplitude and spectral shape should be interpreted with caution.

3.2 Baryogenesis and Leptogenesis from Supercooled confinement

3.2.1 Introduction

FOPTs with fast bubble walls are currently receiving massive attention because they produce GWs [304, 305] observable at current [64, 306, 307] and foreseen [308] telescopes. In addition to detectability in GW, FOPTs with fast walls are motivated as production mechanisms of DM in the form of very heavy particles [52, 275, 309, 54, 53, 310] or PBHs [311, 312, 283, 313]. PTs with fast bubble walls offer also viable mechanisms to explain the BAU, see e.g. [314, 315, 316]. A particularly simple possibility is to obtain the BAU from out-of-equilibrium decays of particles that obtain their mass at a supercooled PT, as proposed in [316] and worked out so far only for PTs of weakly coupled theories. This mechanism, however, works only for scales of the PT above about 10^8 GeV (see e.g. also [317, 318]), so that it is not testable in any laboratory experiment and only poorly so by GW telescopes, given that the predicted GW are at very high frequencies.

In this section we point out that, if the supercooled PT is a confining one, then with respect to analogous weakly-coupled PTs, both the yield of the mass-gaining particles (i.e. the hadrons) is larger and wash-out processes are suppressed. We will show that these ingredients allow to generate the baryon asymmetry down to PT scales in the TeV range, via hadron's decays. This opens up the possibility to generically test this framework with LISA and the Einstein Telescope. Depending on its specific realisation, we will show that this also allows to test the scenario at colliders and/or to connect leptogenesis with neutrino mass generation in a new framework.

3.2.2 Framework for the generation of the Baryon Asymmetry

Supercooled confining PTs

As the temperature of the early universe bath drops, the vacuum state of the theory that is energetically favoured can change, triggering a PT. If the PT is first order it proceeds via nucleation of bubbles of the new ('true') vacuum in the bath, see e.g. [276, 286] for reviews.

A FOPT in the early universe is controlled by the interplay between the energy density of radiation and the difference ΔV between the ones of the old ('false') and new vacuum. The latter is given by

$$\Delta V \equiv c_{\rm vac}\, f^4\,, \tag{3.41}$$

where f is the VEV of the order parameter ϕ of the PT in the true vacuum (which we will later identify with the dilaton), and $c_{\rm vac}$ is a dimensionless, model dependent, quantity parameterizing the vacuum energy difference, typically $c_{\rm vac} \sim \mathcal{O}(1)$ or smaller. The radiation energy density is given by

$$\rho_{\rm rad} = \frac{g_* \pi^2}{30} T^4\,, \tag{3.42}$$

where g_* counts the effective degrees of freedom of the radiation bath. The PT takes place around the nucleation temperature, $T_{\rm nuc}$, when the bubble nucleation rate per unit volume, Γ, becomes comparable to the Hubble parameter H, namely $\Gamma(T_{\rm nuc}) \sim H^4(T_{\rm nuc})$. The PT is said to be supercooled if it happens when the universe is dominated by the vacuum energy rather than by radiation, $\rho_{\rm rad} < \Delta V$, i.e.

$$\text{supercooling:} \qquad T_{\rm nuc} < T_{\rm eq} \equiv \left(\frac{30\, c_{\rm vac}}{g_* \pi^2}\right)^{1/4} f\,, \tag{3.43}$$

where $T_{\rm eq}$ is defined as the temperature when $\rho_{\rm rad} = \Delta V$. Following the PT, the order parameter ϕ undergoes oscillations and decays. We assume that its width is comparable or larger than the Hubble rate, so that the universe is reheated to a temperature

$$T_{\rm RH} = \left(\frac{30\, c_{\rm vac}}{g_{\rm RH} \pi^2}\right)^{1/4} f\,, \tag{3.44}$$

where $g_{\rm RH}$ is the number of degrees of freedom in the broken phase that are reheated.

A supercooled PT is generically predicted by potentials $V(\phi)$ that are flat enough at the origin at zero temperature [319], see [320] for a recent systematic study. The needed features of $V(\phi)$ are automatically predicted by models that are approximate scale invariant in the UV, and that spontaneously break scale invariance in the IR, like in radiative generation of IR scales à la Coleman-Weinberg [21, 321].

In this work we will be interested in strongly coupled realisations, where confinement occurs from the condensation of an approximately conformal strongly-interacting sector, and which are dual to 5D warped models, see e.g. [322, 323, 324, 325]. The spontaneous breaking results in a Goldstone boson parametrically lighter than f, the dilaton ϕ, which can be thought of as a condensate of UV quanta of the confining theory. Its potential is generated from a small explicit breaking of scale-invariance in the UV, without which the symmetry could not be spontaneously broken, so that (see e.g. [326])

$$\Delta V = V(\phi = 0) - V(\phi = Zf) \simeq \left(\frac{Z m_\phi f}{4}\right)^2, \tag{3.45}$$

where Z is the dilaton's wavefunction renormalization and in strongly coupled theory is expected to be of order one. We clarify that ϕ then denotes the canonically normalized dilaton, and m_ϕ its mass. Eq. (3.45) then implies that m_ϕ and $c_{\rm vac}$ are not independent parameters, but are linked via

$$m_\phi = \frac{4}{Z}\, c_{\rm vac}^{1/2}\, f\,. \tag{3.46}$$

$m_\phi <$ few$\times f$ is enough to achieve values of $T_{\rm nuc}$ orders of magnitude smaller than $T_{\rm eq}$, see e.g. [309, 326]. Larger hierarchies between m_ϕ and f, corresponding to very small values of $c_{\rm vac}$, may imply that the PT never completes. One could then envisage to complete it via the PT associated to another sector, see [327, 328] for examples where the QCD PT triggers a supercooled EW PT that would otherwise not complete. Obtaining large hierarchies between m_ϕ and f is also non-trivial from the theoretical point of view, see e.g. [329, 330, 331, 332, 333] for successful attempts.

Dynamics of the walls

Supercooled PTs generically predict that bubble walls are ultrarelativistic. As bubbles are nucleated and start to expand, the wall's boost factor γ starts growing as well because the surface tension of the wall loses against the difference in pressures. If nothing prevents their acceleration, then walls 'run away' and γ keeps growing linearly with the bubble radius R.

For the values of $\Delta V/\rho_{\rm rad} \gtrsim 1$ of our interest, plasma effects cannot prevent the walls from becoming faster and faster [334, 335]. Particle physics effects however can. They come from particles obtaining a mass at the wall [290] and radiation from these particles [291], which exert a pressure on the walls and can prevent them from running away, see Sec. 3.1.2. In the context of PTs that are both supercooled and confining, the pressure arises from non-perturbative effects and reads [309]

$$\mathcal{P} \simeq \frac{\zeta(3)}{\pi^2} g_{\rm TC}\, \gamma\, T_{\rm nuc}^3 f\,, \tag{3.47}$$

where $g_{\rm TC}$ is the number of degrees of freedom, that are charged under the confining group, in the deconfined phase (see the next two subsections). The non-perturbative effects responsible for this pressure can be thought of as the strong-coupling limit of the resummed radiation at the walls in weakly coupled theories, and indeed the pressure associated to the latter effects also scales linearly in γ [292]. Walls then reach a terminal constant boost, $\gamma_{\rm T}$ as soon as $\Delta V = \mathcal{P}$. If this condition is never met, they run away until they collide with walls from other bubbles.

The wall boost factor at bubbles collision then reads

$$\gamma_{\rm coll} \simeq {\rm Min}\Big[\gamma_{\rm run}, \gamma_{\rm T}\Big] \simeq {\rm Min}\Big[1.7\frac{10}{\beta/H}\Big(\frac{0.01}{c_{\rm vac}}\Big)^{1/2}\frac{T_{\rm nuc}}{f}\frac{M_{\rm Pl}}{f}, 10^{-3}\frac{c_{\rm vac}}{0.01}\frac{80}{g_{\rm TC}}\Big(\frac{f}{T_{\rm nuc}}\Big)^3\Big]\,, \tag{3.48}$$

where the first entry is the runaway value at collision $\gamma_{\rm run} = R_{\rm coll}/(3R_{\rm nuc})$ [292], $R_{\rm coll} = \pi^{1/3}/\beta$ [289] is the typical bubble radius at collision and $R_{\rm nuc}$, of order $T_{\rm nuc}^{-1}$, the one at nucleation. Since in the supercooled PTs of our interest $R_{\rm nuc} \lesssim T_{\rm nuc}^{-1}$ [309], we use $R_{\rm nuc} = T_{\rm nuc}^{-1}/2$ for definiteness (other supercooled PTs may have $R_{\rm nuc} \gtrsim T_{\rm nuc}^{-1}$, see e.g. [336]). We have also introduced the reduced Planck mass $M_{\rm Pl} \simeq 2.4 \times 10^{18}$ GeV and $\beta \equiv (d\Gamma/dt)\Gamma$, where we remind that Γ is the bubble nucleation rate per unit volume, so that β/H controls the typical number of bubbles per Hubble volume and β/H between 10 and 100 is a typical range for supercooled PTs. Whether the bubble-walls stay in the runaway regime or reach a terminal velocity depends on the amount of supercooling of the PT, which we quantify by the ratio $T_{\rm nuc}/f$. Examining Eq. (3.48) it is clear that, in order to have a sufficiently large $\gamma_{\rm coll}$, one needs $T_{\rm nuc} \ll f$.

Abundance of hadrons

We call hadron any composite state of the confining sector. Hadrons are expected to have a mass $M_{\rm hadr} \approx 4\pi f \gg T_{\rm nuc}$ coming from their strong coupling to the dilaton, unless they are lighter for symmetry reasons, like the dilaton itself or other pseudo-goldstone bosons (analogous to pions in QCD). The hadrons do not exist before the PT, where the fundamental 'techniquanta' (TC) are massless (like quarks and gluons in QCD). These are in equilibrium with the thermal bath before the PT and their number density to entropy ratio, the Yield, is given by

$$Y_{\rm TC} \equiv \frac{n_{\rm TC}}{s} = \frac{45\zeta(3) g_{\rm TC}}{2\pi^4 g_*}\,, \tag{3.49}$$

where $g_{\rm TC}$ are the degrees of freedom of the techniquanta and $n_{\rm TC}$ is their number density.

What happens upon the PT was first modeled in [309] and can be summarized as follows. Techniquanta enter the bubble and form fluxtubes that point towards the wall. If techniquanta have more energy than the confinement scale in the wall frame, i.e. if $\gamma T_{\rm nuc} \gtrsim f$, then these fluxtubes break forming a large number of hadrons, which on average follow the bubble walls in the plasma frame[1]. Fluxtube's breaking also results in the ejection of techniquanta outside the wall, to conserve charge. Both hadrons and ejected particles have very high energies in the bath frame, of order γf. As bubbles expand and collide, hadrons and ejected techniquanta collide with those from other bubbles and with particles of the pre(heated) plasma, whose typical energies are of the order of the dilaton mass m_ϕ. These collisions result in deep inelastic scatterings which ultimately convert the large center of mass energies (of order $m_\phi \gamma f$ in the bath frame) into hadron masses. This conversion has been found by simulations of scatterings and hadronization in [309], and its simplicity makes it pretty robust against the details of this simulation and other possible processes affecting the propagation and scatterings of hadrons and ejected techniquanta [337]. This redistribution of large energies into hadron masses then enhances the yield of hadrons, with respect to that of particles that gain mass at a non-confining PT, by a factor $\gamma_{\rm coll} f m_\phi / M_{\rm hadr}^2$. The yield of a given hadron Ψ then reads

$$Y_\Psi \simeq Y_{\rm TC} \times 3 \frac{\gamma_{\rm coll} f m_\phi}{M_{\rm hadr}^2} \, Br\big(\text{hadr} \to \Psi\big) \times \left(\frac{T_{\rm nuc}}{T_{\rm eq}}\right)^3 \frac{T_{\rm RH}}{T_{\rm eq}}, \tag{3.50}$$

where $M_{\rm hadr} \simeq 4\pi f$ and $Br\big(\text{hadr} \to \Psi\big) < 1$ is the number of hadrons Ψ produced over all hadrons in the end of the scattering chains, which is expected to be suppressed if $M_\Psi \gg f$, analogously to QCD. The last factor $(T_{\rm nuc}/T_{\rm eq})^3 \, T_{\rm RH}/T_{\rm eq} \propto (T_{\rm nuc}/f)^3$ is the usual dilution of relics from supercooled PTs, the factor $(3\gamma_{\rm coll} f m_\phi / M_{\rm hadr}^2)$ is its enhancement specific of confining theories discussed before Eq. (3.50).

Baryon asymmetry from hadrons decay

Let us now assume that a portal connects the confining sector and the SM that results in an otherwise-stable hadron Ψ to decay violating B, C and CP. Note that the portal needs not to necessarily violate C and CP, as their violation could rely on the one existing in the SM (see e.g. [338, 339] for a realisation of this idea in composite Higgs models, although for slow bubble walls) or it could be a property of the strong sector. We do not need to specify this nor the UV origin of the portal in this work, we just need to know that each of the Ψ or $\bar{\Psi}$ produces on average a net baryon number ϵ_Ψ. The baryon yield then reads

$$Y_B = \epsilon_\Psi \, K_{\rm Sph} \, Y_\Psi \tag{3.51}$$

$$\simeq Y_{\rm BAU} \times \frac{\gamma_{\rm coll}}{\gamma_{\rm T}} \frac{\epsilon_\Psi \, K_{\rm Sph}}{1.2 \cdot 10^{-4}} \frac{Br\big(\text{hadr} \to \Psi\big)}{10^{-3} \, Z} \left(\frac{107.75}{g_{\rm RH}}\right)^{\frac{1}{4}} \left(\frac{c_{\rm vac}}{0.01}\right)^{\frac{3}{4}} \left(\frac{4\pi f}{M_{\rm hadr}}\right)^2, \tag{3.52}$$

where $K_{\rm Sph}$ is the sphaleron reprocessing factor, $K_{\rm Sph} = 1$ if the baryon asymmetry is generated when electroweak sphalerons are not active, namely when $T \lesssim T_{\rm Sph} = 132$ GeV [23], and $K_{\rm Sph} < 1$ otherwise ($K_{\rm Sph} = 28/79$ in the SM [340]). In general ϵ_Ψ is at most of order

$$\epsilon_\Psi \lesssim \frac{{\rm Im} y^2}{4\pi} \frac{M_\Psi}{\Delta M}\,, \tag{3.53}$$

where by ${\rm Im} y^2$ we mean the imaginary part of some combination of couplings with coupling dimension 2, and where we include possible enhancements from small hadron mass splittings

[1] Other subtleties can change the picture as $c_{\rm vac}$ and $T_{\rm nuc}/f$ approach 1, but they won't matter for the parameter space of our interest.

$\Delta M \ll M_\Psi$. Small hadron mass splittings are actually expected from confining sectors with at least two light quarks (think for example of the neutron and proton masses in QCD).

The discussion so far assumes that the population of hadrons Ψ is unaffected before they decay. First, we estimate the total decay rate of Ψ as $\Gamma_\Psi = C|y|^2 M_\Delta/8\pi$, where C is a model-dependent factor, and observe that they are much faster than the Hubble rate in the entire parameter space that we will consider. So we should compare the rate of Ψ annihilations, i.e. how fast the Ψ want to go to their thermal equilibrium abundance, with Γ_Ψ and not with H. Ψ's annihilate into dilatons ϕ and possibly other particles, depending on the model. As the coupling of Ψ to dilatons is model-independent and large (of order $M_\Psi/(Zf)$), we estimate the annihilation cross section with the analogous QCD one for $p-\bar{p}$ annihilations, $\sigma(\Psi\Psi^* \to \phi\phi)v_{rel} \sim 4\pi/M_\Psi^2$. Therefore, using Eq. (3.52), we obtain the total Ψ annihilation rate

$$\Gamma_{\rm annh} \sim n_\Psi \sigma v_{rel} \sim 8.7 \times 10^{-8} M_\Psi \left(\frac{4\pi f}{M_\Psi}\right)^5 \frac{\gamma_{\rm coll}}{\gamma_{\rm T}} \frac{Br\big(\text{hadr} \to \Psi\big)}{0.1\, Z} \left(\frac{c_{\rm vac}}{0.01}\right)^{\frac{3}{2}} \frac{107.75}{g_{\rm RH}} \frac{g_*}{200}\,. \tag{3.54}$$

In order to not change the abundance of the Ψs before they decay and source the BAU, we require $\Gamma_{\rm annh}$ to be below $\Gamma_\Psi = C|y|^2 M_\Delta/8\pi$, i.e. the following ratio should be smaller than one:

$$\frac{\Gamma_{\rm annh}}{\Gamma_\Psi} \simeq \frac{0.02}{C} \times \left(\frac{0.01}{|y|}\right)^2 \left(\frac{4\pi f}{M_\Delta}\right)^5 \frac{\gamma_{\rm coll}}{\gamma_{\rm T}} \frac{Br\big(\text{hadr} \to \Psi\big)}{0.1\, Z} \left(\frac{c_{\rm vac}}{0.01}\right)^{\frac{3}{2}} \frac{107.75}{g_{\rm RH}} \frac{g_*}{200}\,. \tag{3.55}$$

In the regions where this is larger than one, it could still possible to source the BAU, as there is still a population of Ψs. The determination of the BAU would require additional calculations. Since in most of the parameter space of our interest $\Gamma_{\rm annh} < \Gamma_\Psi$, for simplicity we do not compute the BAU there but just warn the reader whenever we have $\Gamma_{\rm annh} > \Gamma_\Psi$.

The parameter space where our framework can potentially reproduce the observed BAU is displayed in Fig. 3.1 for representative benchmark values of the parameters, for $f \geq$ MeV cause lower values are excluded by Big Bang Nucleosynthesis (BBN), see e.g. [307]. Imposing $Y_B = Y_{\rm BAU}$ fixes the value of $Br\big(\text{hadr} \to \Psi\big)$ in every point of the parameter space. We require $Br\big(\text{hadr} \to \Psi\big) < 0.1$ because string fragmentation is expected to give rise mostly to light hadrons, and at least one light hadron, the dilaton, exists in our picture. We also require $\Gamma_{\rm annh}/\Gamma_\Psi < 1$, for definiteness for $C = 1$ and using $|y|$=3 Imy. As long as the walls are in the terminal velocity regime, Y_B is independent of both f and $T_{\rm nuc}/f$. These parameters play a role as soon as collisions happen in the runaway regime, i.e. in a region of large f and small $T_{\rm nuc}/f$, where Y_B gets quickly suppressed (indeed Fig. 3.1 displays that one cannor reproduce the BAU at large f).

f and $T_{\rm nuc}/f$ also play a role in defining the regions where the BAU can be washed out by various effects. Washout effects are not included in Eq. (3.52), nor they are visualized in Fig. 3.1, because they depend on the specific model realising our framework. One can still identify the following general expectations for them. Concerning inverse decays, they can be neglected as long as $M_\Psi \gg T_{\rm RH}$, because their rate is Boltzmann-suppressed at large $M_\Psi/T_{\rm RH}$. $M_\Psi \gg T_{\rm RH}$ is actually a consequence of $T_{\rm RH} \lesssim f$ (see Eq.(3.44)) and $M_\Psi \simeq 4\pi f$. M_Ψ/f is the hadron coupling to the dilaton, the large values needed to avoid washout from inverse decays can only be obtained in strongly-coupled theories. Other washout processes that generically exist are $2 \to 2$ scatterings mediated by Ψ. Requiring that they are negligible imposes i) an upper bound on Imy^2 of Eq. (3.53), hence our normalization of ϵ_Ψ in Eq. (3.52) to a small number, and ii) an absolute lower limit on M_ψ, because they are suppressed

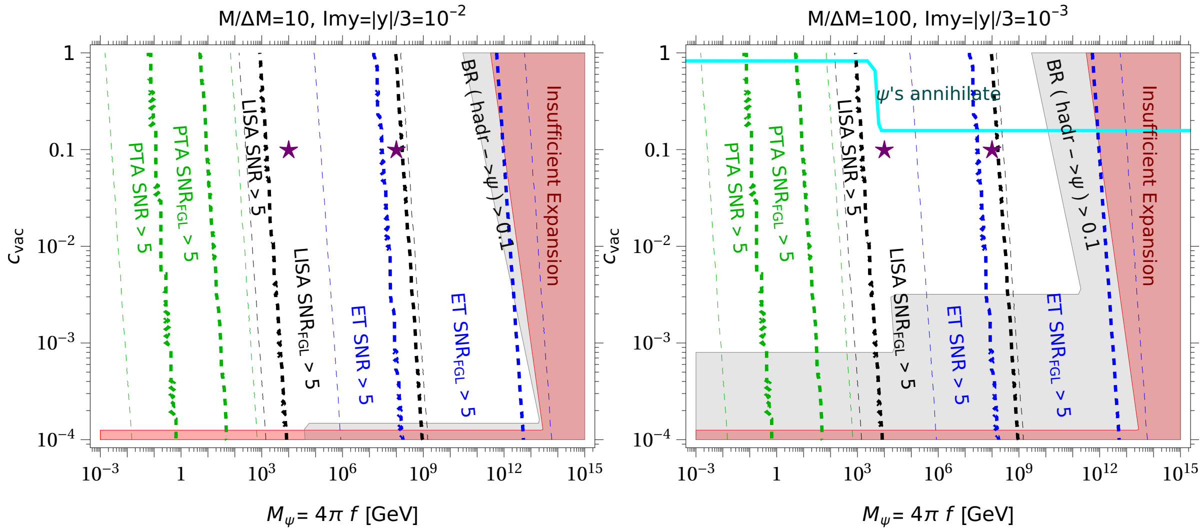

Figure 3.1: Parameter space where our baryogenesis framework manages to reproduce the observed BAU, and its testability in gravity waves with LISA, the Einstein Telescope and the PTA. We choose $g_{\rm TC} = 80$, $g_* = g_{\rm SM} + g_{\rm TC}$ and, for definiteness, $g_{\rm RH} = g_{\rm SM} + 1$ (where the $+1$ accounts for the dilaton), the dilaton wavefunction normalization $Z = 1$ and $T_{\rm nuc}/f = 10^{-3}$. The white area is allowed by the PT dynamics and can accomodate the baryon asymmetry, where we saturate the baryon yield at each point, by obtaining $Br\big(\text{hadr} \to \Psi\big)$ from Eq. (3.52). The excluded gray region presents values of $Br\big(\text{hadr} \to \Psi\big) > 0.1$, chosen as a benchmark upper limit, hence it cannot account for the whole baryon asymmetry of the Universe. The excluded red region presents $\gamma_{\rm coll} < M_\Psi/T_{\rm nuc}$, hence the hadrons cannot enter the bubble and provide the BAU. Above the cyan lines hadrons start to equilibrate with dilatons before they decay, so the computation of the BAU should be different than the one we employed. The regions delimited by the green, black and blue dashed lines are testable, respectively, by PTAs, LISA and the Einstein Telescope, where the astrophysical foregrounds have (not) been taken into account in the thicker (thinner) lines. We denote with violet stars the two points of the parameter space for which we computed the GW spectrum shown in Fig. 3.2. The viable parameter space will be reduced in specific realizations of our framework, by model-dependent washout effects or laboratory searches depending on the SM interactions of the hadrons Ψ, see Figures 3.7 and 3.9.

by some power of M_ψ. Condition ii) is what prevents from going to values of f much below a TeV, although it is possible that a minimal model-building effort weakens this requirement. Another obstruction to achieving $f \lesssim$ TeV arises in models where the confining sector generates a lepton asymmetry, because then one needs $T_{\rm RH} > T_{\rm Sph}$ to transmit it to the baryon sector.

Two key features of our framework, that are different with respect to its weakly coupled analogue of [316, 318], can already be grasped by our general discussion so far:

- the hadron yield is enhanced by the strong dynamics and it allows for a larger BAU;
- the strong coupling $M_\Psi/f \gg 1$ suppresses washout coming from inverse decays.

They imply that this mechanism works for scales of the PT down to (at least) the weak scale, which opens the possibility to test it with both LISA and the Einstein Telescope, which is the topic of Sec. 3.2.3. It also makes the mechanism testable in the laboratory, either directly producing the hadrons at high-energy colliders, or indirectly testing their CP and flavour violating effects. Finally, a scale of the PT down to (at least) the TeV scale also allows for interesting theoretical connections, e.g. with models explaining the origin of the weak scale, or of neutrino masses, with confining dynamics. We will explore some of these consequences in two explicit models that realise our framework, in Secs. 3.2.4 and 3.2.5.

3.2.3 Gravitational wave signal

We now detail the expected GW signal from a supercooled PT. Using the numerical results from [300] and as reviewed in Sec. 3.1.3, the GW energy density power spectrum as measured today, for initially thick walled, runaway bubbles is given by

$$h^2\Omega_{\rm GW}(\nu) \equiv h^2 \frac{d\,\Omega_{\rm GW}}{d\log(\nu)} = h^2\Omega^0_{\rm rad}\left(\frac{g_0}{g_{\rm RH}}\right)^{\frac{1}{3}}\Omega^{\rm PT}_{\rm GW}(\nu) \simeq 4.4\times 10^{-7}\left(\frac{100}{g_{\rm RH}}\right)^{\frac{1}{3}}\left(\frac{\alpha_{\rm GW}}{1+\alpha_{\rm GW}}\right)^2\frac{S_\phi(\nu)}{(\beta/H)^2}\,, \tag{3.56}$$

where $h \simeq 0.67$ is the dimensionless Hubble parameter as determined by Planck [14]. In Eq. (3.56) the factors $\Omega^0_{\rm rad}$ and $(g_0/g_{\rm RH})^{\frac{1}{3}}$ take into account that the GW energy density redshifts as radiation from its value at the PT, $\Omega^{\rm PT}_{\rm GW}$, until today, and $\Omega^0_{\rm rad}$ and g_0 are, respectively, the energy fraction in radiation and the degrees of freedom in entropy today. $\alpha_{\rm GW}$ is the energy released as bulk motion during the PT (which we approximate as the energy difference between the false and true vacuum, ΔV) normalized to the radiation density $\rho_{\rm rad}$, namely

$$\alpha_{\rm GW} \simeq \frac{\Delta V}{\rho_{\rm rad}} = \left(\frac{T_{\rm eq}}{T_{\rm nuc}}\right)^4 = \frac{30 c_{\rm vac}}{\pi^2 g^*}\left(\frac{f}{T_{\rm nuc}}\right)^4, \tag{3.57}$$

thus one expects $\alpha_{\rm GW} \gg 1$ for supercooled PTs. The shape of the spectrum is governed by the spectral function

$$S_\phi(\nu) = \frac{(a+b)\tilde\nu^b\nu^a}{b\,\tilde\nu^{(a+b)} + a\,\nu^{(a+b)}}\,, \tag{3.58}$$

where we adopt the central values for the bubbles in the setup with the thickest walls from [300], namely $\{a,b\} = \{0.742, 2.16\}$. The peak frequency of the signal today is given by

$$\tilde\nu = 33\,\mu{\rm Hz}\left(\frac{g_{\rm RH}}{100}\right)^{1/6}(\beta/H)\left(\frac{T_{\rm RH}}{10^3\ {\rm GeV}}\right). \tag{3.59}$$

Finally, one should impose that $\Omega_{\rm GW} \propto \nu^3$ at small frequencies, due to causality for super-horizon modes at GW production [341]. We therefore apply a cut in the spectrum at the redshifted frequency today of

$$\nu^*(t_0) = \frac{a(T_{\rm RH})}{a_0}\,\frac{H(T_{\rm RH})}{2\pi}\,, \tag{3.60}$$

below which we enforce the correct IR scaling and where $a(T_{\rm RH})/a_0$ is the ratio of the scale factors between the PT and today.

The numerical simulations performed in [300] assume that bubbles effectively runaway until collision, however a large part of our parameter space, notably the one associated to a PT around the TeV scale, sits in the terminal velocity regime, where the vacuum energy pressure is counterbalanced by the friction produced by particles in the plasma. The vacuum energy is thus partly converted into kinetic energy of the particles in the plasma already prior to the bubble wall collision. However, the contribution from sound waves or turbulence [298, 302] in supercooled PTs is not yet clearly understood. Indeed, current hydrodynamical simulations, which aim to capture the contribution of the bulk motion of the plasma to the GW signal, do not yet extend into the regime in which the energy density in radiation is subdominant to the vacuum [299] and analytical studies of shock-waves in the relativistic limit have just started [282]. In this scenario one can argue that derivatives of the envelope approximation such as the so-called bulk flow model are more realistic in modelling the GW signal.

In practice, the difference between [300] and bulk-flow models like [301] is very mild, see e.g. the comparison in [336]. Therefore we use the parametrization from [300], described above, for both regimes of wall velocities. Examples of GW spectra are shown in Fig. 3.2, for $\alpha_{\rm GW} = 100$ and $\beta/H = 15$, both typical of supercooled PTs and for two benchmark values of $c_{\rm vac}$ and M_Ψ.

Our model can be probed by several current or upcoming GW interferometers, due to the wide parameter space allowed. We show our calculations for the PLI sensitivity curves of LISA [256], BDECIGO [257], LIGO-VIRGO-KAGRA [254] and Einstein Telescope (ET) [255] (configuration '2L 0° 20km' for definiteness) in shown in Fig. 3.2, for a fiducial choice of the signal-to-noise ratio SNR=10 and for fiducial observation time which is taken to be which is taken to be t= 10 years for the ET and t=3 years for LISA (see Sec. 3.1.3 for the relevant definitions and Fig. 2.7 for the analogous plot without the FOPT predicted signal).

There are several astrophysical stochastic GW foregrounds which could mimic the GW signal coming from the PT, see Fig. 3.2 for details. In order to take this limitation into account we also define a foreground-limited signal to noise ratio $\mathrm{SNR}_{\rm FGL}$,

$$\mathrm{SNR}_{\rm FGL} = \sqrt{T\int_{\nu_{\rm min}}^{\nu_{\rm max}} d\nu \Big(\frac{\mathrm{Max}[\Omega_{GW}(\nu)-\Omega_{FG}(\nu),0]}{\Omega_{\rm sens}(\nu)}\Big)^2}\,. \tag{3.61}$$

With the above conservative definition we impose that our signal is not detectable if buried under the astrophysical foreground $\Omega_{FG}(\nu)$. We show in Fig. 3.1 the regions of parameter space of our BAU framework that could be probed by Pulsar Timing Arrays (PTA), LISA and the ET, which we define as those where $\mathrm{SNR}_{\rm FGL} \geq 5$. For comparison, we also show the regions that one could probe in absence of astrophysical foregrounds, which could be relevant in case one will envisage ways to tell them apart from a GW signal from PTs. The

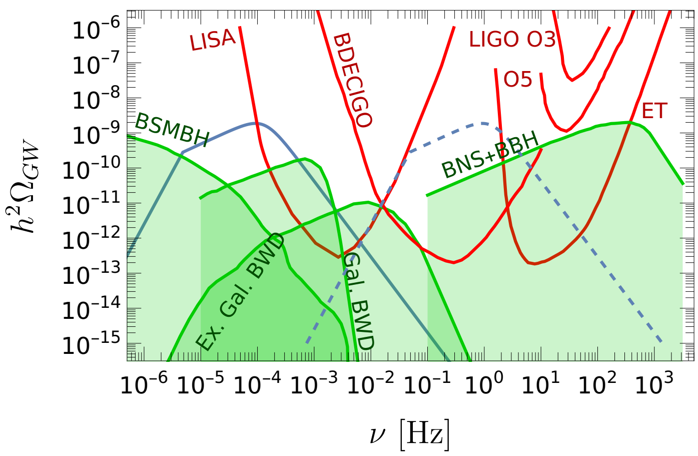

Figure 3.2: Example of GW spectra for two benchmark points of the $\{c_{\rm vac}, M_\Psi\}$ parameter space. The solid (dashed) blue line shows the predicted GW spectrum for the PT, with $\{c_{\rm vac}, M_\Psi\} = \{10^{-1}, 10^4 \text{ GeV}\}$ and $\{c_{\rm vac}, M_\Psi\} = \{10^{-1}, 10^8 \text{ GeV}\}$. We have assumed $T_{\rm nuc}/f = 10^{-3}$, $\alpha_{\rm GW} = 100$ and $\beta/H = 15$ as typical benchmark values for supercooled PTs. The spectra are compared with PLI sensitivity curves, shown as red lines, with signal-to-noise ratio SNR=10 for LISA [256] and the Einstein Telescope (ET) [255]. We also show PLI sensitivity curves for LIGO-VIRGO O3, LIGO-VIRGO Design A+ sensitivity [254] and BDECIGO [257]. Estimated astrophysical foregrounds from binary super-massive black holes [250], galactic white-dwarf binaries [252], extragalactic white-dwarf binaries [253], binary black holes and neutron stars [254] are also shown as green shaded regions.

two sensitivities are anyway very similar for LISA, due to the strong GW signal from the PT in comparison with foregrounds, while for PTAs and ET we find an appreciable difference. The sensitivity showing up for $f \lesssim 100$ GeV is the one attainable using GWs as measured by PTA, which we compute following [258] and identifies yet another way to test our framework, in case one manages to make it work down to such small scales of the PT. If one did, then one could potentially explain the GW background observed by PTAs [342, 343, 344, 345] with a PT [346, 268] that, at the same time, explains the BAU via the framework proposed in this work. In any case, a very large fraction of the allowed space could indeed be probed by GW interferometers.

3.2.4 Model 1: Baryogenesis from a composite scalar

We have so far discussed a general framework for the generation of the baryon asymmetry and we have established that it presents some interesting features, as an enhanced production of the baryon yield with respect to the non-confining case and a GW signal potentially in reach of current and future GW interferometers. We now specify our framework to two models already discussed in the literature, compute their predictions for washout and for the BAU as well as for detection, and show explicitly that we can extend significantly their allowed parameter space for a successful baryogenesis/leptogenesis.

Model and baryon asymmetry

We start by revisiting the model of baryogenesis discussed in [316], where the baryon number is produced by the CP-violating decays of a heavy scalar denoted there as Δ. In our setup Δ is a composite scalar field originating from a dark confining sector and it is a realization of the Ψ hadron discussed above. We introduce $i = 1, 2$ generations of the Δ_i scalars, with $M_{\Delta_2} > M_{\Delta_1}$. We assume these fields to transform as $(3\,, 1\,, 2/3)$ under the SM gauge group $\mathrm{SU}(3)_\mathrm{c} \times \mathrm{SU}(2)_\mathrm{L} \times \mathrm{U}(1)_\mathrm{Y}$. We also introduce a SM gauge singlet fermion χ with mass M_χ and the following baryon number violating Yukawa interactions of Δ_i:

$$\mathcal{L} \supset y_{di}\Delta_i\, \overline{d_R^c}\, d_R \,+\, y_{ui}\Delta_i\, \overline{\chi_R} u_R^c + \text{h.c.}\,, \tag{3.62}$$

where colour indices have been suppressed for simplicity of the notation. y_{di} is antisymmetric in flavour d as a consequence of the antisymmetry of the colour indices. A necessary condition for CP violation is that the above couplings should be complex. Some, but not all the phases, even in the minimal scenario, can be removed through field rephasings $f \to e^{i\alpha_f} f$. To be more concrete let's examine some specific scenarios:

- In the minimal scenario there is only one copy of χ and the $\Delta_{1,2}$ couple each to one up-type quark and to a pair of down-type quarks (that do not have the same flavour). This results in 4 Yukawa couplings y. One can remove 3 out of their 4 phases by rephasing the Δ_i and χ, but one phase survives since in general $\mathrm{Arg}(y_{d2}) - \mathrm{Arg}(y_{d1}) \neq \mathrm{Arg}(y_{u2}) - \mathrm{Arg}(y_{u1})$. Thus in this setup there are 4 couplings and 1 (physical) phase.

- One can switch on all the allowed SM quark Yukawa couplings, keeping a single copy of χ. This setup features 12 couplings, 6 involving down-type quarks and 6 involving the up-type quarks. As in the previous case we can rephase the 3 new fields, so we're left with 9 independent new phases.

- For 3 copies of χ, we find 24 couplings (6 from down- and 18 from up-type quarks). With respect to the previous setup we have the freedom to remove 2 more phases by redefining $\chi_{2,3}$, therefore we end up with 19 independent phases.

Note that in the second and third case (but not the first one) one could remove further phases from the Yukawa couplings of Eq. (3.62) by rephasing the right-handed quarks, but those phases would not be unphysical as they would show up in the quark Yukawas.

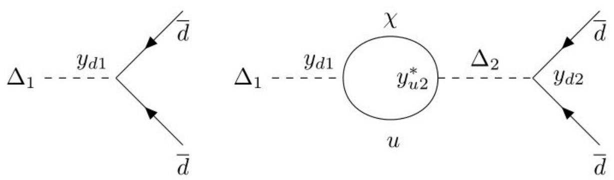

Figure 3.3: Example of the diagrams which interfere and lead to CP violation. The intermediate loop particles are kinematically able to go on-shell.

Assuming $M_\chi \ll M_{\Delta_i}$ to avoid complications with phase space effects, the couplings of the Lagrangian Eq. (3.62) lead to the following tree level decay rates for the scalars Δ_i

$$\Gamma(\Delta_i \to \overline{d_R d'_R}\,) \simeq \frac{|y_{di}|^2}{8\pi} M_{\Delta_i}, \tag{3.63}$$

$$\Gamma(\Delta_i \to \chi u_R) \simeq \frac{|y_{ui}|^2}{16\pi} M_{\Delta_i}, \tag{3.64}$$

where by d'_R we denote a right down quark of different flavour than d_R, we have not summed over flavours and we have summed over final state colours for the first decay. Interference between tree- and loop-level diagrams, as those shown in Fig. 3.3, leads to CP violation in the decays. Focusing on the decays of Δ_1 only, CP violation can be parametrized as

$$\begin{aligned}
\Gamma(\Delta_1 \to \overline{d_R d'_R}) &= \Gamma_{1d}(1+\epsilon_d)\,, \\
\Gamma(\Delta_1^* \to d_R d'_R) &= \Gamma_{1d}(1-\epsilon_d)\,, \\
\Gamma(\Delta_1 \to \chi u_R) &= \Gamma_{1u}(1+\epsilon_u)\,, \\
\Gamma(\Delta_1^* \to \overline{\chi u_R}) &= \Gamma_{1u}(1-\epsilon_u)\,.
\end{aligned} \tag{3.65}$$

Since the total decay widths of Δ_1 and Δ_1^* have to be equal due to the CPT theorem, it follows that $\epsilon_d\Gamma_{1d} = -\epsilon_u\Gamma_{1u}$. The imaginary part of the loop in Fig. 3.3 controls the rate asymmetry between Δ_1 and Δ_1^* decays and can be extracted via Cutkosky rules [347]. One then finds for the rate asymmetry

$$\epsilon_\Delta = \frac{1}{2\pi}\frac{\mathrm{Im}(y_{d1}^* y_{u1} y_{u2}^* y_{d2})}{|y_{ui}|^2 + 2|y_{di}|^2}\frac{M_{\Delta_1}^2}{M_{\Delta_2}^2 - M_{\Delta_1}^2} \sim \frac{\mathrm{Im}[y^2]}{6\pi}\frac{M_{\Delta_1}^2}{M_{\Delta_2}^2 - M_{\Delta_1}^2}\,, \tag{3.66}$$

where from now on we assume that there is no major hierarchy among the Yukawa couplings y and we take generic $\mathcal{O}(1)$ phases. We are also discarding resonant enhancements of the rate asymmetry, namely we are assuming that $M_{\Delta_2} - M_{\Delta_1} \gg \Gamma_{\Delta_i}$. Finally, the baryon asymmetry is obtained by plugging ϵ_Δ of Eq. (3.66) in Y_B of Eq. (3.52).

Washout processes

In our scenario the most constraining washout processes are those occurring after reheating, after the PT. The reason is that the population of the Δ hadrons, yielding the baryon asymmetry via their decays, is mostly sourced by the deep inelastic scatterings of the hadrons (produced upon string fragmentation of incoming or ejected techniquanta) with other hadrons or bath particles. These scatterings mostly happen after bubble percolation, so that washout effects just after wall crossing, like those considered in [316], are not relevant in our framework (but see the end of the previous subsection for Δ annihilations after percolation).

After bubbles percolate and all hadrons are produced, diquark interactions violating $B-L$ can result in washout if $T_{\rm RH}$ is too high. Off-shell $2 \to 2$ scattering processes mediated by Δ that violate baryon number, e.g. $d\,d' \leftrightarrow \overline{\chi\, u}$, have a rate that can be estimated as

$$\Gamma_{WO} \simeq \frac{y^4\, T_{\rm RH}^5}{8\pi M_\Delta^4}\,, \tag{3.67}$$

where we are integrating out Δ because $T_{\rm RH} \ll M_\Delta$ in our framework. This rate is harmless for our scenario provided that it is below the Hubble rate H, namely

$$\frac{M_\Delta}{T_{\rm RH}} \geq \left(\frac{\sqrt{90}y^4 M_{\rm Pl}}{8\pi^2 g^{*1/2} T_{\rm RH}}\right)^{1/4}. \tag{3.68}$$

Moreover, also inverse decays into on-shell Δ can lead to $B-L$ washout. The Boltzmann suppressed rate is given by

$$\Gamma_{ID} \simeq \frac{3\,y^2}{16\pi} M_\Delta \Big(\frac{M_\Delta}{T_{\rm RH}}\Big)^{3/2} \text{Exp}\Big[-\frac{M_\Delta}{T_{\rm RH}}\Big]\,. \tag{3.69}$$

This is safely below H, provided that

$$\frac{M_\Delta}{T_{\rm RH}} \geq \text{Log}\Big[\frac{y^2 M_{\rm Pl}}{8\pi\, g^{*1/2}\, T_{\rm RH}} \Big(\frac{M_\Delta}{T_{\rm RH}}\Big)^{5/2}\Big]\,. \tag{3.70}$$

Proton decays and further washout from χ

So far we have not addressed the detailed nature of χ, which we assume not to be linked to the confining sector, to allow us more freedom with its phenomenology. A first idea is to take χ to be close to massless, which would be the case if the SM neutrinos gain Dirac mass via a Yukawa-type interaction $y_\nu\,\overline{L}H\chi_R$, with $y_\nu \sim 10^{-12}$. However, χ allows nucleon decays via t-channel diagrams mediated by Δ, like $p \to K^+\chi$, as long as $M_\chi < m_p - m_K^+$. Taking the couplings to all the generations to be of the same order, we estimate the decay rate

$$\Gamma(p \to K^+\chi) \sim \frac{y_u^2 y_d^2}{64\pi^3}\frac{m_p^5}{M_\Delta^4} \simeq \Big(\frac{y}{10^{-2}}\Big)^4 \Big(\frac{\text{TeV}}{M_\Delta}\Big)^4 10^{-23}\ \text{GeV}. \tag{3.71}$$

From the experimental bound on the partial proton lifetime, $\tau(p \to K^+\nu) > 5.9 \times 10^{33}$ years [36], it follows that $\Gamma(p \to K^+\nu) < 3.5 \times 10^{-66}$ GeV, therefore a scenario in which $M_\chi < m_p - m_K^+$ would completely rule out our interesting region of the parameter space around the TeV. Considering now the case where $M_\chi > m_p - m_K^+$, a natural assumption would be to assume χ to be Majorana, with a $\frac{1}{2}M_\chi \overline{\chi}_R \chi_R^c$ mass term and to couple it to the SM leptons and the Higgs H via the Yukawa coupling y_ν and provide SM neutrino masses with a standard type-I seesaw. In this case the decay $p \to K^+\nu$ would receive contribution from y_ν and one can get an estimate for the decay width

$$\Gamma(p \to K^+\nu) \sim \frac{y_u^2 y_d^2}{64\pi^3}\frac{m_p^5}{M_\Delta^4}\Big(\frac{y_\nu v}{M_\chi}\Big)^2 \simeq \Big(\frac{y}{10^{-2}}\Big)^4 \Big(\frac{\text{TeV}}{M_\Delta}\Big)^4 \Big(\frac{\text{TeV}}{M_\chi}\Big) 10^{-37}\ \text{GeV}\,, \tag{3.72}$$

which again would exclude the most interesting region of our parameter space. Therefore, in order not to spoil the interesting features discussed so far, one needs $M_\chi > m_p - m_K^+$ and to disentangle χ from the generation of neutrino masses, so that the coupling y_ν can be taken as small as needed to respect limits on nucleon's lifetimes, independently of the other parameters.

Moreover, the same couplings in Eq. (3.62) which produce the baryon asymmetry in our setup also lead to a partial decay width of χ given by

$$\Gamma(\chi \to \overline{udd'}) = \frac{1}{1024\pi^3}\Big|\frac{y_{u1}y_{d1}}{M_{\Delta_1}^2} + \frac{y_{u2}y_{d2}}{M_{\Delta_2}^2}\Big|^2 M_\chi^5\,. \tag{3.73}$$

After baryogenesis there is an excess of χ over $\overline{\chi}$, thus if χ is Dirac and $M_\chi < M_\Delta$ the asymmetry gets erased exactly once χ decay. Indeed the decays $\chi \to \overline{udd'}$ and $\overline{\chi} \to udd'$ would exactly erase the CP asymmetry, due to $\epsilon_d\Gamma_d = -\epsilon_u\Gamma_u$ following from CPT. Note that $M_\chi \geq M_\Delta$ is not a viable option, because then $\Gamma_u = 0$ and so $\epsilon_d = 0$ via CPT, so one would not generate the baryon asymmetry. Instead, if χ is Majorana then both udd and $\overline{udd}$ decays are allowed and the asymmetry is preserved. However, the asymmetry could be spoiled by inverse decays: any excess of udd or $\overline{udd}$ would go back to χ, that would wash it out upon decaying Assuming no hierarchies among the Yukawas y we get the following ratio between the rate of inverse decays and Hubble:

$$\frac{\Gamma(\overline{udd'} \to \chi)}{H(T = M_\chi)} \simeq \frac{(y_u y_d)^2}{256\pi^3 g^{*1/2}} \frac{\pi}{90^{\frac{1}{2}}} \frac{M_\chi^5}{M_\Delta^4} \frac{M_{\rm Pl}}{M_\chi^2} \sim 10^{-7} \Big(\frac{y}{10^{-2}}\Big)^4 \Big(\frac{\rm TeV}{M_\Delta}\Big)^4 \Big(\frac{M_\chi}{\rm GeV}\Big)^3, \tag{3.74}$$

where we have evaluated H at $T = M_\chi$ because that is the range of temperatures for which inverse decays are most efficient: for $T \ll M_\chi$, $\Gamma(\overline{udd'} \to \chi)$ would be exponentially suppressed, for $T \gg M_\chi$, H would be enhanced but not $\Gamma(\overline{udd'} \to \chi)$.

To summarize, χ does not alter our results as long as i) to avoid nucleons decays, $M_\chi > m_p - m_K^+$ and its coupling to neutrinos is small enough (so that it cannot play a role in the generation of neutrino masses) and ii) to avoid further washouts, M_χ is Majorana and it is smaller enough than M_Δ to keep $\Gamma(\overline{udd'} \to \chi)/H \ll 1$, see Eq. (3.74).

Signals of the composite scalar Δ in laboratory experiments

Collider searches

As it turns out (see Fig. 3.7), one can easily accomodate baryogenesis from supercooled confinement with the scalar Δ around or below the electroweak scale, the properties of these particles can be probed thanks to their signatures in high-energy colliders.

A first lower bound on the mass of Δ comes from the measurement of the decay width of the Z boson performed at LEP [348]. Since Δ interacts weakly due to its $U(1)_Y$ charge, it can contribute to the Z boson width, provided that $M_\Delta < M_Z/2$. We compute the following expression for the decay width of Z into a $\Delta\Delta^*$ pair

$$\Gamma(Z \to \Delta\Delta^*) = \frac{3}{16\pi} \Big(\frac{2g \sin^2\theta_W}{3\cos\theta_W}\Big)^2 M_Z \Big(1 - \frac{4M_\Delta^2}{M_Z^2}\Big)^{3/2}. \tag{3.75}$$

Since this value is orders of magnitude larger than the uncertainty on the Z boson width, we exclude $M_\Delta < 45$ GeV.

Then one can note that Δ has the same quantum numbers of a right up-type squark in SUSY, therefore it will share its same production mechanisms at colliders. To our knowledge, the closest searches to our scenario that have been performed are those involving squark decays into diquarks, through R-parity violating (RPV) couplings. Constraints on top squarks decaying through RPV couplings were first set by the ALEPH experiment at LEP [349], excluding at 95% CL masses below 75 GeV via four-jet searches. More stringent bounds come from further searches performed by CDF at Tevatron [350] and by ATLAS [351] and CMS [352] at the LHC. The combination of these searches rules out top squarks with RPV decay in the 45 GeV $< M_\Delta <$ 770 GeV interval. All these searches aim to detect four jets in the final state associated to the decay of pair produced heavy resonances. This is the typical signature that one would expect associated with Δ, as for the allowed values of its mass and coupling constants it would decay promptly in the detector. However, as the diquark and leptoquark couplings of Δ are expected to be of the same size, some significant branching ratio of Δ scalar could reside in the $u\,\chi$ channel, such that the signal would be different than the one assumed in four-jet searches, and the limits would change. Performing a detailed collider study of the Δ's, depending on their branching rations into two-jet and one-jets plus missing energy, is beyond the scope of our work, so for definiteness we use the constraints that assume Δ to dominantly decay into two jets.

Neutron electric dipole moment

As we have seen in the previous section, the new fields Δ_i and χ contain new sources of CP violation and therefore give rise to new contributions to the neutron electric dipole moment (nEDM). The experimental bound set by the nEDM collaboration at the Paul Scherrer Institut is given by $|d_n| < 1.8 \times 10^{-26}\text{e} \cdot \text{cm}$ [353]. In this section we analyze the impact of this bound on our model and show that it does not place further significant constraints on the parameter space.

In an EFT approach the electromagnetic moments of a fermion ψ can be described by the effective Lagrangian

$$\mathcal{L}^{\text{eff}} = c_R \overline{\psi} \sigma_{\mu\nu} P_R \psi F^{\mu\nu} + \text{h.c.}, \qquad \text{where} \qquad d = i(c_R - c_R^*) = -2\,\text{Im}\, c_R \tag{3.76}$$

is the EDM of ψ and $F_{\mu\nu}$ is the field strength tensor of the photon. The diagrams which may give a non-vanishing contribution to the nEDM must have an imaginary component. In general the amplitude of any loop diagram can be recasted as a sum of amplitudes each coming by operators O_i weighted by their coefficients C_i, which can be written as $C = y\,F$. In this notation y stands for the product of the couplings of all the vertices and F is a function coming from the loop integration [354]. In principle both y and F are allowed to be complex, but diagrams with the heavy Δ and χ running in the loop cannot have all the intermediate states go on-shell. Therefore the optical theorem implies that $\text{Im}(F) = 0$ and only y can be complex. Moreover, any combination of couplings entering the expression of the nEDM should be invariant under rephasing of the fields, thus we need at least 4 couplings involving the new BSM states, because $Y = y_{d1}^* y_{u1} y_{u2}^* y_{d2}$ is the simplest combination of the Yukawas with at least one physical phase. As a consequence one needs to go at least to 2-loop to find a possible non-zero contribution.

The relevant topologies of our model are depicted in Fig. 3.4, they include the Barr-Zee diagrams [355]. They all give in principle non-zero contributions to the nEDM. However, for each of them one can always take the contribution of the 'mirrored' diagram, with complex-conjugate Yukawa couplings and with the photon attached to the same type of field. One can decompose the sum of each set of conjugate diagrams as

$$\sum_{j=1}^{\#\text{conj.}} \mathcal{A}_j = Y F(M_{\Delta_1}, M_{\Delta_2}) + Y^* F(M_{\Delta_2}, M_{\Delta_1})\,, \tag{3.77}$$

where $F(i,j)$ is coming from the loop integration. $F(i,j)$ is not generically a symmetric function of the scalar masses, but the asymmetry scales like $F(M_{\Delta_2}, M_{\Delta_1}) = F(M_{\Delta_1}, M_{\Delta_2})(1 + \mathcal{O}(k^2/M^2_{\Delta_{1,2}}))$, therefore it vanishes in the $k^2 = 0$ limit for which the nEDM is measured.

Let us show explicitly that the sum of the diagrams shown in Fig. 3.5 with in addition those with $\Delta_{1,2}$ swapped provides a vanishing contribution to the nEDM.
The starting point is given by the structure of the electromagnetic nucleon vertex in presence of CP-violation, which is given by

$$i\mathcal{M}^\mu = \overline{u_N}(q)\Big[\gamma^\mu F_E(k^2) + \frac{i\sigma^{\mu\nu}k_\nu}{2m_N} F_M(k^2) + \frac{i\sigma^{\mu\nu}k_\nu}{2m_N}\gamma_5 F_D(k^2)\Big] u_N(p). \tag{3.78}$$

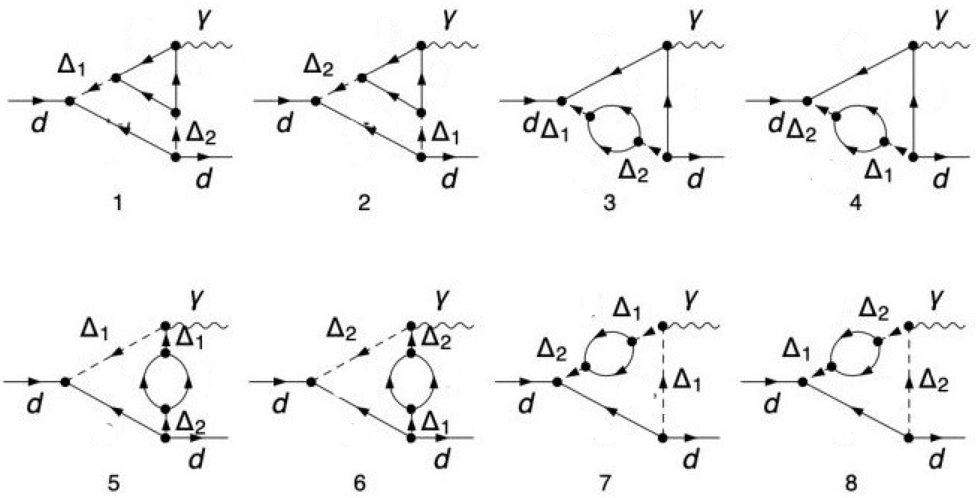

Figure 3.4: Relevant topologies at two loops for the nEDM. Several contributions for each topology occur due to flavour. While diagrams in the upper row are manifestly symmetric under $\Delta_1 \leftrightarrow \Delta_2$ exchange, a more careful analysis is needed to show the cancellation among the diagrams in the lower row, which is non-trivial due to the different number of Δ_i propagators involved when the photon is attached to an internal Δ leg.

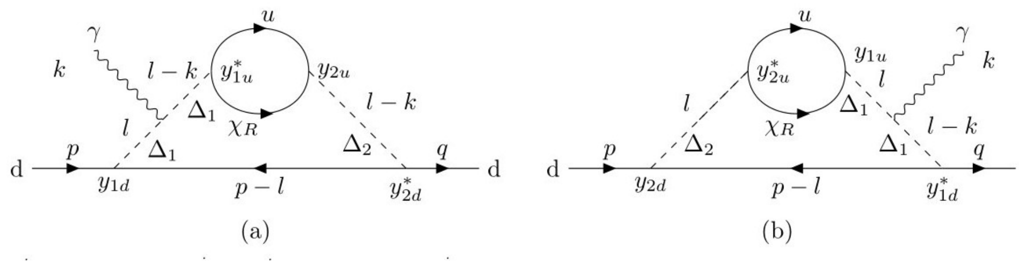

Figure 3.5: Two-loop conjugate diagrams contributing to the nEDM. In order to obtain a cancellation one needs to take into account also the pair of diagrams where Δ_1 and Δ_2 are interchanged.

Here $k = (p - q)$ is the momentum of the photon, m_N is the nucleon mass and the EDM of the nucleon is defined as $d_n = F_D(0)/(2m_N)$. Using the Gordon decomposition of the vector-axial current, the CP violating ($\not{C}\not{P}$) part of the above expression reads

$$i\mathcal{M}^{\mu}_{\not{C}\not{P}} = d_n \overline{u_N}(q)\gamma_5 u_N(p)\,.(p+q)^{\mu} \tag{3.79}$$

Thus we need to concentrate on the $(p+q)\cdot\epsilon$ terms in the computation of the EDM, where ϵ is the photon polarization.

In order to find whether there is a cancellation among the diagrams, we can factor out the upper loop, as it is symmetric under $\Delta_{1,2}$ exchange. Let's focus thus on the lower loop and denote by Y the product of all the Yukawa couplings entering the diagram (a). The relevant amplitude reads

$$\begin{aligned} iM &= Y \int \frac{d^4\ell}{(2\pi)^4} \overline{u}(q) P_L \frac{i}{\not{p} - \not{\ell} - m} P_R u(p) \frac{i}{\ell^2 - M_1^2} \frac{i}{(\ell-k)^2 - M_1^2} \Big(\frac{i(2\ell - k)\cdot \epsilon(k)}{(\ell-k)^2 - M_2^2} \Big) \\ &= Y \overline{u}(q) \gamma^\alpha P_R u(p) \int \frac{d^4\ell}{(2\pi)^4} \frac{(p^\alpha - \ell^\alpha)\ell \cdot \epsilon(k)}{(\ell^2 - M_1^2)((\ell-k)^2 - M_1^2)((\ell-k)^2 - M_2^2)((p-\ell)^2 - m^2)} \,, \end{aligned} \tag{3.80}$$

where m is the mass of the internal quark and $M_{1,2}$ the masses of $\Delta_{1,2}$. Since the Δ_i live at much higher scales than those probed by the EDM we can assume $M_{1,2}^2 \gg k^2, p^2, m^2$. The integrand is dominated by $\ell^2 \sim M_{1,2}^2$, thus one can expand the propagators as

$$\frac{1}{(\ell-k)^2 - M_1^2} \simeq \frac{1}{\ell^2 - M_1^2} \Big[1 + 2\frac{\ell \cdot k}{\ell^2 - M_1^2} + 4 \frac{(\ell\cdot k)^2}{(\ell^2 - M_1^2)^2} \Big] \,, \tag{3.81}$$

with analogous expressions for the other propagators. One obtains

$$iM = Y \overline{u}(q)\gamma^\alpha P_R u(p) \int \frac{d^4\ell}{(2\pi)^4} \frac{(p^\alpha - \ell^\alpha)\ell \cdot \epsilon \Big[1 + 2\frac{\ell\cdot k}{\ell^2 - M_1^2} + 4\frac{(\ell\cdot k)^2}{(\ell^2-M_1^2)^2}\Big] \Big[1 + 2\frac{\ell\cdot k}{\ell^2 - M_2^2} + 4\frac{(\ell\cdot k)^2}{(\ell^2-M_2^2)^2}\Big]}{\ell^2 (l^2 - M_1^2)^2 (\ell^2 - M_2^2)} \Big[1 + 2\frac{\ell\cdot p}{\ell^2} + 4\frac{(\ell\cdot p)^2}{\ell^4} \Big] \,. \tag{3.82}$$

The denominator is now an even function of the loop momentum ℓ, thus we need to focus on terms with an even number of ℓ at numerator. At $\mathcal{O}(\ell^2)$ there are two kind of terms which might contribute to the nEDM,

- $p^\alpha\, \ell^\mu\, \ell^\beta\, p_\beta\, \epsilon_\mu \sim \ell^2\, p^\alpha\, (p\cdot\epsilon)$
- $p^\alpha\, \ell^\mu\, \ell^\beta k_\beta\, \epsilon_\mu \sim \ell^2\, p^\alpha\, (k\cdot\epsilon) = 0$

and as the non-zero one appears also in diagram (b) the sum of the contribution of (a) and (b) to the nEDM would cancel. Let us consider now $\mathcal{O}(\ell^4)$ terms. There are three types of terms which might contribute:

- $\ell^\alpha\, \ell^\mu\, \ell^\beta\, \ell^\gamma\, k_\beta\, k_\gamma\, \epsilon_\mu \sim (\ell^2)^2 \Big[\epsilon_\alpha\, k^2 + 2\, k_\alpha (k\cdot\epsilon) \Big] = 0$
- $\ell^\alpha\, \ell^\mu\, \ell^\beta\, \ell^\gamma\, p_\beta\, p_\gamma\, \epsilon_\mu \sim (\ell^2)^2 \Big[\epsilon_\alpha\, p^2 + 2\, p_\alpha (p\cdot\epsilon) \Big]$
- $\ell^\alpha\, \ell^\mu\, \ell^\beta\, \ell^\gamma\, k_\beta\, p_\gamma\, \epsilon_\mu \sim (\ell^2)^2 \Big[\epsilon_\alpha (k\cdot p) + p_\alpha (k\cdot\epsilon) + k_\alpha (p\cdot\epsilon) \Big] \sim (\ell^2)^2\, k_\alpha (p\cdot\epsilon)\,.$

The second term appears also in the diagram (b) with coefficient Y^* and so it is harmless. The third one receives two contributions from diagram (a), from Δ_1 and Δ_2, while (b) contains only the Δ_1 contribution, as the momentum flowing in Δ_2 doesn't depend on k. Therefore the sum of diagrams (a) and (b) doesn't provide a non-zero nEDM. However, the surviving contribution stems from an integral with a $1/(\ell^2 - M_1^2)^2(\ell^2 - M_2^2)^2$ factor and is cancelled by the couple of conjugate diagrams with $\Delta_{1,2}$ exchanged. We can thus conclude that our model allows new physics contributions to the nEDM to occur only starting at the three loop level.

Therefore the sum in Eq. (3.77) ends up to be real and thus 2-loop diagrams do not produce a non-vanishing nEDM.

At the 3-loop level one expects the dominant contributions to the EDMs to scale as

$$d \sim \frac{y^2 g^4}{(16\pi^2)^3} \times \mathrm{CKM} \times \frac{m_t}{M_\Delta^2} \simeq \frac{10^{-11}}{\mathrm{TeV}} \left(\frac{y}{0.1}\right)^2 \left(\frac{\mathrm{TeV}}{M_\Delta}\right)^2 \frac{\mathrm{CKM}}{0.1}\,, \tag{3.83}$$

where m_t is the top-quark mass, g is the weak gauge coupling and by 'CKM' we mean a combination of non-diagonal elements of the CKM matrix, which is unavoidable to ensure CP violation and is smaller than at least 0.1. Since limits on coefficients of quarks EDMs (and also CEDMs, for which the discussion is analogous) are in the ballpark of 10^{-9}/TeV (see e.g. [356]) and $M_\Delta \geq$ TeV from collider bounds, then 3-loop contributions do not give rise to observable EDMs. To conclude, the constraint set by nucleon EDMs on the mass of Δ turns out to be much less stringent than those coming from colliders.

Flavour violation

Flavour-changing neutral current (FCNC) observables are expected to set powerful constraints on BSM models, due to the non trivial flavour structure that they imply in order to comply with experimental data. In our scenario, $\Delta F = 2$ processes are prohibited at tree level due to the antisymmetric couplings of Δ with the diquarks, which can be parametrized as $y_{ij} = \epsilon_{ijk} y_k$, where i, j, k are flavour indices. These bounds were firstly discussed in [357] and one can identify our state Δ with the diquark denoted as VIII there.

First, it has to be pointed out that the most general flavour structure, with all the flavour off-diagonal couplings switched on, is not needed to account for baryogenesis, as a single non-zero complex coupling is sufficient to provide a physical CP violating phase. In this setup flavour bounds would be evaded completely.

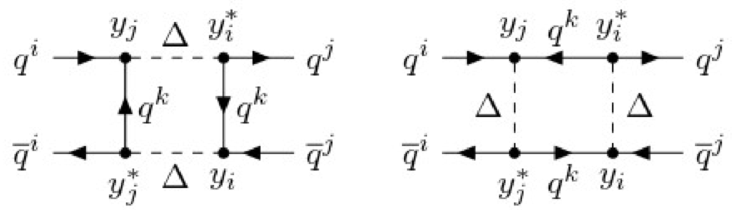

Figure 3.6: Loop level exchange of Δ contributing to $\Delta F = 2$ transitions.

If one wants to stick to the general scenario, bounds coming from the mixing of the neutral K and $B_{d,s}$ mesons have to be taken into account. The Δ scalars then enter the box diagrams in Fig. 3.6 and they generate a four-fermion effective Hamiltonian given by

$$H_{eff}^{NP}(\Delta F = 2) = \frac{1}{32\pi^2}\left(\frac{\lambda_i \lambda_j^*}{M_\Delta^2}\right) G\left(\frac{m_k^2}{M_\Delta^2}\right) (\overline{q_i}\,\gamma^\mu P_R q_j)\,(\overline{q_i}\gamma_\mu P_R\, q_j)\,, \tag{3.84}$$

where i and j are the external quark flavour indices, $k \neq i \neq j$ is the flavour index of the internal quark, colour indices are contracted within the brackets and the loop function G is given by [357]

$$G(x) = \frac{1 - x^2 + 2\,x\,\log x}{(1-x)^3}\,. \tag{3.85}$$

Observable	Bound/(M_Δ/TeV)
ϵ_K	$\lvert \mathrm{Im}(y_1 y_2^*)\rvert \leq 7.8 \times 10^{-4}$
Δm_K	$\lvert \mathrm{Re}(y_1 y_2^*)\rvert \leq 1.4 \times 10^{-2}$
B_d mixing	$\lvert y_1 y_3^*\rvert \leq 1.7 \times 10^{-2}$
B_s mixing	$\lvert y_2 y_3^*\rvert \leq 5.8 \times 10^{-2}$
$b \to s\gamma$	$\lvert y_2 y_3^*\rvert \leq 2.5$
$b \to d\gamma$	$\lvert y_1 y_3^*\rvert \leq 1.2$
R_b	$\lvert y_{1,2}\rvert \leq 24$
$B^\pm \to \phi\pi^\pm$	$\lvert y_1 y_3^*\rvert \leq 3.6 \times 10^{-3}$

Table 3.1: Bounds in units of M_Δ/TeV on antisymmetrically coupled diquarks.

Bounds on representative $D = 6$ effective operators contributing to $\Delta F = 2$ transitions have recently been obtained by the UTfit collaboration [358], from a combination of CP conserving and CP violating observables. We can apply these bounds to our model, results are summarised in Table 3.1. Other constraints which we include in Table 3.1 are those associated to the $\Delta F = 1$ processes $b \to s\gamma$, $b \to d\gamma$, R_b and $B^\pm \to \phi\pi^\pm$. We refer to [357] for more details as the constraints reported there can be easily translated to our notation.

One can note that even the most constraining observable, namely ϵ_k, is compatible with Δ diquark couplings of $\mathcal{O}(0.01)$ around the TeV scale, which, in the absence of major hierarchies in the Yukawa couplings, is the benchmark for our baryogenesis mechanism to work. Therefore, we don't expect flavour physics to exclude values of M_Δ that are not already excluded by collider searches. In fact, even assuming a hierarchy of the type $y_{ui} \gg y_{di}$, in order to lower the bound on M_Δ from colliders, one would get at the same time weaker bounds from flavour.

To conclude, the scalar realisation of our baryogenesis framework may well show-up in current and near-future flavour experiments, but the non-observation of flavour or CP-violation there would only exclude some very specific choices of its parameters and not preclude the realisation of baryogenesis.

Summary of the results

We summarize our results in the plots of Fig. 3.7. We have chosen two different benchmark values for $y = \{0.01, 0.1\}$ and $T_{\rm nuc}/f = \{10^{-3}, 10^{-4}\}$, $M_{\Delta_1} = 4\pi f$ and the dilaton wavefunction normalization $Z = 1$. We compute at each point the boost factor at bubbles collision $\gamma_{\rm coll}$ using Eq. (3.48) and we set $M_{\Delta_2} = 1.2\, M_{\Delta_1}$, $g_{\rm TC} = 80$, $g_{\rm RH} = 107.75$ ($= g_{\rm SM} + 1$, where the $+1$ accounts for the dilaton) and $g_* = g_{\rm TC} + g_{\rm SM}$. We saturate the baryon yield at each point, $Y_B/Y_B^{\rm obs} = 1$, by obtaining $Br\big(\text{hadr} \to \Delta\big)$ from Eq. (3.52). As anticipated in Sec. 3.2.2 we see that Y_B gets suppressed in the runaway regime, hence the allowed parameter space closes at large f and/or small $T_{\rm nuc}/f$. Values of f lower than the weak scale, for large $c_{\rm vac}$, cannot be reached due to washout effects. Δ annihilations before decays instead turn out to not constrain our parameter space, for the values of the parameters that we have chosen.

We also display in Fig. 3.7 collider bounds, discussed in Sec. 3.2.4, and the expected LISA and ET sensitivities to the GW signal from the PT, discussed in Sec. 3.2.3, where to avoid clutter we display only those that include astrophysical foregrounds. By comparing our plots with Fig. 6 of [316], we see that our scenario extends the allowed parameter space by many

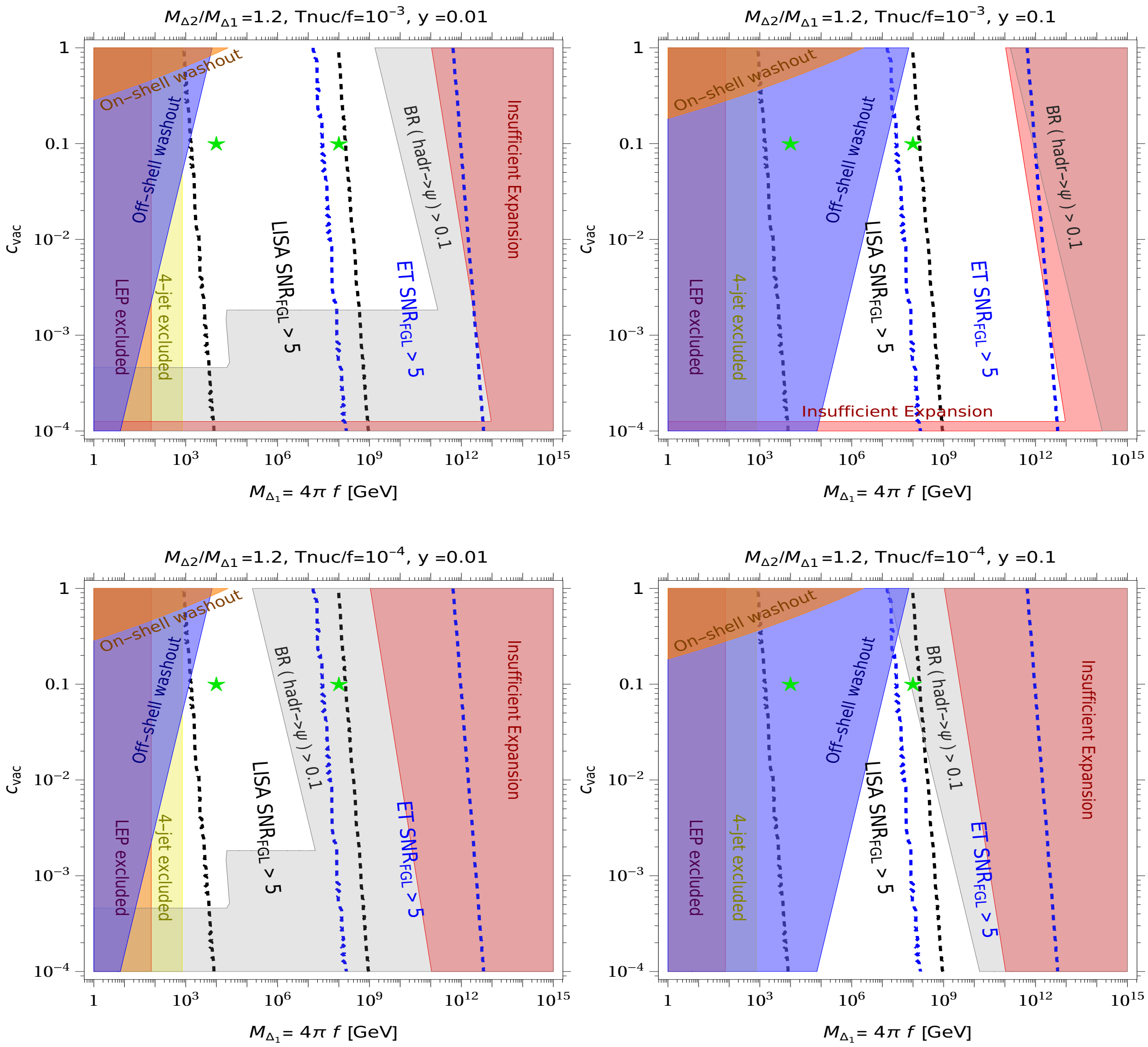

Figure 3.7: Parameter space for the composite scalar realisation of our framework, which realises baryogenesis. We choose $g_{\rm TC} = 80$, $g_* = g_{\rm SM} + g_{\rm TC}$, $g_{\rm RH} = g_{\rm SM} + 1$ and $Z = 1$ for definiteness. The white area is allowed and accommodates the observed baryon asymmetry, the red and gray regions are excluded by the PT dynamics, as in Fig. 3.1. We find that Δ annihilations are slower than Δ decays in the entire parameter space we plot, hence our computation of the BAU is always valid. A value of y smaller than unity is needed to avoid washout. Off-shell and on-shell washout regions are shaded to exclude parameter space where, respectively, $2 \to 2$ interactions Eq. (3.68) and inverse decays Eq. (3.70) are in equilibrium. Constraints from collider experiments include LEP searches, excluding values of $M_\Delta < 75$ GeV and four-jet searches performed at Tevatron and at the LHC, excluding Δ in the 50 GeV $< M_\Delta <$ 770 GeV range. We also show the parameter space testable by the Einstein Telescope (ET) and LISA using $\alpha_{\rm GW} = 100$, $\beta/H = 15$, where the astrophysical foregrounds have been taken into account. We denote with red stars the two points of the parameter space for which we computed the GW spectrum shown in Fig. 3.2.

order of magnitudes towards smaller values of M_Δ, allowing the PT to occur down to the electroweak scale, potentially in reach of LISA and the Einstein Telescope, and making the mechanism testable at the LHC.

3.2.5 Model 2: Leptogenesis from a composite sterile neutrino

Model, neutrino masses and the baryon asymmetry

We now apply our framework for the generation of the baryon asymmetry, based on a supercooled confining PT, to a different model where the observed BAU is sourced via leptogenesis [41] through the decays of composite sterile neutrinos, which in addition provide mass to the SM neutrinos via a seesaw mechanism. This way we both substantiate the statement that our framework is more general than its specific realisations, and we find results that are interesting for leptogenesis per-se. We introduce the sterile neutrinos N_a (and denote their two two-component spinors as N_{aL} and N_{aR}) as hadrons of the confining sector, that is responsible for their Dirac mass $M_{N_a} \sim \mathcal{O}(\pi f)$. We then assume that a portal between the confining sector and the SM breaks the SM lepton number, generating inverse seesaw [359, 360] (ISS) as

$$-\mathcal{L}^{ISS} = y_{a\alpha}\overline{N}_{aR}HL_\alpha + M_{N_a}\overline{N}_a N_a + \frac{\mu_{ab}}{2}\overline{N}^c_{aL}\,N_{bL} + \text{h.c.}, \tag{3.86}$$

where L are the left-handed SM leptons, $\alpha = \{e, \mu, \tau\}$, y is the Yukawa coupling matrix between active and sterile neutrinos, μ is a lepton number breaking Majorana mass matrix, where we further denote by μ_a ($\overline{\mu}$) its complex diagonal (off-diagonal) entries. The presence of μ induces at low energies the $d = 5$ Weinberg operator [90]

$$\delta\mathcal{L}^{d=5} = c^{d=5}_{\alpha\beta}\left(\overline{L^c_\alpha}\,\tilde{H}^*\right)\left(\tilde{H}^\dagger L_\beta\right), \tag{3.87}$$

where $\tilde{H} = i\sigma_2 H^*$ and

$$c^{d=5}_{\alpha\beta} = \left(y^T\frac{1}{M_N^T}\mu\frac{1}{M_N}y\right)_{\alpha\beta}. \tag{3.88}$$

Upon electroweak symmetry breaking, the mass matrix m_ν for the light neutrinos is given by

$$m_\nu = \frac{v^2}{2}y^T M_N^{T-1}\mu M_N^{-1}y\,, \tag{3.89}$$

one can thus express $\mu = \mu(f)$ for a fixed value of the Yukawa coupling y, assuming m_ν to be of the order of the atmospheric neutrino mass, $m_\nu \sim 0.05$ eV.

We now assume the heavy Dirac states N_a to come in two generations, which is the minimum number needed to comply with neutrino oscillations data. Without loss of generality, we choose a basis where M_N is diagonal and real. In the non confining ISS the parameter μ is technically small but the hierarchy $\mu \ll M_N$ is not set by any concrete theoretical justification. The latter is instead naturally justified in our setup of composite sterile fermions. One can indeed envisage the possibility that, while the Dirac mass M_N originates from the confining sector, the Majorana one μ originates from physics external to the confining sector, offering a natural way to accomodate $\mu \ll M_N$. An explicit realization is provided in [361], where the strong dynamics is that of a conformal sector deformed by a relevant operator so that it confines in the IR (giving rise to the Dirac masses M_N), and by another operator with different scaling dimension and a small coefficient that gives rise to $\mu \ll M_N$. As anticipated in Sec. 3.2.2, our framework also leads to the expectations $\Delta M \equiv |M_{N_2} - M_{N_1}| \ll M_{N_1}$, because the N's are all hadrons of the same sector, as well as $y_{a\alpha} \ll 1$, because the Yukawas originate from a portal.

Therefore, under the natural assumption that $\mu_a \sim \overline{\mu} \sim \mu \ll M_{N_{1,2}}, \Delta M$, one can diagonalize the sterile neutrinos mass matrix to first order in $\delta_a = \mu/M_{N_a}$. Defining four Majorana states $\tilde{N}_i$, $i = 1, 2, 3, 4$, with masses M_i, we have

$$-\mathcal{L}^{ISS}_{\text{mass}} \supset h_{i\alpha}\overline{\tilde{N}}_i H L_\alpha + \frac{1}{2} M_i \overline{\tilde{N}}_i \tilde{N}_i + \text{h.c.}, \tag{3.90}$$

To first order in δ_a their masses and couplings are given by [362]

$$\begin{aligned}
M_1 &\simeq M_{N_1}\Big(1 - \frac{\delta_1}{2}\Big), & h_{1\alpha} &\simeq \frac{i}{\sqrt{2}}\Big(y_{1\alpha} + \frac{\delta_1}{4} y_{1\alpha} + \overline{\delta}_1 y_{2\alpha}\Big)\\
M_2 &\simeq M_{N_1}\Big(1 + \frac{\delta_1}{2}\Big), & h_{2\alpha} &\simeq \frac{1}{\sqrt{2}}\Big(y_{1\alpha} - \frac{\delta_1}{4} y_{1\alpha} - \overline{\delta}_1 y_{2\alpha}\Big)\\
M_3 &\simeq M_{N_2}\Big(1 - \frac{\delta_2}{2}\Big), & h_{3\alpha} &\simeq \frac{i}{\sqrt{2}}\Big(y_{2\alpha} + \frac{\delta_2}{4} y_{2\alpha} - \overline{\delta}_2 y_{1\alpha}\Big)\\
M_4 &\simeq M_{N_2}\Big(1 + \frac{\delta_2}{2}\Big), & h_{4\alpha} &\simeq \frac{1}{\sqrt{2}}\Big(y_{2\alpha} - \frac{\delta_2}{4} y_{2\alpha} + \overline{\delta}_2 y_{1\alpha}\Big)
\end{aligned} \tag{3.91}$$

where we defined

$$\overline{\delta}_i = \frac{\overline{\mu} M_{N_i}}{M_{N_2}^2 - M_{N_1}^2}\,. \tag{3.92}$$

Therefore we can see from Eq. (3.91) that the heavy neutrinos form pseudo-Dirac pairs with small Majorana splitting controlled by μ/M_{N_i}.

The CP asymmetry generated by the decays of the sterile neutrino N_a then reads

$$\epsilon_a \equiv \frac{\sum_\alpha \Big[\Gamma\Big(N_a \to \ell_\alpha H\Big) - \Gamma\Big(N_a \to \overline{\ell_\alpha} H^*\Big)\Big]}{\sum_\alpha \Big[\Gamma\Big(N_a \to \ell_\alpha H\Big) + \Gamma\Big(N_a \to \overline{\ell_\alpha} H^*\Big)\Big]} = \frac{1}{8\pi} \sum_{j \neq i} \frac{\text{Im}[(hh^\dagger)^2_{ij}}{(hh^\dagger)_{ii}} f_{ij}\,, \tag{3.93}$$

where we summed over the lepton flavour α in the final state and $f_{ij} \equiv f^V_{ij} + f^{\text{self}}_{ij}$ includes contributions given by vertex and self-energy corrections to the decay, which are given by [363]

$$f^V_{ij} = g\Big(\frac{m_j^2}{m_i^2}\Big), \qquad g(x) = \sqrt{x}\Big[1 - (1+x)\log\frac{x+1}{x}\Big] \tag{3.94}$$

and [364]

$$f^{\text{self}}_{ij} = \frac{(m_i^2 - m_j^2) m_i m_j}{(m_i^2 - m_j^2)^2 + m_i^2 \Gamma_j^2}, \tag{3.95}$$

where $\Gamma_i \sim (yy^\dagger)_{ii} M_i / 16\pi$ is the decay width of N_i and we assume no hierarchies in masses or couplings among the singlet generations and the SM flavours.

Let us now focus on the ϵ_1 and ϵ_2 contributions to Eq. (3.93):

$$\begin{aligned}
\epsilon_1 &= \frac{1}{8\pi (hh^\dagger)_{11}} \text{Im}\Big[(hh^\dagger)^2_{12} f_{12} + (hh^\dagger)^2_{13} f_{13} + (hh^\dagger)^2_{14} f_{14}\Big]\,,\\
\epsilon_2 &= \frac{1}{8\pi (hh^\dagger)_{22}} \text{Im}\Big[(hh^\dagger)^2_{21} f_{21} + (hh^\dagger)^2_{23} f_{23} + (hh^\dagger)^2_{24} f_{24}\Big]\,.
\end{aligned} \tag{3.96}$$

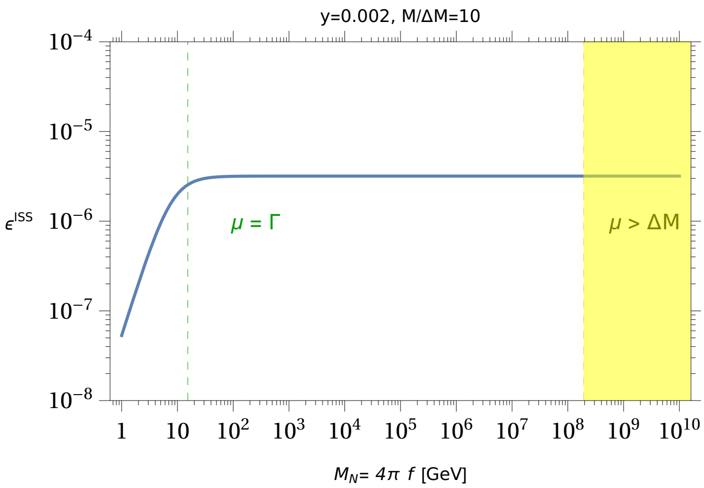

Figure 3.8: Rate asymmetry ϵ^{ISS} in the inverse see-saw mechanism, obtained from Eq. (3.98), for a fixed reference value of the Yukawa coupling $y = 0.002$, a degeneracy $M/\Delta M = 10$ and $\mu = \mu(f)$ fixed by neutrino masses. One can note that an asymptotic value for the produced asymmetry is reached in the $\mu \geq \Gamma$ regime. In the yellow region at large M_N our derivation of Eq. (3.98) breaks down, because it assumed $\mu \ll \Delta M$.

Due to the pseudo-Dirac nature of the $(\tilde{N}_1, \tilde{N}_2)$ pair, it follows that

$$(hh^\dagger)^2_{13} \simeq -(hh^\dagger)^2_{23} \simeq -(hh^\dagger)^2_{14} \simeq (hh^\dagger)^2_{24}; \qquad f_{13} \simeq f_{14} \simeq f_{23} \simeq f_{24}. \tag{3.97}$$

As a consequence, when considering $\epsilon_1 + \epsilon_2$, the f_{12} and f_{21} terms will dominate the sum as those involving f_{i3} and f_{i4} turn out to be of higher order in δ and $\bar{\delta}$ when summed up. An analytical parametric expression for ϵ in the ISS was obtained by the authors of [362], $\epsilon \sim \mu^2/(M_N \Gamma)$, where we dropped the family indices for μ and Γ to show only the parametric dependence. However, the above expression is assuming $\mu \ll \Gamma$, which is not strictly required by the ISS mechanism. We then derive a more general relation that assumes no hierarchy among μ and Γ. In fact as long as $\mu \ll M_N$, ΔM and $\Gamma \ll M_N$, ΔM are satisfied, the dominant one-loop contribution to the rate asymmetry is given by the self energy correction of N, because one has $f^V_{12} - f^V_{21} \sim \delta_1$, therefore the terms involving $f^{\rm self}_{12}$ and $f^{\rm self}_{21} \simeq -f^{\rm self}_{12}$ dominate in $\epsilon_1 + \epsilon_2$. We then obtain the total rate asymmetry ϵ^{ISS}

$$\epsilon^{ISS} \simeq 2(\epsilon_1 + \epsilon_2) \simeq \frac{\mathrm{Im}(yy^\dagger)_{12}}{\pi} \bar{\delta}_1 f^{\rm self}_{12} \simeq \frac{\mathrm{Im} y^2}{\pi} \left(\frac{\mu}{M_N}\right)^2 \frac{M_N}{\Delta M} \frac{M_N^2}{4\mu^2 + \Gamma^2}, \tag{3.98}$$

where the factor of 2 includes the contribution from $\epsilon_3 + \epsilon_4$, which has the same parametric dependence as the one from $\epsilon_1 + \epsilon_2$. We plot ϵ^{ISS} as a function of $M_N \sim M_{N_{1,2}}$ in Fig. 3.8. One can observe from Eq. (3.98) that an enhancement of the rate can be obtained in the presence of a quasi-degeneracy among the Dirac masses M_{N_a}. When the two generations $a = 1, 2$ are nearly degenerate, the CP asymmetry is enhanced compared to the non-degenerate case by a factor $M_N/2\Delta M$, as follows from Eq. (3.92). We stress that Eq. (3.98) holds for $\mu \ll \Delta M$, hence we exclude regions of parameter space where this does not hold from our study. A generalization to the case $\mu \gtrsim \Delta M$ is beyond the scope of this work.

As the baryon asymmetry is now sourced by a lepton asymmetry, one has to require that the reheating temperature, Eq. (3.44), is larger than the sphalerons decoupling temperature,

$T_{\rm RH} \geq T_{\rm sph} \simeq 132$ GeV, in order for the sphalerons to be in thermal equilibrium and therefore to transfer the lepton asymmetry to the baryon sector. Finally, the baryon asymmetry is obtained by plugging ϵ^{ISS} of Eq. (3.98) in Y_B of Eq. (3.52).

Washout processes

Following analogous steps to those discussed in the model with the Δ scalar, we now have to take into account washout effects of the lepton number produced at $T_{\rm RH}$. The $2 \to 2$ scattering rate $\ell H \leftrightarrow \bar{\ell} H^*$, mediated by the sterile fermion N, violates lepton number. Therefore its rate must vanish in the $\mu \to 0$ limit and it can be estimated from the coefficient of the Weinberg operator in the ISS, Eq. (3.88):

$$\Gamma_{WO}(\ell H \to \bar{\ell} H^*) \simeq \frac{y^4 T_{\rm RH}^3 \mu^2}{4\pi M_N^4}\,, \tag{3.99}$$

which presents a μ^2/M_N^2 suppression with respect to the standard Type-I Seesaw one, where one has only one scale $M_N \sim \mu$. We also included a factor of 2 in Eq. (3.99) to account for the contributions given by the degenerate neutrinos. Moreover we assume these washouts to be efficient for $T_{\rm RH} \geq m_H/3$, when a sizable population of H is still present. Anyway the precise value of $T_{\rm RH}$ for the decoupling of washout effects is not crucial as these processes turn out to play a negligible role in our parameter space. In fact this rate does not spoil the lepton number asymmetry produced by the decays of N provided that it is smaller than $H(T_{\rm RH})$, i.e. if

$$T_{\rm RH} < \sqrt{\frac{\pi^2}{90}\frac{\pi v^4\, {g^*}^{1/2}}{M_{\rm Pl}\, m_\nu^2}} \sim 10^{13}\text{GeV}\,, \tag{3.100}$$

where the dependence of Γ_{WO} on y, μ and M_N has been absorbed into m_ν by using Eq. (3.89).

Also the inverse decays processes $\ell H \to N$, $\bar{\ell} H^* \to N$ can lead to a lepton number washout, if they feel lepton number violation. Indeed, if they do, then they distinguish the initial ℓ states from $\bar{\ell}$ ones and convert more ℓ than $\bar{\ell}$ back into N's. We can assume that the lepton asymmetry produced by N decays does not get erased provided that the inverse-decays rate $\Gamma_{ID} \leq H$ at $T_{\rm RH}$. It was found by the authors of [365] that the small mass splitting between the two states among the heavy pseudo-Dirac N_i leads to a destructive interference between their contributions to Γ_{ID}, which has the effect of suppressing the washouts. This can be parametrized by the suppression factor of the decay width

$$k^{\rm eff} = \frac{\rho^2}{1+\sqrt{c}\rho+\rho^2} = \frac{M_N \mu^2}{\Gamma^2 M_N + \mu\Gamma^2 + M_N\mu^2}\,, \tag{3.101}$$

where $\rho \sim \mu/\Gamma$ and $c \sim (\Gamma/M_N)^2$. The quadratic suppression in μ can be again understood from the fact that inverse decays cannot wash out a lepton asymmetry in the lepton conserving limit, hence they should depend on some power of μ in addition to powers of the Yukawa couplings. One can thus estimate Γ_{ID} as

$$\Gamma_{ID} \simeq 2\Gamma\, k^{\rm eff}\Big(\frac{M_N}{T_{\rm RH}}\Big)^{3/2}\text{Exp}\Big[-\frac{M_N}{T_{\rm RH}}\Big]\,, \tag{3.102}$$

where the factor of 2 comes from the fact that both N_1 and N_2 contribute to washout. This means that the rate of the net washout processes $\ell H \to N$, $\bar{\ell} H^* \to N$ at $T_{\rm RH}$ is suppressed by both the Boltzmann factor and the smallness of μ. Therefore, washouts of the lepton asymmetry turns out to be very suppressed.

To summarize we find that, in the model of leptogenesis from inverse-see-saw and composite neutrinos, $2 \to 2$ washout effects are never the leading constraint on the parameter space of our interest, while inverse decays can become an important constraint only if one lifts the Boltzmann suppression by choosing $M_N < 4\pi f$.

Composite sterile neutrinos at colliders and discussion

We are also interested in possible signatures of the sterile fermions N at colliders, coming from their mixing with the active neutrinos. The requirement $T_{\rm RH} > T_{\rm Sph}$ plus $M_N \sim O(\pi f)$ implies $M_N \gtrsim$ TeV, making a future high-energy muon collider [366, 367] the leading proposed collider to test this picture. The authors of [368] estimated the projected sensitivity of a $\sqrt{s} = 10$ TeV muon collider with integrated luminosity 10 ab^{-1} on the squared mixing angle $|U_\ell|^2$ between the sterile N and the SM neutrino of flavour ℓ. The dominant N-production mechanism is $\mu^+\mu^- \to N\bar{\nu}_\mu$, which, being t-channel, is not suppressed at large center-of-mass squared energies s, and the decay mode considered is $N \to W\ell$ which is fully reconstructable and whose branching ratio is approximately independent of U_ℓ.

The best projected sensitivity occurs for the muon flavoured case and reaches $|U_\mu^2| \lesssim 10^{-6}$ for a sterile fermion mass between 1 and 10 TeV, of course it does not extend to larger masses because $\sqrt{s} = 10$ TeV. In the ISS model the active-sterile neutrino mixing is given by $\sin\theta \sim y\, v/(\sqrt{2}M_N)$, hence $|U_\mu^2| = \sin^2\theta \sim y^2v^2/(2M_N^2)$. Therefore, for fixed y, the sensitivity $|U_\mu^2| \lesssim 10^{-6}$ translates into a lower limit on M_N: lighter values of M_N will be potentially discoverable at a future high-energy muon collider, and our model turns out to be able to reproduce the BAU for those light M_N values, compatibly with all other constraints.

Summary of the results

We summarize our findings in Fig. 3.9, where we set different benchmark values for y, $M_N/\Delta M$, M_N/f and we take $T_{\rm nuc}/f = 10^{-3}$ and $Z = 1$. A remarkable feature of our mechanism is that, as it is manifest from the plots, one can accomplish leptogenesis around few TeV in the ISS scenario, while this is not the case for the standard thermal leptogenesis ISS scenario, where washout effects are active already at $T_{\rm RH} \sim M_N$ and are too strong to accomodate the required asymmetry, even taking into account quasi-degeneracy enhancements of the rate asymmetry, as shown in [369, 362].

One can see that we expect our model to be partially in reach of a 10 TeV muon collider, provided some mass degeneracy exists between the N_i, of $M_N/\Delta M \sim \mathcal{O}(10^2 - 10^3)$ and as expected given they are hadrons from the same confining sector. A detailed analysis would be needed to make this statement more precise, but goes beyond the scope of its work. Coming to testability at lower-energy colliders, we find an obstacle to make our model viable at lower values of f. The obstacle comes from the interplay between N annihilations before decays and the bounds from washout effects and from the electroweak sphalerons. The latter need to be active, placing the absolute lower limit $T_{\rm RH} \gtrsim 132$ GeV, and hence demanding f to be roughly larger than the weak scale. One could then try to bring M_N within reach of lower-energy colliders by choosing $M_N < (<)4\pi f$, but washout effects would then kick-in to close the allowed parameter space, as visible in the Fig. 3.9.

A comment on linear see-saw

What about other realizations of the seesaw mechanism, like the linear seesaw (LSS)? In analogy to the ISS, additional sterile Dirac fermions N_a are introduced, which mix with the SM neutrinos. In the LSS $\mu = 0$ at tree level and lepton number is explicitly broken by an additional lepton number breaking Yukawa coupling y' of N_{aL} to the SM and we can assume without loss of generality that $y' < y$. The LSS Lagrangian is given by

$$-\mathcal{L}^{LSS} = y_{a\alpha}\overline{N}_{aR}HL_\alpha + M_{N_a}\overline{N}_a N_a + y'_{a\alpha}\overline{N}^c_{aL}HL_\alpha + \text{h.c.}, \tag{3.103}$$

and the light neutrinos mass matrix reads $m_\nu = v^2(y'^T M_N^{T-1} y + y^T M_N^{-1} y')$. A parametrical expression for the rate asymmetry ϵ^{LSS} was obtained in [362], $\epsilon^{LSS} \sim y'^2/(16\pi)$. Fixing now y as a function of y' and M_N by using the neutrino mass matrix relation and imposing for consistency that $y' < y$, one obtains an upper bound on y',

$$y' < \left(\frac{M_N m_\nu}{v^2}\right)^{1/2} \sim 10^{-6}\left(\frac{M_N}{\text{TeV}}\right)^{1/2}, \tag{3.104}$$

which translates into a rate asymmetry $\epsilon^{LSS} \leq 10^{-12}$ around the TeV scale, way too small to account for the observed baryon yield. Therefore the pure LSS is not a viable model for TeV leptogenesis in our framework.

The discussion above however holds only at tree level. Starting from the pure LSS, a Majorana mass term μ for the N_a is generated at the one-loop level, of the size $\mu \sim M_N y y'/(16\pi^2)$, thus one expects a general LSS+ISS model to arise from a LSS tree level Lagrangian [362]. We may then wonder if a new interesting region of the parameter space opens up in the region where the interference between ISS and LSS contributions produces the relevant term for the rate asymmetry: it turns out that the neutrino mass matrix formula is dominated by the LSS term, while the rate asymmetry by the ISS piece and it reads

$$\epsilon^{LSS+ISS} = \frac{m_\nu^2 M_N^2}{v^4 y^4}. \tag{3.105}$$

The y coupling needed for leptogenesis, $y \sim \mathcal{O}(10^{-4} - 10^{-5})$ for $M_N \sim$ TeV, is way too small to provide any signatures at colliders, so we will not explore in more detail this model within our supercooled confinement BAU framework.

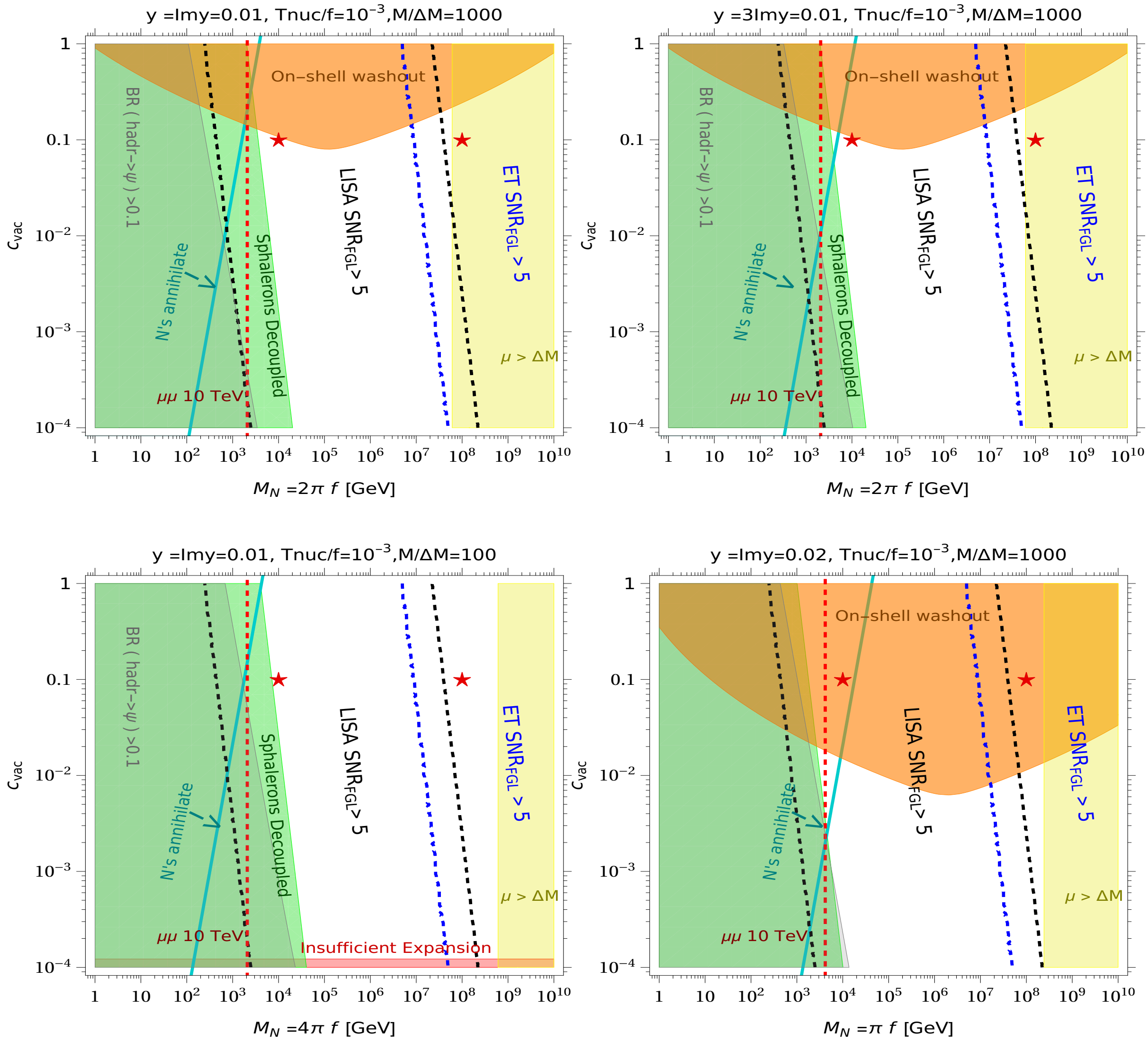

Figure 3.9: Parameter space for the composite singlet fermion realisation of our framework, which constitutes a variation on inverse see-saw leptogenesis. We choose $g_{\rm TC} = 80$, $g_* = g_{\rm SM} + g_{\rm TC}$, $g_{\rm RH} = g_{\rm SM} + 1$ and $Z = 1$ for definiteness. The white area is allowed and accomodates the observed baryon asymmetry, the red and gray regions are excluded by the PT dynamics and above the cyan line the N's start to equilibrate with the dilaton before they decay and our computation of the BAU should be changed, as in Fig. 3.1. The dashed red line is obtained from the projected sensitivity of a 10 TeV muon collider on the active-sterile neutrino mixing, see [368]. The green region is excluded from requiring electroweak sphalerons to be out of equilibrium for reheating temperature $T_{\rm RH} < 132$ GeV. In the orange exclusion regions the on-shell washout processes, i.e. inverse decays of Eq. (3.102), are in equilibrium at $T_{\rm RH}$. The yellow region is excluded by requiring $\mu < \Delta M$ for our expression of the rate asymmetry Eq. (3.98) to hold. We also show the parameter space testable by the Einstein Telescope (ET) and LISA using $\alpha_{\rm GW} = 100$, $\beta/H = 15$, where the astrophysical foregrounds have been taken into account. We denote with red stars the two points of the parameter space for which we computed the GW spectrum shown in Fig. 3.2.

3.2.6 Conclusions and Outlook

In this section of the thesis we have proposed a new framework for the generation of the observed baryon asymmetry of the universe (BAU), based on a first order supercooled PT of a confining sector. In our framework $B - L$ violating processes are driven by the decays of some composite states (hadrons) of the confined phase. The main advantages with respect to the analogous non-confining mechanism [316] are that in our setup the rate asymmetry is enhanced due to the deep inelastic scatterings occurring upon bubble percolation, which increase the population of the decaying hadrons, and due to the suppression of washout processes because of the hierarchy between the hadron masses and the reheating temperature. Independently of its specific realization, our framework allows to reproduce the observed BAU down to the weak scale, and potentially down to the MeV one. A first important consequence of this result is that, contrarily to its weakly coupled realisations, the framework is testable in GWs not only by the Einstein Telescope but also by lower frequency ones like BDECIGO and LISA. Based on the current understanding of astrophysical foregrounds, the absence of a signal in these experiments will exclude the framework down to the TeV scale, see Fig. 3.1.

We have then studied two specific models within our proposed framework, one realising baryogenesis from the decays of composite scalars, charged under the SM, one realising leptogenesis from the decays of composite fermions, singlets under the SM gauge. This allows to include effects that could potentially washout the BAU, to determine other experimental signals, and to possibly connect our framework with open SM problems in addition to the BAU.

- ⋄ Concerning baryogenesis from composite scalars, we have found that washout effects prevent PT scales f lower than a few GeV, see Fig. 3.7. We have then studied collider searches for the composite scalars, finding they exclude values of f lower than the weak scale, and that future LHC searches, like 4-jet ones, will test new open territory of this model. The model could also manifest itself in flavour and CP-violating observables, although the size of the effects depends on further details of the model and an absence of deviation from the SM would not exclude it. Finally, we find that the dominant contribution to the neutron EDM arises at 3 loops and the model is not expected to show up there.

- ⋄ Concerning leptogenesis from composite sterile neutrinos, it offers a natural implementation of inverse and linear see-saw scenarios (ISS and LSS), that also explains the small SM neutrino masses. Focusing on the ISS for definiteness, we found that we can reproduce the observed BAU down to scales of the PT $f \sim$ TeV, see Fig. 3.9. A degeneracy at the level of 10^{-2} or more is required between the masses of two composite neutrinos, but that is actually expected from a confining sector, while in the standard thermal leptogenesis one generally needs tuning. The obstacle to reach f below the electroweak scale comes from the requirement of a reheating temperature larger than about 130 GeV, so that sphalerons are active. Washout effects are further suppressed, with respect to a generic case, by the insertion of an extra parameter to break lepton number, and only inverse decays can lead to appreciable washout in case $M_N < 4\pi f$. We find that the model is barely testable by N searches at a future muon collider. Our results concerning this model are also interesting from the ISS and LSS points of view, because we enlarge the parameter space where these leptogenesis models work.

Our study opens several interesting avenues of further investigation, both on the model-building and on the phenomenology sides. Concerning the former, it would be for example interesting to connect our framework for the generation of the BAU with solutions to the hierarchy problem of the Fermi scale, given that it works down to the electroweak scale. Concerning phenomenology, it would be interesting to find a specific model realising our framework which allows to go down to the MeV scale for the PT, so to possibly explain the GWs observed by pulsar timing arrays [342, 343, 344, 345]. We leave these and other directions for future work.

3.3 The PTA signal from the baryon dark matter coincidence

Introduction

The recent evidence of a SGWB detection made by the PTAs [244] have sparked renewed interest in cosmological FOPTs as a potential source of the observed signal. If such a signal is sourced by a FOPT, its scale should be of $\mathcal{O}$ (1 GeV), as discussed in Sec. 2.2.4. This opens up an exciting possibility: a low-scale FOPT could not only generate a detectable SGWB, but also be connected with the BAU generation.

A promising class of models for the BAU generation, see Sec 3.3.1, is *darkogenesis*, where the baryon asymmetry is dynamically linked to the DM abundance, as motivated by the coincidence problem of the baryon and DM relic abundances, suggesting a common origin for both components.

In a realization of darkogenesis proposed by [63], the baryon asymmetry is first generated in a dark sector containing a fermionic DM candidate χ, and then partially transferred to the visible sector. This transfer occurs via higher-dimensional operators that connect χ with SM quarks. In particular, the dimension-six operator

$$\mathcal{O}_6 = \frac{1}{\Lambda^2}\chi udd \tag{3.106}$$

becomes relevant below the QCD confinement scale. After confinement, this operator induces an off-diagonal mass term between χ and the neutron:

$$\mathcal{L}_{\text{mix}} = -\delta m\, \bar{n}\chi + \text{h.c.}, \tag{3.107}$$

allowing *neutron-DM oscillations*. The existence of this operator has also been suggested as a possible explanation for the so-called *neutron lifetime anomaly* [370]. However, in the present work we will not focus on this aspect. Instead, our interest lies in the role of this mixing in enabling oscillations that can transfer a dark-sector asymmetry into the visible sector. Crucially, the authors find that these oscillations are resonantly enhanced at finite temperature of $\mathcal{O}$ (10-100) MeV, compatible with the generation of the observed BAU well below the EW scale.

Therefore, this mechanism offers a new connection: a low-scale supercooled FOPT (potentially generating the PTA signal) could at the same time trigger baryogenesis via χ–n oscillations. While the authors of [63], proved how baryogenesis could be sorced via χ–n mixing, they did not explore the possibility that the same underlying dynamics could also generate a stochastic GW background observable by PTAs. In this section we explore how a sub-GeV FOPT can simultaneously account for both the observed BAU and the PTA signal. In the following, we will illustrate how this mechanism operates in a dark sector charged under a $U(1)'$ gauge symmetry, and discuss the conditions under which the correct BAU and the observed GW signal can both be obtained.

3.3.1 Generation of the baryon asymmetry

We adopt the setup introduced in [63] for the generation of the baryon asymmetry. We consider DM to be a Dirac fermion χ, with mass m_χ, unit baryon number and carrying no other conserved charge. Assuming its couplings to baryonic matter not to be highly suppressed, m_χ is bounded from below by nuclear decays. The most stringent bound comes from the stability of ^{9}Be, which sets $\Delta m \equiv m_n - m_\chi < 1.665$ MeV [370] (with neutron mass

$m_n = 939.565$ MeV). In the darkogenesis model of [63], the authors consider a scenario where the pre-existing asymmetry in the χ sector is transferred to the SM via $\chi - n$ oscillations.

These are controlled by the 2×2 Hamiltonian

$$H = \begin{pmatrix} m_n + \Delta E_n & \delta m \\ \delta m & m_\chi + \Delta E_\chi \end{pmatrix}, \tag{3.108}$$

where ΔE_n and ΔE_χ are the thermal mass shifts of the neutron and DM respectively. We extract the former from [371] and we estimate $\Delta E_\chi = g'^2 T_\gamma'^2/(8m_\chi)$ from the dark photon contribution to the χ self energy, where g' the gauge coupling of the $U(1)'$ and T'_γ the temperature of the dark sector, related to that in the visible sector by

$$\xi = \frac{T'_\gamma}{T_\gamma}. \tag{3.109}$$

The mixing angle θ, obtained by diagonalizing H, reads

$$\tan(2\theta) = \frac{2\delta m}{\Delta m + \Delta E_n - \Delta E_\chi} \equiv \frac{2\delta m}{\delta E}, \tag{3.110}$$

and the difference between the eigenvalues of H is given by:

$$|\delta\omega| = \sqrt{(\delta E)^2 + 4\delta m^2}. \tag{3.111}$$

To find the efficiency of $\chi - n$ oscillations, we start with the initial state $\psi(0) = |\chi\rangle$ and evolve it with the Hamiltonian Eq. 3.108, giving:

$$|\psi(t)\rangle = e^{-i(\omega_1+\omega_2)t/2}\left(\left(\cos\frac{\delta\omega}{2}t - i\cos 2\theta \sin\frac{\delta\omega}{2}t\right)|\chi\rangle - i\sin 2\theta \sin\frac{\delta\omega}{2}t|n\rangle\right), \tag{3.112}$$

therefore the probability of oscillating into a neutron is

$$P_n(t) = \sin^2(2\theta)\sin^2(\delta\omega t/2). \tag{3.113}$$

Because of the large rate of interactions Γ_n of neutrons on heat bath pions, however, there may not be time for a full oscillation. In general one should carry out a time average, over the short time scale $1/\Gamma_n$,

$$\bar{P}_n = \Gamma_n \int_0^\infty dt\, e^{-\Gamma_n t} P_n(t) = \frac{2\delta m^2}{\delta w^2 + \Gamma_n^2}. \tag{3.114}$$

The neutron scattering rate Γ_n on the pions in the thermal bath is given by $\Gamma_n = n_\pi\langle\sigma_{n\pi}v\rangle$, with n_π the pion thermal number density, including a factor of 3 due to isospin, $\langle v\rangle = \sqrt{8T/(\pi\, m_\pi)}$ and $\sigma_{n\pi} \simeq 0.1/m_\pi^2 \simeq 2$ mb [372, 373], with $m_\pi \simeq 140$ MeV the pion mass. The rate of production of neutrons via oscillations per χ particle is given by $\Gamma_{\rm osc} = \overline{P_n}\Gamma_n$. Similarly, the rate of production of χ per neutron must proceed with the same rate, therefore the number density of χ decreases as:

$$\dot{n}_\chi = -\Gamma_{\rm osc}(n_\chi - n_n) \tag{3.115}$$

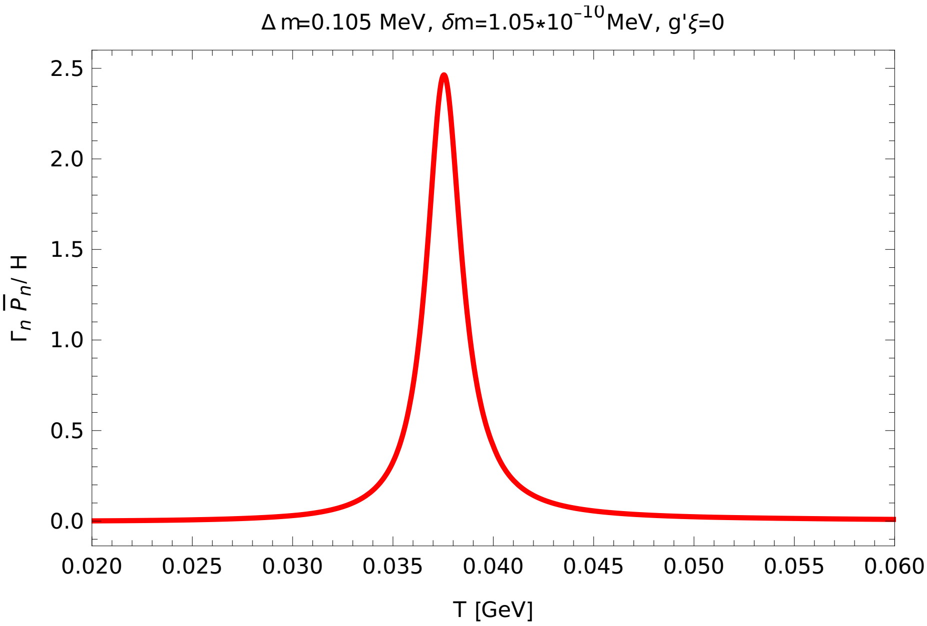

Figure 3.10: The integrand $\Gamma_n \bar{P}_n / H$ of Eq. 3.117 as a function of the temperature T, showing the resonant enhancement of $\chi - n$ oscillations, using benchmark values $\Delta m = 0.105$ MeV, $\delta m = 1.05 \times 10^{-10}$ MeV. and $g'\xi = 0$.

As in our model the baryon number is conserved, then $n_\chi + n_n$ is constant. The equation controlling the fraction $f = n_n/(n_n + n_\chi)$ of DM converting to neutrons, is thus given by

$$\dot{f} = \Gamma_{\rm osc}(1 - 2f) \tag{3.116}$$

which has the solution

$$f = \frac{1}{2}\Big(1 - {\rm Exp}\Big(- 2\int dt\, \Gamma_{\rm osc}\Big)\Big) \simeq \frac{1}{2}\Big(1 - {\rm Exp}\Big(- 2\int \frac{dT}{T}\frac{\Gamma_n(T)\bar{P}_n(T)}{H(T)}\Big)\Big)\,, \tag{3.117}$$

$f \simeq 0.16$ to obtain the observed baryon over DM abundance.

As shown in Eq. (3.117), the final baryon abundance is controlled by the time (or equivalently, temperature) integral of the oscillation rate. The integrand, $\Gamma_n(T)\,\bar{P}_n(T)\,/H(T)$, encodes the interplay between the oscillation probability and the Hubble rate $H(T) = \rho_{\rm rad}(T)/3M_{\rm Pl}^2$. This quantity exhibits a sharp peak at the resonance temperature T_r, defined by the condition $\delta E(T_r) = 0$, where the mixing between χ and the neutron is maximal. However, the oscillation probability is still suppressed by the damping rate Γ_n, as described in Eq. (3.114). Therefore, the dominant contribution to the baryon asymmetry arises from resonant χ - n oscillations occurring near this T_r. An example of this feature is shown for benchmark values of the relevant parameters in Figure 3.10, for which $T_r \sim 37$ MeV, in agreement with the result obtained by [63].

We now explore the parameter space relevant for baryon asymmetry generation, in the $\delta m - \Delta m$ and for the benchmarkvalues $g'\xi = 0, 0.5, 1$. The same parameter space is constrained by the null searches for the decay $n \to \chi\gamma$, which were proposed as a possible explanation for the neutron lifetime anomaly. In particular, the constraint takes the form

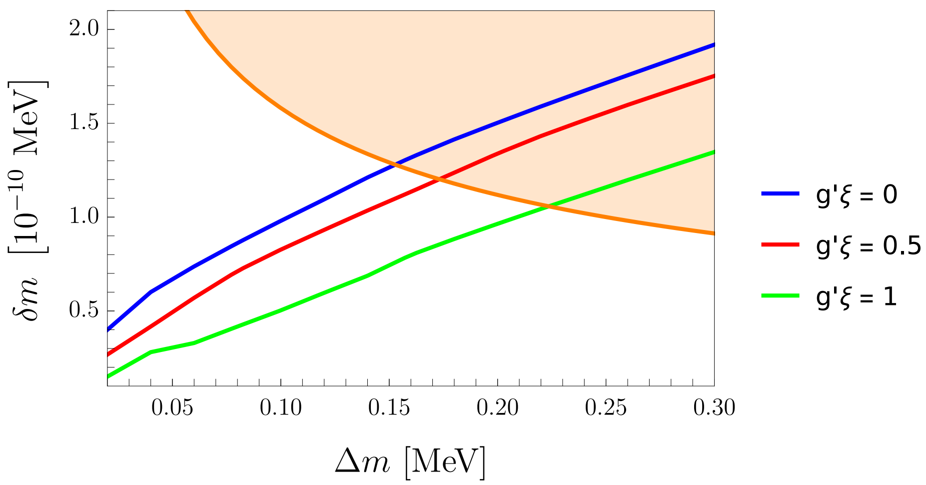

Figure 3.11: Solid lines yield the observed baryon asymmetry in the $\delta m - \Delta m$ plane for benchmark values of $g'\xi = 0, 0.5, 1$ as in Eq. 3.117. The orange area is excluded from $n \to \chi\gamma$ measurements [374].

[374]

$$\delta m \lesssim 5 \times 10^{-11}\ \text{MeV} \left(\frac{1\ \text{MeV}}{\Delta m}\right)^{1/2}, \tag{3.118}$$

implying a sharp upper limit on the allowed region in the $\delta m - \Delta m$ plane. Nevertheless, we find that the observed baryon asymmetry can still be successfully generated along the colored lines in Fig. 3.11 for $\Delta m \lesssim 0.2$ MeV, safely below the experimental bound.

3.3.2 Phase transition and Gravitational Wave parameters

In the original proposal of Ref. [63], the spontaneous breaking of the dark $U(1)'$ gauge symmetry is driven by a scalar field ϕ acquiring a VEV from a classical potential of the form

$$V_0 = \lambda_\phi \left(|\phi|^2 - \frac{v'^2}{2}\right)^2 . \tag{3.119}$$

In this scenario, the dark scalar VEV v' is crucial for generating the mass mixing $\delta m \propto \langle\phi\rangle$ between the neutron and the DM χ, and thus for enabling the baryon asymmetry generation through $\chi - n$ oscillations. The associated PT occurs around a critical temperature $T_c \sim \mathcal{O}(100\,\text{MeV})$, well above the resonance temperature for oscillations, $T_r \sim 30\,\text{MeV}$.

In this work, we propose a modification to the scalar potential by assuming classical scale invariance in the dark sector. Namely, we assume the VEV of the scalar ϕ to arise radiatively via the Coleman-Weinberg (CW) mechanism [21]. This approach eliminates the need for an explicit mass term in the tree level scalar potential, which now is just given by

$$V(\phi) = \lambda|\phi|^4 . \tag{3.120}$$

We can now compute the one-loop corrections to the potential à la CW, introducing the constant field background ϕ_c. Heavy scalar fields charged under $U(1)'$ are expected to lie around the TeV scale in the UV completion of [375], so they can be safely integrated out.

We are then only left with the contributions from the scalar ϕ and the gauge boson A'. We write the complex scalar in terms of its real and imaginary component:

$$\phi = \frac{\varphi_r + \varphi_i + \phi_c}{\sqrt{2}}\,. \tag{3.121}$$

The field dependent masses for the real, imaginary components of ϕ and for the gauge boson A' are given respectively by:

$$m_r^2(\phi_c) = 3\lambda\phi_c^2 \tag{3.122}$$

$$m_i^2(\phi_c) = \lambda\phi_c^2 \tag{3.123}$$

$$m_{A'}^2(\phi_c) = g'^2\phi_c^2\,. \tag{3.124}$$

In the end, the one-loop effective potential at $T = 0$, computed using the dimensional regularization and the $\overline{\text{MS}}$ renormalization scheme, is:

$$\begin{aligned} V_{eff}(\phi_c) = \lambda\phi_c^4 + \frac{1}{64\pi^2}\Bigg[3m_{A'}(\phi_c)^4\left(\log\frac{m_{A'}^2(\phi_c)}{M^2} - \frac{5}{6}\right) \\ + m_r^4(\phi_c)\left(\log\frac{m_r^2(\phi_c)}{M^2} - \frac{3}{2}\right) + m_i^4(\phi_c)\left(\log\frac{m_i^2(\phi_c)}{M^2} - \frac{3}{2}\right)\Bigg] \end{aligned} \tag{3.125}$$

where M is a renormalization scale. Following the method in Ref. [21], since M is arbitrary, we can fix it to be at the location of the minimum, $\langle\phi\rangle = \frac{v}{\sqrt{2}}$. Therefore, by imposing that $V'(\langle\phi\rangle) = 0$ we find the value of $\lambda \propto g'^4$ for which we have the desired minimum.

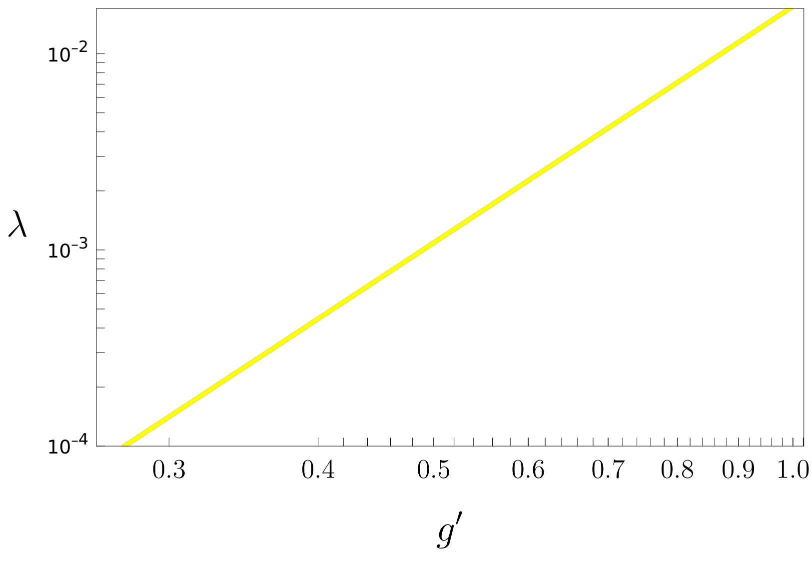

Figure 3.12: Values of the quartic coupling λ as a function of the gauge coupling g' that allow the generation the VEV of the scalar $\langle\phi\rangle = v/\sqrt{2}$.

A potential that leads to a supercooled PT is flat around the origin and finite temperature effects become very important as they induce a positive curvature at the origin, making $\phi = 0$ a metastable vacuum [376]. The finite temperature corrections are given by:

$$\Delta V^T(\phi, T) = \sum_{i=\text{bosons}} \frac{n_i T^4}{2\pi^2} J_b\left(\frac{m_i^2(\phi)}{T^2}\right) + \sum_{i=\text{fermions}} \frac{n_i T^4}{2\pi^2} J_f\left(\frac{m_i^2(\phi)}{T^2}\right), \tag{3.126}$$

where the thermal functions $J_{B/F}$ are given by:

$$J_{B/F} = \int_0^\infty dk\, k^2 \log\left[1 \mp \exp\left(-\sqrt{k^2 + m_i^2(\phi)/T^2}\right)\right], \tag{3.127}$$

where the minus (plus) sign stands for bosons (fermions) and their high-temperature expansions $x \equiv \frac{m_i(\phi)}{T}$ read [377]

$$J_B(x) = -\frac{\pi^4}{45} + \frac{\pi^2}{12}x - \frac{\pi}{6}x^{3/2} - \frac{x^2}{32}\log\frac{x}{a_b} + \mathcal{O}\left(x^3 \log\frac{x^{3/2}}{\text{const.}}\right), \tag{3.128}$$

$$J_F(x) = \frac{7\pi^4}{360} - \frac{\pi^2}{24}x - \frac{x^2}{32}\log\frac{x}{a_f} + \mathcal{O}\left(x^3 \log\frac{x^{3/2}}{\text{const.}}\right), \tag{3.129}$$

with $\log a_b \simeq 5.4076$ and $\log a_f \simeq 2.6350$.

Because of the absence of tree level mass terms, the degrees of freedom of the model will be massless close to the origin, hence we can use the high temperature expansion. We only compute the contribution from the gauge boson, as that from the scalar is negligible due to $\lambda \ll g'$. The potential can then be approximated by [320] [2]:

$$V(\phi) = \frac{1}{2}m^2(T)\phi^2 - \frac{\delta(T)}{3}\phi^3 + \frac{\lambda(T)}{4}\phi^4\,, \tag{3.130}$$

where the coefficients are given by

$$m^2(T) = \frac{1}{4}g'^2 T^2\,, \tag{3.131}$$

$$\delta(T) = \frac{3}{4\pi}g'^3 T\,, \tag{3.132}$$

$$\lambda(T) = \frac{3}{8\pi^2}g'^4 \log\left(\frac{T}{B}\right) \tag{3.133}$$

with $B = M/\sqrt{a_b}$.

It has been show in Ref. [320] that for the CW potential the tunneling rate is dominated by the $O(3)$ symmetric thermal bounce, hence the nucleation temperature $T_{\rm nuc}$ is controlled by the S_3/T bounce action. We can then write the nucleation condition Eq. 3.1 as follows:

$$\Gamma(T) = T^4\left(\frac{S_3/T}{2\pi}\right)^{3/2}\exp(-S_3/T) \simeq H(T)^4\,. \tag{3.134}$$

We adopt the analytical result given in [320] for the computation of the S_3 bounce action, which is given by

$$\frac{S_3}{T} \simeq \frac{3\pi^3}{g'^3}\left(\frac{1 + e^{-1/\sqrt{|k|}}}{1 + \frac{9}{2}|\kappa|}\right), \tag{3.135}$$

[2] In the computation of the bounce action presented in this work we follow the prescription of [320, 275], where the authors set the renormalization scale M to the VEV of the scalar field. However, as for supercooled PTs the tunneling occurs at a field value $\phi* \ll$ VEV, a more accurate approach involves the inclusion of RG running of the couplings and fields, as shown e.g. in [378, 379].

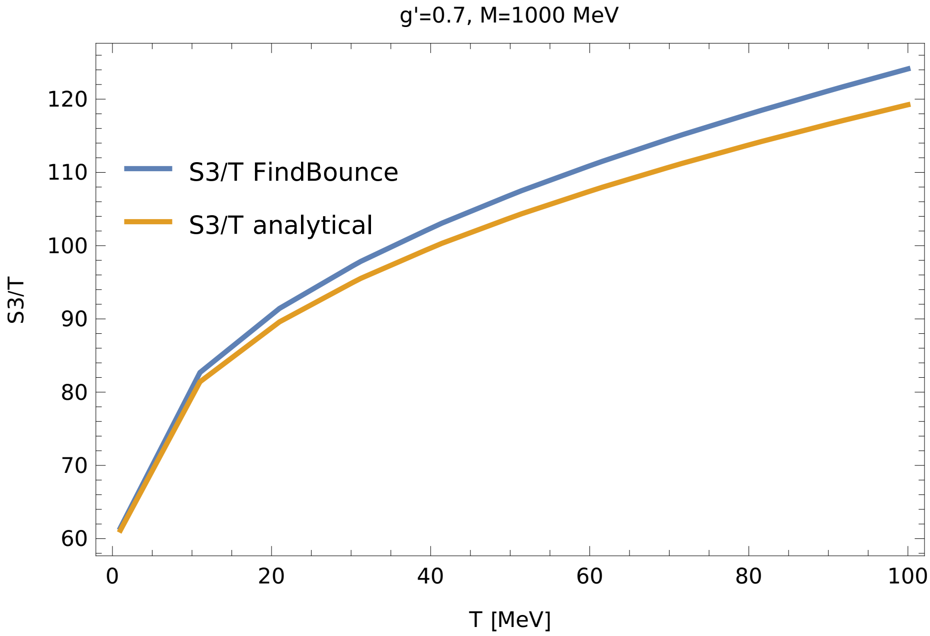

Figure 3.13: Comparison between our numerical estimate of the $O(3)$ symmetric bounce action associated to the quartic potential in Eq. 3.130 using the FindBounce package [380] and the analytical expression Eq. 3.135 obtained in [320] for the benchmark values $g' = 0.7$, $M = 1$ GeV.

where the dimensionless parameter κ is given by:

$$\kappa(T) \equiv \frac{\lambda(T)m^2(T)}{\delta^2(T)} = \frac{1}{6}\log\left(\frac{T}{B}\right). \tag{3.136}$$

We checked numerically this analytical result with the FindBounce package [380], see Figure 3.13 for a comparison between the analytical and numerical values of S_3/T for a benchmark point in the parameter space.

Therefore, in the vacuum domination phase, which is needed to address the PTAs signal in terms of a FOPT, the nucleation condition Eq. (3.1) reads:

$$\frac{3\pi^3}{g'^3}\left(\frac{1+e^{-1/\sqrt{|\kappa_n|}}}{1+\frac{9}{2}|\kappa_n|}\right) = 4\log\left(\frac{B}{H_V}\right) - 24|\kappa_n| \tag{3.137}$$

where we have defined $\kappa_n \equiv \kappa(T_n) = 1/6\log(T_n/B)$ and H_V is the contribution to the Hubble rate due to the vacuum energy, that is $H_V^2 = \Delta V_0/3M_{\rm Pl}^2$, where ΔV_0 is the the potential energy difference between the false and the true minimum at zero temperature. From Eq. 3.135 it is clear that $g' > g'_{\rm min}$ is needed for the bubbles to nucleate ($S_3/T \lesssim 150$) and $g' < g'_{\rm max}$ needed for the FOPT to occur during vacuum domination, hence a supercooled FOPT occurs in the window $[g'_{\rm min}, g'_{\rm max}]$. The authors of [320] show that the boundary of this window is roughly $[0.5, 0.8]$ for $B \sim$ GeV and we find agreement.

We can now compute the nucleation temperature using Eq. (3.137). The results of the nucleation temperature, as a function of the gauge coupling g', computed for different values of the VEV are represented in Figure 3.14. We also show in Fig. 3.15 the GW parameters α

and β/H as a function of the gauge coupling g' for the same benchmark values of the VEV. One can see that for $g \sim 0.5 - 0.7$ the PT exhibits moderate or large supercooling, therefore compatible with the origin of the PTAs signal from a FOPT.

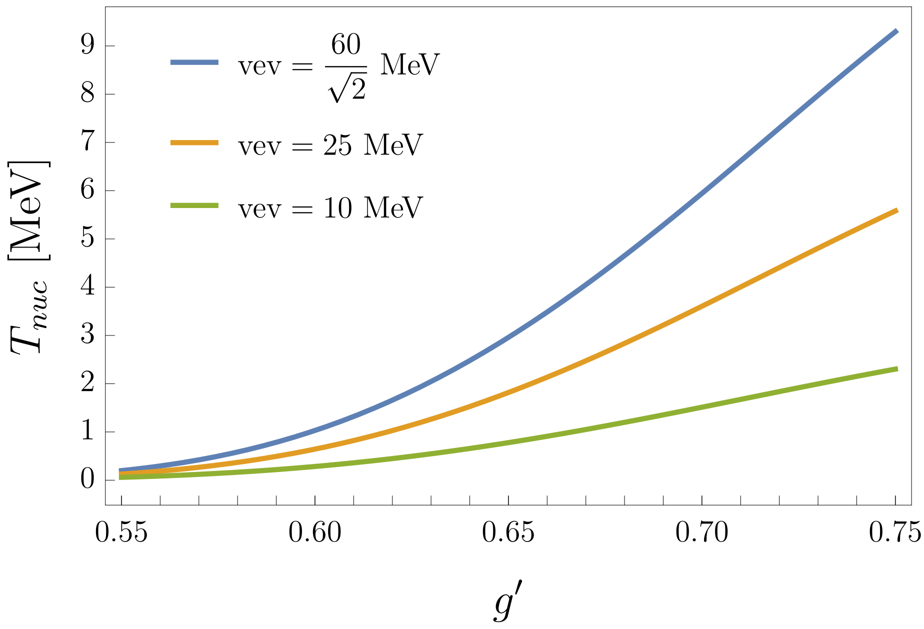

Figure 3.14: Nucleation temperature $T_{\rm nuc}$, as a function of the gauge coupling g' for benchmark values of the VEV.

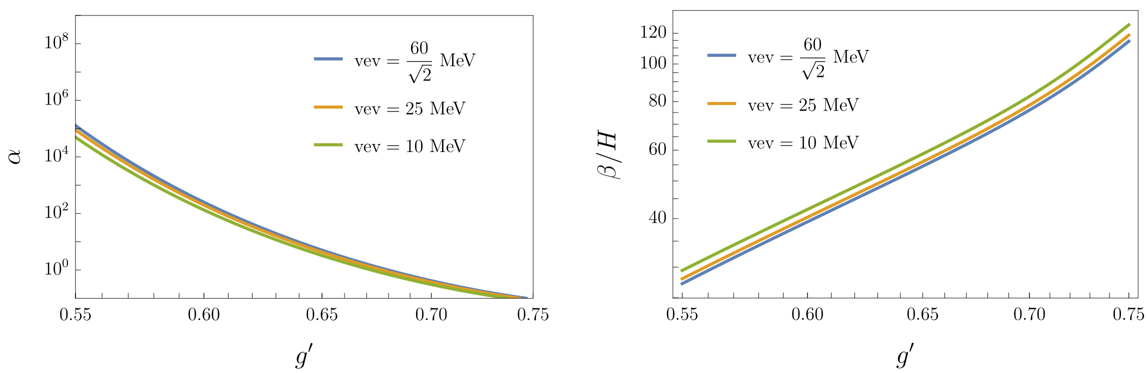

Figure 3.15: PT strength α (left) and inverse duration β/H (right) as a function of the gauge coupling g' for benchmark values of the VEV.

3.3.3 Constraints on the parameter space

Limits from the Mass-Radius relation of Neutron Stars

It has been observed that a single new state that carries baryon number, χ, and has a mass m_χ that is close to the one of the neutron can alter the Equation of State (EoS) of NSs [381]. For a given EoS, one can solve numerically the Tolman-Oppenheimer-Volkoff (TOV) equations of general relativistic hydrostatic structure to obtain the mass-radius curves of

NS. In the simplest scenario where the dark baryon is not charged under any new force, the solutions of the TOV equation tell us that the maximum NS mass attained as a function of its radius falls below the largest observed masses, $2M_\odot$. One way to solve this problem is to assume that χ is charged under a $\mathrm{U}(1)'$ symmetry. In this way, χ particles have repulsive self-interactions and if the gauge boson mediating the interaction is massive, the pressure inside the NS would reduce since the range of interaction becomes $m_{A'}^{-1}$.
In [375], following the work of [381], it was first presented the computation of the maximum values of $m_{A'}$ that allow the existence of a $2M_\odot$ NS. The key points of their are study are:

- The state χ is treated as a degenerate Fermi gas with self-interactions and its energy density and pressure will be added to those of the nuclear matter to find the modified EoS
- Specify the equation of state. Consider a polytropic EoS of the form

$$E_n(x) = ax^\alpha + bx^\beta \tag{3.138}$$

  where we have defined the dimensionless nuclear density $x = n_n/n_0$, where $n_0 = 0.16\,\mathrm{fm}^{-3}$. Eq. (3.138) has been fit to the results of Quantum Monte Carlo calculations incorporating realistic 3-nucleon forces. The authors considered different choices for the fitting parameters of EoS, taken from Ref. [382]. [3]

In the end, the authors find that

$$\frac{m_{A'}}{g'} \lesssim (45-60)\,\mathrm{MeV} \tag{3.141}$$

is needed to attain a maximum mass of the NSs compatible with the observed $2M_\odot$. The strength of these bounds depends on the form adopted for the EoS of the NSs. A recent study, following the same reasoning of Ref. [375], was presented in the review [383]. Considering the same microscopic model as in Ref. [375] and adopting a family of EoS based on the state of art N3LO Chiral Effective Field theory, the authors have obtained similar bounds, although slighly weaker ($m_{A'}/g' < 100$ MeV for a stiff EoS).

The constraints from NS internal heating were analyzed in more detail in a subsequent work [384] where the authors treated in more detail the dynamics and constituents of the

[3] Few more details on the EoS: An EoS that has higher pressure at given energy density is said to be *stiff*, and those with smaller pressure are typically called *soft*. There has been indication that the EoS of dense matter makes a transition from soft to stiff at super-nuclear density and the three neutron force ($3n$) is the key microscopic ingredient that determines the nature of this transition. In particular in the nuclear Hamiltonian:

$$\mathcal{H} = \mathcal{H}_{\mathrm{kin}} + V_{2n} + V_{3n} \tag{3.139}$$

where, in particular,

$$V_{3n} = V_{2\pi}^{PW} + V_{2\pi}^{SW} + V_{3\pi} + V_R \tag{3.140}$$

which represent respectively the long-range p wave and s wave interaction 2π exchange contributions, the intermediate-range (3π loops) contribution and the spin-dependent short-range repulsive term. Cline and Cornell considered in Ref. [375] the following terms/models for the $3n$ force:

1. $V_{3\pi} + V_R$, obtaining a *moderately stiff* EoS
2. Stiffer EoS: Urbana IX fit
3. $V_{2\pi}^{PW} + V_{\mu=150}^{R}$ (μ is a paramter in the repulsive potential) obtaining a soft EoS (does not reproduce the $2M_\odot$ NS)

NS core and their implications for neutron disappearance, and astronomical measurements. However, again these limits don't apply because the study only considers $\delta m \lesssim 2 \times 10^{-9}\,\mathrm{eV}$ (set by the age of Cas A), while we require for our parameter space $\delta m \sim \mathcal{O}(10^{-4})\,\mathrm{eV}$. In order to treat this region, a nontrivial density of χ should be considered.

3.3.4 Outlook

The results presented in this section provide a still preliminary but promising step towards establishing a connection between low-scale baryogenesis and the stochastic gravitational wave background (SGWB) recently detected by the PTAs. While our mechanism for baryogenesis follows closely the setup introduced in [63], we go beyond that work by embedding it into a concrete phase transition (PT) scenario from a classically scale-invariant potential: the VEV of the dark Higgs ϕ is not treated as a free parameter, but is instead bounded from both below and above by physical considerations. On the one hand, the reheating temperature following the supercooled PTs must be sufficiently high to avoid conflict with BBN, placing a lower bound on the VEV. On the other hand, neutron star stability imposes an upper bound on it. Remarkably, the region of parameter space compatible with the nanohertz SGWB reported by the PTAs lies within this window. This implies that the same dynamics responsible for generating the baryon asymmetry may also be responsible for the observed PTA signal.

Several directions remain open to improve the robustness and generality of our findings. A key refinement concerns the treatment of the effective potential and the bounce action. In this work, we followed the approach of [320, 275], where the renormalization scale is fixed to the VEV of the scalar field. While this prescription is appropriate in many scenarios, it becomes less accurate in the case of supercooled PTs, where the tunneling typically occurs at field values $\phi_* \ll$ VEV. A more reliable computation would require incorporating the full RG improvement of the effective potential (see [378, 379]), allowing both the couplings and the field to run with the scale. This would ensure better control over theoretical uncertainties and allow a more precise determination of the relevant PT parameters $(T_{\mathrm{RH}}, \alpha, \beta/H)$ for the computation of the GW signal.

Moreover, to fully assess the viability of the scenario, it is important to analyze cosmological constraints on supercooled PTs. In particular, for nucleation temperatures close to the MeV scale, modifications to the expansion history of the Universe and entropy injection from vacuum reheating can significantly impact BBN and CMB observables. This could lead to changes in the effective number of relativistic degrees of freedom N_{eff} [268, 385]. As shown in Fig. 3.14, our scenario allows for $T_{\mathrm{nuc}} \sim \mathcal{O}(\mathrm{MeV})$, motivating a dedicated study of the parameter space consistent with current and future bounds from BBN and CMB experiments.

Finally, another important future direction lies in exploring UV completions beyond those proposed in [63]. While we have extended their model by introducing a classically scale-invariant potential with Coleman-Weinberg symmetry breaking, alternative UV completions could give rise to similar baryogenesis mechanisms and GW signatures, possibly with different phenomenological implications. This may open up an even broader class of models where PTA observations serve as a novel window into the baryon generating dynamics of dark sectors.

Chapter 4

High-Energy Neutrinos as portals for BSM Physics

4.1 Signals from sub-GeV Dark Matter around Blazars

4.1.1 Introduction

Active galactic nuclei (AGN) are the most powerful steady luminous sources in the Universe, fueled by SMBHs in their center [202]. If they feature visible jets of relativistic particles and one of them is in close alignment with our line-of-sight (LOS) then AGN are called blazars [202, 201], see Sec. 2.1.2 for details on blazar astrophysics. Their properties are still not well understood and are the subject of active scrutiny, propelled by many observations of blazar photons and by the tentative detection by IceCube at the 3σ level of a ~ 290 TeV neutrino associated with the blazar TXS 0506+056 [184] in 2017, in association with a gamma-ray counterpart.

Given that extremely high-densities of DM are expected to accumulate into "spikes" around black holes [386], and that the nature of both DM and AGN jets is still elusive, it appears natural to inquire what such observations can teach us about the DM nature via AGN and viceversa. This direction has been pioneered in [387], which studied the DM effects on photons from AGNs. It has recently been revived in [166, 388], which proved that the DM fluxes upscattered by blazars' jets could induce measurable recoils on Earth, that lead to promising sensitivities on SM interactions of sub-GeV DM, a scenario known as blazar boosted DM (BBDM).

The main phenomenological motivation to focus on sub-GeV DM around blazars is that the energy of DM constituents within the MW halo is too low to induce nuclear recoils detectable with the leading "direct detection" experiments, if their mass $m_{\mathrm{DM}} \lesssim$ few GeV. The best sensitivities in that mass range then come either from new detection techniques of halo DM [389], or from searches with DM [163, 390] or neutrino experiments [165, 391] for the subpopulation of energetic DM that necessarily exist, e.g. DM upscattered by galactic cosmic rays (CR) [163, 164] or from atmospheric production [392]. While BBDM admittedly suffers from larger astrophysical uncertainties than the latter two mechanisms, it is well worth exploring because it could be the first one to lead to DM detection, and because it offers unique experimental opportunities thanks to its distinct temporal, spatial and energetic properties.

Furthermore, the same DM-nucleon interactions that are responsible for the BBDM signal could also induce inelastic DM-proton scatterings that break the proton apart, triggering hadronic cascades and neutrino emission. The computation and the phenomenological implications of such a neutrino flux produced upon DM-SM interactions in blazar jets will be the core of this section. Indeed, while existing models of blazar jets allow to explain their photon emission across a vast range of energies, they typically predict too few neutrinos to be possibly seen by existing telescopes, see e.g. [393] and Sec. 2.1.2. In particular, different models of TXS 0506+056 jets all predict [394, 208, 395, 207] a neutrino flux too low to satisfactorily explain IceCube's observations, strongly motivating our investigation of its possible DM origin.

It is also worth going beyond the investigation of single blazars and computing the diffuse neutrino flux from DM-proton scatterings in the jets of an ensemble of blazars. Indeed, as there is lack of consensus on the origin of the diffuse astrophysical neutrino flux measured by IceCube [220], it is tempting to generalize the same mechanism to a wider population of blazars and test whether DM-proton scatterings around these sources could be a viable explanation for the diffuse flux. This direction is additionally encouraged by existing and planned observations of high-energy blazar neutrinos and by their current understanding. To this purpose, we adopt the lepto-hadronic fit performed by [396] for a sample of 324 blazars as an input for our calculation of the diffuse astrophysical neutrino flux.

While our main proposals are that both IceCube measured neutrino fluxes from i) TXS 0506+056 and ii) the diffuse astrophysical neutrino flux originate from DM-proton scatterings in blazar jets, we also study the BBDM signal associated to the same interactions at neutrino detectors as a test of this hypothesis. Namely, we ask whether the absence of a measured BBDM signal is compatible with the proposed origin of the astrophysical neutrinos. To properly address this question, we must go beyond the simplistic assumption of a constant DM-nucleon cross section as done in the previous literature for DM around blazars [397, 388] and instead specify DM-quark interactions in concrete models. This is necessary not only for consistency, as no known DM interaction with an energy independent cross section can produce a detectable neutrino signal, but also for comparing BBDM searches to other DM signals, such as the neutrino flux discussed above.[1] Furthermore, the studies on BBDM have focused so far on single sources, whereas thousands of blazars are known and potentially many of them could contribute to a diffuse BBDM flux. Improving these studies by considering multiple sources is crucial, as searches involving a population of emitters are potentially more robust and statistically significant than those based on individual sources.

The present section is organized as follows:

- In Sec. 4.1.2 we review the properties of blazars and of DM clustering around them.
- In Sec. 4.1.3 we define the DM-quark interactions which are the object of our study and compute the relevant interaction cross sections, elastic and inelastic, including terms usually omitted in the literature but important in our context. We defer details on elastic and inelastic cross section respectively to App. A.1 and A.2.
- In Sec. 4.1.4 we compute the neutrino flux at Earth from inelastic DM-quark interactions for i) TXS 0506+056 and ii) a sample of 324 blazars.
- In Sec. 4.1.5 we show that the above DM interactions can explain Icecube neutrinos

[1] The necessity of each of these improvements in the study of BBDM has instead been demonstrated for DM interacting with electrons [388, 398, 399].

observed from i) and ii) compatibly with all existing laboratory constraints for the considered DM-quark interactions.

- In Sec. 4.1.6 we compute the BBDM fluxes at the Earth surface from i) and ii), taking into account the effect of the redshift on the BBDM flux at production.

- In Sec. 4.1.7 we compute BBDM signals from the same sources, at a variety of large neutrino detectors, including the impact of the Earth attenuation on the BBDM signal (for which we provide more details in App. A.3). We then derive limits and sensitivities on DM-nucleon interactions from the BBDM fluxes at present and future neutrino detectors (Super-K, KamLand, Borexino, Hyper-K, DUNE, JUNO).

- In Sec. 4.1.8 we compare them with a variety of other tests of the same DM dynamics, along with the DM origin of the high-energy neutrinos, both diffuse and from TXS 0506+056. Our main result is that, overall, the sub-GeV DM hypothesis for the origin of IceCube neutrinos remains consistent with BBDM searches at neutrino detectors. The reader can find further details on the depletion of the DM density around blazar via its self interactions and the DM-proton interactions considered in our work in Appendix B.

- In Sec. 4.1.9 we discuss in details the constraints on the DM-quark interactions that we analyzed, both model independent as from BBN and DD searches and model dependent as from collider experiments.

- Finally, in Sec. 4.1.10 we conclude and discuss other directions worth future exploration.

4.1.2 Blazars and and Dark Matter around them

Blazars and their jet

Although blazars are relatively rare, with more than 3500 identified to date (see, e.g., [400]), they dominate the γ-ray sky within the 50 MeV to 1 TeV energy range, comprising $\sim 56\%$ (up to $\lesssim 88\%$) of the fourth *Fermi*-LAT catalogue [401, 402]. Their electromagnetic activity is mainly non-thermal, with a spectral energy distribution (SED) of photons that covers the entire electromagnetic spectrum and exhibits two distinct peaks: one in the infrared/X-ray band and the other at γ-ray frequencies [202]. Understanding the origin of this broad and doubly-peaked SED requires detailed modelling of the blazar jet physics. Based on the spectral features in the optical frequencies, blazars are further subdivided into: Flat Spectrum Radio Quasars (FSRQs), which, besides the flat radio spectrum that gives them their name, exhibit strong and broad optical emission lines; and BL Lacs, the optical spectrum of which shows at most very weak lines, if present at all [205]. Some blazars are classified as "masquerading" BL Lacs, when their optical spectrum is of the FSQR-type but is hidden by the non-thermal jet emission [403] (the well-studied blazar TXS 0506+056 is an example of this kind [404]).

The main structures in blazar jet models are the so-called *blobs*: spherical regions of plasma which move at a bulk relativistic speed β_B along the jet axis. The accelerated charged particles that are confined within the blobs radiate non-thermally while propagating through magnetic fields and ambient radiation. A particularly compelling category of blazar jet models is that of the hybrid lepto-hadronic ones, according to which both electrons and protons are present in the blob with ultra-relativistic velocities, and the SED arises from a combination of leptonic and hadronic processes (see, e.g., [204] for a review). A distinctive prediction of this class of models is the production of neutrino fluxes from hadronic cascades initiated when protons collide with photons or other protons in the blazar environment. After IceCube's first $\gtrsim 3\sigma$ spatial association between multi-TeV neutrino events and a blazar, TXS 0506+056 [184, 211, 405], [2] an intense campaign to explain both the neutrino emissions and the electromagnetic activities of TXS 0506+056 with lepto-hadronic modelling has been carried out [394, 407, 208, 395, 207] (see also [408, 409, 410, 411, 412]), supporting the hypothesis that highly-accelerated protons are present in its jets. Other tentative associations of different neutrino events with other blazars, albeit with lower significance, have also been reported [413, 414, 415, 416, 417, 418, 406, 419, 420, 421] (see also [422, 423]) [3], and the same class of models has been applied to several other sources (as, e.g., in [396]), advancing the idea that the lepto-hadronic framework may constitute a comprehensive description of blazar jet emission.

Motivated by these studies and observations, we concentrate on lepto-hadronic models to describe the proton content in blazar jets. Specifically, we model the proton energy spectrum in blazar jets with a homogeneous and isotropic single power-law in the blob's frame:

$$\frac{d\Gamma'_p}{d\gamma'_p\, d\Omega'} = \frac{\kappa_p}{4\pi} \gamma'^{\,-\alpha_p}_p\, e^{-\gamma'_p/\gamma'_{\mathrm{max}_p}} \,. \tag{4.1}$$

Here, $d\Gamma'_p$ is the infinitesimal rate of particles ejected in the blobs along the direction $d\Omega'$ and with $\gamma'_p \equiv E'_p/m_p$ lying in the range $[\gamma'_p,\ \gamma'_p + d\gamma'_p]$, E'_p being the energy of the proton and $m_p = 0.938\,\mathrm{GeV}$ its mass; $\alpha_p \geq 0$ is the slope of the power-law; κ_p is an overall normalisation constant. We have also included an exponential cut-off at γ'_{max_p}. In the rest of this section, primed (unprimed) symbols denote non-invariant quantities computed in the blob's (observer's) rest frame. The spectrum in Eq. (4.1) is related to that in the observer's frame by a Lorentz transformation of boost factor $\Gamma_B \equiv (1-\beta_B^2)^{-1/2}$ along the jet axis, which gives [166, 388] (see also [387]):

$$\frac{d\Gamma_p}{d\gamma_p d\Omega} = \frac{\kappa_p}{4\pi}\, \gamma_p^{-\alpha_p}\, \frac{\beta_p(1-\beta_p\beta_B\mu)^{-\alpha_p}\Gamma_B^{-\alpha_p} e^{-\gamma_p/\gamma_{\mathrm{max}_p}}}{\sqrt{(1-\beta_p\beta_B\mu)^2 - (1-\beta_p^2)(1-\beta_B^2)}} \,, \tag{4.2}$$

where $\beta_p = [1 - 1/\gamma_p^2]^{1/2}$ is the proton's speed and μ is the cosine of the angle between its direction of motion and the jet axis.

In our analysis, we focus on the single source TXS 0506+056, as well as a sample of blazars in steady activity. For TXS 0506+056, we fix the parameters of the proton spectrum according to the lepto-hadronic model of [207] fitted to the observed SED during the six-month flaring activity of 2017. For the blazar sample, we consider the 324 blazars and their corresponding lepto-hadronic fit of their steady activity as presented in [396]. The relevant parameters that we use from the fits [207, 396] are the minimal and maximal Lorentz boost

[2] Two significant associations of neutrino signals and TXS 0506+056 have been reported: one single neutrino event in 2017 in coincidence with a six-month γ-ray flaring episode [184], and ~ 13 events in 2014/2015 [211]. The latter, however, were not accompanied by an enhanced electromagnetic activity of the same blazar [406].

[3] Also, the active galaxy NGC 1068 has shown evidence of neutrino emission at 4.2σ [424], but this object is not a blazar. Furthermore, the study [425] suggests a correlation at the level of 3.3σ of IceCube neutrinos with a catalogue composed of 110 known γ-ray emitters, of which TXS 0506+056 and NGC 1068 are two main contributors.

Lepto-Hadronic Model Parameters		
Parameter (units)	**TXS 0506+056 [207]**	**Blazars sample [396]**
z	0.337	$[0.04, 3.41]$
d_L (Mpc)	1765	$[171, 30.2\times10^3]$
$M_{\rm BH}(M_\odot)$	3×10^8	$[10^8, 10^9]$
R_S (pc)	3×10^{-5}	$[10^{-5}, 10^{-4}]$
Γ_B	24.2	$[3.4, 31.5]$
$\theta_{\rm LOS}(^\circ)$	2.37	$[1.81, 16.95]$
α_p	2	1
$\gamma'_{\min_p}$	1	100
$\gamma'_{\max_p}$	1.6×10^7	$[10^6, 3.1\times10^7]$
L_p (erg/s)	1.85×10^{50}	$[2.2\times10^{44}, 3.1\times10^{50}]$
$\kappa_p\,(\mathrm{s}^{-1}\mathrm{sr}^{-1})$	1.27×10^{49}	$[3.1\times10^{37}, 1.3\times10^{46}]$

Table 4.1: The relevant jet parameters from the single-zone lepto-hadronic fit [207] for the blazar TXS 0506+056 (during its 2017 flare) and the sample of blazars [396] (average steady flux) used in our calculations. Values in brackets denote the ranges for the sources in [396]. Also listed are the redshift z; the luminosity distance d_L, which we compute from z assuming a standard cosmological model and taking the value of the Hubble constant today as $H_0 = 70.2\,\mathrm{km\,s^{-1}\,Mpc^{-1}}$. The BH mass in solar mass units $M_\odot$, and the corresponding Schwarzschild radius R_S. The values of z and $M_{\rm BH}$ are taken from [426, 404] for TXS 0506+056 and [396] for the sample of blazars.

factors of the protons $\gamma'_{\min_p}$, $\gamma'_{\max_p}$; the blob Lorentz factor Γ_B; the LOS angle of the jet $\theta_{\rm LOS}$ assumed to be $\theta_{\rm LOS} = 1/\Gamma_B$; [4] the proton luminosity L_p, which is related to the normalisation constant κ_p via [388]

$$L_p = \kappa_p m_p \Gamma_B^2 \int_{\gamma'_{\min_p}}^{\gamma'_{\max_p}} dx\, x^{1-\alpha_p}\,. \tag{4.3}$$

We summarise in Table 4.1 the relevant jet parameters of TXS 0506+056 and of the sample of blazars [396], together with the redshift z, the luminosity distance $d_L \equiv (1+z)\,c\int_0^z dz'/H(z')$ (c being the speed of light, $H(z) = H_0\sqrt{\Omega_m(1+z)^3+\Omega_\Lambda}$ the Hubble expansion rate, H_0 its present value, Ω_m the matter density parameter and Ω_Λ the dark energy one), the BH mass $M_{\rm BH}$ and the corresponding Schwarzschild radius R_S.

Dark matter around blazars

DM is expected to form dense spikes in the vicinity of supermassive BHs, like those that power blazars. As demonstrated in [386], the adiabatic growth of BH at the centre of a spherical DM halo with a power-law density $\rho_{\rm DM}^{\rm halo}(r) = \mathcal{N} r^{-\gamma}$ reshapes the halo profile into

[4] In [207], the LOS angle was taken to be zero, given the assumed relation $\Gamma_B = \mathcal{D}/2$, where $\mathcal{D} \equiv [\Gamma_{\rm B}\,(1-\beta_{\rm B}\cos\theta_{\rm LOS})]^{-1}$ is the Doppler factor determined by the fit. Here, we prefer to consider a non-vanishing angle and use the condition $\Gamma_B = \mathcal{D}$, which implies $\theta_{\rm LOS} = 1/\Gamma_B$. Under this assumption, the proton luminosity given in [207] should be multiplied by a factor of 4 for consistency. However, for the sake of conservativeness, we refrain from applying this correction.

a steeper distribution

$$\rho_{\rm DM}^{\rm spike}(r) = \mathcal{N} R_{\rm sp}^{-\gamma} \left(\frac{R_{\rm sp}}{r}\right)^{\alpha(\gamma)}, \quad \text{with} \quad \alpha(\gamma) = \frac{9-2\gamma}{4-\gamma}, \tag{4.4}$$

where $\mathcal{N}$ is a normalisation constant, r the radial distance from the central BH, $\epsilon(\gamma) \approx 0.1$ for $0.5 \leq \gamma \leq 1.5$ [427], and $R_{\rm sp}$ the radial extension of the spike. The latter is given as a function of γ, the BH mass and the normalisation constant by [386]

$$R_{\rm sp} \simeq \epsilon(\gamma) \left(\frac{M_{\rm BH}}{\mathcal{N}}\right)^{1/(3-\gamma)}. \tag{4.5}$$

For the blazars under consideration, we model the total DM profile $\rho_{\rm DM}(r)$ as

$$\rho_{\rm DM}(r) = \mathcal{N} R_{\rm sp}^{-\gamma} \begin{cases} 0 & r \leq 2R_S\,; \\ g(r)(R_{\rm sp}/r)^{\alpha(\gamma)} & 2R_S \leq r < R_{\rm sp}\,; \\ (R_{\rm sp}/r)^{\gamma} & r \geq R_{\rm sp}\,; \end{cases} \tag{4.6}$$

where $g(r) = (1 - 2R_S/r)^{3/2}$ accounts for the inevitable capture of DM onto the BH after including relativistic effects [428]. In the analysis that follows, we fix $\gamma = 1$ for the initial DM profile, inspired by a Navarro-Frenk-White (NFW) distribution [429, 430], so that $\alpha(\gamma = 1) = 7/3$.

Due to the blazar jet emission outshining the dynamics of the host galaxy, information on the DM distribution around blazars is limited. Consequently, the normalization of the DM profile remains somewhat arbitrary. Following the same procedure as in [3], we fix $R_{\rm sp} = R_\star$, $R_\star \approx 10^6 R_S$ being the typical radius of influence of a BH on stars [431]. This normalisation, for $\gamma = 1$, results in

$$\mathcal{N} \simeq 10^{-6} M_\odot / R_S^2 \left(\frac{M_{\rm BH}}{10^8 M_\odot}\right). \tag{4.7}$$

As can be easily checked, the total DM mass contained within $R_{\rm sp}$ is $M_{\rm DM}^{\rm spike} \simeq 18.5\%\, M_{\rm BH}$. This means that our normalization does not interfere with typical BH mass estimates, which are performed within the sphere of BH influence [432, 433], at least up to corrections of order $\mathcal{O}(10\%)$ (the uncertainty in the BH mass estimate in these objects is in any case much larger). Furthermore, our normalisation is more conservative than that adopted in similar studies on DM around AGN [387, 166, 388, 434, 435, 398, 436, 437, 438].

All the information on the DM distribution that is relevant to our calculation ultimately reduces to the following parameter [166, 388] (see also [387]):

$$\Sigma_{\rm DM}(r) \equiv \int_{R_{\rm min}}^{r} \rho_{\rm DM}(r')dr', \tag{4.8}$$

where $R_{\rm min}$ is the minimal radial extension of the blazar jet. The above integral is quickly saturated by the spike contribution, which reads

$$\Sigma_{\rm DM}^{\rm spike} \equiv \Sigma_{\rm DM}(R_{\rm sp}) \simeq \frac{\epsilon(\gamma)^{3-\gamma}}{\alpha(\gamma)-1} \frac{M_{\rm BH}}{R_{\rm min}^2} \left(\frac{R_{\rm min}}{R_{\rm sp}}\right)^{3-\alpha(\gamma)}, \tag{4.9}$$

where we have used the DM profile in Eq. (4.6) without fixing γ, after inverting the relation in Eq. (4.4) to get $\mathcal{N}$, and integrated Eq. (4.8) up to $R_{\rm sp}$. For $\gamma = 1$ and $R_{\rm sp} = 10^6 R_S$, the above relation gives

$$\Sigma_{\rm DM}^{\rm spike} \simeq 3 \times 10^{-7} \frac{M_{\rm BH}}{R_S^2} \left(\frac{2R_S}{R_{\rm min}}\right)^{4/3} \simeq 1.28 \times 10^{31}\,{\rm GeV\,cm^{-2}} \left(\frac{3 \times 10^8 M_\odot}{M_{\rm BH}}\right) \left(\frac{2R_S}{R_{\rm min}}\right)^{4/3} . \tag{4.10}$$

Various effects can alter the formation and evolution of the DM spike. For instance, DM annihilations over the BH lifetime $t_{\rm BH}$ [386] flatten the DM profile at inner radii reducing the slope of the spike to ≤ 0.5 for $r < r_{\rm ann}$ [439], $r_{\rm ann}$ being defined by the condition $\rho_{\rm DM}(r_{\rm ann}) = \rho_{\rm core} \equiv m_{\rm DM}/(\langle\sigma_{\rm ann} v_{\rm rel}\rangle t_{\rm BH})$, which gives

$$r_{\rm ann} = R_{\rm sp} \left[\frac{M_{\rm BH}\epsilon(\gamma)^{3-\gamma}}{R_{\rm sp}^3 \rho_{\rm core}}\right]^{1/\alpha(\gamma)} \quad \text{for} \quad 2R_S \leq r_{\rm ann} \leq R_{\rm sp}, \tag{4.11}$$

and $\langle\sigma_{\rm ann} v_{\rm rel}\rangle$ is the DM averaged annihilation cross section times relative velocity. The DM profile including the effects of DM annihilation can be approximated as $\tilde{\rho}_{\rm DM}(r) \equiv \rho_{\rm DM}(r)\rho_{\rm core}/(\rho_{\rm DM}(r) + \rho_{\rm core})$ [386]. Other effects can influence the DM spike, such as merging of galaxies [440, 441] and the gravitational interaction of stars close to the BH [442, 443]. Sizeable uncertainties also reside in $R_{\rm min}$, the minimal radius of the jet, and they have a substantial impact on $\Sigma_{\rm DM}$. Therefore, to effectively account for all these astrophysical effects on the DM spike, instead of considering different scenarios of softenings or depletions, we find it more practical to adopt the density profile in Eq. (4.6) and consider different benchmark cases (BMCs) for $R_{\rm min}$. In particular, as in [3], we choose $R_{\rm min} = 10^2 R_S$ (BMCI) and $R_{\rm min} = 10^4 R_S$ (BMCII), based on results from blazar studies indicating where the jet is likely well-accelerated [396].

For the adopted density profile, $M_{\rm BH} = 3 \times 10^8\, M_\odot$ and $\gamma = 1$, we find

$$\Sigma_{\rm DM}^{\rm spike} \simeq \begin{array}{ll} 6.9 \times 10^{28}\,{\rm GeV\,cm^{-2}} & \text{for BMC I} \\ 1.5 \times 10^{26}\,{\rm GeV\,cm^{-2}} & \text{for BMC II} \end{array} \tag{4.12}$$

We note that taking $\langle\sigma_{\rm ann} v_{\rm rel}\rangle$ such that $r_{\rm ann} \leq R_{\rm min}$, and calculating the DM column density for $\tilde{\rho}_{\rm DM}(r)$, would practically lead to values of $\Sigma_{\rm DM}^{\rm spike}$ between the two BMCs considered. Imposing $r_{\rm ann} \leq R_{\rm min}$ gives

$$\begin{array}{ll} \langle\sigma_{\rm ann} v_{\rm rel}\rangle \lesssim \sigma_{\rm BMCI} \equiv 3.1 \times 10^{-31}\ {\rm cm^3\,s^{-1}}\,(m_{\rm DM}/{\rm GeV})(10^{10}\,{\rm yr}/t_{\rm BH}) & \text{for BMCI,} \\ \langle\sigma_{\rm ann} v_{\rm rel}\rangle \lesssim \sigma_{\rm BMCII} \equiv 1.4 \times 10^{-26}\ {\rm cm^3\,s^{-1}}\,(m_{\rm DM}/{\rm GeV})(10^{10}\,{\rm yr}/t_{\rm BH}) & \text{for BMCII.} \end{array} \tag{4.13}$$

Then, values of $\langle\sigma_{\rm ann} v_{\rm rel}\rangle \lesssim \sigma_{\rm BMCI}$ would yield DM column density consistent with the BMCs considered. Intermediate values $\sigma_{\rm BMCI} \lesssim \langle\sigma_{\rm ann} v_{\rm rel}\rangle \lesssim \sigma_{\rm BMCII}$ would correspond to situations between BMCI and BMCII. Larger values $\langle\sigma_{\rm ann} v_{\rm rel}\rangle \gtrsim \sigma_{\rm BMCII}$ would lead to DM column densities smaller than that of our BMCII. However, values of $\langle\sigma_{\rm ann} v_{\rm rel}\rangle$ larger than about 10^{-28} cm^3/s, for sub-GeV DM, are very hard to realise because of stringent indirect detection constraints, see, e.g., Sec. 6.13 of [115] for a recent summary. Our BMCII can then be considered as very conservative with respect to possible DM annihilations. To clarify this discussion, we depict in Fig. 4.1 the DM profile (green curves) adopted in our analysis (thick solid), as well as the core plus spike profile in case $r_{\rm ann} = R_{\rm min}$ (thin dashed). In the same plot, we show the corresponding DM column density for BMCI and BMCII.

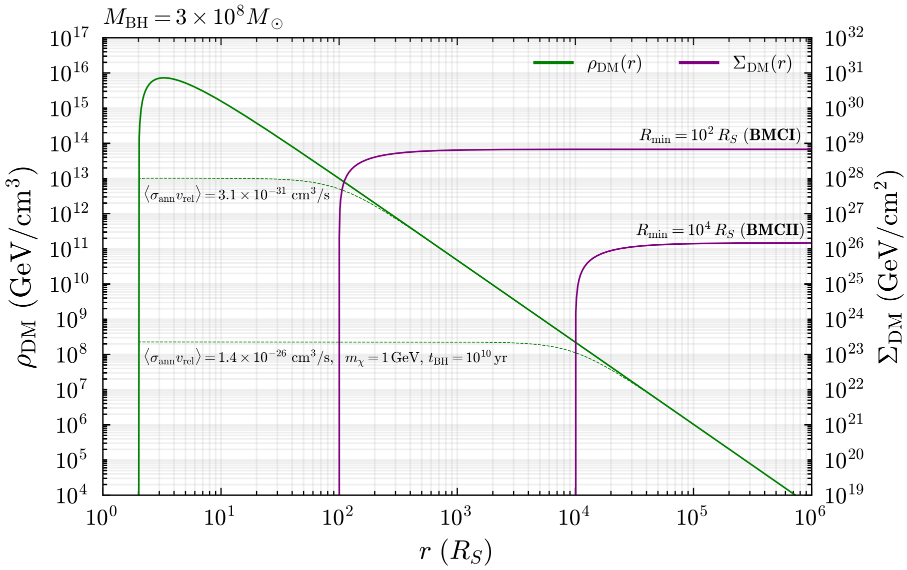

Figure 4.1: The DM density profile $\rho_{\rm DM}(r)$ (solid green, left axis) and its column density $\Sigma_{\rm DM}(r)$ (solid purple, right axis) for BH mass $M_{\rm BH} = 3 \times 10^8 M_\odot$. The DM column density is plotted for the two BMCs: $R_{\rm min} = 10^2 R_S$ (BMCI, upper curve) and $R_{\rm min} = 10^4 R_S$ (BMCII, lower curve). We also plot the DM profile $\tilde{\rho}_{\rm DM}(r)$ (green dashed) which includes DM annihilations for the maximal values of $\langle\sigma_{\rm ann} v_{\rm rel}\rangle$ which yield $\Sigma_{\rm DM}$ consistent with BMCI and BMCII, taking the BH lifetime $t_{\rm BH} = 10^{10}$ yr and DM mass $m_{\rm DM} = 1$ GeV.

4.1.3 Dark Matter-nucleon interactions

We consider a DM particle consisting, for definiteness, of a Dirac fermion χ with mass $m_{\rm DM}$. Modelling the DM-nucleon interactions with a constant cross section would be inconsistent for our purposes, which involve processes (upscatterings in blazar-jets, scatterings on nuclei on Earth) that happen in a range of energies that spans orders of magnitude. We are not aware of any particle DM model, within reach of the searches object of this work, that results in a cross section with the same value over that range of energies. We therefore model the DM-nucleon interactions by specifying their mediator, in particular we consider vector, scalar, axial and pseudoscalar mediators. We report the associated Lagrangians for DM-quark interactions below. They induce non-relativistic DM-nucleon interactions of different kinds, relevant for experiments looking for the halo DM components. Our toy-models thus allow to explore the complementarity of those “standard” DM searches with the ones proposed here. To make this manifest, we report below also the nonrelativistic operator induced by each mediator.

- **Scalar mediator**: DM-quark interactions are mediated by a scalar ϕ with mass m_ϕ as

$$\mathcal{L}_{\chi q\phi} = g_{\chi\phi}\bar{\chi}\chi\phi + g_{q\phi}\bar{q}q\phi \quad \to \quad \mathcal{O}_{\chi N\phi} = \mathbb{1}\,, \quad \text{(SI)} \tag{4.14}$$

  where q runs over light quarks and $\mathcal{O}_{\chi N\phi}$ is the spin-independent (SI) DM interaction with nucleons N induced by $\mathcal{L}_{\chi q\phi}$.

- **Vector mediator**: DM-quark interactions are mediated by a vector V with mass m_V as
$$\mathcal{L}_{\chi qV} = g_{\chi V}\bar{\chi}\gamma^{\mu}\chi V_{\mu} + g_{qV}\bar{q}\gamma^{\mu}qV_{\mu} \quad \rightarrow \quad \mathcal{O}_{\chi NV} = \mathbb{1}\,, \quad \text{(SI)} \tag{4.15}$$
where q runs over light quarks and $\mathcal{O}_{\chi NV}$ is the spin-independent DM interaction with nucleons induced by $\mathcal{L}_{\chi qV}$.

- **Axial mediator**: We consider the interaction with an axial mediator V' with mass $m_{V'}$ as follows
$$\mathcal{L}_{\chi qV'} = g_{\chi V'}\bar{\chi}\gamma^{\mu}\gamma_5\chi V'_{\mu} + g_{qV'}\bar{q}\gamma^{\mu}\gamma_5 qV'_{\mu} \quad \rightarrow \quad \mathcal{O}_{\chi NV'} = \vec{S}_{\chi}\cdot\vec{S}_N\,, \quad \text{(SD)} \tag{4.16}$$
where q runs over light quarks, $\vec{S}_{\chi}$ and $\vec{S}_N$ denote the DM and nucleon spin respectively, and $\mathcal{O}_{\chi NV'}$ is the spin-dependent (SD) DM interaction with nucleons induced by $\mathcal{L}_{\chi qV'}$.

- **Pseudoscalar (ALP) mediator**: DM-quark interactions are mediated by a pseudoscalar a with mass m_a (i.e. an axion-like particle, or ALP) as
$$\mathcal{L}_{\chi qa} = ig_{\chi a}\bar{\chi}\gamma_5\chi a + ig_{qa}\bar{q}\gamma_5 qa, \quad \rightarrow \quad \mathcal{O}_{\chi Na} = \left(\vec{S}_{\chi}\cdot\frac{\vec{Q}}{m_N}\right)\left(\vec{S}_N\cdot\frac{\vec{Q}}{m_N}\right), \quad \text{(SMD)} \tag{4.17}$$
where q runs over light quarks, $\mathcal{O}_{\chi Na}$ is the spin- and momentum-dependent (SMD) DM-nucleon interaction induced by $\mathcal{L}_{\chi qa}$, and $\vec{Q}$ is the 3-momentum transfer.

The DM-quark interactions above do not respect the electroweak (EW) symmetry and so are valid below its breaking scale. We will briefly comment on possible EW-invariant UV completions in Sec. 4.1.9, together with the constraints that they induce on the couplings $g_{\chi Y}$ and g_{qY} of Eqs. (4.14-4.17), where Y is the mediator under consideration.

In order to ease the comparison of our results with the literature, it is convenient to recast them in terms of the non-relativistic spin-independent (σ^N_{SI}) and spin-dependent (σ^N_{SD}) DM–nucleon scattering cross sections, $N = p, n$. These are obtained by integrating out the mediator Y from $\mathcal{L}_{\chi qY}$ and by computing the cross sections in the limit of vanishing momentum transfer and $s \rightarrow (m_{\mathrm{DM}} + m_N)^2$, being s the centre-of-mass energy squared. For $Y = \phi, V$ ($\sigma^{\mathrm{NR}}_{Y\chi N} = \sigma^N_{\mathrm{SI}}$) and $Y = V'$ ($\sigma^{\mathrm{NR}}_{Y\chi N} = \sigma^N_{\mathrm{SD}}$), with DM spin $s_\chi = 1/2$, one obtains
$$\sigma^{\mathrm{NR}}_{Y\chi N} = \frac{g^2_{\chi Y}g^2_{NY}}{\pi}\frac{\mu^2_{\chi N}}{m^4_Y}\,, \quad Y = \phi, V, V'\,, \tag{4.18}$$
where $\mu_{\chi N}$ is the DM-nucleon reduced mass and g_{NY} the DM-nucleon coupling, which we derive for each model in Appendix A.1. For $Y = a$ instead, the tree-level SMD contribution to the non-relativistic cross section is suppressed by the exchanged momentum, as shown by $\mathcal{O}_{\chi Na}$ in Eq.(4.17). In this pseudoscalar-mediated model a spin-independent cross section σ^N_{SI} is generated at higher orders, by box diagrams with a's running in the loop, whose contributions have been computed in [444]. This one-loop SI cross section dominates over the tree-level SMD one in determining the direct detection signals of halo DM, which are anyway considerably weaker than those induced by the other mediators.

The neutrino and BBDM signals object of this work require relativistic DM-quark interactions. To understand their interplay with the standard searches for non-relativistic halo DM, it is necessary to perform one extra step down the ladder of effective theories, and determine the DM scatterings with nuclei induced by the relativistic interactions of Eqs. (4.14-4.17). For the SI case, DM couples coherently to all the nucleons inside a given nucleus, and the DM-nucleus cross section is enhanced as

$$\sigma_{\rm SI}^A = A^2 \frac{\mu_{\chi A}^2}{\mu_{\chi N}^2} \sigma_{\rm SI}\,, \quad \text{where} \quad \sigma_{\rm SI} = \frac{\mu_{\chi N}^2}{\pi A^2}\left[Z\frac{g_{\chi Y} g_{pY}}{m_Y^2} + (A-Z)\frac{g_{\chi Y} g_{nY}}{m_Y^2}\right]^2\,, \quad Y = \phi, V\,, \tag{4.19}$$

being $Z(A)$ the atomic (mass) number of the target nucleus. For the pseudoscalar mediator a, $\sigma_{\rm SI}^A$ is given by the same expression of Eq. (4.19), where instead $\sigma_{\rm SI}$ is given by a loop-suppressed contribution [444]. Finally, the SD scattering is not coherently enhanced,

$$\sigma_{\rm SD}^A = S(0) \frac{\mu_{\chi A}^2}{\mu_{\chi N}^2} \sigma_{\rm SD}\,, \quad \text{where} \quad \sigma_{\rm SD} = \frac{g_{\chi V'}^2 g_{NV'}^2}{\pi} \frac{\mu_{\chi N}^2}{m_{V'}^4}\,, \tag{4.20}$$

i.e. $\sigma_{\rm SD} = \sigma_{Y\chi N}^{\rm NR}$ of Eq. (4.18) for the axial mediator $Y = V'$, and where $S(0)$ is a combination of nuclear response functions in the limit of vanishing momentum transfer, which is not A^2-enhanced and depends on the magnitude of the spin of the nucleus and on the spatial distribution of the individual nucleons, and can be found e.g. in [115].

Elastic scattering

We now move beyond the fully non-relativistic limit and present cross sections that include the dependence on $Q^2 \neq 0$. For sufficiently small momentum transfer, the collision of a proton p and a DM particle can be regarded as elastic. We define the 4-momentum of the incoming proton in the DM rest frame as $p_p = (E_p, \vec{p}_p)$ while for the DM particle $p_\chi = (m_{\rm DM}, \vec{0})$. Concerning the final states, we denote the 4-momenta of the scattered DM particle and the outgoing proton, respectively, as $k_p = (E_p, \vec{k}_p)$ and $k_\chi = (E'_\chi, \vec{k}_\chi)$. The Feynman diagram for the process is sketched below using the package Ti*k*Z-Feynamn [445]

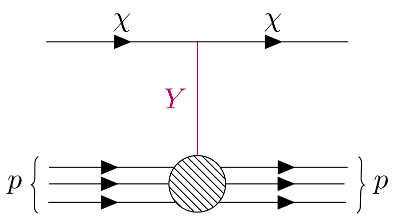

where $Y = \phi$, a, V, V' denotes either the scalar, pseudoscalar, vector or axial mediator. For the $2 \to 2$ elastic scattering under consideration, the differential cross section can be computed as $d\sigma_{Y\chi p}^{\rm EL}/d\mu_s^* = |\overline{\mathcal{M}_{Y\chi p}}|^2/(32\pi s)$, with $-1 \leq \mu_s^* \leq 1$ being the cosine of the scattering angle of emission in the center-of-mass rest frame, $s = (p_\chi + p_p)^2$ and $|\overline{\mathcal{M}_{Y\chi p}}|^2$ the squared matrix element averaged over the initial spins and summed over the final spins. The momentum transfer squared in the rest frame of χ reads $Q^2 = -(p_\chi - k_\chi)^2 = 2m_{\rm DM}T_\chi$, with $T_\chi \equiv E_\chi - m_{\rm DM}$ the kinetic energy of the outgoing χ. The latter is given as a function of μ_s^* by

$$T_\chi(\mu_s^*) = T_\chi^{\rm max}(T_p)\frac{1+\mu_s^*}{2} \quad \text{with} \quad T_\chi^{\rm max}(T_p) = \frac{2m_{\rm DM}T_p\,(T_p + 2m_p)}{2m_{\rm DM}T_p + (m_p + m_{\rm DM})^2}\,, \tag{4.21}$$

where $T_p = E_p - m_p$ is the kinetic energy of the incoming proton. Consider now the following "trick":

$$\frac{d\sigma^{\rm EL}_{Y\chi p}}{dT_\chi} = \int d\mu_s \frac{d\sigma^{\rm EL}_{Y\chi p}}{dT_\chi d\mu_s} = \int d\mu_s \frac{d\sigma^{\rm EL}_{Y\chi p}}{d\mu_s}\delta(T_\chi - T_\chi(\mu_s^*)) = 2\int d\mu_s \frac{d\sigma^{\rm EL}_{Y\chi p}}{d\mu_s^*}\frac{\delta(\mu_s - \mu_s^{\rm EL}(T_p, T_\chi))}{T_\chi^{\rm max}(T_p)}, \tag{4.22}$$

with

$$\mu_s^{\rm EL}(T_p, T_\chi) \equiv \frac{(T_p + m_p + m_{\rm DM})T_\chi}{\sqrt{(T_p^2 + 2m_pT_p)(T_\chi^2 + 2m_{\rm DM}T_\chi)}}\,. \tag{4.23}$$

From the relation in Eq. (4.22) we obtain

$$\frac{d\sigma^{\rm EL}_{Y\chi p}}{dT_\chi d\mu_s} = \frac{|\overline{\mathcal{M}_{Y\chi p}}|^2}{16\pi s}\frac{\delta(\mu_s - \mu_s^{\rm EL}(T_p, T_\chi))}{T_\chi^{\rm max}(T_p)}\,. \tag{4.24}$$

By computing the averaged Feynman amplitude squared $|\overline{\mathcal{M}_{Y\chi p}}|^2$ we obtain the following differential elastic cross sections for $Y = \phi, a, V, V'$:

$$\frac{d\sigma^{\rm EL}_{\phi\chi p}}{dT_\chi d\mu_s} = \frac{\sigma^{\rm NR}_{\phi\chi p}}{s}\frac{m_\phi^4}{16\mu_{\chi p}^2}\frac{(4m_{\rm DM^2} + Q^2)(4m_p^2 + Q^2)}{(m_\phi^2 + Q^2)^2}G_S^2(Q^2)\frac{\delta(\mu_s - \mu_s^{\rm EL}(T_p, T_\chi))}{T_\chi^{\rm max}(T_p)}, \tag{4.25}$$

$$\frac{d\sigma^{\rm EL}_{a\chi p}}{dT_\chi d\mu_s} = \frac{g_{\chi a}^2 g_{pa}^2}{16\pi s}\frac{(Q^2)^2}{(m_a^2 + Q^2)^2}\widehat{G}^2_{5,\,p}(Q^2)\frac{\delta(\mu_s - \mu_s^{\rm EL}(T_p, T_\chi))}{T_\chi^{\rm max}(T_p)}, \tag{4.26}$$

$$\frac{d\sigma^{\rm EL}_{V\chi p}}{dT_\chi d\mu_s} = \frac{\sigma^{\rm NR}_{V\chi p}}{s}\frac{m_p^4}{4\mu_{\chi p}^2}\left[A^{V,p}(Q^2) + \frac{(s-u)^2}{m_p^4}C^{V,p}(Q^2) + \frac{m_{\rm DM^2}}{m_p^2}D^{V,p}(Q^2)\right]\frac{\delta(\mu_s - \mu_s^{\rm EL}(T_p, T_\chi))}{T_\chi^{\rm max}(T_p)(1 + Q^2/m_V^2)^2}, \tag{4.27}$$

$$\frac{d\sigma^{\rm EL}_{V'\chi p}}{dT_\chi d\mu_s} = \frac{\sigma^{\rm NR}_{V'\chi p}}{s}\frac{m_p^4}{4\mu_{\chi p}^2}\left[A^{V',p}(Q^2) + \frac{(s-u)^2}{m_p^4}C^{V',p}(Q^2) + \frac{m_{\rm DM^2}}{m_p^2}D^{V',p}(Q^2)\right]\frac{\delta(\mu_s - \mu_s^{\rm EL}(T_p, T_\chi))}{T_\chi^{\rm max}(T_p)(1 + Q^2/m_{V'}^2)^2}, \tag{4.28}$$

where the functions $G_S, \widehat{G}_{5,\,p}, A^{V,p}, C^{V,p}, D^{V,p}$, $A^{V',p}$, $C^{V',p}$ and $D^{V',p}$ are nuclear form factors for the proton. Details on the derivation and on the expressions of the form factors are given in Appendix A.1.

Inelastic scattering

When the momentum transfer becomes of $\mathcal{O}(\text{GeV}^2)$, the contribution of the *deep inelastic scattering* (DIS) starts to be relevant. The process is represented diagrammatically below [445]

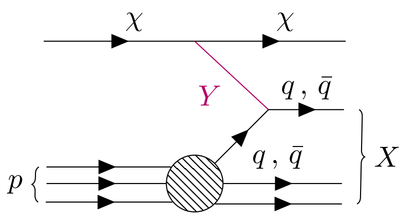

where Y denotes the mediator, p the initial proton, $q\,(\bar{q})$ the (anti)quark participating the scattering, and X the outgoing hadronic state. We fix the momenta of the initial DM and proton respectively as $p_\chi = (E_\chi, \vec{p}_\chi)$ and $p_p = (E_p, \vec{p}_p)$, with $k_\chi = (E'_\chi, \vec{k}_\chi)$ and $k_q = (E'_q, \vec{k}_q)$ that of the outgoing DM and scattered quark momenta. We further denote the squared centre-of-mass energy and momentum transfer respectively as $s = (p_p + p_\chi)^2$ and $Q^2 = (p_\chi - k_\chi)^2$. The differential DIS cross section for DM-proton scattering can be expressed as (see Appendix A.2 for details):

$$\frac{d\sigma^{\rm DIS}_{Y\chi p}}{dxdy} = \frac{y}{16\pi}\frac{Q^2 \sum_{\kappa=q,\bar{q}} f^p_\kappa(x,\, Q^2)|\overline{\mathcal{M}^{\rm quark}_{Y\chi}}|^2}{(Q^2)^2 - 4m_p^2 m_{\rm DM^2} x^2 y^2}\,, \tag{4.29}$$

being $f^p_{q(\bar{q})}$ the parton distribution functions (PDFs) for the (anti)quark in the proton, $\overline{\mathcal{M}^{\rm quark}_{Y\chi}}$ is the spin-averaged Feynman amplitude at the quark level, $y \equiv p_p \cdot q/(p_p \cdot p_\chi)$ the *inelasticity* parameter and $x \equiv Q^2/(2p_p \cdot q) = Q^2/[(s - m_p^2 - m_{\rm DM^2})\, y]$ the *Bjorken scaling variable.* After expanding the matrix element for the various toy models considered, we obtain the following final expressions for the DIS differential cross section:

$$\frac{d\sigma^{\rm DIS}_{\phi\chi p}}{dxdy} = \frac{\sigma^{\rm NR}_{\phi\chi p}}{16\mu^2_{\chi p} g^2_{p\phi}} \frac{(Q^2)^2(Q^2 + 4m_{\rm DM^2})\, y \sum_{\kappa=q,\bar{q}} g^2_{\kappa\phi} f^p_\kappa(x, Q^2)}{[(Q^2)^2 - 4m_N^2 m_{\rm DM}^2 x^2 y^2](1 + Q^2/m_\phi^2)^2}\,, \tag{4.30}$$

$$\frac{d\sigma^{\rm DIS}_{a\chi p}}{dxdy} = \frac{g^2_{\chi a}}{16\pi m_a^4} \frac{(Q^2)^3 y \sum_{\kappa=q,\bar{q}} g^2_{\kappa a} f^p_\kappa(x, Q^2)}{[(Q^2)^2 - 4m_N^2 m_{\rm DM}^2 x^2 y^2](1 + Q^2/m_a^2)^2}\,, \tag{4.31}$$

$$\frac{d\sigma^{\rm DIS}_{V\chi p}}{dxdy} = \frac{\sigma^{\rm NR}_{V\chi p}}{8\mu^2_{\chi p} g^2_{pV}} \frac{(Q^2)^3 y \sum_{\kappa=q,\bar{q}} g^2_{\kappa V} f^p_\kappa(x, Q^2)}{[(Q^2)^2 - 4m_N^2 m_{\rm DM^2} x^2 y^2](1 + Q^2/m_V^2)^2} \left(1 + \frac{2}{y^2} - \frac{2}{y} - \frac{2m_p^2 x^2}{Q^2}\right). \tag{4.32}$$

The DIS cross section in the case of an axial mediator, $\sigma^{\rm DIS}_{V'}$, coincides with $\sigma^{\rm DIS}_{V}$ provided that the formal substitutions $g_{\chi V} \to g_{\chi V'}$, $g_{pV} \to g_{pV'}$, $\sigma^{\rm NR}_{V\chi p} \to \sigma^{\rm NR}_{V'\chi p}$, $g_{\kappa V} \to g_{\kappa V'}$, $\kappa = q, \bar{q}$, and $m_V \to m_{V'}$ are made. To align the notation with the elastic case, we perform the change of variables $(x, y) \to (T_\chi, \mu_s)$, which yields

$$\frac{d\sigma^{\rm DIS}_{Y\chi p}}{dT_\chi d\mu_s} = \frac{\sqrt{(T_p^2 + 2m_pT_p)(T_\chi^2 + 2m_{\rm DM}T_\chi)}}{\sqrt{(T_p^2 + 2m_pT_p)(T_\chi^2 + 2m_{\rm DM}T_\chi)}\,\mu_s - T_\chi(T_p + m_p)} \frac{1}{T_p + m_p} \frac{d\sigma^{\rm DIS}_{Y\chi p}}{dxdy}\,, \tag{4.33}$$

where the DIS quantities can be written in terms of the new variables as

$$x = \frac{T_\chi m_{\rm DM}}{\sqrt{(T_p^2 + 2m_pT_p)(T_\chi^2 + 2m_{\rm DM}T_\chi)}\,\mu_s - T_\chi(T_p + m_p)}\,, \tag{4.34}$$

$$y = \frac{\sqrt{(T_p^2 + 2m_pT_p)(T_\chi^2 + 2m_{\rm DM}T_\chi)}}{m_{\rm DM}(T_p + m_p)}\,\mu_s - \frac{T_\chi}{m_{\rm DM}}. \tag{4.35}$$

4.1.4 Neutrino flux from DM-proton scatterings

If DM interacts with hadrons, protons in the relativistic jets of a blazar can collide with the DM particles along their way. These collisions have a centre-of-mass energy $\sqrt{s} \sim \sqrt{2m_{\rm DM}m_p\gamma_p}$, which can be much larger than a GeV, depending on $m_{\rm DM}$. At these energies, the DM-proton scattering is dominated by the inelastic contribution. When protons scatter inelastically with DM, they disintegrate and generate hadronic showers, with subsequent production of several final-state neutrinos from meson and secondary lepton decays.

The single-flavour neutrino flux exiting the blazar as a result of DM-proton DIS can be computed as [3]

$$\frac{d\Phi_\nu}{d\bar{E}_\nu} \simeq \frac{1}{3}\frac{\Sigma_{\rm DM}^{\rm spike}}{m_{\rm DM} d_L^2} \int_{\gamma_p^{\rm min}(\bar{E}_\nu, m_{\rm DM})}^{\gamma_{\max_p}} d\gamma_p\, \sigma_{Y\chi p}^{\rm DIS} \left.\frac{d\Gamma_p}{d\gamma_p d\Omega}\right|_{\theta_{\rm LOS}} \left\langle \frac{dN_\nu}{d\bar{E}_\nu} \right\rangle , \tag{4.36}$$

where $\gamma_p^{\rm min}(\bar{E}_\nu, m_{\rm DM})$ is the minimum proton boost factor necessary to produce a neutrino of energy $\bar{E}_\nu$, $\gamma_{\max_p}$ is the maximal boost factor of the protons in the observer's frame of reference, related to the same quantity in the blob's frame of reference reported in Table 4.1, $\gamma'_{\max_p}$, via a Lorentz boost $\gamma_{\max_p} = \Gamma_{\rm B}\gamma'_{\max_p}$, $\sigma_{Y\chi p}^{\rm DIS}$ is the integrated DM-proton DIS cross section, for mediator $Y = \phi$, a, V, V', and the overall $1/3$ factor accounts for neutrino oscillations over astronomical distances. The quantity $dN_\nu/d\bar{E}_\nu$ is the total (i.e. summed over flavours) number of neutrinos per unit of energy produced by each DM-proton DIS, and $\langle\cdot\rangle$ denotes the average over all possible scatterings with the quarks inside the proton, each weighted by its respective differential cross section. The averaged number of neutrinos is formally defined as

$$\left\langle \frac{dN_\nu}{d\bar{E}_\nu} \right\rangle = \frac{1}{\sigma_{Y\chi p}^{\rm DIS}} \int_{x_{\rm min}}^{1} dx \int_{Q^2_{\rm min}}^{x\cdot s} dQ^2\, \frac{d^2\sigma_{Y\chi p}^{\rm DIS}}{dQ^2 dx}\, \frac{dN_\nu}{d\bar{E}_\nu} , \tag{4.37}$$

and depends on γ_p, $\bar{E}_\nu$ and $m_{\rm DM}$ (the masses of the neutrinos can be safely ignored).

We do not compute the integral above analytically but rather we implement each Lagrangian of the considered toy models in FeynRules [446], simulate the quark-level scattering process $\chi + p \to \chi +$jet via Madgraph5 [447], as well as the hadronisation and showering of the outgoing quarks with Pythia8 [448]. We set all of Madgraph5's kinematic cuts to zero, as we are interested in all events that produce neutrinos, regardless of their kinematics. Finally, we select the outgoing neutrinos and bin them in energy.

For our computation we used the "CT10" [449] PDFs set, which extends down to $x_{\rm min}^{\rm pdf} = 10^{-8}$. The extrema of integration are set by Madgraph5's aforementioned $Q^2_{\rm min}$, and by kinematics, as the parton-level centre-of-mass energy squared $\hat{s} = x\cdot s$ must satisfy $\hat{s} \geq Q^2_{\rm min}$ for the scattering to be kinematically allowed, thus setting a lower extremum on x, $x_{\rm min}^{\rm kin}$. In order to perform the computation, the PDFs must be well defined, hence the overall extremum is $x_{\rm min} \equiv \max\{x_{\rm min}^{\rm kin}, x_{\rm min}^{\rm pdf}\}$.

We perform the parton-level simulation and subsequent hadronization and decay in the $\chi - p$ centre-of-mass frame, as opposed to the observer's one, thus the following Lorentz boost is needed to go back and forth between the two:

$$\gamma_{\rm COM} = \frac{m_{\rm DM} + E_p}{\sqrt{s}} . \tag{4.38}$$

Let us now define $\hat{z}$ as the proton direction. Given a final state neutrino ν, the $\hat{z}$-component of its momentum, energy and angle with respect to $\hat{z}$ transform as

$$\begin{aligned} p_{\nu,z} &= \gamma_{\rm COM}(p^*_{\nu,z} + \beta\bar{E}^*_\nu), \\ \bar{E}_\nu &= \gamma_{\rm COM}(\bar{E}^*_\nu + \beta p^*_{\nu,z}), \\ \cos\theta &= \frac{p_{\nu,z}}{\sqrt{{p^*_\perp}^2 + p^2_{\nu,z}}}, \end{aligned} \tag{4.39}$$

where (un)starred quantities refer to the centre-of-mass (observer) frame, $\beta = \sqrt{1 - 1/\gamma_{\rm COM}^2}$, $p_\perp^*$ is the component of the neutrino's 3-momentum in the plane perpendicular to the $\hat{z}$ axis. Given the large value of $\gamma_{\rm COM}$, $p_{\nu,z}$ will in general be very large with respect to the transversal components of the momentum, thus $\cos\theta$ will be very close to 1, i.e. for sufficiently high proton energy the outgoing neutrinos are almost collinear with the initial state proton. For this reason Eq. (4.36) lacks an angular integral, as the only neutrinos that reach the detector are the ones coming from protons closely aligned to the LOS. To formalize this statement, we only consider protons moving within a narrow cone around the LOS direction, with angular opening δ such that $\cos\delta = 1 - 10^{-5}$, and only select neutrinos whose angle θ with respect to the proton direction satisfies $\theta \leq \delta$. Within this narrow cone, the jet's proton spectrum is practically constant in angle and can thus be taken out of the angular integral, which reduces to counting all neutrinos that satisfy $\theta \leq \delta$.

The procedure described so far allows to obtain $\langle dN_\nu/d\bar{E}_\nu\rangle$ of Eq. (4.37) and the neutrino flux of Eq. (4.36) (where $\gamma_p^{\rm min}(\bar{E}_\nu, m_{\rm DM})$ does not need to be computed explicitly). Our calculation actually underestimates $d\Phi_\nu/d\bar{E}_\nu$, because i) MADGRAPH5 avoids any $Q^2 \to 0$ divergent behaviour by only generating events with $Q^2 > Q^2_{\rm min} = 4$ GeV^2, ii) we did not include the effect of resonances, of particular relevance for $Q^2 \sim$ GeV^2, iii) nor the one of the next-to-leading-order processes with sea-gluons in the initial state.

Finally, cosmological redshift modifies the neutrino flux at Earth into

$$\frac{d\Phi_\nu}{dE_\nu} = (1+z)\frac{d\Phi}{d\bar{E}_\nu}\bigg|_{\bar{E}_\nu = E_\nu(1+z)}, \tag{4.40}$$

where $E_\nu \equiv \bar{E}_\nu/(1+z)$ is the redshifted neutrino energy, i.e. the one that we measure on Earth.

Neutrinos from TXS 0506+056

Having outlined the procedure to compute the neutrino flux for any model of particle DM and of blazar jets, we now present our results for the blazar TXS 0506+056. Our predicted neutrino flux is shown in Fig. 4.2 for the vector mediator scenario (left panel), where we choose $m_V = 5$ GeV. It features a larger amplitude and a different shape than the neutrino flux predicted, independently of DM, by the lepto-hadronic jet model of the same blazar, also shown in Fig. 4.2. We display in the same figure various neutrinos observations and limits. In the right panel of Fig. 4.2 we show the resulting neutrino fluxes for the four different toy models described in Sec. 4.1.3, for a common choice of DM parameters as indicated in the caption.

The dependence of $d\Phi_\nu/dE_\nu$ on $m_{\rm DM}$ is encoded in $s = 2m_{\rm DM}E_p$. Once $\sqrt{s} >$ few GeV, so that ν production via DIS is possible, $\langle dN_\nu/dE_\nu\rangle$ is determined by E_p and not by $m_{\rm DM}$ (we find that it is peaked roughly at $E_p/10$, see Figure 4.3, where we show the neutrino flux in the case of a monochromatic blazar jet). Therefore, the high-E_ν cutoff of our spectra depends on the properties of the jet proton spectrum and not on $m_{\rm DM}$. $\sigma^{\rm DIS}_{Y\chi p}$ becomes instead suppressed once $\sqrt{s} <$ few tens of GeV, explaining the dependence of $d\Phi_\nu/dE_\nu$ on $m_{\rm DM}$ that we find at small E_ν.

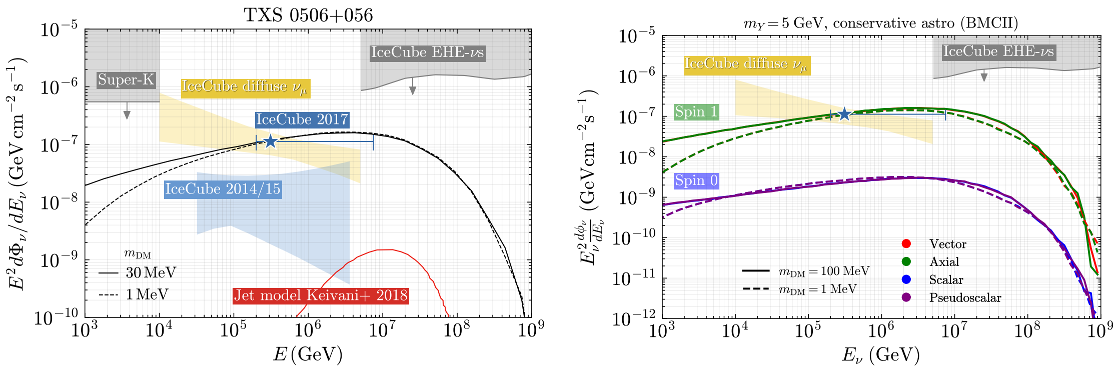

Figure 4.2: Neutrino flux from the blazar TXS 0506+056 induced by deep inelastic scatterings (DIS) between protons in the jet and DM surrounding the central black hole. **Left:** Our predictions for two benchmark DM masses ($m_{\rm DM} = 30$ and 1 MeV, with $m_V = 5$ GeV) are shown as **black solid/dashed lines**, compared to the standard jet model prediction [207] in **red**. IceCube detections are displayed as a **blue segment** (2017 event [184]) and a **blue band** for the 2014/15 flare [211], rescaled to 6 months. The diffuse $\nu_\mu + \bar{\nu}_\mu$ flux from IceCube is shown as **yellow bands** [220]. Upper limits at 90% C.L. from Super-K and IceCube EHE searches [450, 232] are in **grey**. **Right:** Comparison of neutrino fluxes for four types of DM-quark mediators (vector, axial, scalar, pseudoscalar) using a common mediator mass $m_Y = 5$ GeV, line-of-sight integral $\Sigma_{\rm DM} = 1.5 \times 10^{26}$ GeV cm^{-2}, and two benchmark DM masses ($m_{\rm DM} = 100$ MeV and 1 GeV).

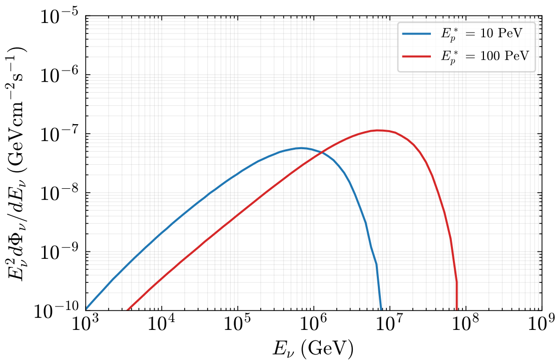

Figure 4.3: Neutrino flux from blazar TXS 0506+056 in the case of a monochromatic jet, assuming proton luminosity $L_p = 1.85 \times 10^{50}$ erg s^{-1} and $E_p^* = 10,\ 100$ PeV. We also fix $g_\chi g_q = 10^{-3}$ and $\Sigma_{\rm DM} = 6.9 \times 10^{28}$ GeV cm^{-2}.

Diffuse astrophysical neutrinos from an ensemble of blazars

We then repeat the same procedure for each of the 324 blazars modelled in [396], where the authors perform a lepto-hadronic fit to their multiwavelength electromagnetic emissions. Our results for the DM-induced neutrino fluxes are displayed in Fig. 4.4 for a common choice of DM parameters. The cumulative flux from 322 blazars is shown as a thick blue line. The two purple lines that dominate below and above 10 PeV correspond to blazars 3C 371 and PKS B1413+135, respectively. We do not include them in the cumulative flux because their uniquely huge neutrino fluxes require a more careful and specific analysis than

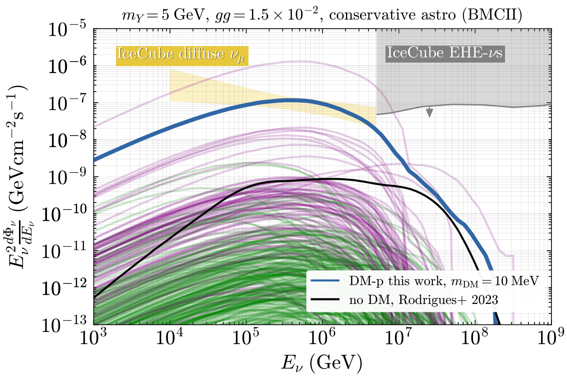

Figure 4.4: Neutrino flux from $p - \mathrm{DM}$ deep inelastic scatterings around 324 blazars that have been fitted with single-zone lepto-hadronic jet models in [396]. The lines correspond to spin-1 DM mediators with mass $m_Y = 5$ GeV, for $m_{\rm DM} = 1$ GeV, $g_{\chi Y} g_{qY} = 1.5 \times 10^{-2}$, $R_{\rm min} = 10^4 R_S$. The case of spin-0 mediators is a simple rescaling of the spin-1, as in Fig. 4.2. Blazars in the sample are separated into FSRQ (green) and BL Lac (purple) objects, the cumulative flux of all of them except the two outliers (see text) is shown as a thick blue line. In black is the neutrino flux computed in [396] as a result of $p - \gamma$ interactions, with no DM. The gray shaded area is excluded by the null detection of extremely-high-energy (EHE) neutrinos in 9 year of IceCube data [232], the yellow band is as in Fig. 4.2.

the global fit [396], which was carried out for other purposes. In addition, both blazars lie in the northern sky and so their PeV neutrinos, before reaching IceCube, suffer significant attenuation which is not included in our fluxes.

We find that the cumulative DM-induced neutrino flux can saturate the diffuse astrophysical neutrino flux observed by IceCube [220], for DM parameter space allowed by all existing constraints (discussed in Sec. 4.1.9). We now comment on some crucial points and subtleties needed to fully appreciate our results:

◇ First and foremost, our results suggest the intriguing possibility that IceCube's diffuse astrophysical neutrinos above $O(100)$ TeV are explained by protons-DM interactions in blazars. For that to be possible, one would need to find some correlation between IceCube's skymap and the one of blazars. The analyses of [221, 222] indeed do find a strong correlation in the southern sky in the energy range $E_\nu \gtrsim 100$ TeV, and a smaller but still significant correlation for the northern sky and energies $E_\nu \lesssim 100$ PeV, in accord with the expectations of our mechanism. However, the analysis of an updated dataset reported in [223] finds no significant correlation, although it is unclear to us whether this holds also for the highest-energy neutrinos predicted by our mechanism. The recent IceCube analysis [224] finds no significant correlation between high-energy neutrinos and a Fermi-LAT catalog of $O(2000)$ blazars, but it relies on the assumption that the neutrino flux can be described by a single power-law, which is not the case for our predicted fluxes. All in all, our proposal calls for implementing its specific characteristics in the searches for correlations between IceCube's skymap and the one of blazars.

◇ The DM-induced neutrino fluxes (purple and green lines in Fig. 4.4) have a significantly different shape than those for the same blazar sample but in the absence of DM (see

Fig. 11 of [396], only their sum is shown in Fig. 4.4). This deserves some clarification. As in [396], we separate blazars into their subcategories FSRQ (in green) and BL Lac objects (in purple). While [396] finds comparable fluxes from these two classes of objects, for us BL Lac objects completely dominate. The reason is that FSRQ have intense ambient photon fields for the protons to interact with and produce neutrinos, due to efficient accretion and bright broad line region (BLR), while BL Lac do not. As a consequence, to achieve a given neutrino flux in the absence of DM, FSRQ need a lower proton luminosity with respect to BL Lac, due to abundance of targets. For our mechanism, ambient photons are of no consequence and the only relevant parameter is the proton luminosity, thus breaking the degeneracy between number of protons and target photons in favour of BL Lac objects.

◇ Another difference between our neutrino fluxes and those of [396] lies in the peak neutrino energy for each blazar. The photons produced by the BLR are in the eV-keV range, which requires very large proton energies to reach the threshold for photo-meson production of neutrinos. Depending on how the photons are boosted/deboosted by the motion of the blob, the threshold moves to higher or lower proton energies, explaining the large variability in the neutrino peak energy. For our case, the threshold for neutrino production is always achieved for small proton energies because the DM has a mass larger than the energies of BLR photons, and the cross section increases with $\sqrt{s}$. Thus, the peak depends only on the maximal proton energy and the variability is greatly reduced.

4.1.5 Tests of dark matter origin for ν's

We find that DM-p inelastic scatterings around blazars could explain IceCube's observations, of both diffuse neutrinos and of the neutrino from TXS 0506+056, for several choices of DM models and parameters. These are indicated in Fig. 4.5 by four lines per plot, where each line corresponds to either TXS 0506+056 or the diffuse neutrinos and to one of our two benchmarks for $\Sigma_{\rm DM}^{\rm spike}$ of Sec. 4.1.2. Each plot is then repeated for the four mediators of DM-quark interactions (see Sec. 4.1.3) and for two values of the mediator mass.

While the lines explaining TXS 0506+056 do not overlap with those explaining the IceCube diffuse neutrinos, it would be incorrect to conclude that the two observations cannot be explained at once for the same DM particle model and parameters. Indeed, these lines could be easily brought to overlap by minor modifications in the jet parameters of some of the blazars involved in this study, a possibility which would be interesting to explore in future fits of blazar jets that include our DM mechanism. Independently of jet parameters, the lines could also overlap because of minor modifications in the line-of-sight integral of DM $\Sigma_{\rm DM}^{\rm spike}$ around specific blazars, because that integral depends on blazar-specific properties like their recent history and their exact starting jet points, and our choice of a single $\Sigma_{\rm DM}^{\rm spike}$ value for all of them has been driven by simplicity.

In Fig. 4.5 we also display, to the best of our knowledge, existing limits on the same DM models from cosmology, from DM-induced recoils and from searches of DM produced in the lab, see Section 4.1.9 for more details on them. Our comprehensive exercise teaches us that DM could be the origin of (both TXS 0506+056 and diffuse) IceCube's neutrinos for several different DM dynamics, proving the generality of our proposal. It also informs us that missing-energy searches in the laboratory are a generic test of our mechanism. Other

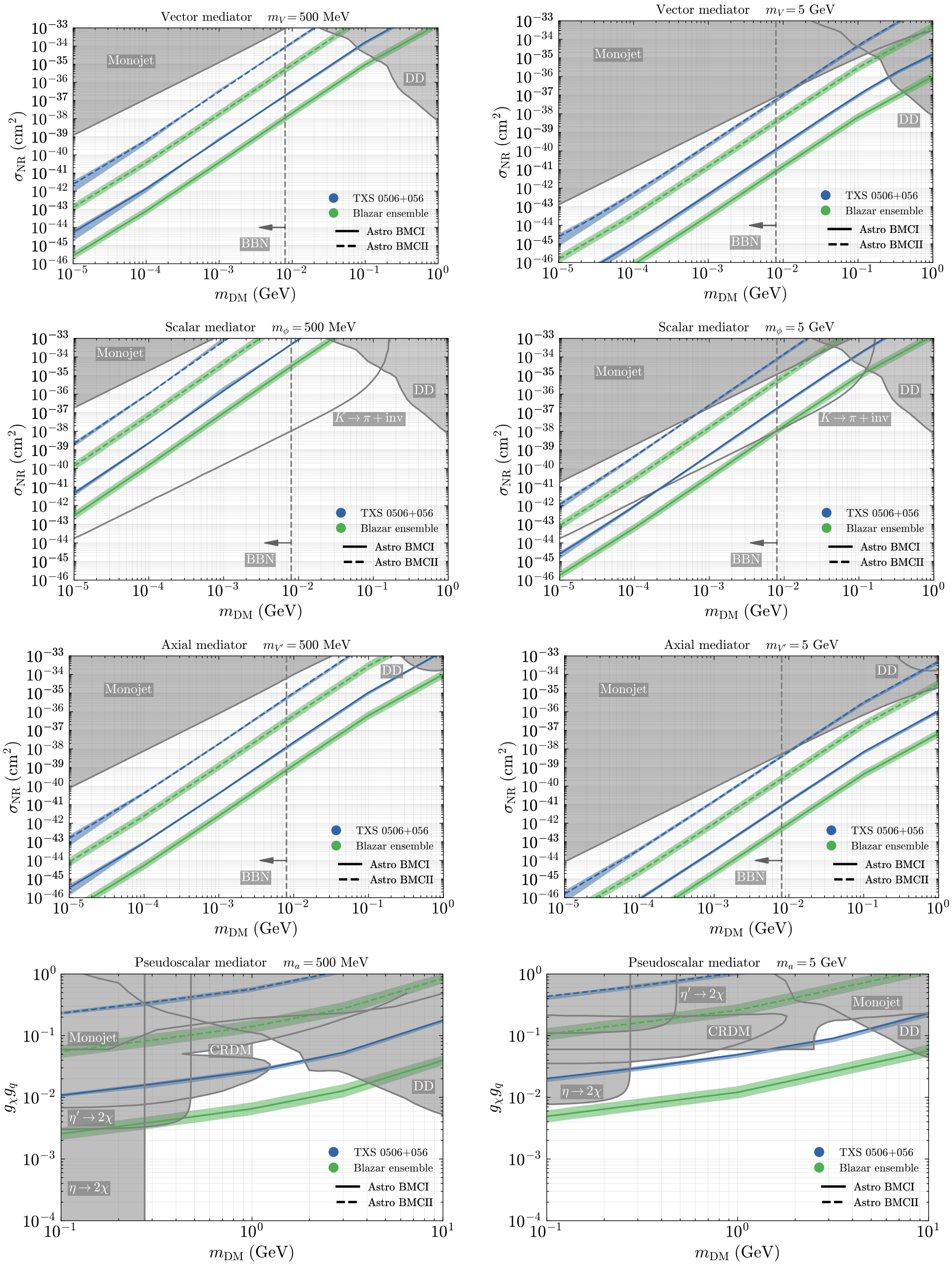

Figure 4.5: DM parameter space of Eqs. (4.14)–(4.17) for mediator mass $m_Y = 500$ MeV (left column) and $m_Y = 5$ GeV (right column), where $\sigma_{\mathrm{NR}} = (g^2_{\chi Y} g^2_{NY}/\pi)(\mu^2_{\chi N}/m^4_Y)$. For the pseudoscalar case (fourth row), the limits are shown in the $g_{\chi a} g_{qa} - m_{\mathrm{DM}}$ plane. High-energy diffuse neutrinos [220] and the IC-170922A neutrino from TXS 0506+056 [184] are explained, respectively, along the green and blue lines, where their width accounts for uncertainty on the energy E_ν of the TXS 0506+056 neutrino and on the diffuse neutrino flux. Continuous (dashed) lines correspond to BMCI (BMCII) for the DM LOS integral, see Sec. 4.1.2. The shaded grey areas are excluded by direct detection and various model-dependent searches, while the vertical dashed gray line marks the Big Bang nucleosynthesis limit, evadable if the dark sector thermalises with the SM below photon-neutrino decoupling. See Sec. 4.1.9 for extensive details on these constraints and Figures 4.12 and 4.13 for the predicted BBDM signal from TXS 0506+056 and the blazar sample respectively.

tests depend instead on the DM dynamics under consideration. For example, the vector- and scalar-mediated models will be best tested (each one to different extents) by direct searches for halo DM, while the pseudoscalar-mediated one by searches for CR-upscattered DM like [165, 391]. These will also be important in the case DM is inelastic (see e.g. [451, 452] for recent studies), where our proposal still works, but that we have not explicitly included in our toy models to keep the discussion contained. Indeed, inelastic DM evades halo-DM detection but not searches for DM signals that rely on larger exchanged momenta, like our DM-induced neutrinos here, CR-upscattering and accelerator probes.

Other DM-induced signals from the same blazars depend on exactly the same DM and astrophysical parameters as the neutrino signals discussed in this work, and provide therefore a robust test of our mechanism. A first such example is given by BBDM, which can be detectable at direct detection facilities and neutrino detectors, as first shown in [166, 388]. The computation of this signal will be the object of Sec. 4.1.7. A second example of signals induced by the same DM-p scatterings in blazars is given by the photons that they produce, see [387] for a pioneering study. At the source and before any propagation, these photons are indeed comparable to the neutrinos computed here, because they also mostly come from the pions produced in the hadronic showers. The determination of such photon fluxes on Earth is a necessary future step to test our mechanism, but it requires to implement exactly the same assumptions (on photon propagation, in particular on the astrophysical environment close to, and far from, the blazar) as the blazar fits that we employed, otherwise it would not be consistent. This exercise then goes far beyond the purposes of this thesis and we leave it for future work. [5]

4.1.6 Blazar-boosted DM fluxes at the Earth surface

Boosted-DM flux from blazars

Having discussed the observable neutrino signals upon DM–proton scattering in blazar jets, we now turn to the associated BBDM fluxes and their potential signals in terrestrial detectors. These fluxes arise naturally within our framework: the same high-energy protons in the jet that scatter off the ambient DM to produce neutrinos can, in doing so, also transfer energy to DM particles and boost them toward Earth, via both inelastic and elastic scatterings. Studying these BBDM fluxes provides an important and independent handle on our mechanism. While the IceCube neutrino signal offers a possible indication of DM–proton interactions near blazars, BBDM signals in large-volume neutrino detectors offers a complementary test of the same hypothesis.

For a single blazar, we estimate the BBDM flux exiting its jet and going in our direction as

$$\frac{d\Phi_\chi}{dT_\chi} = \frac{\Sigma_{\rm DM}^{\rm spike}}{2\pi m_{\rm DM} d_L^2} \int_0^{2\pi} d\phi_s \int_{\gamma_p^{\rm kin}(T_\chi)}^{\gamma_p^{\rm upper}} d\gamma_p \int d\mu_s \frac{d\Gamma_p}{d\gamma_p d\Omega} \frac{d\sigma_{Y\chi p}^{\rm EL+DIS}}{dT_\chi d\mu_s}\,, \tag{4.41}$$

where the differential cross section includes both the elastic and inelastic contributions, while μ_s is the cosine of the DM-proton scattering angle in the frame where DM is at rest. The proton spectrum is expressed in terms of μ, which is related to μ_s and ϕ_s by a rotation of

[5] Note that it is not consistent either to compute the photon spectrum from DM-p DIS in jets and include, in its propagation to the Earth, only the effects from CMB and extragalactic background light, as done in [438]. This indeed ignores interactions in the environment close to the blazar which, from studies of blazar jets (see e.g. [453, 208]), are known to importantly affect photon spectra on Earth.

an angle $\theta_{\rm LOS}$ [166]

$$\mu(\mu_s, \phi_s) = \mu_s \cos\theta_{\rm LOS} + \sin\phi_s \sin\theta_{\rm LOS}\sqrt{1-\mu_s^2}\,. \tag{4.42}$$

In the elastic case, μ_s is fixed by kinematics to be $\mu_s = \mu_s^{\rm EL}(T_p, T_\chi)$, as defined in Eq. (4.23). In the inelastic case, the integration over μ_s is non-trivial and has to be performed in the range $\mu_s^{\rm EL}(T_p, T_\chi) \leq \mu_s \leq 1$, where the lower extremum represents the elastic scattering limit of the DIS ($x = 1$). [6]

The DM flux shows mild dependence on the upper extreme of integration over γ_p, which we set to $\gamma_p^{\rm upper} = 1 + 10^8\,{\rm GeV}/m_p$ for all the considered blazars.

The lower extremum is a function of the DM kinetic energy T_χ, reading

$$\gamma_p^{\rm kin}(T_\chi) = \frac{1}{2m_p}\left[(T_\chi - 2m_p) + \sqrt{(T_\chi + 2m_p)^2 + (m_p - m_{\rm DM})^2\frac{2T_\chi}{m_{\rm DM}}}\right] + 1. \tag{4.43}$$

We also define $T_p^{\rm kin}(T_\chi) \equiv m_p[\gamma_p^{\rm kin}(T_\chi) - 1] \geq T_\chi$, and note that the equality only holds if $m_{\rm DM} = m_p$.

The expression of the differential BBDM flux in Eq. (4.41) is written in terms of the DM kinetic energy T_χ at the source. However, the DM momentum at Earth $|\vec{p}_\chi^{(0)}|$ is related to that at source $|\vec{p}_\chi|$ by $|\vec{p}_\chi^{(0)}| = |\vec{p}_\chi|/(1+z)$ – we remind that z is the redshift of the source – and the DM kinetic energy at Earth $T_\chi^{(0)}$ can be expressed in terms of T_χ at production as

$$T_\chi^{(0)} = m_{\rm DM}\left[\sqrt{\frac{T_\chi(T_\chi + 2m_{\rm DM})}{(1+z)^2 m_{\rm DM}{}^2} + 1} - 1\right]. \tag{4.44}$$

Therefore, upon inverting Eq. (4.44), the BBDM flux at Earth is given by

$$\frac{d\Phi_\chi}{dT_\chi^{(0)}} = \frac{dT_\chi}{dT_\chi^{(0)}}\frac{d\Phi_\chi}{dT_\chi}\bigg|_{T_\chi = T_\chi(T_\chi^{(0)})}, \tag{4.45}$$

where

$$\frac{dT_\chi}{dT_\chi^{(0)}} = (1+z)\frac{T_\chi^{(0)} + m_{\rm DM}}{\sqrt{T_\chi^{(0)}(T_\chi^{(0)} + 2m_{\rm DM})}}\,. \tag{4.46}$$

To ensure that DM particles are not boosted before the formation of the blazar, leading to an inconsistency, the DM travel time from the source to Earth ($t_{\rm DM}$) must not exceed the estimated age of the central BH. That is, $t_{\rm DM} \leq t_{\rm BH} \simeq 10^{10}$ yr, where $t_{\rm DM}$ is given by

$$t_{\rm DM} = \int_0^z \frac{dz'}{(1+z')H(z')}\sqrt{1 + \left(\frac{1+z}{1+z'}\right)^2 \frac{m_{\rm DM}{}^2}{T_\chi(T_\chi + 2m_{\rm DM})}}\,. \tag{4.47}$$

We further note that, since DM travels slower than light, it arrives at Earth with a delay with respect to the photons emitted at the same time. In particular, a BBDM-induced signal would lag behind any γ-ray and/or neutrino flaring activity. We show in Fig. 4.6 the time

[6] A similar calculation has been carried out in [438] where the integration over μ_s has been performed only for the cross section, while the proton spectrum was calculated at a fixed angle. This approach results in an approximation that, when $m_\chi \gtrsim \mathcal{O}(10)$ MeV, is too conservative for the BBDM flux at the relevant energies, which comes out considerably smaller than that obtained by us using Eq. (4.41).

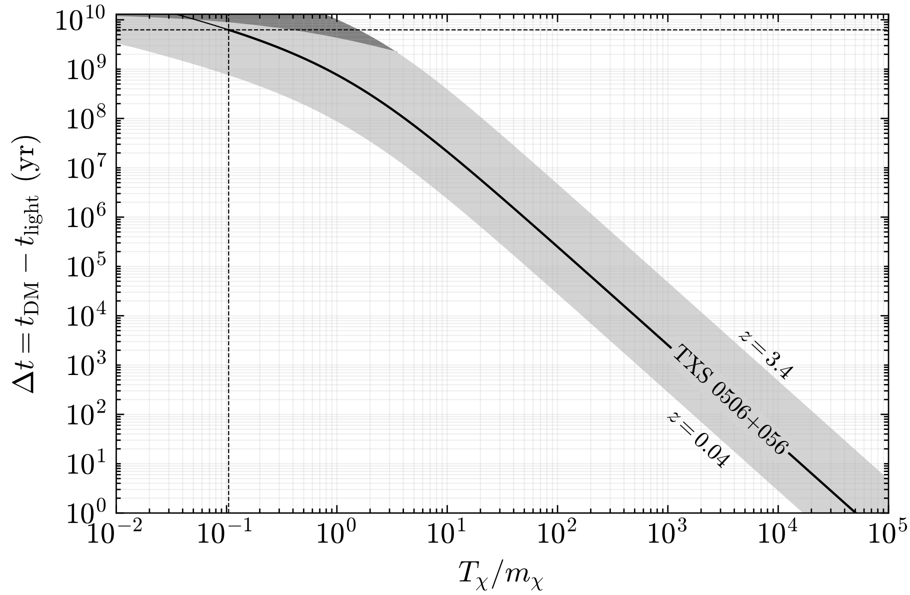

Figure 4.6: Time delay of the BBDM flux at Earth with respect to the photons emitted by TXS 0506+056 (black solid) and the blazar sample (gray area) as a function of $T_\chi/m_{\rm DM}$. Also shown in dashed is the cut $T_\chi/m_{\rm DM} \geq 0.104$ (vertical line) and the relative $\Delta t = t_{\rm DM} - t_{\rm light}$ (horizontal line) for TXS 0506+056 obtained by imposing $t_{\rm DM} \leq t_{\rm BH} \simeq 10^{10}$ yr. In the darker gray region we find $t_{\rm DM}(z) \geq t_{\rm Universe} \simeq 1.379 \times 10^{10}$ yr for the considered sample of blazars.

delay $\Delta t = t_{\rm DM} - t_{\rm light}$ of the BBDM flux at Earth with respect to the photons emitted by the same source for TXS 0506+056 and for the sample of blazars in [396] as a function of $T_\chi/m_{\rm DM}$, where $t_{\rm light}(z) = \int_0^z dz'/[(1+z')H(z')]$. For the former, we require that $t_{\rm DM} \leq t_{\rm BH} = 10^{10}$ yr, which yields $T_\chi/m_{\rm DM} \geq 0.104$ using $H_0 = 70.2\,{\rm km\,s^{-1}\,Mpc^{-1}}$, $\Omega_\Lambda = 0.685$, $\Omega_m = 0.315$ [74]. In what follows, we artificially set the BBDM flux to zero when this condition is not satisfied. In the plot, the black solid curve corresponds to TXS 0506+056, the vertical dashed line to the cut on $T_\chi/m_{\rm DM}$, while the horizontal line corresponds to $t_{\rm DM}(z_{\rm TXS} = 0.337) = t_{\rm BH}$. For all the sources in the sample, corresponding the gray area in the plot, we impose instead a cut on $T_\chi/m_{\rm DM}$ by requiring that $t_{\rm DM}(z) \leq t_{\rm Universe} = 1.38 \times 10^{10}\,$yr. The cut on the sample applies to the darker gray region of the figure. One can observe that Δt can exceed by many orders of magnitude the typical duration of the flaring activity, which is $\mathcal{O}$(yr). Therefore, as our BBDM estimates for TXS 0506+056 are based on the prominent six-month flare observed in 2017, they should be considered optimistic, as they implicitly assume that similar flaring activity has persisted throughout the blazar's past emission history. Our results on the sample of blazars are instead based on steady activities, and are thus more solid in this regard.

We show in Fig. 4.7 the BBDM fluxes from TXS 0506+056 at Earth for our DM models, where we set the mediator masses to $m_Y = 500\,$MeV and $5\,$GeV, the couplings to $g_{\chi Y} g_{uY} = g_{\chi Y} g_{dY} = 0.1$, and choose $m_{\rm DM} = 1$ MeV, 10 MeV, 100 MeV, 1 GeV as benchmark values for the DM mass. We separate the contribution of the elastic scatterings only (dashed) from the total elastic + DIS (solid).

The figure highlights the role of the inelastic contributions as the DM mass approaches the GeV scale. Indeed, DIS requires $m_{\rm DM} T_\chi \gtrsim \mathcal{O}({\rm GeV}^2)$, and the scattering imposes $T_p \geq$

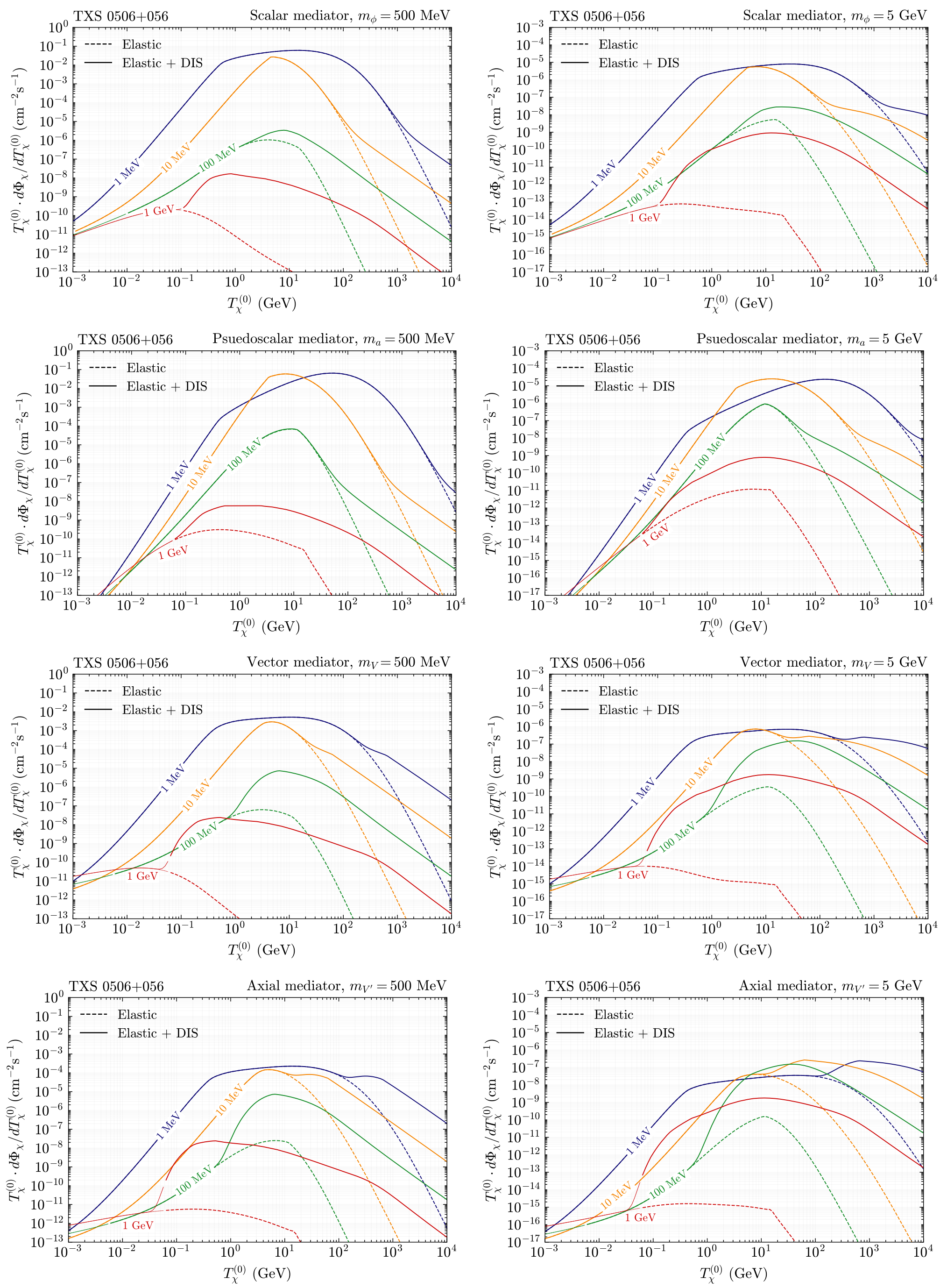

Figure 4.7: BBDM flux at Earth surface from TXS 0506+056 for $m_{\rm DM} = 1\,$MeV (blue), $10\,$MeV (orange), 100 MeV (green), $1\,$GeV (red). Dashed (solid) curves correspond to the elastic (elastic + DIS) contribution, for a scalar (first row), pseudoscalar (second row), vector (third row) and axial (last row) mediator with mass $m_Y = 500\,$MeV (left panels) and $5\,$GeV (right panels). The plots are obtained for $g_{\chi Y} g_{uY} = g_{\chi Y} g_{dY} = 0.1$ and $\Sigma_{\rm DM} = 6.9 \times 10^{28}\,$GeV cm^{-2}. The thick (thin) lines are obtained after imposing the cut $T_\chi/m_{\rm DM} \geq 0.104$ (< 0.104). Note: the range of the the vertical axes differ between left and right panels.

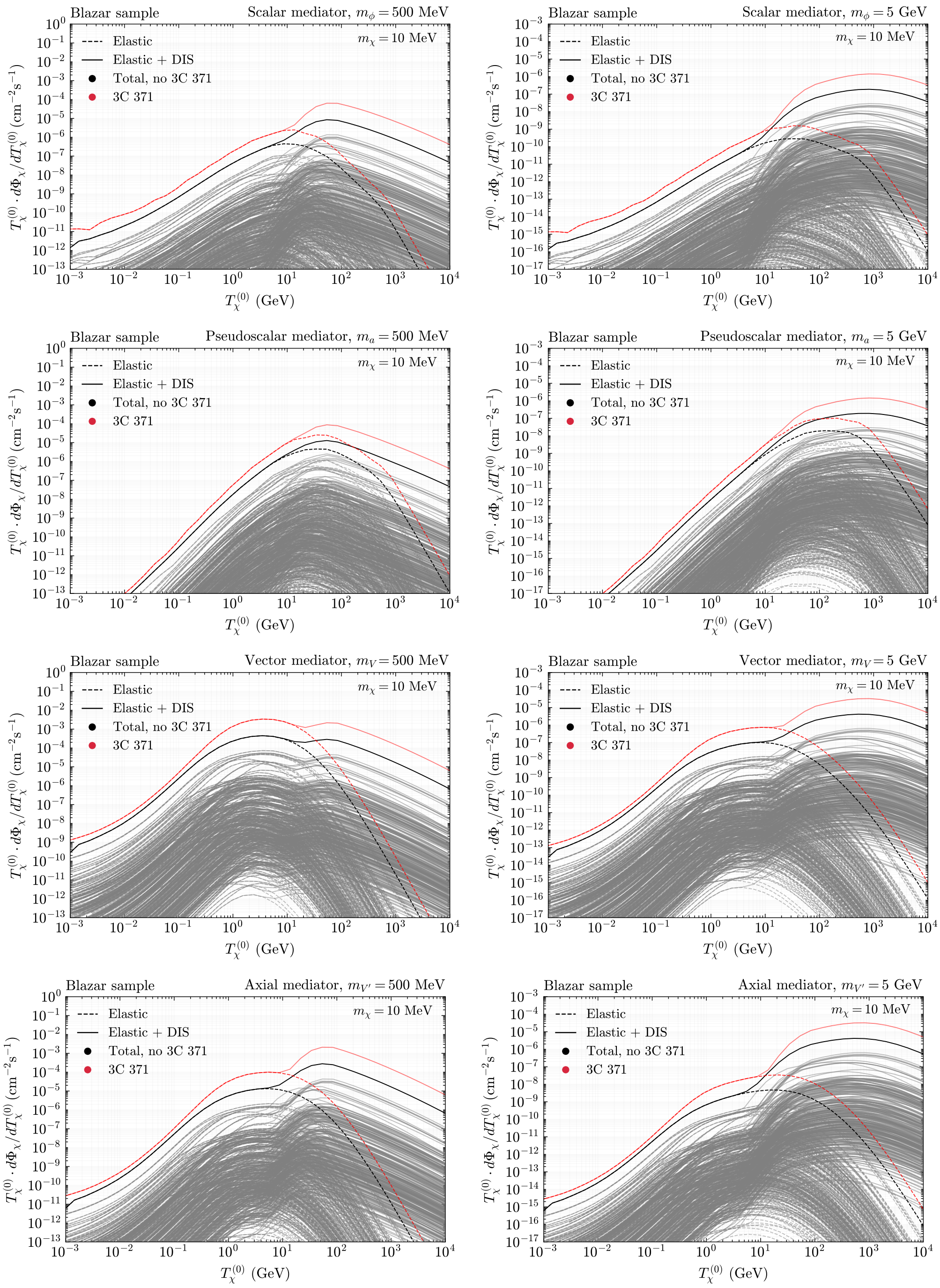

Figure 4.8: BBDM flux from 324 blazars for scalar (top), pseudoscalar (second row), vector (third row), and axial (bottom) mediators. Gray lines show individual blazars; red highlights 3C 371, which dominates the flux; black is the total excluding 3C 371. Dashed and solid lines represent elastic and elastic + DIS contributions, respectively. We fix $m_Y = 500\,\text{MeV}$ ($m_Y = 5\,\text{GeV}$) in the left (right) panels, with $m_{\text{DM}} = 10\,\text{MeV}$, and the overall normalisation with $g_{\chi Y} g_{uY} = g_{\chi Y} g_{dY} = 0.1$ and $\Sigma_{\text{DM}}^{\text{spike}}$ as in BMCI. For each blazar we have imposed the cut on T_χ/m_{DM} that results from the condition $t_{\text{DM}} \leq t_{\text{Universe}} \simeq 1.379 \times 10^{10}\,\text{yr}$. Note: the range of the the vertical axes differ between left and right panels.

$T_p^{\rm kin}(T_\chi) \geq T_\chi$: the lower the DM mass, the higher the required proton energy to contribute to the DIS. Due to the power-law spectrum of protons in blazar jets, the contribution of inelastic scatterings to the flux becomes increasingly suppressed as the DM mass decreases. Also, the DIS has a milder impact for the pseudoscalar mediator case. This is because, for a fixed value of the quark couplings to the mediator, the pseudoscalar scenario enhances the associated coupling to the nucleons, leading to an increased contribution to the flux from elastic scatterings, see Appendix A.1 for details. Analogously, due to a similar conspiracy of couplings, the elastic contribution in the vector mediator case is larger than in the axial scenario, while the respective DIS contributions are equivalent. The scalar mediator case is intermediate between the vector/axial and pseudoscalar scenarios. The mediator mass m_Y also controls the relative importance of elastic and inelastic contributions to the flux. Increasing m_Y tends to suppress elastic scattering more strongly than DIS, due to the lower momentum transfer involved.

We show in Fig. 4.8 the diffuse BBDM flux originating from the sample of 324 blazars analyzed in [396], choosing the benchmark parameters $m_{\rm DM} = 10\,{\rm MeV}$, couplings $g_{\chi Y} g_{uY} = g_{\chi Y} g_{dY} = 0.1$, mediator masses $m_Y = 500\,{\rm MeV}$ and $5\,{\rm GeV}$. By comparing these fluxes with the BBDM flux from TXS 0506+056 shown in Fig. 4.7 for $m_{\rm DM} = 10\,{\rm MeV}$, we find that inelastic contributions play a significantly larger role in the blazar sample. This difference arises due to the minimal proton boost factor $\gamma'_{{\rm min}_p} = 10^2$ adopted in [396] for the whole sample. As a result, elastic contributions, being more suppressed at higher proton energies, are relatively weaker compared to inelastic ones. The fact that $\gamma'_{{\rm min}_p} = 10^2$ for the blazar sample also exacerbates the different dependence on T_χ of the elastic contributions between the spin-0 (scalar and pseudoscalar mediators) and spin-1 cases (vector and axial mediator).

4.1.7 Blazar-boosted DM signals at neutrino detectors

The impact of the Earth attenuation

The flux of BBDM will be attenuated from the Earth surface to the location of the detector due to the scatterings with nuclei in the Earth crust. As a result, a detector can develop a blind spot to the incoming BBDM flux if the DM–nucleon interaction is sufficiently strong, causing significant depletion before reaching the detector. Various methods with varying levels of complexity have been developed to estimate the energy loss of DM as it travels inside the Earth. The simplest approach consists of approximating the energy loss by its averaged value and evolve it using a corresponding differential equation under the assumption of forward scattering, see, e.g., [163, 164, 165, 454]. We give more details on this approach applied to our toy models in Appendix A.3. More advanced methods employ Monte Carlo simulations to track the stochastic nature of the scatterings and energy loss in detail, often incorporating a three-dimensional description of particle propagation (see, e.g., [455]). In this work, we decide to adopt a simplistic but more conservative treatment by requiring that DM gets lost after a single scattering in the Earth crust.

To estimate how many scatterings DM undergo in the Earth crust, we assume that the interactions take place only with protons p and neutrons n at rest. This treatment is valid as long as $Q^2 \gtrsim \mathcal{O}(0.04\,{\rm GeV}^2)$, whereas below this value the DM particles can probe the nuclear structure of the target nuclei. Then, we consider only the elastic contribution to the DM-nucleon scattering, but evaluate all the nucleon form factors in $\sigma^{\rm EL}_{Y\chi N}$ at zero momentum transfer, noting that this approach is more conservative than evaluating the cross section including the full Q^2-dependence of the form factors (see, e.g., [455]) and the

DIS contribution. Also, in our analysis, we consider $m_N \equiv m_p \simeq m_n$ and concentrate on quark couplings to the mediator such that $g_{qY} \equiv g_{uY} = g_{dY}$, and thus $g_{NY} \equiv g_{pY} = g_{nY}$. Under these assumptions, and following the derivation presented in Appendix A.1, the elastic scattering cross sections for pseudoscalar, vector, and axial toy models are the same for proton and neutron. The same goes for the scalar mediator case if we neglect small corrections arising from nuclear isospin symmetry breaking. We thus adopt the approximation $\sigma^{\rm EL}_{Y\chi N} \equiv \sigma^{\rm EL}_{Y\chi p} \simeq \sigma^{\rm EL}_{Y\chi n}$ throughout our subsequent analysis. Then, the expressions for $d\sigma^{\rm EL}_{Y\chi p}/dT_p$ that are needed for our treatment can be readily obtained from those in Eqs. (4.25-4.28) by replacing $T_\chi^{\max}(T_p) \to T_p^{\max}(T_\chi^x)$, evaluating the form factors at $Q^2 = 0$, performing the trivial integration over μ_s. These can then be integrated from 0 to $T_p^{\max}(T_\chi^x)$ to get the total cross section. Furthermore, we consider the average mass density of the Earth crust to be $\rho_{p+n} \simeq 2.7\,{\rm g/cm^3}$ [456], and fix the proton and neutron number densities by assuming an equal ratio, $n_N \equiv n_p \simeq n_n \simeq \rho_{p+n}/(2m_N)$.

With all these approximations made, we investigate the quantity $\ell^{-1} \equiv 2n_N\sigma^{\rm EL}_{Y\chi N}$, which is the mean path travelled by the DM particle before undergoing a scattering. In particular, we show in Fig. 4.9 the product $x\ell^{-1}(T_\chi^{(0)})$ versus $T_\chi^{(0)}$, x being the distance travelled by DM in the Earth crust, which we fix at $x = 1\,{\rm km}$. In the plot, the other parameters are fixed as $g_{\chi Y}g_{qY} = 0.1$, $m_Y = 5\,{\rm GeV}$ (left panel), $500\,{\rm MeV}$ (right panel), and $m_{\rm DM} = 1\,{\rm GeV}$ (solid), $100\,{\rm MeV}$ (dashed), $10\,{\rm MeV}$ (dotted). The different colours correspond to the four considered toy models for the DM-nucleon interaction, as specified in the figure. It is immediate to rescale the plots for different values of x and couplings $g_{\chi Y}g_{qY}$ since $x\ell^{-1}(T_\chi) \propto x\, g^2_{\chi Y}g^2_{qY}$. For instance, the same curves can be obtained for $x = 10^4\,{\rm km}$ and $g_{\chi Y}g_{qY} = 10^{-3}$. The dependence on m_Y is less straightforward, this being the reason why we show two benchmark cases. We also point out that, if $Q^2 < 0.04\,{\rm GeV}^2$ (shaded gray areas in the figure), the dominant contribution to the Earth attenuation originates from DM scattering with nuclei, hence we are underestimating the attenuation in this kinematic region. When $x\ell^{-1} \geq 1$, the average number of scattering over a distance x, $N^x_{\rm sct}$, exceeds one. In the figure, the threshold $N^x_{\rm sct} = 1$ is marked by a thick black horizontal line. The Earth attenuation becomes relevant when $N^x_{\rm sct} \gtrsim$ few, with the DM undergoing multiple scatterings and its energy dropping exponentially (see Appendix A.3, and the left panel of Fig. A.1 there, where we prove this in a more refined approach). According to the left panel of Fig. 4.9, this never happens for $m_Y = 5\,{\rm GeV}$, and thus, for the parameters of the figure, the effects of the Earth attenuation can be neglected. For the case $m_Y = 500\,{\rm MeV}$ the situation is more subtle: the Earth attenuation remains negligible for the axial toy model; it becomes more important for the vector case for relatively large masses; it affects the pseudoscalar and scalar mediator cases for all the depicted DM mass benchmarks. We note, however, that attenuation in this case is significant only for relatively large couplings. A simple rescaling of $g_{\chi Y}g_{qY}$ to smaller values would significantly reduce its impact.

Based on this qualitative description and, *a posteriori*, on our final results, we note that Earth attenuation on the kilometer distance affect our conclusions only for relatively large couplings. In the scalar and vector scenarios, the region where attenuation starts playing a role is already excluded by other DM searches, while, in the axial case, it matters when couplings approach, if not exceed, the non-perturbative regime. *De facto*, attenuation is crucial to determine an upper limit on DM-nucleon interaction, in a region that is still allowed by current constraints, only in the pseudoscalar scenario for $m_{\rm DM} \gtrsim 300$ MeV. For our subsequent analysis, we account for the Earth attenuation in the pseudoscalar scenario only, and we do it as follows. We set the attenuated BBDM flux to be equal to that at

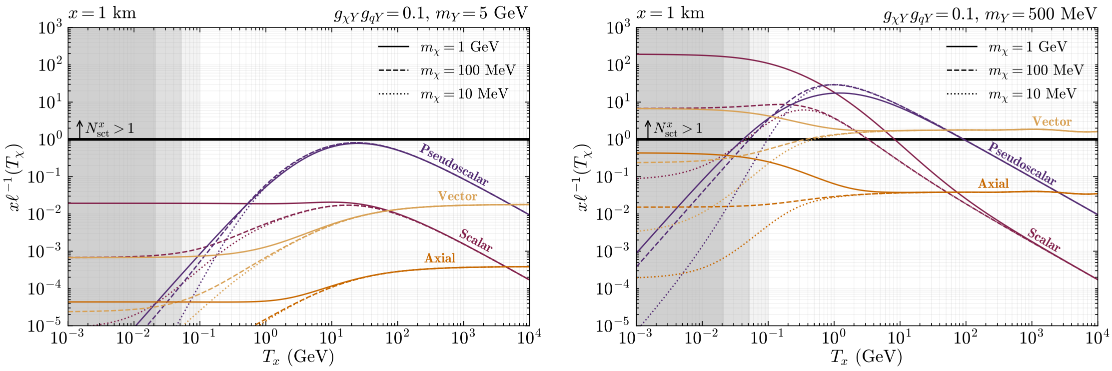

Figure 4.9: Distance x travelled by DM in the Earth crust, in units of the mean path ℓ travelled by DM before it undergoes a scattering with nucleons, as a function of the DM kinetic energy at surface $T_\chi^{(0)}$. We consider the cases of scalar, pseudoscalar, vector and axial mediators and we choose as benchmark values $x = 1\,\mathrm{km}$, $m_Y = 500\,\mathrm{MeV}$ ($5\,\mathrm{GeV}$), $m_\chi = 10\,\mathrm{MeV}$, $100\,\mathrm{MeV}, 1\,\mathrm{GeV}$ and $g_{\chi Y} g_{qY} = 0.1$ for the left (right) panel. Attenuation effects become relevant when $N_{\rm sct} \geq 1$ (thick black line). Inside the gray shaded areas, one for each value of DM mass, we have $Q^2 < 0.04\,\mathrm{GeV}^2$ and the DM scattering with nuclei, which we have not included in our treatment, is dominant.

the Earth surface for $T_\chi^{(0)}$ as long as $N_{\rm sct}^{x_{\rm det}} < 1$, i.e. $x_{\rm det}\ell^{-1}(T_\chi^{(0)}) < 1$, being $x_{\rm det}$ the depth of a given detector. For the energies such that $x_{\rm det}\ell^{-1}(T_\chi^{(0)}) \geq 1$, a DM particle undergoes on average at least one scattering. When such condition is satisfied, we artificially set the BBDM flux to zero. This method is clearly conservative, as it does not account for the fact that the BBDM flux at these energies is not necessarily stopped, but rather redistributed to lower energies (see Appendix A.3). However, A more accurate analysis would require substantial computational effort, and we prefer to proceed with our conservative approach to ensure the numerical evaluation remains tractable.

Finally, we note that the effect of Earth attenuation depends on the path length travelled by DM particles through the Earth from the surface to the detector, which varies over time. This variation has a daily periodicity, as the position of each source in the sky changes with the Earth's rotation. When the blazar moves below the horizon, the distance DM must travel through the Earth increases significantly, making attenuation rapidly more important. To remain conservative, we set the BBDM flux to zero whenever the originating blazar goes below the horizon. In practice, this implies multiplying the BBDM flux by an overall factor $f_{\rm det}$ that accounts for the fraction of the day during which the source remains above the horizon, as seen from the detector's location. We depict in Fig 4.10 the depth in the direction of TXS 056+056 for the neutrino detectors Super-Kamiokande (SK, or Super-K), Borexino, JUNO and DUNE. According to the figure, for this particular blazar the fraction of the day for which it stays above the horizon for each detector is $f_{\rm det} \simeq 1/2$. We compute analogously $f_{\rm det}$ for each blazar of the sample in [396].

We summarise our methodology for incorporating the effects of the Earth attenuation by writing the BBDM flux from a single blazar at a given detector as:

$$\frac{d\Phi_\chi^{\rm det}}{dT_\chi^{(0)}} = \frac{d\Phi_\chi}{dT_\chi^{(0)}} f_{\rm det}\Theta[1 - x_{\rm det}\ell^{-1}(T_\chi^{(0)})], \tag{4.48}$$

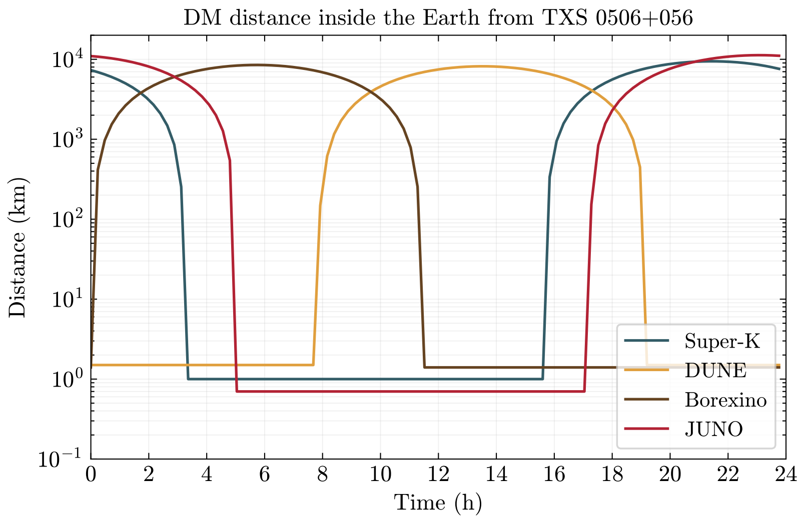

Figure 4.10: Daily variation of the DM path length from TXS 0506+056 to various underground detectors, measured from the Earth's surface. The constant x intervals correspond to times where the source is above the horizon of the detector, hence $x \simeq x_{\rm det}$, where $x_{\rm SK} = 1$ km, $x_{\rm DUNE} = 1.5$ km, $x_{\rm JUNO} = 0.7$ km and $x_{\rm Borexino} = 1.4$ km. We refrain to show KamLAND and Hyper-Kamiokande as their associated daily variation of the DM path inside the Earth differ from the one of Super-K only due to the different depths of the detectors, which we take as $x_{\rm KamLAND} = 1$ km and $x_{\rm HK} = 0.65$ km.

where the Heaviside Θ-function ensures that $x_{\rm det}\ell^{-1}(T_\chi^{(0)}) \leq 1$.

The recoil spectrum and number of events at neutrino detectors

Once a DM particle reaches a detector, it may transfer part of its kinetic energy to a target nucleus. In our study, we focus on the signal produced by elastic DM scatterings at neutrino detectors. Given their typical energy sensitivity, DM dominantly scatters off individual nucleons of the detector material, thus we consider DM scatterings on $N = p, n$, using $\sigma^{\rm EL}_{Y\chi N} \equiv \sigma^{\rm EL}_{Y\chi p} \simeq \sigma^{\rm EL}_{Y\chi n}$ and $m_N \equiv m_p \simeq m_n$. We denote as T_N the nucleon kinetic energy upon DM scattering. We compute the differential recoil rate $dR_N^{\rm det}/dT_N$ at a given detector as

$$\frac{dR_N^{\rm det}}{dT_N} \simeq N_{\rm target}^{\rm det} \int_{T_\chi^{\rm min}(T_N)}^{+\infty} dT_\chi \frac{d\sigma^{\rm EL}_{Y\chi N}}{dT_N} \frac{d\Phi_\chi^{\rm det}}{dT_\chi} \,, \tag{4.49}$$

where $N_{\rm target}^{\rm det}$ is the total number of target nuclei in the detector, $T_\chi^{\rm min}$ the minimal DM kinetic energy needed to produce a recoil energy T_N and the DM flux is evaluated according to Eq. (4.48).

We can now extract the sensitivities on DM-nucleon interactions by computing the expected number of BBDM events at the selected detectors. This is given by

$$N_{\rm BBDM}^{\rm det} = t_{\rm exp}^{\rm det} N_{\rm target}^{\rm det} \int_{T_{\rm min}^{\rm det}}^{T_{\rm max}^{\rm det}} dT_N \, \epsilon^{\rm det}(T_N) \frac{dR_N^{\rm det}}{dT_N} < N_{\rm events}^{\rm det} \,, \tag{4.50}$$

where $t_{\rm exp}^{\rm det}$ denotes the exposure time, $[T_{\rm min}^{\rm det}, T_{\rm max}^{\rm det}]$ the energy range sensitivity, $\epsilon^{\rm det}$ the efficiency and $N_{\rm events}^{\rm det}$ the experimental upper limit on the number of events. We set limits

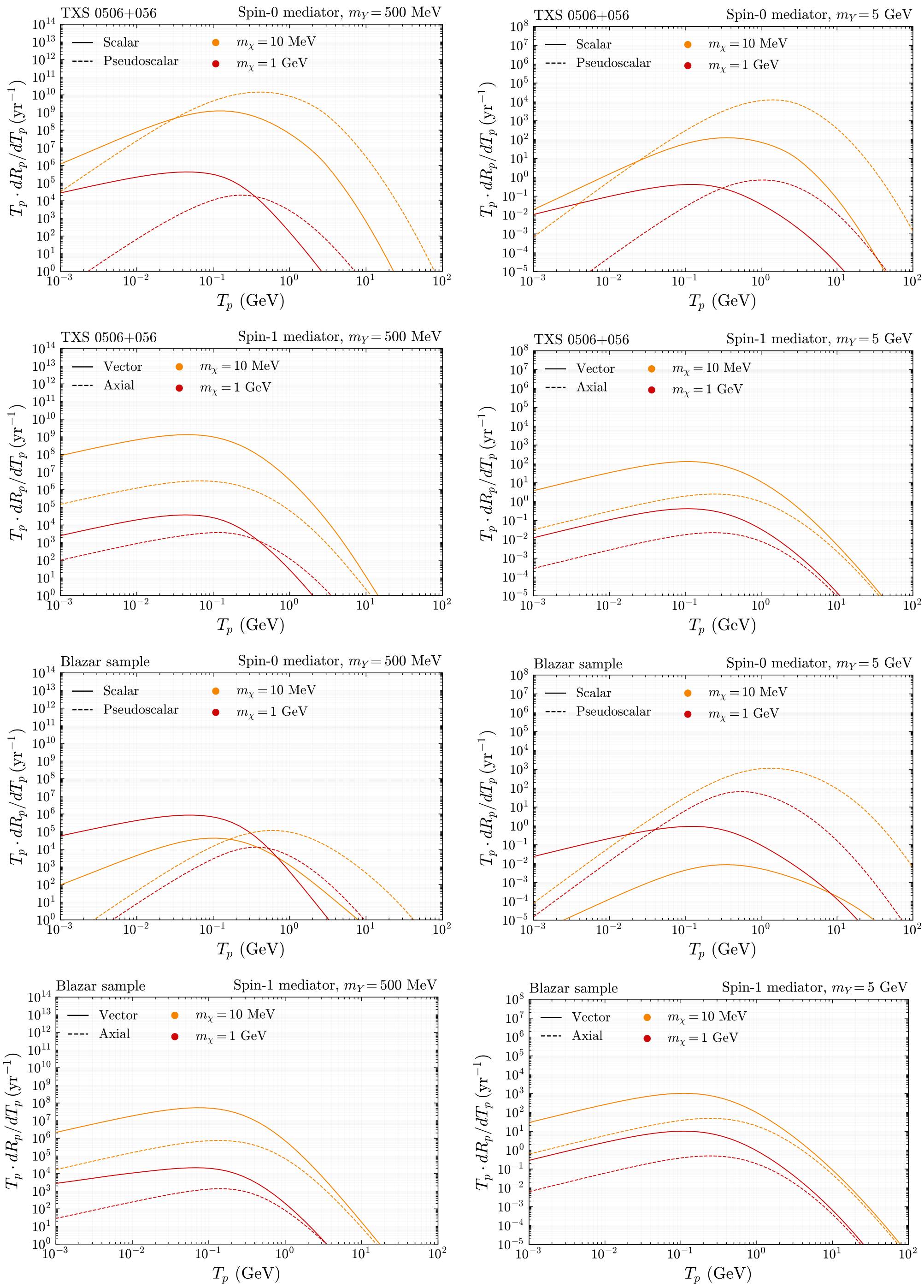

Figure 4.11: The proton recoil spectrum from BBDM from TXS 0506+056 (first and second rows) and the sample of blazars excluding 3C 371 (third and fourth rows), for $m_\chi = 10\,\text{MeV}$ (orange), $1\,\text{GeV}$ (red), before attenuation. The first and third rows correspond the case of a scalar (solid) and pseudoscalar (dashed) spin-0 mediators, while the second and fourth rows to vector (solid) and axial (dashed) spin-1 mediators. The mass of the mediator is fixed at $m_Y = 500\,\text{MeV}$ (left panels) and $5\,\text{GeV}$ (right panels). We have used $g_{\chi Y} g_{uY} = g_{\chi Y} g_{dY} = 0.1$, Σ_{DM} as in BMC I and, for definiteness, $N_{\text{target}} = 7.5 \times 10^{33}$. Note: the range of the the vertical axes differ between left and right panels.

using Super-K, KamLAND and Borexino data and we compute the projected sensitivities at Hyper-K, JUNO and DUNE.

We extract current bounds on DM-proton interaction from Super-K based on the search [391] performed by the collaboration investigating interactions with protons. The efficiency factor $\epsilon(|\vec{p}_p|)$ is given in [391] in the proton momentum range $1.2 \leq |\vec{p}_p|/\mathrm{GeV} \leq 2.3$, with the corresponding kinetic energy range $0.58 \lesssim T_p/\mathrm{GeV} \lesssim 1.55$. The total exposure time in Super-K is $t_{\rm exp}^{\rm SK} = 6050.3\,\mathrm{days}$, the number of proton targets (including those in oxygen, as these should also be relevant when $Q^2 = 2m_N T_N > \mathrm{GeV}^2$) in its 22.5 kton fiducial mass of water is $N_{\rm target}^{\rm SK} = 7.5 \times 10^{33}$ and by selecting only the 60 events in [391] where the signal comes from above the horizon we extract the limit on the BBDM events $N_{\rm events}^{\rm SK}(0.58 < T_p/\mathrm{GeV} < 1.55) = 18$.

Hyper-Kamiokande (HK, or Hyper-K) will be a 187-kton fiducial volume detector, $N_p^{\rm HK} = 6.2 \times 10^{34}$, and is expected to start taking data in 2027 [79]. We obtain its projected limits by setting the exposure time $t_{\rm exp}^{\rm HK} = 10\,\mathrm{yr}$ and assuming same background event rate, energy range and efficiency as Super-K. This procedure gives us the upper limit $N_{\rm events}^{\rm HK}(0.58 < T_p/\mathrm{GeV} < 1.55) = 37$.

The DUNE detector will consist of four modules, with a combined fiducial volume of 40 ktons [457]. As DUNE relies on the scintillation light and not on the Cherenkov one, its energy threshold will be lower than Super-K. We take it as $T_p > 50\,\mathrm{MeV}$ as given by [78]. We set the upper energy threshold as 10 GeV, although our results are insensitive to the precise choice as long as it is much larger than 50 MeV. In this energy range, DM dominantly interacts with individual nucleons and so we take the number of the target particles as $N_{\rm target}^{\rm DUNE} = 2.4 \times 10^{34}$ where we summed over protons and neutrons. We are not aware of any detailed study concerning background events that is applicable to our setup, hence we set our bounds by choosing exposure time of $t_{\rm exp}^{\rm DUNE} = 5\,\mathrm{yr}$, $\epsilon^{\rm DUNE} = 1$ and as a benchmark value $N_{\rm events}^{\rm DUNE}(0.05 < T_p/\mathrm{GeV} < 10) = 30$.

KamLAND observed one event in the energy bin $[13.5, 20]\ \mathrm{MeV_{ee}}$ [458], where $\mathrm{MeV_{ee}}$ stands for MeV electron equivalent. From the detector information and following the approach performed in [459] (see Eq. (11) therein), we infer the equivalent proton recoil energy $22.5 \lesssim T_p/\mathrm{MeV} \lesssim 30.7$ and impose our limit on the BBDM signal in this energy bin as $N_{\rm events}^{\rm KamLAND}(22.5 \lesssim T_p/\mathrm{MeV} \lesssim 30.7) = 3$. The exposure time is $t_{\rm exp}^{\rm KamLAND} = 123\,\mathrm{days}$ and the number of proton targets in the detector $N_{\rm target}^{\rm KamLAND} = 3.4 \times 10^{32}$, including those in carbon nuclei.

JUNO is a reactor neutrino experiment with a 20 kton liquid scintillator detector volume [77] expected to be operational within 2025. The JUNO projection [460] estimates the SM background from elastic scatterings on hydrogen and quasi-elastic scatterings on carbon, in the visible scintillation energy ($E_{\rm vis}$) range $15 \lesssim E_{\rm vis}/\mathrm{MeV} \lesssim 100$, corresponding to a kinetic proton recoil energy within $21.2 \lesssim T_p/\mathrm{MeV} \lesssim 112$, where the relation between $E_{\rm vis}$ and T_p is given in [460]. We consider for our signal elastic scatterings on all the protons in the detector, $N_{\rm target}^{\rm JUNO} = 6.8 \times 10^{33}$. Setting an exposure time $t_{\rm exp}^{\rm JUNO} = 10\,\mathrm{yr}$, $\epsilon^{\rm JUNO} = 1$ and adopting the expected background rate from atmospheric neutrinos as [460] yields the limit on the signal $N_{\rm events}^{\rm JUNO}(21.2 \lesssim T_p/\mathrm{MeV} \lesssim 112) = 79$.

We finally compute limits from Borexino [461]. We use the number of proton targets $N_{\rm target}^{\rm Borexino} = 3.2 \times 10^{31}$, with an exposure time $t_{\rm exp}^{\rm Borexino} = 446.1$ days and then impose our signal $N_{\rm events}^{\rm Borexino} < 3$ in the energy range $21.6 \lesssim T_p/\mathrm{MeV} \lesssim 24.9$. This limit follows from the absence of events in the interval $[12.5, 15]\,\mathrm{MeV_{ee}}$.

We summarize the relevant parameters adopted in our analysis for each detector in Table

Experiment	Mass (kton)	$N_{\rm target}^{\rm det}(N)$	$t_{\rm exp}^{\rm det}$ (years)	$[T_{\rm min}^{\rm det}, T_{\rm max}^{\rm det}]$ (GeV)	$N_{\rm BBDM}^{\rm det}$	$\epsilon^{\rm det}$
SK	22.5	$7.5 \times 10^{33}(p)$	16.56	$[0.58, 1.55]$	18	[391]
HK	187	$6.2 \times 10^{34}(p)$	10	$[0.58, 1.55]$	37	[391]
DUNE	40	$2.4 \times 10^{34}(p,n)$	5	$[0.05, 10]$	30	1
JUNO	20	$6.8 \times 10^{33}(p)$	10	$[0.0212, 0.1112]$	79	1
KamLAND	1	$3.4 \times 10^{32}(p)$	0.337	$[0.0225, 0.0307]$	3	1
Borexino	0.278	$3.2 \times 10^{31}(p)$	1.22	$[0.0212, 0.0245]$	3	1

Table 4.2: Specification of the detector parameters that we adopted in our analysis, see Eq. (4.50). We consider the free nucleons $N = p, n$ as targets as specified for each experiment.

4.2. In addition, to facilitate a direct comparison of the recoil spectrum with the energy range within which each specific detectors operate, we show in Fig. 4.11 the proton recoil spectrum for both the individual source TXS 0506+056 and the sample of 323 blazars (excluding 3C 371). Note that the plots in the figure are obtained neglecting attenuation, as this would depend on the specific detector's depth and position.

4.1.8 Searches for sub-GeV DM test blazar-DM signals

In this section, we project the limits and sensitivities to BBDM computed earlier in the $\sigma_{Y\chi p}^{\rm NR} - m_\chi$ plane for the scalar, vector and axial mediator cases ($g_{\chi Y} g_{qY} - m_\chi$ plane for the pseudoscalar mediator case), and compare them against current constraints from various DM searches, as well as to the neutrino prediction via the same DM-proton scatterings in blazar jets estimated in [3, 4]. We show our results in Figs. 4.12 and 4.13 for TXS 0506+056 and the blazar sample [396], respectively, focusing on two benchmark values of the mediator mass $m_Y = 500\,\text{MeV}$ and $5\,\text{GeV}$. For these plots, to keep the discussion minimal, we have fixed $R_{\rm min} = 10^2\, R_S$ as in BMCI. However, we recall that the BBDM and neutrino signals have distinct dependences on the strength of DM-nucleon interactions. The former scales quadratically with the cross section, involving both DM upscattering at the source and elastic scattering at detection. In contrast, the neutrino signal depends linearly on the cross section, as detection proceeds via SM interactions. Consequently, the corresponding bounds scale with the LOS integral as $\Sigma_{\rm DM}^{-1/2}$ for BBDM and as $\Sigma_{\rm DM}^{-1}$ for the neutrino signal. Knowing such scaling, the computed limits and sensitivities to BBDM, and to the blazar neutrinos from DM-proton interaction, can be straightforwardly rescaled for different values of $\Sigma_{\rm DM}$. We show the results for BMCII ($R_{\rm min} = 10^4\, R_S$) in Figure 4.14.

Limits and sensitivities on blazar-boosted DM at neutrino detectors

In general, we find that the most constraining limits from the BBDM signals are currently set by Super-K (we do not show in the plots the limits from KamLAND and Borexino as the ones from SK are more stringent across all the scenarios considered in this work) and are expected to be tightened in the near future by Hyper-K, JUNO, and DUNE: the former due to its larger volume and the latter thanks to their lower energy thresholds, which encompass the peak of the proton recoil spectrum (see Fig. 4.11).

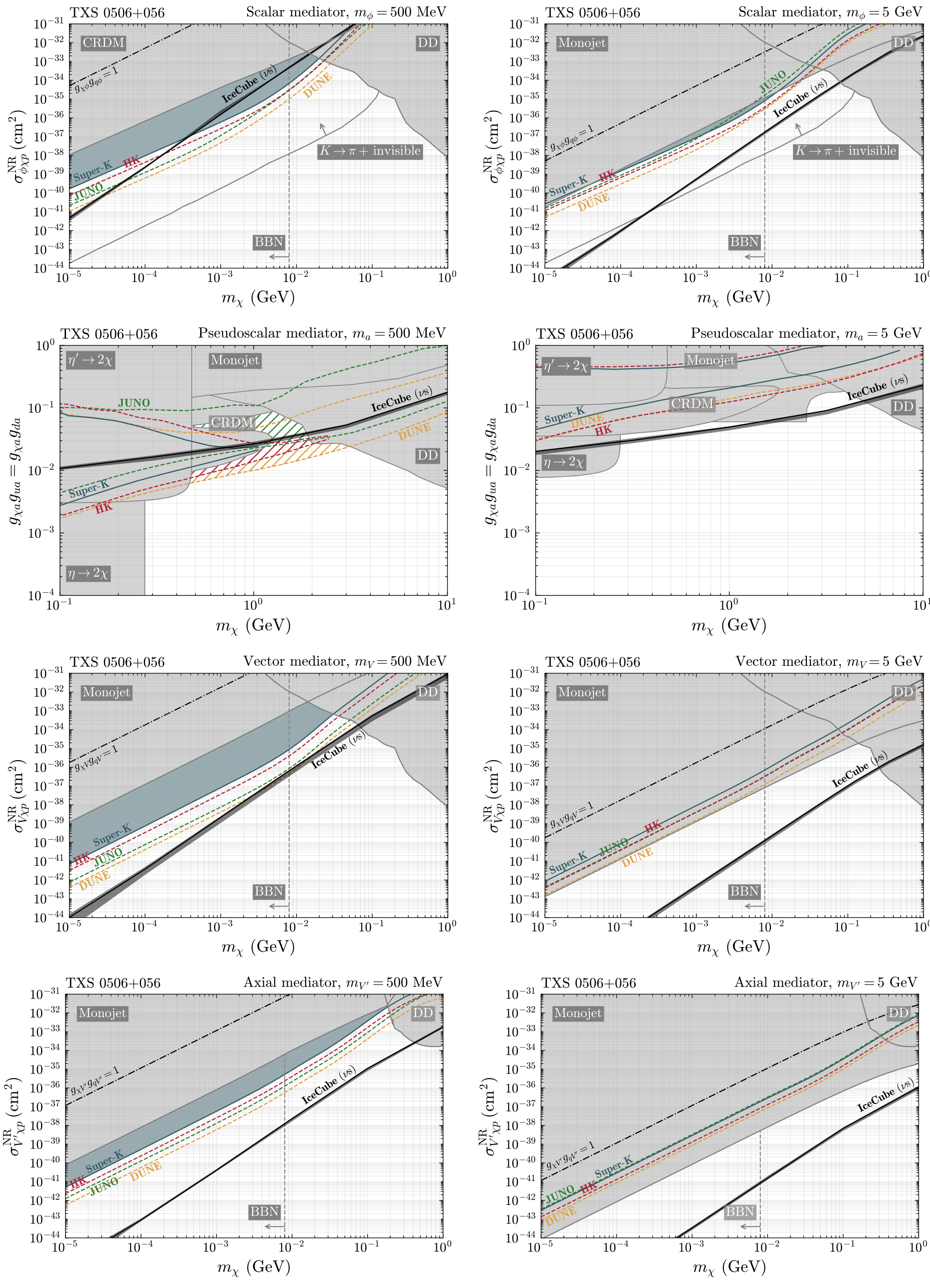

Figure 4.12: **TXS 0506+056.** Limits and sensitivities from TXS 0506+056 in the plane of $\sigma^{\rm NR}_{Y\chi p}$ against DM mass for a scalar (top), vector (third row), and axial (bottom) mediator. For the pseudoscalar case (second row), the limits are shown in the $g_{\chi a} g_{qa} - m_\chi$ plane. We set $m_Y = 500\,\text{MeV}$ (left panels) and $m_Y = 5\,\text{GeV}$ (right panels) for the mass of the mediator and BMCI for the DM LOS integral. Blue shaded areas denote the limits set by SK. Future sensitivities are shown in dashed red (HK), orange (DUNE) and green (JUNO). The 2017 neutrino detected from TXS 0506+056 is explained by the same DM interactions along the black lines [4]. The vertical gray line marks the BBN limit [462, 463] evadable if DM couples to neutrinos. The black dot-dashed line ($g_{\chi Y} g_{qY} = 1$) marks the non-perturbative regime. The shaded grey areas are excluded by various model-dependent searches, see Section 4.1.9 for extensive details on these constraints.

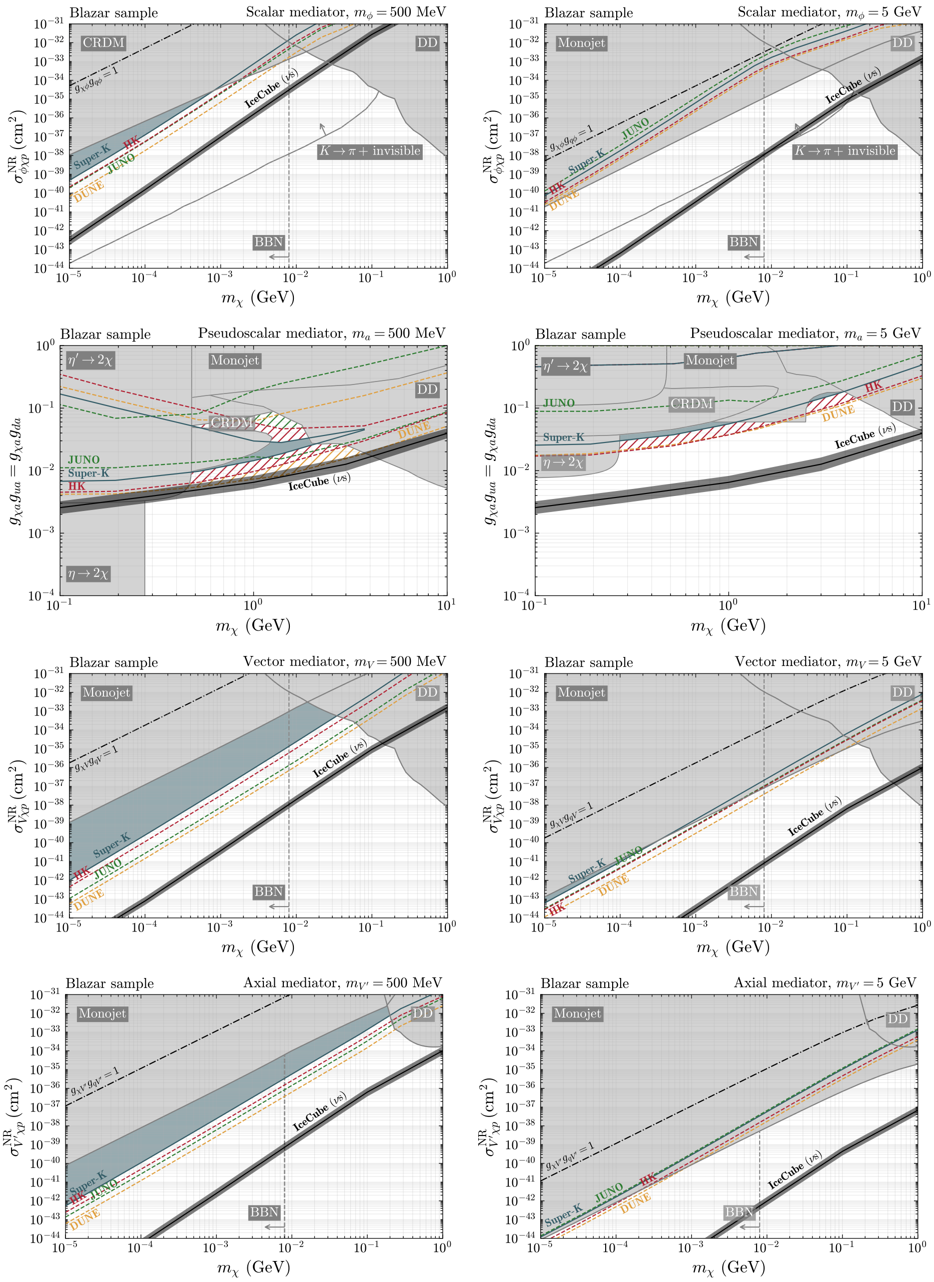

Figure 4.13: **Blazar sample.** Same as in Fig. 4.12 but for the sample of 323 blazars taken from [396] (excluding 3C 371). Along the black continuous lines, the diffuse neutrino flux detected by IceCube [220] is saturated by the same DM interactions from the considered blazar sample. All other details are as in Fig. 4.12.

For $m_Y = 500\,\mathrm{MeV}$, we find that BBDM can probe regions of the parameter space that are currently allowed by existing experiments, for all the four DM-quark interactions that we studied. On the other hand, increasing the mediator mass to $m_Y = 5\,\mathrm{GeV}$ leads to a degradation of the BBDM sensitivity, as collider constraints are only weakly dependent on the value of m_Y, while our BBDM signal gets suppressed. We find indeed that for

$m_Y = 5\,\mathrm{GeV}$ BBDM limits are no longer competitive with existing constraints, even in the optimistic BMCI scenario, as shown in Figs. 4.12 and 4.13.

It is interesting to compare the projected sensitivities of detectors across different interactions and DM masses. In particular, we obtain that JUNO performs relatively worse than the other detectors in the pseudoscalar case for each of the considered benchmark mediator masses, and in all the cases for $m_Y = 5\,\mathrm{GeV}$. The loss of sensitivity of JUNO detector in the pseudoscalar case is due to the suppression at low momentum transfer Q^2 of the pseudoscalar interaction cross section. The dependence on the mediator mass instead arises from the shift of the proton recoil spectrum peak toward higher energies as the mediator mass increases, moving outside JUNO's sensitivity range. For the same reason, we find that DUNE, which has a lower energy threshold than Super-K, leads only to a marginal improvement in the pseudoscalar mediator case, as shown in Figs. 4.12 and 4.13.

Overall, we find that the hierarchy among detectors is non-trivial and strongly depends on the choice of the DM mass, mediator mass, and interaction type, highlighting the importance of using explicit DM models when comparing the reach of different experiments.

Results for BMCII

We show in Fig. 4.14 our limits and sensitivities to BBDM and neutrino signals for TXS 0506+056 and for the blazar sample, derived by assuming the conservative BMCII for the DM spike, namely $R_{\min} = 10^4\,R_S$, and choosing $m_Y = 500\,\mathrm{MeV}$. For this benchmark choice, we find that the BBDM signal can test the DM hypothesis for the 2017 IceCube neutrino event from TXS 0506+056 in the vector mediator case in regions of the parameter space that are still allowed by current DM searches at terrestrial laboratories. This is true also in the scalar mediator case for DM masses approaching the $\mathcal{O}(10\,\mathrm{keV})$ scale (if the $K \to \pi +$ invisible bound does not apply), while otherwise the DM hypothesis for the neutrino signal at IceCube is incompatible with current DM searches. In the case of an axial mediator instead, a neutrino signal from DM around blazar always come before any BBDM signal at neutrino detectors. In the pseudoscalar case, the DM hypothesis is completely ruled out by current DM searches. We further notice that here, for the mass range considered in the plot, the selected neutrino detectors are not sensitive to any BBDM signal. This loss of sensitivity arises from the scaling of the BBDM signal with the LOS integral: both the projected limits and sensitivities obtained for BMCI are suppressed in BMCII by a factor of $\left(R_{\min}^{\mathrm{BMCII}}/R_{\min}^{\mathrm{BMCI}}\right)^{1/3} = 10^{2/3}$, resulting in a substantial reduction in the detectable signal strength.

Conversely, we find that the diffuse neutrino signal from DM-proton interaction in the blazar sample remains always dominant over the BBDM one. In the vector and axial mediator scenarios, both the diffuse BBDM signal at future neutrino detectors and the diffuse neutrino signal at IceCube from DM around blazar are currently allowed by existing DM constraints. However, the neutrino signal is expected to appear first, as the corresponding curve lies below the BBDM sensitivities. In contrast, the pseudoscalar case is entirely excluded by current bounds, while the scalar case remains largely, but not completely, ruled out.

We do not show the case of $m_Y = 5\,\mathrm{GeV}$ for the BMCII scenario, as the BBDM mechanism would already be excluded by current DM search constraints for all the considered toy models of DM-quark interactions. However, the DM interpretation for the IceCube neutrinos remains viable, see [3, 4].

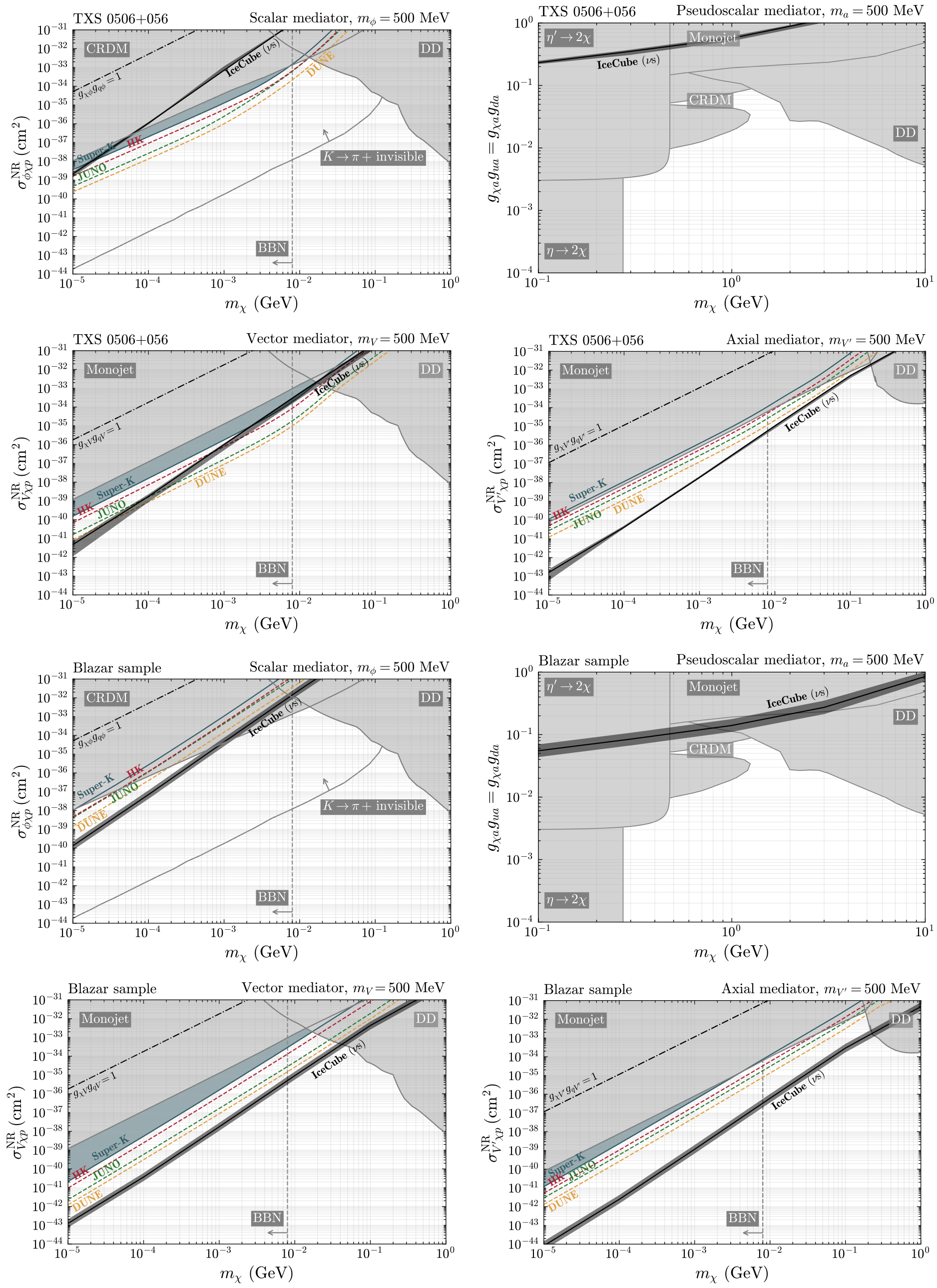

Figure 4.14: Limits and sensitivities to DM blazar signals from TXS 0506+056 (first four panels) and the considered blazar sample (last four panels) for $m_Y = 500\,\mathrm{MeV}$ and $R_{\rm min} = 10^4\,R_S$ as in BMCII. All the other details are as in Fig. 4.12 and Fig. 4.13.

Neutrino signals from DM around blazars survive BBDM searches

Inelastic DM-proton interactions can induce proton disintegration, leading to the emission of high-energy neutrinos which can be detected at large-volume neutrino telescopes, such as IceCube. Clearly, the parameters governing the production of neutrino from DM-proton inelastic scatterings are the same as those that control the BBDM signal discussed in this work. This naturally raises the question of whether the two types of signals are mutually compatible, if one should be observed before the other, or if the absence of one of the two could constrain the viability of the other.

In [3], we computed the neutrino flux from DM-proton inelastic interactions around the blazar TXS 0506+056, and identified the regions in the $\sigma^{\rm NR}_{Y\chi p} - m_\chi$ plane allowing to explain the 2017 IceCube neutrino event via this mechanism, specifically for vector and scalar mediator models with $m_Y = 5\,\text{GeV}$. We have extended such analysis for TXS 0506+056 in [4] covering the same DM models considered here, both for $m_Y = 500\,\text{MeV}$ and $5\,\text{GeV}$. Furthermore, in the same work, we have also evaluated the diffuse neutrino flux arising from DM-proton interactions across the same blazar sample analysed in this study and extracted the corresponding combinations of DM parameters that leads to saturation of the diffuse neutrino flux observed by IceCube [220]. The results of the analyses performed in [3, 4] for BMCI, are represented in Figs. 4.12 and 4.13 in black, in order to compare them against BBDM limits and sensitivities.

A non-trivial hierarchy immediately emerges between the BBDM and neutrino signals: the former is primarily controlled by elastic interactions, while the latter relies on inelastic processes. As a result, increasing the mediator mass tends to enhance the relative strength of the latter.

In general, we highlight that when the region that corresponds to the neutrino prediction lies inside the BBDM sensitivity regions, the observation (or non-observation) of a BBDM signal at future neutrino detectors can serve as a test of the DM interpretation of the IceCube neutrinos. According to the Figs. 4.12 and 4.13, this situation arises in the case of TXS 0506+056 when $m_Y = 500\,\text{MeV}$: for the scalar mediator scenario at $m_\chi \lesssim 0.2\,\text{MeV}$ DM masses, for the pseudoscalar case around $m_\chi \sim \mathcal{O}(\text{GeV})$, and for the vector mediator around $m_\chi \sim \mathcal{O}(10\,\text{MeV})$. For the blazar sample, a similar overlap occurs only mildly, and only for DUNE.

If the neutrino prediction region lies below the BBDM ones, any future observation of a BBDM signal would imply that a corresponding neutrino flux should have already been observed, thereby disfavouring the DM origin of the BBDM signal under the same interaction model. Conversely, a null observation of BBDM in this situation would remain fully compatible with the DM interpretation of the neutrino signal. This scenario occurs in all other cases we considered, except for the scalar mediator scenario for TXS 0506+056 with $m_\phi = 500\,\text{MeV}$ and $m_\chi \gtrsim 0.2\,\text{MeV}$, where the DM hypothesis for the IceCube neutrinos is incompatible with the null observations of BBDM signals at Super-k.

Finally, we comment on the differences between the signals from TXS 056+056 and the blazar sample. These are mainly due to the astrophysical parameters of the lepto-hadronic fits. In the case of the blazar sample, the proton spectral index and the minimum proton Lorentz factor in the blob are taken to be $\alpha_p = 1$ and $\gamma'_{\min_p} = 100$, respectively, thus enhancing the contribution of higher-energy protons. In contrast, for TXS 0506+056, we adopt $\alpha_p = 2$ and $\gamma'_{\min_p} = 1$, thereby giving more weight to lower-energy protons. This, overall, leads to differences in the resulting BBDM flux and nuclear recoil spectra (see Figs. 4.7, 4.8 and 4.11), which ultimately translate into distinct projected limits and sensitivities for the two cases. Regarding neutrino production from DM-proton scattering, this is more prominent in scenarios where high-energy protons dominate, as they are more efficient at producing neutrinos through inelastic collisions. It is worth emphasising that this choice of α_p is not strongly motivated for the considered sample, and was effectively fixed in the fit by hand [396]. Indeed, variations in α_p would significantly affect the relative strength of the neutrino and BBDM signals and could make the latter a test of the former signal over a wider range of parameters.

4.1.9 Constraints on the parameter space

Model independent constraints

The effect of a new particle species ψ with thermal abundance and energy density ρ_ψ is to increase the Hubble parameter H at a given epoch as $H^2 \propto \rho_{\rm tot}$. Assuming that ψ does not have a large chemical potential, ρ_ψ is controlled only by its mass m_ψ and temperature T. As in our benchmark points we assume for the mediators $m_Y \sim \mathcal{O}(1)$ GeV, for the range of couplings that we probe, Y decays well before BBN, thus not altering its predictions. However the presence of thermal DM affects $N_{\rm eff}$, hence the values of helium and deuterium primordial abundances, requiring $m_{\rm DM} \geq \mathcal{O}(10)$ MeV. This bound can actually be relaxed by switching on a coupling of the mediators to neutrinos [463, 462].

Constraints from telescope searches of DM annihilation products, including those coming from CMB, are more dependent on the cosmological DM history. For example they (almost [464, 465, 466]) disappear in the case of asymmetric DM, where instead our mechanism works the same, both in explaining IceCube's neutrinos and in BBDM. Therefore we do not display any indirect detection limit in Figs. 4.12 and 4.13, keeping in mind that possible signals of sub-GeV DM at telescopes could test our mechanism in some of its specific realisations.

The parameter space is constrained also by conventional direct detection (DD) experiments. For the spin-independent DM-nucleon interaction cross section we combine the constraints from TESSERACT [467], SuperCDMS [151], SENSEI's [157], CRESST-III [154], DarkSide-50 [155], LUX-ZEPELIN (LZ) [121], XENONnT [468, 120], and we show the DD bounds in Figs. 4.12 and 4.13. For spin-dependent interactions we combine bounds from Borexino [163], delayed coincidence searches in near-surface detector [469] and NEWS-G [156]. We do not include in our plots bounds based on the Migdal effect in liquid Xenon (e.g. [470, 471]) because the theory prediction of this effect in liquid Xenon is in conflict with SM experiments [160].[7]

Model dependent constraints

While BBN and DD constraints are largely model-independent, laboratory bounds crucially depend on the nature of the DM interactions with SM particles. We summarize below the most relevant limits for each of the mediator cases studied in this work.

- **Scalar mediator**

  Scalar mediators can be constrained by both meson decays and collider searches. Rare kaon decays [472] impose strong bounds on decays to invisible final states, including DM. We report as solid grey line in our Figs. 4.12 and 4.13 the bound for $g_{t\phi} = 0$, corresponding to the gluon coupled case in Fig. 2 of [473]. DM pairs can be produced at colliders together with SM radiation via processes like $q\bar{q} \to g\,\phi \to g\,\chi\bar{\chi}$. Based on the recasting performed in [165], we show constraints from monojet plus missing energy searches at the LHC [474]. These are stronger than the ATLAS [475] and CMS [476]

[7] Ref. [160] reported a number of Migdal events, from neutrons off liquid Xenon, compatible with zero and with the uncertainty of the theory prediction, whose central value is one order of magnitude larger.

limits, which moreover rely on the mediator coupling to top quarks. Stringent constraints also arise from searches for cosmic ray accelerated DM (CRDM) [163, 164]. CRDM limits imposed by SK and KamLAND searches in the same scalar scenario considered by us has been computed in [165] for $m_Y = 1\,\text{GeV}$ and $3\,\text{GeV}$ (which we consider in place of $m_Y = 500\,\text{MeV}$ and $5\,\text{GeV}$, respectively), and these are stronger than those obtained from monojet searches at colliders when $m_Y = 500\,\text{MeV}$.

- **Pseudoscalar mediator**

  Processes such as $\pi^0 \to 2\chi$, $\eta \to 2\chi$, and $\eta' \to 2\chi$ constrain this scenario through the mixing between the pseudoscalar mediator and light mesons. Bounds are derived from the upper limits on the invisible decay width of these states [74]. As shown in [165], introducing a coupling g_{sa} between the strange quark and the pseudoscalar mediator can relax the constraints. However, we conservatively shade the excluded regions assuming $g_{sa} = 0$ and $g_{ua} = g_{da}$. Bounds from monojet searches at the LHC apply similarly to the scalar case. We also consider CRDM limits from SK and KamLAND for this scenario, recasting them from [165].

- **Vector and axial mediators**

  Limits from monojet searches at TeVatron and the early LHC, as recasted [477], read $g_q \leq 0.02$ and are independent of the mediator mass, as long as it is significantly lighter than the cuts used in those searches (which is true for all m_Y benchmarks that we use. These limits are stronger than monojet CMS ones on light spin-1 mediators [476].

Among the limits discussed so far, the only ones that do not scale with powers of $g_{\chi Y} g_{qY}$ are those coming from monojet searches for $m_Y > 2m_\chi$, which are proportional to g_{qY} only. In drawing them in Figs. 4.12 and 4.13 we then need to make an assumption for one of the couplings, and we choose $g_{\chi Y} = 1$. Had we chosen smaller values of $g_{\chi Y}$, this would have implied larger values of g_{qY} on the plots, so that monojet limits would have become relatively stronger. The reader interested in the benchmark $g_{\chi Y} \simeq g_{qY}$, for example, can obtain its status by leaving all limits where they are on the plots, and making the monojet limits stronger by a factor $(g_{\chi Y} g_{qY})^{1/2}_{\text{lim}}$, where $(g_{\chi Y} g_{qY})_{\text{lim}}$ is the monojet limit. The limit $(g_{\chi Y} g_{qY})_{\text{lim}}$ can be directly read-off the plot for the pseudoscalar mediator, and for the other mediators it can be obtained from the line $g_{\chi Y} g_{qY} = 1$ knowing that $\sigma^{\text{NR}}_{Y\chi p} \propto (g_{\chi Y} g_{qY})^2$. Compared to our $g_{\chi Y} = 1$ benchmark, the one $g_{\chi Y} \simeq g_{qY}$ would then restrict the parameter space where blazar signals (either neutrinos produced by DM-p scatterings or BBDM) are the dominant probe of DM, but would not change the qualitative message of our study.

While we have assumed the mediators to couple to u and d quarks only, let us briefly comment that new strong limits would arise if they also coupled to heavier quarks. A coupling to top quarks would for example induce, at one loop, sizeable decays of B mesons into lighter mesons plus DM, see e.g. [153]. Couplings to the charm or bottom quarks would induce invisible (plus possibly other particles, depending on the mediator) decays of the QCD vector resonances J/ψ or Υ. Searches for their invisible decays at BES and BABAR would translate into limits on those couplings, see e.g. [165] for light scalars and [478] for light vectors.

We finally comment on possible EW-invariant realization of our toy-models of Eqs (4.14), (4.15), (4.16) and (4.17) and on their implications for the DM couplings. While the couplings $g_{\chi Y}$ do not involve SM fields and therefore pose no problems in this respect, those to quarks

g_{qY} require some specification. They can for instance be obtained via mixing of SM fermions with vector-like heavy quarks, see e.g. [165] for scalar and pseudoscalar mediators and [478] for vector and axial vector ones. Such UV-completions also allow to obtain the hierarchy $g_{\chi Y}/g_{qY} \ll 1$, that we assumed for monojet limits in Figs 4.12 and 4.13.[8] However, it can be challenging to obtain $g_{\chi Y}/g_{qY} \ll 1$ in other UV completions, see [479].

4.1.10 Conclusions and Outlook

This thesis has explored a new origin for high-energy astrophysical neutrinos observed by IceCube, based on deep inelastic scatterings between protons in blazar jets and sub-GeV DM clustered around these sources. We first applied this mechanism to TXS 0506+056, the only blazar associated at the 3σ level with an extragalactic neutrino detected by IceCube in 2017. Standard one-zone lepto-hadronic models of blazar jets, commonly employed to explain the spectral energy distribution (SED) and neutrino emission, fall short in reproducing the neutrino flux observed from TXS 0506+056 [207, 395]. In contrast, our proposed explanation based on DM–proton inelastic scatterings can reproduce the observed neutrino flux from this event using the same jet models, under conservative assumptions for DM clustering around the blazar. We demonstrated that this mechanism remains viable across the full set of DM–quark interaction types analyzed in [3], and that the required DM parameter space is compatible with all current collider and direct detection constraints.

We further extended this mechanism to the diffuse astrophysical neutrino flux above 100 TeV, showing that it can be saturated by the same class of interactions, across different jet models and DM–quark mediators [4].

While our scenario introduces additional parameters like multi-zone models of blazar jets do, it offers a key advantage: the potential for independent testing in terrestrial DM searches, such as standard direct detection experiments, collider experiments and neutrino detectors. To this purpose, we studied the blazar-boosted DM (BBDM) signal at neutrino detectors (Super-K, Hyper-K, DUNE, JUNO) using the same DM parameter space that explains the TXS 0506+056 and the diffuse neutrino fluxes. Importantly, we found that in many viable regions of the parameter space, the non-observation of BBDM recoil events does not rule out the DM explanation of IceCube neutrinos. Therefore, our scenario remains viable even in the absence of direct BBDM signals, while still allowing for potential discovery prospects in future experiments.

Therefore, high-energy neutrino observations performed by IceCube could provide the first hints of non-gravitational DM interactions. Our findings open several directions for future work, including the study of DM-induced photon signatures via the inclusion of DM in blazar fits, refined modeling of jet-DM interactions, and improved understanding of DM clustering near active galactic nuclei. Together, our results suggest that neutrinos from blazars may offer a new window into both astrophysical environments and fundamental particle physics.

[8] In such UV-completions, both axial and vector couplings are generated unless one is willing to tune the UV parameters. This does not pose a problem to our mechanism, it just makes DD limits slightly stronger for the axial case.

4.2 Boosted Relic Neutrinos and Cosmic Ray Upscattering

4.2.1 Introduction

The relic neutrino background (RνB), see Sec. 2.1, is referred to as the "Holy Grail" of neutrino physics. It is the only sub-component of DM that is predicted by the standard cosmological model (ΛCDM), with a present temperature and number density per-flavour (counting neutrinos and antineutrinos separately) of [480]

$$T_{\nu,0} \simeq 1.67 \times 10^{-4}\,\text{eV}, \quad n_{\nu,0} \simeq 56\,\text{cm}^{-3}. \tag{4.51}$$

Its detection would give new observational access to the earliest cosmological times ever probed. We have indirect evidence for it via early Universe observations [14, 150], but none of the existing techniques to detect the local RνB is expected to discover it in the foreseeable future, see [481] for a recent overview. It has been furthermore pointed out that the PTOLEMY [174, 482] experiment, which aims at detecting the RνB by capture on tritium, is insensitive to it, if graphene is used to stock tritium, because of Heisenberg uncertainty [483, 484]. Experiments aiming at detection of the local RνB then only test the case where its local density is much larger than the diffuse cosmological one $n_{\nu,0}$ by an overdensity factor $\eta_\nu^{\text{Earth}} > 1$. The strongest such limit has been set by the KATRIN experiment [485] and reads $\eta_\nu^{\text{Earth}} < 1.3 \times 10^{11}$, in the same ballpark of limits from the RνB gravitational effects in the Solar System [486]. Given that gravitational clustering can induce at most $\eta_\nu^{\text{Earth}} \sim 10^2$ [487], these experiments then only test the BSM scenarios, if any, that lead to those large local overdensities. The RνB could also be indirectly tested via features that its scatterings induce in UHE neutrinos on their way to Earth [488, 489]. IceCube observations constrain this way $\eta_\nu \lesssim 10^{11}\,(10^8)$ on scales of 10 kpc (of the 14 Mpc that separate us from NGC 1068) [490]. Resonant dips in UHE cosmogenic neutrinos [491], not observed so far [232, 229], could at best test $\eta_\nu \sim 10^{11}$ on scales of the entire Universe [492], which are already ruled-out by not over-closing it.

The main challenge to detect the RνB is its tiny energy, as a consequence of its low temperature $T_{\nu,0}$. A possible way-out consists in looking for consequences of the highest-energy scatterings that the RνB can undergo in the Universe, so to maximise their SM cross sections. To our knowledge, the first exploration along these lines was the computation of the RνB flux up-scattered by ultra-high-energy (UHE) cosmic rays (CRs), carried out by Hara and Sato in the 80's [493, 494], when much less than today was known about both neutrinos and UHECRs. This idea has been dormant for forty years, until the authors of [495] revived it and, from the non-observation of such an up-scattered RνB flux at IceCube, constrained overdensities in the ballpark of $10^{13}\,(10^{11})$ on scales of about 10 kpc in the MW (around the blazar TXS 0506+056). While the study [495] is sufficient to set a rough limit, it has limitations, like assuming that all UHECRs are protons (which we know is not the case [215, 496]), as well as using an oversimplified SM cross section. These should be addressed in order to possibly hope to detect the up-scattered RνB flux and disentangle it from other neutrinos that could show up in a similar energy range, like cosmogenic ones.

The RνB overdensities tested by the techniques above are not only considerably larger than those achievable via gravitational clustering [487], but also violate the Pauli exclusion principle unless one introduces BSM physics that would cluster the RνB more than gravity, see [497] for a systematic assessment. To our knowledge, the largest overdensities achieved in a fully worked-out BSM model rely on a tiny long-range neutrino self-interaction [498]. They read $\eta_\nu^{\text{BSM}} \simeq 10^7\,(m_\nu/0.1\text{ eV})^3$, where m_ν is the neutrino mass scale, and extend up to a volume of the size of a galaxy cluster, motivating to test large overdensities in these environments.

In this section we propose to look for the RνB up-scattered by UHECRs in clusters that act as CR-reservoirs [499, 500, 501, 502, 503, 186, 504] and calculate the associated fluxes. This idea benefits from the long trapping times of CRs in these environments, and from the knowledge on them that is available today and will increase with upcoming observations in the near future. Additionally, we improve over [495] in the calculation of UHECR-up-scattered RνB fluxes in a number of ways, which we will show to be quantitatively important.

4.2.2 Up-scattering the relic neutrino background with cosmic rays

The flux of accelerated relic neutrinos per unit energy E_ν, from the up-scattering environments of interest, can be written as

$$\frac{d\Phi_\nu}{dE_\nu} = D_{\rm eff}\, n_{\nu,0}\, \bar{\eta}_\nu \int_{E_{\rm CR}^{\rm min}(E_\nu)}^{E_{\rm CR}^{\rm max}} dE_{\rm CR} \frac{d\Phi_{\rm CR}}{dE_{\rm CR}} \frac{d\sigma_{\nu{\rm CR}}}{dE_\nu}, \tag{4.52}$$

where the effective distance $D_{\rm eff}$ contains information on the spatial distribution of relic neutrinos and CRs; $\bar{\eta}_\nu \equiv (1/V) \int_V d^3\vec{r}\, \eta_\nu(\vec{r})$ is the RνB overdensity averaged over the volume V, with $\eta_\nu(\vec{r}) = n_\nu(\vec{r})/n_{\nu,0}$ and $n_\nu(\vec{r})$ being the neutrino number density at position $\vec{r}$; $E_{\rm CR}^{\rm min}(E_\nu)$ is the greatest value between the minimal available CR energy and the lowest energy required by the kinematics of the scattering; $E_{\rm CR}^{\rm max}$ is the largest CR energy in their flux; $d\Phi_{\rm CR}/dE_{\rm CR}$ is the CR flux per unit of CR energy $E_{\rm CR}$; $d\sigma_{\nu{\rm CR}}/dE_\nu$ is the differential cross section for the ν-CR scattering. The dependence on the up-scattering environment, in this letter either the MW or CR-reservoirs, is contained in $D_{\rm eff}$ and $d\Phi_{\rm CR}/dE_{\rm CR}$. The total neutrino flux is understood to be the sum of Eq. (4.52) over all neutrinos and nuclear species composing CRs.

Neutrino-nucleus scattering at UHEs

We consider the up-scattering of a relic (anti)neutrino ν ($\bar{\nu}$) by a cosmic nucleus $\mathcal{N}$ via pure SM neutral current (NC) interaction. At the ν-$\mathcal{N}$ exchanged energies that we are interested in, the scattering is described by that on the nucleons $N = p, n$ as

$$\frac{d\sigma_{\nu\mathcal{N}}}{dE_\nu}(E_\mathcal{N}) \simeq \frac{A_\mathcal{N}}{2} \left[\frac{d\sigma_{\nu p}}{dE_\nu} \left(\frac{E_\mathcal{N}}{A_\mathcal{N}} \right) + \frac{d\sigma_{\nu n}}{dE_\nu} \left(\frac{E_\mathcal{N}}{A_\mathcal{N}} \right) \right], \tag{4.53}$$

where we have focused for simplicity on isoscalar nuclei with equal number $A_\mathcal{N}/2$ of protons and neutrons, each carrying a fraction $1/A_\mathcal{N}$ of the nucleus's energy $E_\mathcal{N}$, and summed over elastic scattering (ES) and deep inelastic scattering (DIS) contributions: $d\sigma_{\nu N}/dE_\nu = d\sigma_{\nu N}^{\rm ES}/dE_\nu + d\sigma_{\nu N}^{\rm DIS}/dE_\nu$. The ES part, summed over ν and $\bar{\nu}$, reads [505, 506]

$$\frac{d\sigma_{\nu N}^{\rm ES}}{dE_\nu} = \frac{2G_F^2 m_\nu m_N^4}{\pi (s - m_N^2)^2} \left[A_N(Q^2) + C_N(Q^2) \frac{(s-u)^2}{m_N^4} \right], \tag{4.54}$$

where G_F is the Fermi constant; $s = 2m_\nu E_N + m_N^2 + m_\nu^2$, $Q^2 = 2m_\nu(E_\nu - m_\nu)$ is the momentum transfer squared, $u = 2m_\nu^2 + 2m_N^2 - s + Q^2$; $m_{N(\nu)}$ is the nucleon (neutrino) mass and $E_{N(\nu)}$ is the energy of the incoming nucleon (outgoing neutrino) in the frame in which the initial neutrino is at rest. The functions A_N and C_N are given in Appendix C.1 (see, e.g., [505, 506]) and strongly suppress ES for $Q^2 \gtrsim m_N^2 \approx \text{GeV}^2$. The DIS, in which the initial neutrino interacts directly with the quark constituents of the nucleons, takes over for $E_N \gtrsim 10^{10-11}$ GeV, given $Q^2 \lesssim s$ and $m_\nu \approx 0.1\,\text{eV}$, thus being necessary to describe the highest-energy part of the up-scattered RνB flux. For the NC ν-N DIS cross section we adopt

$$\begin{aligned}\frac{d\sigma_{\nu N}^{\text{DIS}}}{dE_\nu} \simeq \sum_{a=q,\bar{q}} & \frac{G_F^2[(g_V^a)^2+(g_A^a)^2]}{2\pi E_N} \\ & \times \int_{y_{\min}}^1 \frac{dy}{y^2}\,\frac{Q^2 f_a^N(x,Q^2)}{[1+Q^2/M_Z^2]^2}\, g(y,Q^2,m_N),\end{aligned} \tag{4.55}$$

where $g(y,Q^2,mN) \equiv (y^2-2y+2-2m_N^2x^2y^2/Q^2)$, M_Z is the Z boson mass, y is the inelasticity parameter satisfying $y_{\min} = (E_\nu - m_\nu)/E_N \lesssim y \le 1$, $x = (E_\nu - m_\nu)/(E_N y)$ is the Bjorken scaling variable and $f_a^N(x,Q^2)$ is the parton distribution function (PDF) for the quark a having NC vector and axial coupling g_V^a and g_A^a, $a = u,d,s,c,b$ (we neglect any contribution from the top quark). We evaluate the PDFs with the Python package `parton` using the "CT10" PDF set [449] (see also this website for more details). For simplicity, we do not take the coherent ν-$\mathcal{N}$ scattering into account as it could contribute only at energy scales smaller than those of interest to our study [507, 506], and neglect the contribution to $d\sigma_{\nu\mathcal{N}}/dE_\nu$ from hadronic resonances [508, 509], relevant for $Q^2 \approx \text{GeV}^2$, so that in the considered range our results are conservative. Details on the derivation of Eq. (4.55) are given in Appendix C.2.

CRs up-scattering RνB *en route* to Earth

As they travel towards the Earth, UHECRs up-scatter the RνB with the largest cross sections among all CRs, and induce a flux described by Eq. (4.52). While the bulk of CRs with energy much below the EeV are believed to originate within the MW [212, 213] and to be mostly protons below the PeV [510], UHECRs above the EeV scale are today understood as having an extragalactic origin, see e.g. [511, 512, 513], and a mixed composition with heavier nuclei dominating over protons, see e.g. [514, 515, 516, 496, 517, 215, 518, 214]. We therefore employ the CR spectrum $d\Phi_{\text{CR}}/dE_{\text{CR}}$ from [215] and, by considering up-scatterings in the MW with the line-of-sight integral $D_{\text{eff}} \approx 10$ kpc as in [495] (see e.g. [519, 455, 520] for studies of the uncertainties on D_{eff}, where the RνB case is analogous to relativistic DM fluxes and cored profiles like Isothermal), we obtain the flux reported as a dot-dashed line in Fig. 4.16 (see further). Our calculation improves over the analogous one [495] by going beyond the proton-only composition of CRs and by implementing the momentum transfer dependence and DIS in the cross section. It results in a significantly different flux with respect to [495], see Figure 4.15 for details of the comparison.

Since tentative sources of UHECRs are located at $1 \sim 100\,\text{Mpc}$ from Earth [521, 522, 523, 524, 525], D_{eff} can be larger than 10 kpc by orders of magnitude, resulting in a sensitivity to $\bar{\eta}_\nu \sim 10^{10-11}$. Still, these enormous $\bar{\eta}_\nu$ over such long distances are hard to justify without spoiling the large-scale homogeneity of the Universe, motivating us to look for environments where D_{eff} can be sizeable while keeping neutrino overdensities localised on smaller scales.

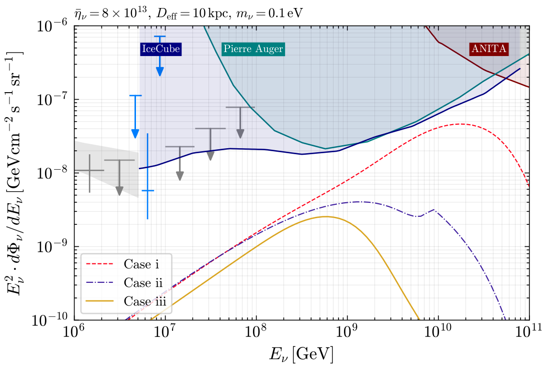

Figure 4.15: Comparison between different procedures used to calculate the boosted all-flavour relic neutrino flux according to Eq. (4.52), with $\bar{\eta}_\nu = 8 \times 10^{13}$, $D_{\rm eff} = 10\,{\rm kpc}$ and $m_\nu = 0.1\,{\rm eV}$. The dashed red line corresponds to case i) for which a low-energy limit of the elastic scattering cross section and a pure proton CR flux are considered; the dot-dashed purple line to case ii) with a full elastic plus inelastic cross section and a pure proton CR flux; the thick yellow line to case iii) with a full cross section and a mixed CR composition according to Scenario 1 of [215]. See the text for further details. The excluded regions and data points are as in Fig. 4.16.

Boosted Relic Neutrinos from Cosmic Rays: Revisited

We revisit the computation of the CR-induced boosted relic neutrino flux discussed in [495], implementing the full cross section with Q^2-dependence of the form factors, the DIS contribution and a mixed CR composition. Firstly, we note that the ES cross section in the low-energy limit $2m_\nu E_N \lesssim m_N^2$ [505] reads:

$$\frac{d\sigma_{\nu N}^{\rm ES}}{dE_\nu} \simeq \frac{G_F^2 (s - m_N^2)^2}{16\pi s\, T_\nu^{\rm max}(T_N)} [(1 - 4s_{\rm W}^2)^2 + 3\,(G_{\rm A}(0))^2], \tag{4.56}$$

with $T_\nu^{\rm max}(T_N)$ as given in Eq. (C.23). The expression in Eq. (4.56) resembles the expression reported in [495] in the same limit, apart from an overall $\mathcal{O}(1)$ factor. Our calculation of the cross section differs instead more with respect to the one in [495] for $2m_\nu E_N \gtrsim m_N^2$.

We show in Fig. 4.15 the neutrino flux computed according to Eq. (4.52), with $m_\nu = 0.1\,{\rm eV}$, $D_{\rm eff} = 10\,{\rm kpc}$, $\bar{\eta}_\nu = 8 \times 10^{13}$ roughly saturating the limit given in [495], and different benchmark cases described in what follows. Our choice of $D_{\rm eff}$ is motivated if the neutrino overdensity is localised on a scale of the order of the MW radius.

i) The red dashed line is obtained by taking the cross section as in (4.56) after recasting the all-species CR flux as observed at Earth from [214] in the energy range $10^5\,{\rm GeV} \lesssim E_{\rm CR} \lesssim 200\,{\rm EeV}$ and assuming a pure proton composition from the lowest to the largest energies. With this procedure we obtain results that are comparable (but not overlapping) with those presented in [495].

ii) The dot-dashed purple line is obtained by considering the full Q^2-dependent cross section as a sum of the elastic and deep inelastic contributions, while keeping the pure proton CR flux as in case i). We note a suppression compared to case i) starting from $E_\nu \sim {\rm EeV}$ due to the form factors $A_N(Q^2)$ and $C_N(Q^2)$ of the elastic cross section, as well as a kick at $E_\nu \sim 10\,{\rm EeV}$ because of the DIS.

iii) The thick yellow curve is obtained by considering the full cross section as in case ii) and a mixed composition for the CR flux according to the analysis presented in [215]. Concentrating on the extragalactic contribution only, we considered this flux in the energy range $10^8\,\mathrm{GeV} \lesssim E_{\mathrm{CR}} \lesssim 200\,\mathrm{EeV}$. For definiteness, we focused on the Scenario 1 described in [215], in which the proton composition gets suppressed earlier compared to heavier nuclei, thus implying an attenuation of the boosted relic neutrino flux.

We point out that the analogous flux in Fig. 4.16 is obtained as in case iii), but considering three neutrino species with masses that saturate the cosmological bound [76] – while that in Fig. 4.15 is for three degenerate neutrinos with reference mass $m_\nu = 0.1\,\mathrm{eV}$ – and starting the integration from $E_{\mathrm{CR}}^{\mathrm{ankle}}$ to remain conservative on the galactic-to-extragalactic transition.

We find that the implementation of the full momentum transfer dependence of the neutrino-nucleus cross section, the deep inelastic scattering contribution and a mixed CR composition, leads to a boosted relic neutrino flux suppressed significantly with respect to what reported in [495], and, correspondingly, the bounds on the local neutrino overdensity are weakened by an overall $\mathcal{O}(10)$ factor.

Boosted RνB from CR-reservoirs

A possible explanation for the extragalactic origin of UHECRs is that they are produced inside galaxy clusters, in which they reside up to cosmological times before escaping and contributing to the UHECR flux on Earth [499, 500, 501, 502, 503, 186, 504] (see also [218] for a review). The distance they travel inside these gigantic CR-reservoirs would be roughly $c\tau_{\mathrm{esc}} \simeq 0.3\,\mathrm{Gpc}\,(\tau_{\mathrm{esc}}/1\,\mathrm{Gyr})$, where τ_{esc} is the time CRs spend in the cluster before their release. The effective distance entering Eq. (4.52) can be written as $D_{\mathrm{eff}} = \mathcal{B} c\tau_{\mathrm{esc}}$, having defined the spatial boost factor

$$\mathcal{B} \equiv \int_V d^3\vec{r} f_{\mathrm{CR}}(x)\, \delta_\nu(\vec{r})\,, \tag{4.57}$$

with $\delta_\nu(\vec{r}) \equiv \eta_\nu(\vec{r})/\bar{\eta}_\nu$ and $f_{\mathrm{CR}}(\vec{r})$ the spatial profile of the CR flux inside a CR-reservoir of volume V, normalised such that $\int_V d^3\vec{r} f_{\mathrm{CR}}(\vec{r}) = 1$. One has $\mathcal{B} = 1$ for a homogeneous RνB, $\delta_\nu(\vec{r}) = 1$, while $\mathcal{B} > 1$ if, e.g., the number densities of both UHECRs and neutrinos are peaked at small radii. In what follows, we fix $\mathcal{B} = 1$ and $\tau_{\mathrm{esc}} \simeq 2\,\mathrm{Gyr}$ [186], neglecting any dependence on the CR energy that τ_{esc} (and $\mathcal{B}$) may have. We checked that implementing the τ_{esc} energy-dependence as in [504] would only slightly (enhance) suppress the (low-energy) high-energy tail of the boosted RνB spectrum, without altering significantly our final results.

We model UHECRs in cluster reservoirs following [186]. For each nucleus $\mathcal{N}$, we write

$$\frac{d\Phi_{\mathcal{N}}}{dE_{\mathcal{N}}} = K_{\mathcal{N}} \left(\frac{E_{\mathcal{N}}^{\max}}{E_{\mathcal{N}}}\right)^{\alpha} e^{-E_{\mathcal{N}}/E_{\mathcal{N}}^{\max}}\,, \tag{4.58}$$

where $2 \leq \alpha \leq 2.5$ and $E_{\mathcal{N}}^{\max}/Z_{\mathcal{N}} \simeq 7.69 \times 10^{10}\mathrm{GeV}$, $Z_{\mathcal{N}}$ being the atomic number of $\mathcal{N}$. We checked that varying $E_{\mathcal{N}}^{\max}$ within a factor of up to five from our benchmark choice has a comparable impact, on the detectability of the RνB flux, to varying $2 \leq \alpha \leq 2.5$. We consider the relative nuclear abundances as given in [186] and fix the normalisation factors $K_{\mathcal{N}}$ by requiring that the total luminosity emitted from the entire population of CR-reservoirs matches with the one observed at Earth. Concerning the flux, one could proceed by summing the contribution from all CR-reservoirs in the entire Universe, but this requires

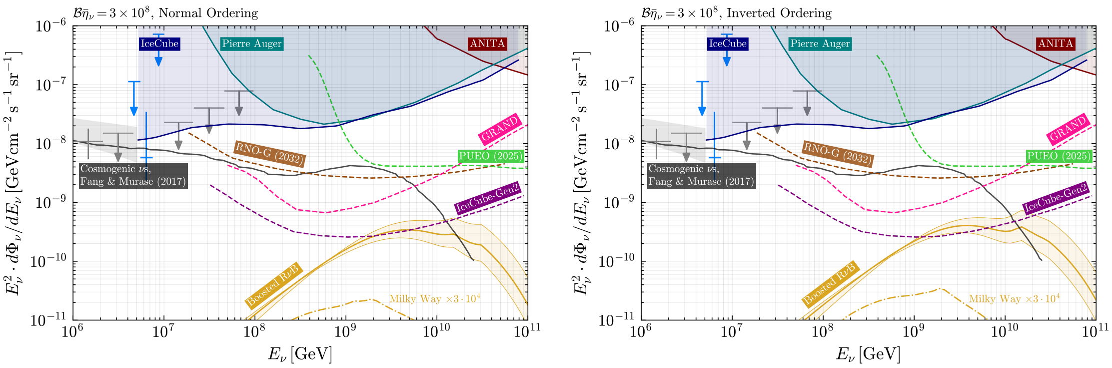

Figure 4.16: All-flavour RνB fluxes on Earth as up-scattered by UHECRs inside galaxy clusters acting as CR-reservoirs (continuous gold lines) or from UHECRs in the MW (dot-dashed gold line, multiplied by 3×10^4). The yellow shaded region is obtained for $2 \leq \alpha \leq 2.5$ (central thick line, $\alpha = 2.3$), a weighted RνB overdensity $\mathcal{B}\bar{\eta}_\nu = 3\times10^8$, a neutrino mass spectrum with NO (IO) in the upper (lower) panel and $\sum_i m_i = 0.113\,(0.145)\,\mathrm{eV}$ [76]. In grey and azure are the astrophysical neutrinos events observed at IceCube [526, 527] (see also [528, 529], the KM3NeT ARCA detector will have a similar sensitivity [530]). Fluxes of UHE neutrinos lying in the upper shaded regions are excluded at 90% C.L. by the null-detection at IceCube [232], Pierre Auger Observatory [229] and ANITA [195]. Sensitivities of PUEO (2025) [239], RNO-G (2032, first stations already taking data) [238], IceCube-Gen2 [531] (planned) and GRAND [198] (proposed) are depicted as dashed lines. The black line displays the cosmogenic neutrino flux from [186].

knowledge on details of the population of clusters that is not really necessary if one assumes that most UHECR observed on Earth originate in these CR-reservoirs. Therefore, under this assumption and as we explain below, we extract the flux from [186], where it has been determined by comparison with the observed UHECR.

The flux of cosmic nucleus $\mathcal{N}$ as given in [186]:

$$\frac{d\Phi_\mathcal{N}}{dE_\mathcal{N}} = K_\mathcal{N}\left(\frac{R_{\max}}{R}\right)^{\alpha} e^{-R/R_{\max}}. \tag{4.59}$$

where the rigidity parameter R is defined as $R \equiv E_\mathcal{N}/(Z_\mathcal{N} q_e)$, q_e being the electric charge unit, with $R_{\max} = 2\times10^{21}/26\,\mathrm{eV}$ [186] (for convenience, we absorb the electric charge q_e in the definition of R so that it is measured in eV rather than V). According to [186], at fixed R the chemical composition of $E_\mathcal{N}^2 d\Phi_\mathcal{N}/dE_\mathcal{N}$ is (0.625, 0.252, 0.053, 0.009, 0.124) for (^{1}H, ^{4}He, CNO, ^{28}Si, ^{56}Fe) respectively (as reference for CNO we have considered ^{14}N only). Thus, at fixed R, we have

$$E_\mathcal{N}^2\frac{d\Phi_\mathcal{N}}{dE_\mathcal{N}} = Z_\mathcal{N}^2 K_\mathcal{N} R^2\left(\frac{R_{\max}}{R}\right)^{\alpha} e^{-R/R_{\max}}, \tag{4.60}$$

so that the aforementioned proportions are reflected in the ratios of $Z_\mathcal{N}^2 K_\mathcal{N}$. Therefore, $K_\mathcal{N} \equiv (C_\mathrm{N}/Z_\mathrm{N}^2)K_\mathrm{H}$, with $C_\mathrm{He} \simeq 0.4032$, $C_\mathrm{N} \simeq 0.0848$, $C_\mathrm{Si} \simeq 0.0144$ and $C_\mathrm{Fe} \simeq 0.1984$. The only parameter left to determine is K_H, which we fix by requiring that the luminosity emitted from the population of CR-reservoirs matches with the one observed at Earth, by, e.g., Pierre Auger above the ankle. More specifically, we impose

$$\sum_{\mathcal{N}} \int_{E_{\rm CR}^{\rm ankle}}^{E_{\rm CR}^{\rm max}} dE_{\mathcal{N}} E_{\mathcal{N}} \frac{d\Phi_{\mathcal{N}}}{dE_{\mathcal{N}}} = \int_{E_{\rm CR}^{\rm ankle}}^{E_{\rm CR}^{\rm max}} dE_{\rm CR} E_{\rm CR} \frac{d\Phi_{\rm CR}}{dE_{\rm CR}}, \tag{4.61}$$

where the CR flux at Earth is taken from [532] to be $d\Phi_{\rm CR}/dE_{\rm CR} \simeq (d\Phi_{\rm CR}/dE_{\rm CR})_{\rm ankle}\,(E_{\rm CR}^{\rm ankle}/E_{\rm CR})^{2.5}$, with $(d\Phi/dE_{\rm CR})_{\rm ankle} \simeq 10^{-27}\,{\rm GeV}^{-1}{\rm cm}^{-2}{\rm s}^{-1}{\rm sr}^{-1}$, within the range $E_{\rm CR}^{\rm ankle} = 5\,{\rm EeV} \leq E_{\rm CR} \leq E_{\rm CR}^{\rm max} = 200\,{\rm EeV}$. The CR flux observed at Pierre Auger and reported in [532] is actually more complicated than the single power-law considered above, including changes in the slopes at and above the ankle, mixed composition and a suppression at $\sim 50\,{\rm EeV}$. We have checked, however, that such additional features do not change appreciably the value of the integral in the right-hand-side of Eq. (4.61), to which the shape at lower energies dominates. The integral on the left-hand-side can be computed analytically as follows:

$$\begin{aligned}
\sum_{\mathcal{N}} \int_{E_{\rm CR}^{\rm ankle}}^{E_{\rm CR}^{\rm max}} dE_{\mathcal{N}} E_{\mathcal{N}} \frac{d\Phi_{\mathcal{N}}}{dE_{\mathcal{N}}} &= K_{\rm H} \sum_{\mathcal{N}} \frac{C_{\mathcal{N}}}{Z_{\mathcal{N}}^2} \int_{E_{\rm CR}^{\rm ankle}}^{E_{\rm CR}^{\rm max}} dE_{\mathcal{N}}\; E_{\mathcal{N}} \left(\frac{E_{\mathcal{N}}^{\rm max}}{E_{\mathcal{N}}}\right)^{\alpha} e^{-E_{\mathcal{N}}/E_{\mathcal{N}}^{\rm max}} \\
&= K_{\rm H} \sum_{\mathcal{N}} C_{\mathcal{N}} R_{\rm max}^2 \int_{E_{\rm CR}^{\rm ankle}/(Z_{\mathcal{N}} R_{\rm max})}^{E_{\rm CR}^{\rm max}/(Z_{\mathcal{N}} R_{\rm max})} dx\; x^{1-\alpha} e^{-x} \\
&= K_{\rm H} \sum_{\mathcal{N}} C_{\mathcal{N}} R_{\rm max}^2 \left[\Gamma\left(2-\alpha, \frac{E_{\rm CR}^{\rm ankle}}{Z_{\mathcal{N}} R_{\rm max}}\right) - \Gamma\left(2-\alpha, \frac{E_{\rm CR}^{\rm max}}{Z_{\mathcal{N}} R_{\rm max}}\right)\right],
\end{aligned} \tag{4.62}$$

where $\Gamma(a,z)$ is the upper incomplete Gamma function. For different values of the slope α, we find the normalisation factors listed in Table 4.3. These normalisation factors *de facto* encode all the information about CR-reservoirs (distance, spatial distribution, CR-spectrum escaping them), that is not needed for our purposes as long as one assumes (as done in [186]) that most UHECRs observed on Earth originate from CR-reservoirs.

Normalisation factors			
	$\alpha = 2$	$\alpha = 2.3$	$\alpha = 2.5$
$K_{\rm H}$	1.94×10^{-30}	9.44×10^{-31}	5.20×10^{-31}
$K_{\rm He}$	1.96×10^{-31}	9.52×10^{-32}	5.24×10^{-32}
$K_{\rm N}$	3.36×10^{-33}	1.63×10^{-33}	8.99×10^{-34}
$K_{\rm Si}$	1.43×10^{-34}	6.94×10^{-35}	3.82×10^{-35}
$K_{\rm Fe}$	5.70×10^{-34}	2.77×10^{-34}	1.52×10^{-34}

Table 4.3: Flux normalisation factors for each nuclear species considered and different benchmark values of α. All listed values are in units of ${\rm GeV}^{-1}{\rm cm}^{-2}{\rm s}^{-1}{\rm sr}^{-1}$.

The resulting total flux on Earth of relic neutrinos up-scattered in CR-reservoirs is shown in Fig. 4.16. We compare it with current observations, limits and future sensitivities, and with the flux of cosmogenic neutrinos arising as secondary products of UHECRs interactions inside reservoirs as computed in [186], because that could constitute a background to our signal. The total flux is obtained by summing over all neutrino mass eigenstates ν_i having non-zero masses m_i, $i = 1, 2, 3$. The upper and lower panels are respectively for a light neutrino mass spectrum with normal ordering (NO) $m_1 < m_2 < m_3$, and inverted ordering (IO) $m_3 < m_1 < m_2$. For NO (IO), the squared mass differences are fixed to $\Delta m_{21}^2 \equiv$

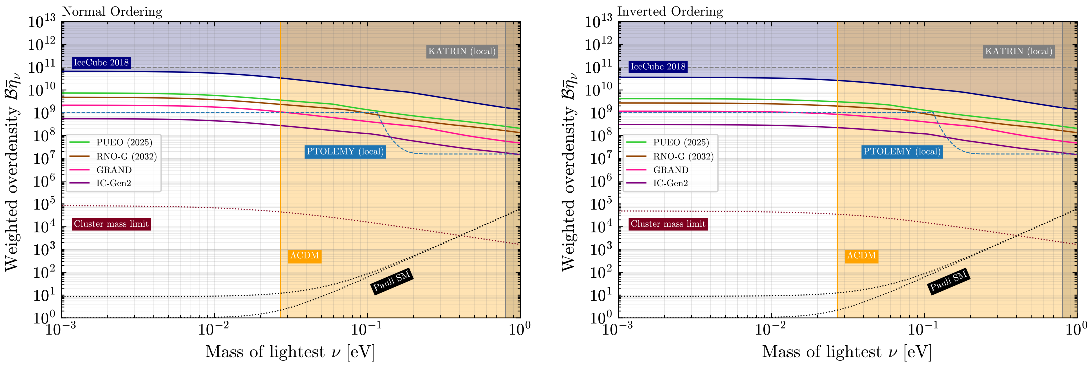

Figure 4.17: Limits and sensitivities of $\mathcal{B}\bar{\eta}_\nu$, versus the lightest neutrino mass. Assuming the reference slope $\alpha = 2.3$ in the CR spectrum in CR-reservoirs, and a neutrino mass spectrum with NO (IO) in the upper (lower) panel, we show the 90% C.L. constraint set by the null-detection at IceCube [232] (blue shaded) and the sensitivities at PUEO (2025) [239], RNO-G (2032) [238], GRAND [198] and IceCube-Gen2 [531] (solid lines, top to bottom). Also shown are: the KATRIN limits on neutrino masses (solid), $m_\nu < 0.8\,\mathrm{eV}$ at 90% C.L. [534]; the KATRIN limit on local neutrino overdensities (dashed gray), $\eta_\nu^{\mathrm{Earth}} < 9.7 \times 10^{10}$ [485]; the limit on the sum of neutrino masses from DESI, $\sum_i m_i < 0.113\,(0.145)\,\mathrm{eV}$ at 95% C.L. assuming ΛCDM [76] (orange shaded); the maximum $\mathcal{B}\bar{\eta}_\nu$ allowed by the Pauli exclusion principle (black dotted, $\mathcal{B} = 1$), respectively for the heaviest (upper line) and lightest (lower line) neutrino; the cluster mass limit (red dotted); the PTOLEMY sensitivity (dashed cyan) on the local overdensity [484]. See the text for further details.

$m_2^2 - m_1^2 = 7.42 \times 10^{-5}\,\mathrm{eV}^2$ and $\Delta m^2_{31(23)} \equiv m^2_{3(2)} - m^2_{1(3)} = 2.507\,(2.486)\ \times 10^{-3}\,\mathrm{eV}^2$ [533], the sum of neutrino masses saturates the cosmological limit $\sum_i m_i = 0.113\,(0.145)\,\mathrm{eV}$ [76], and the weighted overdensity is set to $\mathcal{B}\bar{\eta}_\nu = 3 \times 10^8$ for concreteness.

We further note that RνB-UHECRs scatterings could in principle also alter the measured spectrum of UHECRs. While a detailed study goes beyond the purpose of this work, here we simply estimate the mean free path of UHECRs in CR-reservoirs, due to RνB scatterings as $\lambda \sim 1/(\sigma_{\nu\mathrm{CR}}\bar{\eta}_\nu n_{\nu,0})$, finding that the R$\nu$B has a smaller impact on UHECRs than the CMB as long as $\bar{\eta}_\nu \lesssim 10^9$.

4.2.3 Limits and sensitivities on relic neutrino overdensities

In Fig. 4.17 we show the limits and sensitivities on the combination $\mathcal{B}\bar{\eta}_\nu$, against the lightest neutrino mass assuming NO (IO) in the upper (lower) panel. We derive them by imposing that our flux line touches the relevant limit/sensitivity curve. These limits and sensitivities are shown as solid curves in Fig. 4.17 with different colours, depending on the experiment (see the legend in the plot and the caption for more details).

Our limits and sensitivities are compared with the Pauli exclusion principle constraining the number density of gravitationally-bound neutrinos, when no BSM clustering effect is assumed. We compute the local maximum overdensity as prescribed in [487] for a galaxy cluster of mass $M = 5 \times 10^{15} M_\odot$, assuming a Navarro-Frenk-White (NFW) [535] profile for the surrounding dark matter halo, and then average over the cluster volume. The results of this procedure are shown in dotted black in Fig. 4.17.

We also evaluate the overdensity $\bar{\eta}_\nu$ for which the RνB mass equals that of the entire galaxy cluster. We consider a NFW dark matter density profile whose virial radius scales as $R_{\rm vir} \sim M^{1/3}$, such that the average mass density in clusters $\rho_{\rm cluster}$ is independent of the cluster mass. In particular, $\rho_{\rm cluster} \approx 200\rho_c$, with $\rho_c \simeq 1.05 \times 10^{-5} h^{-2}\,{\rm GeV\,cm^{-3}}$ the critical density of the Universe and $h \simeq 0.674$ the dimensionless Hubble parameter [536]. We then impose a rough cluster mass limit by requiring $\bar{\eta}_\nu n_{\nu,0} \sum_i m_i \leq \rho_{\rm cluster}$, taking equal averaged overdensity for each neutrino species. The corresponding limit on the weighted overdensity $\mathcal{B}\bar{\eta}_\nu$ can be relaxed for non-uniform neutrino and CR spatial distributions. This is shown in dotted red in Fig. 4.17.

Finally, we estimate the sensitivity of the proposed PTOLEMY experiment [484] on local neutrino overdensities, considering the configuration where the final $^3{\rm He}^+$ is in the bound ground state. Depending on the neutrino mass compared to the experimental resolution Δ (we use $\Delta = 0.05$ eV as reference), the RνB absorption peak can be well-separated from the continuous β-decay spectrum or hidden under it. Accordingly, we require at least $N_{\rm peak} = 10$ events/yr to call a detection in the first situation, or $N_{\rm peak} \gtrsim 3\sqrt{N_{\rm bkg}}$, with $N_{\rm bkg}$ the number of β-decay events/yr in the same energy range in the second. The PTOLEMY sensitivity is shown in dashed cyan in Fig. 4.17.

For IO and in the hierarchical limit with $m_3 \ll m_1 \lesssim m_2$, there are two heavy and one light neutrino implying a flux that is larger by a factor ~ 2 with respect to the results in the NO case. Correspondingly, the limits and sensitivities on $\mathcal{B}\bar{\eta}_\nu$ are slightly improved compared to the case of NO. We note, however, that also the cluster mass limit becomes more stringent by an equal amount, for the same reason. In the degenerate limit $m_1 \simeq m_2 \simeq m_3$, the IO case is practically identical to the scenario with NO.

4.2.4 Flavour composition of up-scattered relic neutrinos

Neutrinos produced in astrophysical environments typically exhibit precise flavour composition at the source, but neutrino oscillations over astronomical distances tend to homogenise any flavour disparity [537, 538].

Instead, the boosted RνB exhibits a peculiar flavour composition. At first, the RνB is evenly distributed among the mass eigenstates, which directly take part in the NC scatterings with UHECRs. The mass eigenstates ν_i then propagate freely and their fluxes $d\Phi_i/dE_\nu$ are preserved. At detection, the probability of observing a massive neutrino ν_i in a flavour $\ell = e, \mu, \tau$ is $\mathcal{P}_{\ell i} = |U_{\ell i}|^2$, with $U_{\ell i}$ being the entries of the Pontecorvo-Maki-Nakagawa-Sakata (PMNS) neutrino mixing matrix [68, 69, 73]. Then, the flux of boosted neutrinos with flavour ℓ is given by $d\Phi_\ell/dE_\nu = \sum_i |U_{\ell i}|^2\, d\Phi_i/dE_\nu$. Clearly, the relative flux in each flavour depends on the neutrino mixing parameters through the PMNS matrix and neutrino masses via the differential flux.

As the fluxes of the different mass eigenstates have distinct energy dependence, the flavour composition of the boosted RνB flux depends on the energy as well. It is nevertheless practical to calculate an integrated flavour ratio $\Phi_\ell/\Phi_{\rm tot} \equiv \sum_i |U_{\ell i}|^2\Phi_i/\sum_i \Phi_i$. The predicted integrated flavour composition is shown in Fig. 4.18. In the plot, the parameters of the PMNS matrix are varied within the 3σ ranges allowed by the `NuFit 5.2` global analysis of neutrino oscillation data [533], while $m_{1(3)}$ in the range $10^{-3} \leq m_{1(3)}/{\rm eV} \leq 1$, for NO (IO). As $m_{1(3)}$ increases, the mass eigenstates become nearly degenerate, implying $\Phi_1 \simeq \Phi_2 \simeq \Phi_3$ and an unflavoured composition $\Phi_e : \Phi_\mu : \Phi_\tau = 1:1:1$, due to the unitarity

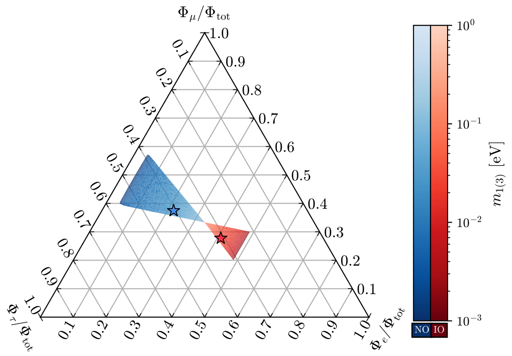

Figure 4.18: Flavour composition of the boosted RνB. The blue (red) area is obtained by varying the PMNS matrix entries and squared neutrino mass splittings within the 3σ allowed range [533], assuming NO (IO). Darker regions correspond to lighter $m_{1(3)}$. The stars mark the flavour composition of the boosted RνB for the best-fit values of the neutrino oscillation data and $m_{1(3)}$ saturating the cosmological bounds $\sum_i m_i = 0.113\,(0.145)\,\mathrm{eV}$ [76] (the flavour composition depends only very slightly on the slope of the CR spectrum).

of the PMNS matrix. By decreasing $m_{1(3)}$, the mass spectrum becomes hierarchical with $m_1 \lesssim m_2 \ll m_3$ ($m_3 \ll m_1 \lesssim m_2$) with the (two) heaviest neutrino(s) dominating the total flux. In this situation, because of the structure of the PMNS matrix, the flavour flux composition is approximately $0:1:1$ $(2:1:1)$ for NO (IO). This could help UHE neutrino observatories discriminate between a boosted RνB signal and other kinds of astrophysical neutrino fluxes [539, 540, 198, 239, 191, 541].

Relic neutrinos Beyond the Standard Model

Given that gravitational clustering can provide at most a neutrino overdensity of $\bar{\eta}_\nu \sim 10^2$ [487], while our mechanism, with the current neutrino detectors, is sensitive to local overdensities $\bar{\eta}_\nu \gtrsim 10^{10}$, we need some BSM physics to be at play in order to provide enough neutrino clustering. The simplest BSM extension that could provide this feature is a Yukawa interaction between neutrinos and a light scalar field ϕ. The maximal neutrino density in a cluster due to Yukawa interactions induced by a massless scalar mediator ϕ has been determined as [498]

$$\eta_\nu^{\rm max} \sim 10^6 \left(\frac{m_\nu}{0.1\mathrm{eV}}\right)^3 , \tag{4.63}$$

while in the massive ϕ case, the radius of scalar interaction becomes smaller and hence the interactions between ϕ and the relic neutrinos become weaker.
Other BSM scenarios feature a secondary, non-thermal component of relic neutrinos, that could be provided by late time decays of Majorons, [542, 543]. This production mechanism is motivated in setups where neutrino masses are associated with the spontaneous breaking of the lepton number. According to the authors of [542, 543], the neutrinos produced from these decays can potentially be visible at experiments that hope to directly observe the cosmic neutrino background through neutrino capture on tritium, such as PTOLEMY.

4.2.5 Summary and Conclusions

We computed the flux of relic neutrinos up-scattered by UHECRs via SM NC interactions, taking into account the full Q^2-dependence and DIS in the cross section, and the mixed CR composition. Our results are shown in Fig. 4.16 for up-scatterings in the MW by UHECRs travelling towards Earth and in galaxy clusters acting as CR-reservoirs. These objects constitute an ideal environment because of the long trapping times of CRs inside them, and indeed lead to the largest RνB up-scattered fluxes. Our calculation is conservative, having not included the hadron-resonances contributions to ν-UHECR scatterings, nor the secondary neutrinos produced by their SM charged-current interactions.

We find that IceCube [232] excludes $\mathcal{B}\bar{\eta}_\nu \gtrsim 10^{10}$ in galaxy clusters, where we weighted the average overdensity $\bar{\eta}_\nu$ by a spatial boost factor $\mathcal{B}$, and that future telescopes [239, 238, 198, 531] could possibly detect the boosted RνB for $\mathcal{B}\bar{\eta}_\nu \gtrsim 10^8$, see Fig. 4.17. These large overdensities require a BSM origin, as could be obtained on the scales of galaxy clusters via, e.g., long-range interactions.

To distinguish a boosted RνB signal from other UHEν fluxes, such as cosmogenic neutrinos, we propose to rely on i) the shape of the energy spectrum, DIS being crucial in determining the one of the up-scattered RνB, and ii) the flavour composition, the specific one of the up-scattered RνB being displayed in Fig. 4.18.

Our study motivates further UHEν searches at telescopes, a direct implementation of RνB-UHECR scatterings in the modelling of CR-reservoirs and sources, and research on how to obtain the sizeable neutrino overdensities required for a potential detection.

Chapter 5

Summary and Conclusions

The search for new physics beyond the Standard Model (BSM) requires broadening both the energy range and the cosmological epochs accessible to experiments. On the one hand, high-energy neutrinos could grant access to particle interactions at energies far beyond those attainable by terrestrial colliders. On the other hand, gravitational waves (GWs) carry information from the earliest moments of the Universe, preceding even the formation of the cosmic microwave background. These emerging cosmic messengers, neutrinos and GWs, are rapidly becoming essential tools in the quest to address some of the most profound open questions in fundamental physics and cosmology.

In this thesis, we have investigated how each of these messengers can be harnessed to test well motivated BSM scenarios. Regarding GWs, we focused in Section 3.2 on first-order phase transitions (FOPTs) in the early Universe, in connection with the generation of the baryon asymmetry. We proposed a novel framework in which the baryon asymmetry originates from the decays of composite states formed in a confining hidden sector undergoing a supercooled FOPT. This setup enhances the baryon asymmetry generation, with respect to the non-confining realizations explored by the previous literature for ultrarelativistic wall baryogenesis, via deep inelastic scatterings, while suppressing washout processes due to the mass hierarchy between the composite states and the reheating temperature. Remarkably, this mechanism allows for successful baryogenesis down to the electroweak scale and, potentially, even the MeV scale. As a consequence, the attractiveness of this framework for baryogenesis with ultrarelativistic bubble walls is twofold: i) the associated stochastic GW signal constitutes a distinctive observational target, potentially within reach of next generation detectors such as LISA, BDECIGO, and the Einstein Telescope; ii) it makes the baryogenesis mechanism potentially testable at present and future colliders. Furthermore, our framework significantly enlarges the viable parameter space for inverse and linear seesaw leptogenesis scenarios down to the TeV scale. This stands in contrast to standard thermal leptogenesis for the same models, which typically requires much higher scales, and highlights the potential of confining hidden sectors to naturally realize low-scale leptogenesis without severe fine-tuning.

Furthermore, in light of the recent evidence for a nanohertz stochastic GW background reported by pulsar timing array (PTA) collaborations, we discussed in Section 3.3 the intriguing possibility that such a signal could originate from a cosmological FOPT connected to baryogenesis. While the precise nature of the PTA signal remains to be clarified, our model opens the avenue for realizing successful baryogenesis at scales low enough to be compatible with the frequency range probed by PTA experiments and makes a step in addressing the baryon-dark matter (DM) abundance coincidence. These results underscore the unique opportunity provided by GW observations to probe baryogenesis scenarios across a broad range of energy scales, including those inaccessible to current laboratory experiments.

Turning to high-energy neutrinos, we examined two distinct avenues for exploring BSM physics. Firstly, motivated by the fact that single-zone lepto-hadronic models of blazar jets fall short in explaining the neutrino event detected by IceCube in 2017 from TXS 05065+056, the first identified extragalactic neutrino source, and that we still do not know the origin of the IceCube diffuse neutrino flux, we have explored in Section 4.1 the possibility that they could both originate from sub-GeV DM-proton scatterings in the dense environments surrounding blazars. A key advantage of our proposed mechanism with respect to standard astrophysical scenarios is its testability through complementary searches, including direct detection experiments, collider probes and neutrino observatories. Given that no direct detection of the associated blazar-boosted dark matter (BBDM) component has been achieved so far, our analysis shows that significant portions of the parameter space remain viable for several DM-quark interaction models, keeping the door open for discovery in forthcoming experiments. We point out that our analysis relies on specific choices of lepto-hadronic parameters for the blazar jets, which could affect significantly our results, and that DM itself can have an impact on the physics of blazar jets: indeed, the same DM-proton inelastic collisions that generate neutrinos also inject γ-rays into the jet environment, potentially altering the observed electromagnetic spectrum of blazars. One should incorporate DM-proton interactions directly into the modelling of blazars, allowing for a unified treatment of all the relevant signals (neutrinos, γ-rays and BBDM) and to properly assess how DM itself can influence the blazar fit parameters. Finally, the presence of DM could even help alleviate existing tensions in lepto-hadronic models, such as the long-standing issue of super-Eddington proton luminosities. A comprehensive study of these possible directions is left for future work.

Secondly, we studied in Section 4.2 the up-scattering of relic neutrinos by ultra-high-energy cosmic rays (UHECRs) occurring in galaxy clusters, which due to their magnetic field act as cosmic-ray reservoirs. This process is potentially capable of amplifying the otherwise elusive relic neutrino background. While the up-scattering process itself proceeds via SM neutral current interactions, detecting a significant flux of boosted relic neutrinos would require large local overdensities of relic neutrinos, potentially achievable only through BSM physics, such as new long range interactions in the neutrino sector. We demonstrated that current and future neutrino telescopes could be sensitive to such a signal. The specific spectral shape and flavor composition of the up-scattered relic neutrinos would provide a distinctive signature, offering a potential handle to distinguish them from other UHE neutrino populations, such as the cosmogenic neutrinos.

A common thread running through these studies is the indispensable role of an interdisciplinary approach. Disentangling BSM signatures from standard astrophysical phenomena demands both a detailed understanding of the particle physics models and a deep knowledge of the astrophysical environments where these processes occur. Astrophysical inputs, such as source properties, CR dynamics, and DM distributions, are often essential for making reliable BSM predictions. Furthermore, interpreting potential discoveries will require close collaboration between theorists and experimentalists across different fields.

Looking ahead, we are entering a particularly promising era for both GW and high-energy neutrino astronomy. The next round of PTA analyses is expected to shed light on the tantalizing evidence for a stochastic GW background reported in 2023, potentially confirming its cosmological origin. The upcoming LIGO fifth observing run (O5) is anticipated to reach the sensitivity necessary for detecting the stochastic background from binary black hole and neutron star mergers, further enriching our understanding of the gravitational wave Universe. Meanwhile, high-energy neutrino observatories, including IceCube-Gen2, KM3NeT and upcoming radio-based detectors, are poised to detect cosmogenic neutrinos, a long sought milestone in the exploration of ultra-high-energy astrophysics.

The fast experimental progress in these fields opens unprecedented opportunities for probing fundamental physics. By using gravitational waves and high-energy neutrinos as complementary messengers, we can explore new frontiers in our understanding of the Universe. The results presented in this thesis aim to contribute to this collective endeavor, highlighting the role of multi-messenger astroparticle physics as a pathway in the search for new physics.

Appendix A

Details on the boosted DM signal computation

A.1 Elastic DM-nucleon scattering cross section

We detail in this section the derivation of the elastic scattering cross section in the cases of scalar, pseudoscalar, vector and axial mediators for the toy models described in Sec. 4.1.3. We derive the expressions for the scattering with a generic nucleon N, either the proton p or the neutron n. However, we consider the proton and neutron to have equal masses $m_N \equiv m_p \simeq m_n$ when necessary.

■ **Scalar mediator.** In the case of a scalar mediator, the Feynman amplitude reads

$$i\mathcal{M}_{\phi\chi N} = g_{\chi\phi}\bar{u}(k_\chi)u(p_\chi)\frac{1}{m_\phi^2 + Q^2}\sum_q g_{q\phi}\frac{m_N}{m_q}f_q^N G_S(Q^2)\bar{u}(k_N)u(p_N). \tag{A.1}$$

The function G_S is the scalar form factor accounting for the internal structure of the nucleon. We approximate it with a dipole-like function $G_S(Q^2) = 1/(1 + Q^2/\Lambda_p^2)^2$ [544] and use the value of Λ_p, for both protons and neutrons, that stems from measurements of the averaged electric charge radius $\langle r_{\mathrm{E}}^2\rangle^{1/2} = \sqrt{12}/\Lambda_p \simeq 0.85\,\mathrm{fm}$ [545], giving $\Lambda_p \simeq 0.8\,\mathrm{GeV}$. The quantities f_q^N are defined as $f_q^N = m_q \langle N|\,\bar{q}q\,|N\rangle/(2m_N^2)$ computed at $Q^2 = 0$, and can be extracted from data and lattice computation: $f_u^p \simeq 1.97\times 10^{-2}$, $f_u^n \simeq 1.78\times 10^{-2}$, $f_d^p \simeq 3.83\times 10^{-2}$ and $f_d^n \simeq 4.23\times 10^{-2}$ [546].

After some manipulations, we arrive to the following expression for the differential elastic scattering cross section in the case of a scalar mediator, in agreement with the results of, e.g., [165]:

$$\boxed{\frac{d\sigma^{\mathrm{EL}}_{\phi\chi N}}{dT_\chi d\mu_s} = \frac{\sigma^{\mathrm{NR}}_{\phi\chi N}}{s}\frac{m_\phi^4}{16\mu_{\chi N}^2}\frac{(4m_{\mathrm{DM}^2} + Q^2)(4m_N^2 + Q^2)}{(m_\phi^2 + Q^2)^2}G_S^2(Q^2)\frac{\delta(\mu_s - \mu_s^{\mathrm{EL}}(T_N, T_\chi))}{T_\chi^{\max}(T_N)},} \tag{A.2}$$

where $\mu_{\chi N} = m_N m_{\mathrm{DM}}/(m_N + m_{\mathrm{DM}})$ is the reduced mass of the system, T_N is the kinetic energy of the nucleon, and $\sigma^{\mathrm{NR}}_{\phi\chi N}$ is the cross section computed in the non-relativistic limit at zero momentum transfer $Q^2 = 0$ and for $s = (m_N + m_{\mathrm{DM}})^2$, namely

$$\sigma^{\mathrm{NR}}_{\phi\chi N} \equiv \frac{g_{\chi\phi}^2 g_{N\phi}^2}{\pi}\frac{\mu_{\chi N}^2}{m_\phi^4} \simeq g_{\chi\phi}^2 g_{N\phi}^2 \left(\frac{\mu_{\chi N}}{1\,\mathrm{GeV}}\right)^2\left(\frac{1\,\mathrm{GeV}}{m_\phi}\right)^4 1.08\times 10^{-30}\mathrm{cm}^2, \tag{A.3}$$

with $g_{N\phi} \equiv m_N(g_{d\phi} f_d^N/m_d + g_{u\phi} f_u^N/m_u)$.

■ Pseudoscalar mediator. In the pseudoscalar case, the Feynman amplitude of the elastic process reads:

$$i\mathcal{M}_{a\chi N} = g_{\chi a}\bar{u}(k_\chi)\gamma_5 u(p_\chi)\frac{i}{m_a^2+Q^2}\frac{m_N}{\hat{m}}\sum_q g_{qa}G^q_{5,N}(Q^2)\bar{u}(k_N)\gamma_5 u(p_N). \tag{A.4}$$

where $G^q_{5,\,N}(Q^2)$ is the pseudoscalar form factor associated to the quark $q = u$, d and nucleon N. In the above expression we considered the masses of the up and down quarks to be equal, and approximated their values with their averaged mass, that is $m_u \simeq m_d \simeq \hat{m} = (m_u + m_d)/2$. The combination $\sum_q g_{qa}G^q_{5,\,N}(Q^2)$ can be computed as a linear combination of the form factors $G^{u-d}_{5,\,N}(Q^2)$ and $G^{u+d}_{5,\,N}(Q^2)$ associated respectively to the isovector current $j^\mu_{u-d} = \bar{u}\gamma^\mu\gamma^5 u - \bar{d}\gamma^\mu\gamma^5 d$ and the isoscalar current $j^\mu_{u+d} = \bar{u}\gamma^\mu\gamma^5 u + \bar{d}\gamma^\mu\gamma^5 d$. the nuclear isospin symmetry, which heuristically means to exchange $u \leftrightarrow d$ to get $p \leftrightarrow n$, implies that $G^{u+d}_5 \equiv G^{u+d}_{5,\,p} \simeq G^{u+d}_{5,\,n}$, $G^{u-d}_5 \equiv G^{u-d}_{5,\,p} \simeq -G^{u-d}_{5,\,n}$. The partially conserved axial current (PCAC) relation imposes that [87, 547]

$$G_5^{u-d}(Q^2) \;=\; G_A^{u-d}(Q^2) - \frac{Q^2}{4m_p^2}G_P^{u-d}(Q^2), \tag{A.5}$$

$$G_5^{u+d}(Q^2) \;\simeq\; G_A^{u+d}(Q^2) - \frac{Q^2}{4m_p^2}G_P^{u+d}(Q^2), \tag{A.6}$$

where $G_A^{u-d}(Q^2)$ and $G_A^{u+d}(Q^2)$ are the axial form factors, while $G_P^{u-d}(Q^2)$ and $G_P^{u+d}(Q^2)$ are the induced pseudoscalar form factors, respectively associated to the isovector and isoscalar currents. In the isoscalar case we have neglected the contribution of the sub-leading anomalous gluon form factor. The form factors $G_A^{u-d}(Q^2)$ and $G_A^{u+d}(Q^2)$ can be written under the dipole ansatz:

$$G_A^{u\pm d}(Q^2) = \frac{g_A^{u\pm d}}{(1+Q^2/M_A^2)^2}, \tag{A.7}$$

with the axial charges g_A^{u-d} and g_A^{u+d} and axial mass M_A extracted from lattice computations as $g_A^{u-d} = 1.25$, $g_A^{u+d} = 0.44$ and $M_A = 1.2\,\mathrm{GeV}$ [87, 547]. The induced pseudoscalar form factors $G_P^{u-d}(Q^2)$ and $G_P^{u+d}(Q^2)$ can be written according to the pole mass ansatz

$$G_P^{u\pm d}(Q^2) = G_A^{u\pm d}(Q^2)\frac{C^2_{u\pm d}}{Q^2+M^2_{u\pm d}} \tag{A.8}$$

where $C_{u-d} = 4m_N^2$, $C_{u+d} = 0.9\,\mathrm{GeV}^2$, $M_{u-d} = m_\pi \simeq 0.137\,\mathrm{GeV}$ and $M_{u+d} = 0.330\,\mathrm{GeV}$ [87, 547], so that the pseudoscalar form factors associated to the isovector and isoscalar currents are given by

$$G_5^{u-d}(Q^2) \;=\; \frac{g_A^{u-d}}{(1+Q^2/m_A^2)^2}\frac{m_\pi^2}{Q^2+m_\pi^2}, \tag{A.9}$$

$$G_5^{u+d}(Q^2) \;=\; \frac{g_A^{u+d}}{(1+Q^2/m_A^2)^2}\left(1-\frac{Q^2}{4m_N^2}\frac{C_{u+d}}{Q^2+M^2_{u+d}}\right). \tag{A.10}$$

and the linear combinations of interest to us reads

$$G_{5,\,p}(Q^2) \equiv \sum_q g_{qa} G^q_{5,\,p}(Q^2) = \frac{g_{ua}}{2}[G_5^{u+d} + G_5^{u-d}] + \frac{g_{da}}{2}[G_5^{u+d} - G_5^{u-d}] \quad (A.11)$$

$$G_{5,\,n}(Q^2) \equiv \sum_q g_{qa} G^q_{5,\,n}(Q^2) = \frac{g_{ua}}{2}[G_5^{u+d} - G_5^{u-d}] + \frac{g_{da}}{2}[G_5^{u+d} + G_5^{u-d}]. \quad (A.12)$$

We note that in this case the cross section vanishes for $Q^2 = 0$. Hence, we do not define any "non-relativistic" cross section in this case. Then, we obtain

$$\boxed{\frac{d\sigma^{\rm EL}_{a\chi N}}{dT_\chi d\mu_s} = \frac{g^2_{\chi a} g^2_{Na}}{16\pi s} \frac{(Q^2)^2}{(m_a^2 + Q^2)^2} \widehat{G}^2_{5,\,N}(Q^2) \frac{\delta(\mu_s - \mu_s^{\rm EL}(T_N, T_\chi))}{T_\chi^{\max}(T_N)},} \quad (A.13)$$

where $g_{Na} \equiv m_N[g_{ua}(g_A^{u+d} \pm g_A^{u-d}) + g_{da}(g_A^{u+d} \mp g_A^{u-d})]/(2\hat{m})$, with $+$ $(-)$ holding for $N = p$ $(N = n)$, and $\widehat{G}_{5,\,N}(Q^2) \equiv G_{5,\,N}(Q^2)/g_{Na}$.

■ **Vector mediator.** In the case of a vector mediator, the Feynman amplitude reads

$$i\mathcal{M}_{V\chi N} = g_{\chi V}\, \bar{u}(k_\chi)\gamma^\mu u(p_\chi) \frac{-g_{\mu\nu} + q_\mu q_\nu/m_V^2}{m_V^2 + Q^2} \langle N(k_N)|v^\nu_{V,Q}|N(p_N)\rangle, \quad (A.14)$$

where $q = p_\chi - k_\chi = k_N - p_N$ is the 4-momentum transfer and $v^\nu_{V,Q} = g_{uV}\bar{u}\gamma^\nu u + g_{dV}\bar{d}\gamma^\nu d$ is the quark vector current associated to the V boson. The hadronic matrix element can be decomposed as

$$\langle N(k_N)|v^\mu_{V,Q}|N(p_N)\rangle = \bar{u}(k_N)\left[\gamma^\mu F_1^{V,\,N}(Q^2) + \frac{i}{2m_p}\sigma^{\mu\nu} q_\nu F_2^{V,\,N}(Q^2)\right] u(p_N) \quad (A.15)$$

where $F_{1,2}^{V,\,N}(Q^2)$ are the vector form factors associated to the nucleon N [1]. The current $v^\mu_{V,Q}$ can be written as a linear combination of the electromagnetic current $j^\mu_{{\rm EM},Q} \equiv (2/3)\bar{u}\gamma^\mu u - (1/3)\bar{d}\gamma^\mu d$ and the 3-isospin current $v^\mu_{3,Q} = (1/2)(\bar{u}\gamma^\mu u - \bar{d}\gamma^\mu d)$ via

$$v^\mu_{V,Q} = 3(g_{uV} + g_{dV}) j^\mu_{{\rm EM},Q} - 2(g_{uV} + 2g_{dV}) v^\mu_{3,Q}. \quad (A.16)$$

Consequently, assuming nuclear isospin symmetry, the vector form factors can be expressed in terms of the electromagnetic ones (see, e.g., [505]) as

$$F_{1,2}^{V,\,p}(Q^2) = g_{pV} F^p_{1,2}(Q^2) + g_{nV} F^n_{1,2}(Q^2), \quad (A.17)$$

$$F_{1,2}^{V,\,N}(Q^2) = g_{nV} F^p_{1,2}(Q^2) + g_{pV} F^n_{1,2}(Q^2) \quad (A.18)$$

where $F^{p,n}_{1,2}(Q^2)$ are the proton and neutron electromagnetic form factors, $g_{pV} \equiv 2g_{uV} + g_{dV}$ and $g_{nV} \equiv g_{uV} + 2g_{dV}$. The latter can be expressed in terms of the electric and magnetic form factors $G^{p,n}_{E,M}(Q^2)$, which are defined as [549, 550, 551]

$$G^{p,n}_{\rm E}(Q^2) \equiv F_1^{p,n}(Q^2) - \frac{Q^2}{4m_N^2} F_2^{p,n}(Q^2), \quad (A.19)$$

$$G^{p,n}_{\rm M}(Q^2) \equiv F_1^{p,n}(Q^2) + F_2^{p,n}(Q^2), \quad (A.20)$$

[1] Any term proportional to Q^μ has to vanish due to vector current conservation [548].

satisfying $G_{\rm E}^p(0) = 1$, $G_{\rm E}^n(0) = 0$, $G_{\rm M}^p(0) = \mu_p/\mu_N$ and $G_{\rm M}^n(0) = \mu_n/\mu_N$, with μ_N being the nuclear magneton, while $\mu_p \simeq 2.79\mu_N$ and $\mu_n \simeq -1.91\mu_N$ respectively the magnetic moments of the proton and of the neutron [536]. We then approximate the from factors $G_{E,M}(Q^2)$ with a dipole-like function $G_{E,M}^{p,n}(Q^2) \simeq G_{E,M}^{p,n}(0)/(1+Q^2/\Lambda_p^2)^2$ [552, 545]. The differential cross section in this case reads

$$\boxed{\frac{d\sigma^{\rm EL}_{V\chi N}}{dT_\chi d\mu_s} = \frac{\sigma^{\rm NR}_{V\chi N}}{s}\frac{m_N^4}{4\mu^2_{\chi N}}\left[A^{V,N}(Q^2) + \frac{(s-u)^2}{m_N^4}C^{V,N}(Q^2) + \frac{m_{\rm DM^2}}{m_N^2}D^{V,N}(Q^2)\right]\frac{\delta(\mu_s - \mu_s^{\rm EL}(T_N,T_\chi))}{T_\chi^{\rm max}(T_N)(1+Q^2/m_V^2)^2},} \tag{A.21}$$

where $\sigma^{\rm NR}_{V\chi N} \equiv g^2_{\chi V}g^2_{NV}\mu^2_{\chi N}/(\pi m_V^4)$ is total cross section in the non-relativistic limit and for $Q^2 = 0$ (which is non-zero only if $g_{dV} \neq -2g_{uV}$), and $A^{V,N}(Q^2)$, $C^{V,N}(Q^2)$ and $D^{V,N}(Q^2)$ are the following functions of the normalised form factors $\widehat{F}^{V,N}_{1,2}(Q^2) = F^{V,N}_{1,2}(Q^2)/g_{NV}$:

$$\begin{aligned} A^{V,N}(Q^2) &= -\frac{Q^2}{m_N^2}\left\{\left(1-\frac{Q^2}{4m_N^2}\right)\left[\left(\widehat{F}_1^{V,N}(Q^2)\right)^2 - \frac{Q^2}{4m_N^2}\left(\widehat{F}_2^{V,N}(Q^2)\right)^2\right]\right. \\ &\qquad \left. -\frac{Q^2}{m_N^2}\widehat{F}_1^{V,N}(Q^2)\widehat{F}_2^{V,N}(Q^2)\right\} \end{aligned} \tag{A.22}$$

$$C^{V,N}(Q^2) = \frac{1}{4}\left[\left(\widehat{F}_1^{V,N}(Q^2)\right)^2 + \frac{Q^2}{4m_N^2}\left(\widehat{F}_2^{V,N}(Q^2)\right)^2\right], \tag{A.23}$$

$$D^{V,N}(Q^2) = -\frac{Q^2}{m_N^2}\left[\widehat{F}_1^{V,N}(Q^2) + \widehat{F}_2^{V,N}(Q^2)\right]^2. \tag{A.24}$$

As can be checked, the above expressions agree with the corresponding ones associated to neutral current neutrino-proton elastic scattering reported, e.g., in [505] (see also [506]) when the axial contribution is neglected, but here we are keeping the contributions of order $\mathcal{O}(m_{\rm DM^2}/m_N^2)$. We note that terms $\mathcal{O}(Q^2/m_V^2)$ in the form factors cancel and thus do not appear in the expressions above.

■ **Axial mediator.** In the case of an axial mediator, the Feynman amplitude reads

$$i\mathcal{M}_{V'\chi N} = g_{\chi V'}\,\bar{u}(k_\chi)\gamma^\mu\gamma^5 u(p_\chi)\frac{-g_{\mu\nu} + q_\mu q_\nu/m^2_{V'}}{m^2_{V'} + Q^2}\langle N(k_N)|a^\nu_{V',Q}|N(p_N)\rangle, \tag{A.25}$$

where $a^\mu_{V',Q} = g_{uV'}\bar{u}\gamma^\mu\gamma^5 u + g_{dV'}\bar{d}\gamma^\mu\gamma^5 d$ is the quark axial current associated to the V' boson. We decompose the hadronic matrix element as

$$\langle N(k_N)|a^\mu_{V',Q}|N(p_N)\rangle = \bar{u}(k_N)\left[\gamma^\mu G_A^{V'N}(Q^2) - \frac{q^\mu}{2m_p}G_P^{V'N}(Q^2)\right]\gamma^5 u(p_N) \tag{A.26}$$

with the functions $G^{V'N}_{A,P}(Q^2)$ being the associated axial and pseudoscalar form factors[2]. The current $a^\mu_{V',Q}$ can be decomposed in terms of the isoscalar and isovector currents

$$a^\mu_{V',Q} = \frac{g_{uV'}}{2}(j^\mu_{u+d} + j^\mu_{u-d}) + \frac{g_{dV'}}{2}(j^\mu_{u+d} - j^\mu_{u-d}), \tag{A.27}$$

[2]We neglect the contribution from any term proportional to $\sigma^{\mu\nu}Q_\nu$ as it would violate $\mathcal{G}$ conjugation, i.e. a combination of charge conjugation and a rotation by π in isospin space [553].

and, correspondingly, the form factors can be expressed in terms of $G_{A,P}^{u\pm d}(Q^2)$ defined in Eqs. (A.7) and (A.8) as

$$G_{A,P}^{V',p}(Q^2) = \frac{g_{uV'}}{2}[G_{A,P}^{u+d}(Q^2) + G_{A,P}^{u-d}(Q^2)] + \frac{g_{dV'}}{2}[G_{A,P}^{u+d}(Q^2) - G_{A,P}^{u-d}(Q^2)], \tag{A.28}$$

$$G_{A,P}^{V',n}(Q^2) = \frac{g_{uV'}}{2}[G_{A,P}^{u+d}(Q^2) - G_{A,P}^{u-d}(Q^2)] + \frac{g_{dV'}}{2}[G_{A,P}^{u+d}(Q^2) + G_{A,P}^{u-d}(Q^2)], \tag{A.29}$$

The differential cross section in this case reads

$$\boxed{\frac{d\sigma_{V'\chi N}^{\mathrm{EL}}}{dT_\chi d\mu_s} = \frac{\sigma_{V'\chi N}^{\mathrm{NR}}}{s}\frac{m_N^4}{4\mu_{\chi N}^2}\left[A^{V',N}(Q^2) + \frac{(s-u)^2}{m_N^4}C^{V',N}(Q^2) + \frac{m_{\mathrm{DM}^2}}{m_N^2}D^{V',N}(Q^2)\right]\frac{\delta(\mu_s - \mu_s^{\mathrm{EL}}(T_N, T_\chi))}{T_\chi^{\max}(T_N)(1+Q^2/m_{V'}^2)^2},} \tag{A.30}$$

where $\sigma_{V'\chi N}^{\mathrm{NR}} \equiv g_{NV'}^2 {g_{\chi V'}}^2 \mu_{\chi N}^2/(\pi m_{V'}^4)$ is the total cross section computed in the non-relativistic limit and for $Q^2 = 0$, with $g_{NV'} \equiv (\sqrt{3}/2)[g_{uV'}(g_{V'}^{u+d} \pm g_{V'}^{u-d}) + g_{dV'}(g_{V'}^{u+d} \mp g_{V'}^{u-d})]$, with $+$ $(-)$ holding for $N = p$ $(N = n)$, while $A^{V',N}(Q^2)$, $C^{V',N}(Q^2)$ and $D^{V',N}(Q^2)$ are the following functions of the normalised form factors $\widehat{G}_{A,P}^{V',N}(Q^2) \equiv G_{A,P}^{V',N}(Q^2)/g_{NV'}$:

$$A^{V',N}(Q^2) = \frac{Q^2}{m_N^2}\left(1 + \frac{Q^2}{4m_N^2}\right)\left(\widehat{G}_A^{V',N}(Q^2)\right)^2, \tag{A.31}$$

$$C^{V',N}(Q^2) = \frac{1}{4}\left(\widehat{G}_A^{V',N}(Q^2)\right)^2, \tag{A.32}$$

$$\begin{aligned} D^{V',N}(Q^2) = {} & 8\left[1 + \frac{Q^2}{8m_N^2} + \frac{Q^2}{m_V'^2} + \frac{1}{2}\left(\frac{Q^2}{m_V'^2}\right)^2\right]\left(\widehat{G}_A^{V',N}(Q^2)\right)^2 + \\ & + 2\frac{Q^2}{m_N^2}\left(1 + \frac{Q^2}{m_V'^2}\right)^2 \widehat{G}_A^{V',N}(Q^2)\widehat{G}_P^{V',N}(Q^2) + \\ & + \frac{1}{4}\left(\frac{Q^2}{m_N^2}\right)^2\left(1 + \frac{Q^2}{m_V'^2}\right)^2\left(\widehat{G}_P^{V',N}(Q^2)\right)^2. \end{aligned} \tag{A.33}$$

It can be checked that the above expressions agree with the corresponding ones associated to neutral current neutrino-proton elastic scattering reported, e.g., in [505] (see also [506]) when the vector contribution is neglected, but here we are keeping the contributions of order $\mathcal{O}(m_{\mathrm{DM}^2}/m_N^2, Q^2/m_{V'}^2)$.

A.2 Deep inelastic scattering cross sections

We give here more details on the derivation of the DIS cross section that we reported in the main text. We consider a nucleon $N = p, n$ scattering inelastically off a DM particle. If the momentum transfer is large enough, the DM particles interacts directly with the quarks that constitute the nucleon via *deep inelastic scattering* (DIS). The process is diagrammatically represented below [445]

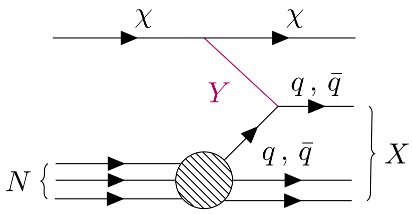

where $Y = \phi, a, V, V'$ denotes either the scalar, pseudoscalar, vector or axial mediator, N the initial nucleon and X the outgoing hadronic state. We fix the momenta of the initial DM and quark respectively as $p_\chi = (E_\chi, \vec{p}_\chi)$ and $p_q = (E_q, \vec{p}_q)$, and, analogously, for the outgoing DM and quark $k_\chi = (E'_\chi, \vec{k}_\chi)$ and $k_q = (E'_q, \vec{k}_q)$. We furthermore neglect the quark masses. The DIS is typically studied in the context of neutrino interactions, in the frame of reference in which the nucleon is at rest $\vec{p}_N = 0$ (LAB) and neglecting neutrino masses. A comprehensive discussion of the SM neutrino-nucleon interaction can be found, e.g., in [505]. Here, we will follow an approach similar to that outlined in [2], namely we derive the DIS cross section in the LAB frame and write it in terms of Lorentz invariants, so to render any change of reference frame immediate. We will also keep the DM masses non-zero as they are not necessarily negligible compared to the other mass and energy scales involved in the process. It will prove useful to define also the initial nucleon momentum $p_N = p_q/a = (E_N, \vec{p}_N)$ and the 4-momentum transfer $q = p_\chi - k_\chi$. We denote the squared centre-of-mass energy and momentum transfer respectively as $s = (p_N + p_\chi)^2$ and $Q^2 = -q^2$. We also define the following Lorentz invariant quantities: the *energy transfer* $\nu \equiv p_N \cdot q/m_N$, the *inelasticity* parameter $y \equiv p_N \cdot q/(p_N \cdot p_\chi) = 2\nu m_N/(s - m_N^2 - m_{\mathrm{DM}^2})$ and the *Bjorken scaling variable* $x \equiv Q^2/(2p_N \cdot q) = Q^2/[(s - m_N^2 - m_{\mathrm{DM}^2})\, y]$. Moreover, we have the following set of relations in the LAB frame:

$$
\begin{aligned}
Q^2 &\overset{\text{LAB}}{=} -2m_{\mathrm{DM}^2} + 2E_\chi E'_\chi - 2|\vec{p}_\chi||\vec{k}_\chi| \cos\theta, && \text{(A.34)}\\
E_\chi &\overset{\text{LAB}}{=} (s - m_N^2 - m_{\mathrm{DM}^2})/(2m_N), && \text{(A.35)}\\
E'_\chi &\overset{\text{LAB}}{=} E_\chi(1-y), && \text{(A.36)}\\
v_{\mathrm{rel}} &\overset{\text{LAB}}{=} |\vec{p}_\chi| m_N/(E_\chi E_N), && \text{(A.37)}
\end{aligned}
$$

where θ is the scattering angle in the LAB frame and v_{rel} is the relative velocity between the DM and the nucleon. The master formula for the DIS differential cross section can be written as [554]:

$$
d\sigma^{\mathrm{DIS}}_{Y\chi N} = \frac{1}{4E_\chi E_N v_{\mathrm{rel}}} \frac{d^3k_\chi}{(2\pi)^3 2E'_\chi} \sum_{\kappa=q,\bar{q}} \int_0^1 d\xi f^N_\kappa(a, Q^2) \frac{E_N}{E_\kappa} \int \frac{d^3k_a}{(2\pi)^3 2E'_\kappa} (2\pi)^4 \delta^{(4)}(\xi p_N + q - k_\kappa) \overline{|\mathcal{M}^{\mathrm{quark}}_{Y\chi}|^2}, \tag{A.38}
$$

where $\overline{|\mathcal{M}^{\mathrm{quark}}_{Y\chi}|^2}$ is the squared Feynman amplitude of the DM-quark scattering averaged over the initial spins, while $f^N_{q(\bar{q})}$ is the Lorentz scalar *parton distribution function* (PDF) for the (anti)quark $q = u, c, t, d, s, b$ ($\bar{q} = \bar{u}, \bar{c}, \bar{t}, \bar{d}, \bar{s}, \bar{b}$). The expression above is Lorentz invariant except for the factor $E_\chi E_N v_{\mathrm{rel}}$. This factor is, however, invariant in all the reference frames in which the particles are collinear (see, e.g., [554]), so that if we find a Lorentz invariant expression for the differential cross section in the rest frame of the proton, the same expression can be used in the rest frame in which the DM particle is at rest instead. We have that

$$
\frac{4\pi}{4E_\chi E_N v_{\mathrm{rel}}} \frac{d^3k_\chi}{(2\pi)^3 2E'_\chi} \overset{\text{LAB}}{=} \frac{d\nu dQ^2}{16\pi m_N (E_\chi^2 - m_{\mathrm{DM}^2})} = \frac{y}{8\pi} \frac{(Q^2)^2}{(Q^2)^2 - 4m_N^2 m_{\mathrm{DM}^2} x^2 y^2} dx dy, \tag{A.39}
$$

where we have used the relations

$$
d^3k_\chi \overset{\text{LAB}}{=} \frac{2\pi E'_\chi}{2|\vec{p}_\chi|} d\nu dQ^2 \quad \text{and} \quad d\nu dQ^2 = \frac{(Q^2)^2}{2m_N x^2 y} dx dy. \tag{A.40}
$$

Then, the δ-function in the DIS differential cross section can be integrated out via the four integrals over the final quark's 3-momentum $\vec{k}_\kappa$ and the variable ξ to give:

$$d\sigma^{\rm DIS}_{Y\chi N} \overset{\rm LAB}{\simeq} \frac{\sum_\kappa f^N_\kappa(x,\,Q^2)|\overline{\mathcal{M}^{\rm quark}_{Y\chi}}|^2}{32\pi m_N Q^2(E^2_\chi - m_{\rm DM^2})} d\nu dQ^2 = \frac{y}{16\pi}\frac{Q^2\sum_\kappa f^N_\kappa(x,\,Q^2)|\overline{\mathcal{M}^{\rm quark}_{Y\chi}}|^2}{(Q^2)^2 - 4m_N^2 m_{\rm DM^2} x^2 y^2} dx dy, \quad \text{(A.41)}$$

where we have neglected quarks' masses, so that $\nu \overset{\rm LAB}{=} E_\chi - E'_\chi \simeq E'_\kappa$, $\kappa = q,\, \bar{q}$. This last expression reproduces Eq. (4.29) in the main text for $N = p$.

A.3 A different approach for the Earth attenuation

We now investigate the effects of the Earth attenuation on DM in our toy models following the approaches of, e.g., [163, 164, 165, 454]. In particular, we approximate the DM energy loss, dT^x_χ, during a single scattering event occurring within the infinitesimal distance interval $[x, x + dx]$, with its average value. We also assume the scatterings to occur only on protons and neutrons at rest. Then, the resulting DM kinetic energy at distance x, T^x_χ, is controlled by the differential equation:

$$\frac{dT^x_\chi}{dx} = -\sum_{N=p,\,n} n_N \int_0^{T_N^{\rm max}(T^x_\chi)} dT_N\, T_N \frac{d\sigma^{\rm EL+DIS}_{Y\chi N}}{dT_N}(T_N, T^x_\chi)\,, \quad \text{(A.42)}$$

where n_N is the number density of the nucleon $N = p, n$ and

$$T_N^{\rm max}(T^x_\chi) = \frac{2m_N T^x_\chi\left(T^x_\chi + 2m_{\rm DM}\right)}{2m_N T^x_\chi + (m_{\rm DM} + m_N)^2}\,, \quad \text{(A.43)}$$

with m_N the nucleon's mass. By solving numerically Eq. (A.42), for given DM mass, couplings $g_{\chi Y}$, g_{qY}, and distance x, with the initial condition $T^{x=0}_\chi = T^{(0)}_\chi$, we extrapolate $T^x_\chi(T^{(0)}_\chi)$ and $dT^x_\chi/dT^{(0)}_\chi$, as well as $T^{(0)}_\chi(T^x_\chi)$ and $dT^{(0)}_\chi/dT^x_\chi$. We also keep track of the average number of scatterings taking place over a distance x, $N^x_{\rm sct}$, by solving

$$\frac{dN^x_{\rm sct}}{dx} = \sum_{N=p,\,n} n_N \sigma^{\rm EL+DIS}_{Y\chi N}(T^x_\chi). \quad \text{(A.44)}$$

together with Eq. (A.42) and the initial condition $N^{x=0}_{\rm sct} = 0$.

To ensure the feasibility of the numerical evaluation, we adopt all the approximations as in our procedure described in the main text. Namely, we take the nucleon density $n_N \equiv n_p \simeq n_n \simeq \rho_{p+n}/(2m_N)$, with $\rho_{p+n} \simeq 2.7\,{\rm g/cm^3}$ and $m_N \equiv m_p \simeq m_n$; we focus only the elastic scattering contribution with the form factor evaluated at zero momentum transfer; we consider equal DM-proton and DM-neutron cross sections $\sigma^{\rm EL}_{Y\chi N} \equiv \sigma^{\rm EL}_{Y\chi p} \simeq \sigma^{\rm EL}_{Y\chi n}$. Furthermore, we neglect the change of DM direction after each scattering and compute the differential DM flux at depth x assuming flux conservation as

$$\frac{d\Phi^x_\chi}{dT^x_\chi} = \frac{dT^{(0)}_\chi}{dT^x_\chi}\frac{d\Phi_\chi}{dT^{(0)}_\chi}\Bigg|_{T^{(0)}_\chi = T^{(0)}_\chi(T^x_\chi)}. \quad \text{(A.45)}$$

In order to visualize the role played by the Earth attenuation within this approach, we show in the left panel of Fig. A.1 the ratio $T^x_\chi/T^{(0)}_\chi$ and $N^x_{\rm sct}$ (solid) obtained by solving the

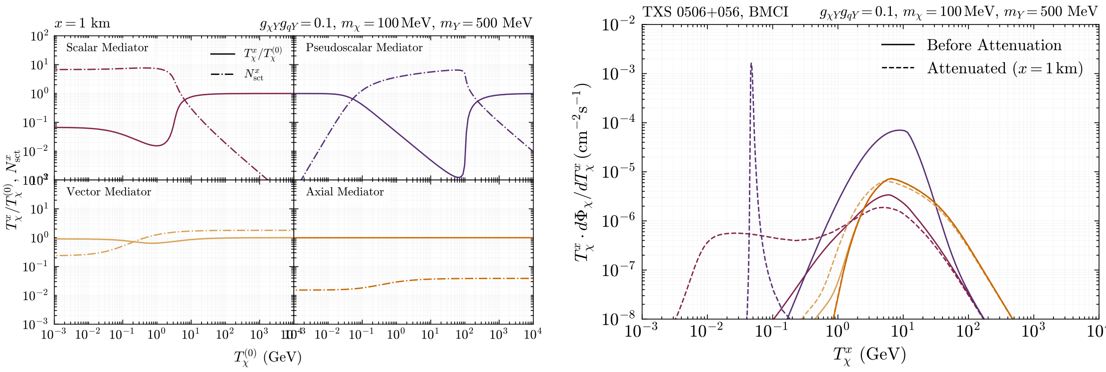

Figure A.1: Effect of the Earth attenuation. Left panel: ratio of the attenuated DM kinetic energy to its value at the Earth surface $T^x_\chi/T^{(0)}_\chi$ (solid) and the DM average number of scatterings $N^x_{\rm sct}$ (dashed) for a scalar (top left), pseudoscalar (top right), vector (bottom left) and axial (bottom right) mediator. Right panel: BBDM flux from TXS 0506+056 before (solid) and after (dot-dashed) Earth attenuation. We set $x = 1\,$km, $m_Y = 500\,$MeV, $m_{\rm DM} = 100\,$MeV, $g_{\chi Y} g_{qY} = 0.1$, $\Sigma^{\rm spike}_{\rm DM} = 6.9 \times 10^{28}\,$GeV cm^{-2} (BMCI).

differential Eqs. (A.42) and (A.44) for our DM models, with mediator mass $m_Y = 500\,$MeV, DM mass $m_{\rm DM} = 100\,$MeV, couplings $g_{\chi Y} g_{qY} = 0.1$ at depth $x = 1$ km. In the right panel of the same figure, we plot the BBDM flux before attenuation (solid) and the attenuated flux (dashed) for the same DM model parameters and $\Sigma^{\rm spike}_{\rm DM} = 6.9 \times 10^{28}\,$GeV cm^{-2} as in BMCI.

From the left panel of Fig. A.1 one can see that as long as $N^x_{\rm sct} < 1$, then $T^x_\chi \simeq T^{(0)}_\chi$, hence the effect of the Earth attenuation is negligible. In this situation, the average number of scatterings can be computed by integrating Eq. (A.44), which, under the adopted approximation, gives $N^x_{\rm sct} \simeq x\ell^{-1}$ with $\ell^{-1} \equiv 2 n_N \sigma^{\rm EL}_{Y\chi N}$. Earth attenuation becomes relevant when $N^x_{\rm sct} >$ few, leading eventually to an exponential suppression of $T^x_\chi/T^{(0)}_\chi$.

The effect of the attenuation treated in this way on the BBDM flux is shown in the right panel of Fig. A.1. For the pseudoscalar mediator case one has a sharp peak in the attenuated flux, which is produced by the DM particles whose $T^{(0)}_\chi$ is such that their average $N^x_{\rm sct}$ is larger than 1. This peak forms because $N^x_{\rm sct}$ eventually becomes smaller than 1 for sufficiently small $T^{(0)}_\chi$, due to the vanishing of the pseudoscalar elastic cross section, as it follows from Eq. (4.26) in the $T_\chi \to 0$ limit. For the scalar case, instead, as the elastic cross section does not vanish for $T_\chi \to 0$, the effect of Earth attenuation is to smooth the peak of the unattenuated BBDM flux towards smaller kinetic energies. Finally, for the vector and the axial mediators Earth attenuation is marginal for the adopted choice of parameters.

However, in our treatment of the Earth attenuation discussed in Section 4.1.7 we have chosen not to follow the approach described in this Appendix, but rather to adopt the conservative one encoded in Eq. (4.48), where we set to zero the BBDM flux if the average number of DM scatterings $N^{x_{\rm det}}_{\rm sct} \simeq x_{\rm det}\ell^{-1}(T^{(0)}_\chi)$ gets larger than 1. Two main considerations justify this choice: i) our conservative treatment described in the main text – which, by the way, makes the numerical implementation of the Earth attenuation much faster than the method outlined here – is justified *a posteriori* as the effects of the attenuation become relevant for values of the couplings much larger than the ones probed in our scenario for the scalar, vector and axial mediator cases; ii) in the pseudoscalar mediator scenario, where attenuation effects are more significant, the procedure described above leads to an artificial sharp peak in the flux (see right panel of Fig. A.1). This is a consequence of the assumption that the DM particles maintain their direction and velocity across successive scatterings, which is unphysical. A more accurate treatment would require a dedicated simulation that tracks the change in DM direction and energy loss at each scattering event, which lies beyond the goals of the present study.

Appendix B

Depletion of the Dark Matter spike

In this appendix we investigate processes which can deplete the DM density profile around the BHs that we have discussed in Sec. 4.1.2 and that we have assumed throughout our calculations, by estimating their characteristic timescales. We compare these to the typical timescale $t_{\text{Accr.}}$ for the BH accretion, as this is tied to the formation of the DM spike and its replenishment.

A rough estimate of $t_{\text{Accr.}}$ can be obtained by assuming that the BH's accretion saturates the Eddington limit [555]

$$\frac{M_{\rm BH}}{\dot{M}_{\rm BH}} \sim 3 \times 10^7 \text{yr} \left(\frac{\varepsilon}{0.06}\right), \tag{B.1}$$

where ε is the radiative efficiency, i.e. the fraction of energy that gets converted into radiation during the accretion process. The efficiency ε reads 0.06 for a Schwarzschild BHs, but it can reach 0.4 for Kerr BHs. For definiteness, in the computations that follows, we consider $t_{\text{Accr.}} = 10^8$ years.

B.1 $4\chi \to 2\chi$ annihilation processes

Throughout this work, we have assumed that DM is strongly coupled, i.e. $g_{\chi Y} = 1$. This assumption, together with the very large densities found in the DM spike, could make $4\chi \to 2\chi$ annihilation processes efficient enough to deplete the DM spike itself, as pointed out in [556]. In this section, we estimate the size of this effect. We first approximate the "cross section" (not really an area in this case) for this process as $\sigma_{4\chi\to 2\chi} \sim g_{\chi Y}^8/m_Y^8$, and the energy density depletion rate as $\dot{\rho}_{\rm DM} \sim m_\chi \sigma_{4\chi\to 2\chi}(\rho_{\rm DM}/m_\chi)^4$. Therefore, the timescale for the depletion is given by

$$\tau_{4\chi\to 2\chi} = \frac{\rho_{\rm DM}}{\dot{\rho}_{\rm DM}} = \frac{1}{\sigma_{4\chi\to 2\chi}}\left(\frac{m_\chi}{\rho_{\rm DM}}\right)^3. \tag{B.2}$$

By inverting this relation we can find a maximal DM density that guarantees the spike is not depleted by these processes on a timescale $t_{\text{Accr.}} = 10^8\,$yr:

$$\rho_{\max} \approx 2 \times 10^{16}\,\text{GeV cm}^{-3} \left(\frac{10^8 \text{ yr}}{\tau_{4\chi\to 2\chi}}\right)^{1/3} \left(\frac{m_\chi}{10 \text{ keV}}\right) \left(\frac{m_Y}{1 \text{ MeV}}\right)^{8/3} \left(\frac{1}{g_{\chi Y}}\right)^{8/3}. \tag{B.3}$$

By comparing this result with Fig. 4.1 we note that the spike depletion due to $4\chi \to 2\chi$ processes gets relevant in the inner part of the DM density profile only for benchmark values of m_χ and m_Y well below those considered in our setup. We can thus safely neglect such effect in our calculations.

B.2 Self interacting DM bounds and flattening of the spike

The DM models outlined in the main text, besides describing DM interactions with the SM, induce interaction within the dark sector, thus realizing a self-interacting DM (SIDM) model. This class of models has been invoked to explain small-scale tensions in the ΛCDM model [557] and generally predicts a suppression of the power spectrum at small scales and the formation of isothermal cores in galactic halos. Dwarf galaxies [558] and galaxy clusters [559] put bounds on the size of the SIDM cross section of the order

$$\frac{\sigma_{\rm SIDM}}{m_\chi} \lesssim \mathcal{O}(1)\frac{\rm cm^2}{g}. \tag{B.4}$$

For comparison, we estimate our SIDM cross section as

$$\sigma_{\rm SIDM} \sim \frac{g_\chi^4 m_\chi^2}{m_Y^4}, \tag{B.5}$$

and thus

$$\frac{\sigma_{\rm SIDM}}{m_\chi} \sim \frac{g_\chi^4 m_\chi}{m_Y^4} \sim 2\times 10^{-4} g_\chi^4 \left(\frac{m_\chi}{\rm GeV}\right)\left(\frac{\rm GeV}{m_Y}\right)^4 \frac{\rm cm^2}{\rm g}, \tag{B.6}$$

therefore being well below the maximal allowed value. Additionally, SIDM leads to cores in galactic haloes, and the same should occur around supermassive BHs like those that power blazars. In particular, the effect of $2\chi \to 2\chi$ processes is to suppress the spike [556, 560] to

$$\rho_{\rm SIDM}(r) \sim r^{-(3+k)/4} \tag{B.7}$$

for a SIDM cross section with velocity dependence $\sigma_{\rm SIDM} \sim v^{-k}$. We estimate the DM density required for this process to be efficient in altering the spike profile according to Eq. (3.5) of [556]. This happens approximately when each DM particle undergoes at least one scattering during the age of the halo, that is $(\rho_{\rm SIDM}/m_\chi)\langle\sigma_{\rm SIDM} v\rangle\, t_{\rm Accr.} \sim 1$ where we once again compare to the accretion time as our reference timescale. Then this condition is satisfied when

$$\rho \gtrsim \rho_{\rm SIDM} \sim 3\times 10^3 \ {\rm GeV\ cm^{-3}} \left(\frac{10^8 {\rm yr}}{t_{\rm Accr.}}\right)\left(\frac{10^{-2}}{v}\right)\left(\frac{1}{g_\chi}\right)^4\left(\frac{\rm GeV}{m_\chi}\right)\left(\frac{m_Y}{\rm GeV}\right)^4, \tag{B.8}$$

assuming $k = 0$. This is the maximal density that we can reach while neglecting SIDM effects, and it poses a very stringent constraint. By tweaking m_χ and m_Y alone, BMC II can still be consistent, while BMC I requires $g_\chi \sim 10^{-2}$, thus strengthening all monojet and DD constraints. We point out that a model of inelastic dark matter circumvent this entire discussion as for large enough splitting $2 \to 2$ scattering processes are kinematically forbidden at tree level and are only achievable at 1-loop. Furthermore, if the splitting is small enough in comparison to the typical momentum exchanged in $p - \chi$ scatterings, then BBDM and neutrino signals are unaffected by the inelasticity, and furthermore DD bounds get an additional loop suppression.

B.3 Depletion by the jet

The interaction of the blazar jet protons with the surrounding DM will eventually deplete the DM spike over time.[1] In this section, we estimate to what degree this happens and whether that invalidates our results. As a first step we compute the total cross section for the $\chi - p$ scattering setting $g_{qY} = g_{\chi Y} = 1$, namely

$$\sigma_{\rm tot}(s) = \int_0^{T_\chi^{\max}(T_p)} dT_\chi \frac{d\sigma^{\rm EL}_{Y\chi p}}{dT_\chi} + \int_{Q^2_{\min}/s}^1 dx \int_{Q^2_{\min}}^{xs} dQ^2\, \frac{d\sigma^{\rm DIS}_{Y\chi p}}{dx dQ^2}, \tag{B.9}$$

where $s = m_p^2 + m_{\rm DM}^2 + 2m_\chi(m_p + T_p)$, and convolute it with the proton spectrum in the blazar jet as

$$\langle\sigma\rangle \equiv \int_1^{\Gamma_B \gamma_{\max p}} d\gamma_p\, \sigma_{\rm tot}(s) \int d\Omega\, \frac{1}{\kappa_p} \frac{d\Gamma_p}{d\Omega dT_p}. \tag{B.10}$$

We then consider a spherical shell of thickness dr at a distance r from the central BH and count how many particles the shell contains, as well as the rate of depletion, according to

$$\begin{aligned} N_{\rm DM}(r,t) &= 4\pi r^2 \frac{\rho_{\rm DM}}{m_\chi}\, dr, \\ \dot N_{\rm DM}(r,t) &= -(g_{qY} g_{\chi Y})^2 \kappa_p \langle\sigma\rangle \frac{\rho_{\rm DM}}{m_\chi} dr. \end{aligned} \tag{B.11}$$

We thus obtain a differential equation for $\rho_{\rm DM}(r,t)$:

$$\dot\rho_{\rm DM}(r,t) = -(g_{qY} g_{\chi Y})^2 \frac{\kappa_p \langle\sigma\rangle}{4\pi r^2} \rho_{\rm DM}(r,t), \tag{B.12}$$

which can be easily solved to find

$$\rho_{\rm DM}(r,\tau) = \rho_{\rm DM}(r,0) \exp\left[-\frac{\kappa_p \langle\sigma\rangle \tau}{4\pi r^2}\right], \tag{B.13}$$

having defined, for convenience, the time variable $\tau \equiv (g_{qY} g_{\chi Y})^2 t$.

The DM column density at $t = \tau$ then reads

$$\Sigma^{\rm spike}_{\rm DM}(\tau) = \int_{R_{\min}}^{R_{\rm sp}} dr\ \rho_{\rm DM}(r,0) e^{-\kappa_p \langle\sigma\rangle \tau/(4\pi r^2)}, \tag{B.14}$$

We further define $\tau_{1/2}$ as the time at which the DM column density gets halved by the interactions with the jet, that is $\Sigma^{\rm spike}_{\rm DM}(\tau_{1/2}) \equiv \Sigma^{\rm spike}_{\rm DM}(0)/2$. After computing $\tau_{1/2}$ as a function of the DM mass, we set a limit on the combination $g_{qY} g_{\chi Y}$ by imposing:

$$g_{qY} g_{\chi Y} \le \sqrt{\frac{\tau_{1/2}}{t_{\rm Accr.}}}. \tag{B.15}$$

When the above condition is satisfied, the DM column density is not depleted substantially over a timescale compatible with the accretion onto the BH. By that epoch, we assume that there is enough time for the DM spike to reform and thus that there is no dramatic loss of DM along the blazar jet.

[1] We thank Paolo Salucci for pointing out to us the importance of such an effect in this context.

We show in Fig. B.1 the same SK limits on BBDM and the curve corresponding to the DM hypothesis for the 2017 IceCube neutrino from TXS 0506+056, as in Fig. 4.12, but superimposing in red the constraints from the DM spike depletion given by Eq. (B.15) (for numerical reasons, we have imposed also $g_{qY}g_{\chi Y} \leq 100$ when computing such limits). While this effect is clearly not relevant for BMCII in neither of the cases that we have considered, it is important for BMCI. Concerning the BBDM signal, such limit largely reduce the associated testable region in all the considered toy models. The neutrino prediction is in trouble when $m_Y = 500\,\mathrm{MeV}$, in the scalar case for DM masses in the range $2 \lesssim m_\chi/\mathrm{MeV} \lesssim 20$, and in the entire considered mass range in the pseudoscalar mediator scenario. The reason behind this is that the depletion of the spike is controlled by the elastic scatterings, which are more efficient for these benchmark parameters and DM models. The neutrino signal is instead safe from DM spike depletion in the vector and axial cases.

We emphasize, however, that throughout this work we have assumed that the blazar TXS 0506+056 is characterised for much of its history by parameters corresponding to its flaring state in 2017. In reality, this is an aggressive assumption: the source undergoes flaring episodes only intermittently, and its time-averaged luminosity is most likely lower than our reference value. As a consequence, the efficiency of DM depletion via DM-proton upscattering is reduced on average with respect to what we have estimated. Accounting for the fact that the source is in a flaring state only for a fraction of the time would naturally relax the corresponding constraints, while also modifying the expected BBDM signal from this source. A proper time-dependent treatment of the source activity is beyond the scope of this work, but we remark that this aspect strengthen the robustness of our computation for the blazar sample, which is based on steady activities rather than flaring states.

For the case of the blazar sample, the different power spectrum slope leads to much smaller values of κ_p, as listed in Table 4.1, while giving more weight to higher-energy protons. The mild increase of $\sigma^{\mathrm{DIS}}_{Y\chi p}$ at higher proton energies is, however, not enough to counterbalance the effect of the smaller κ_p. As a result, we find that the spike depletion due to DM-proton interaction in blazar jets is not efficient in depleting the DM column densities along the blazar jets over billions of years, for DM parameters in the viable sub-GeV DM parameter space, neither for the considered BMCI nor BMCII, for both the benchmark values of the mediator mass and all the toy models that we have considered. Thus, the blazar DM signals that we have evaluated here and in [4] for the blazar sample are safe from the spike depletion induced by the same DM-proton scatterings that generate such signals.

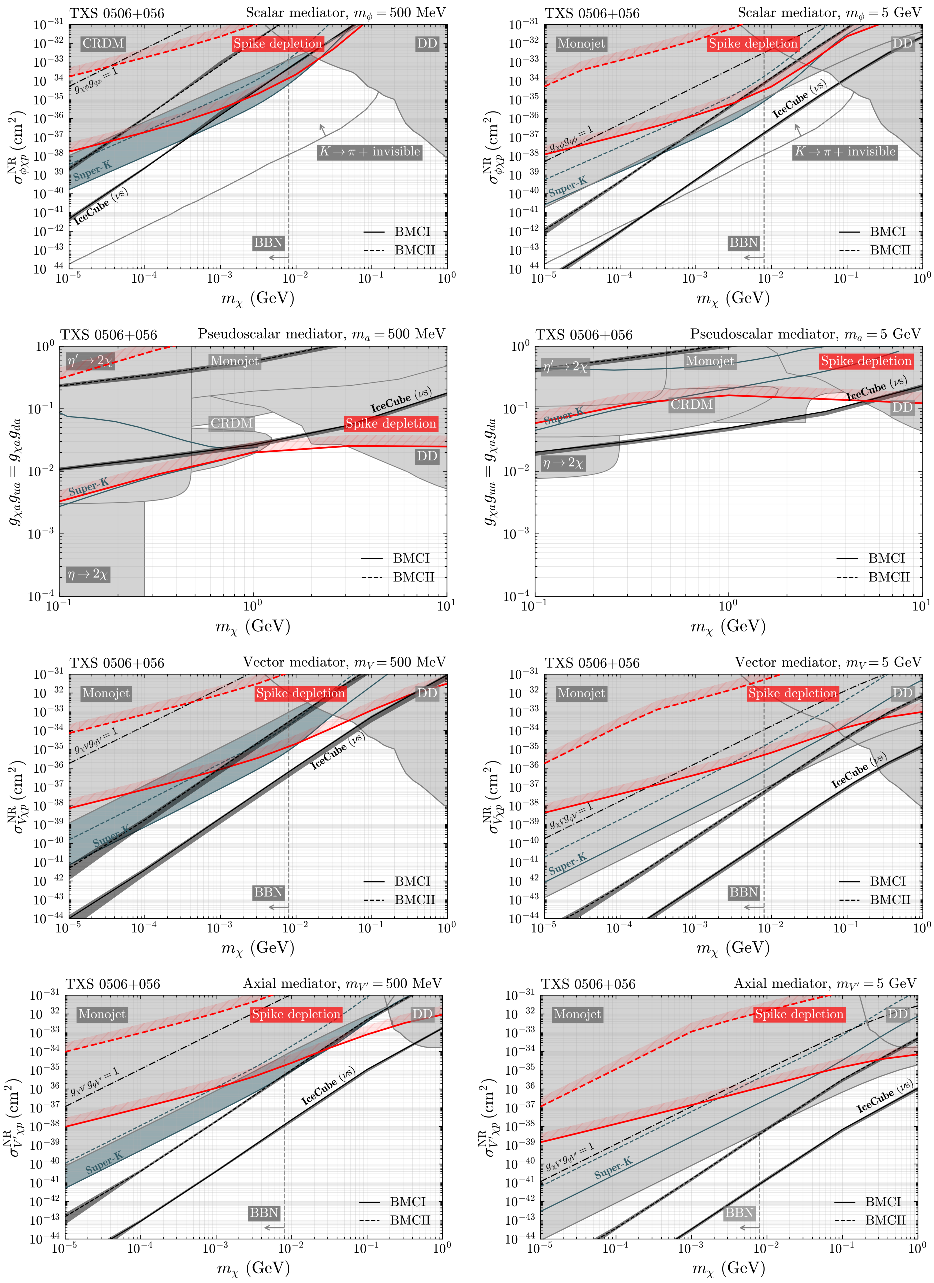

Figure B.1: Same as Fig. 4.12, but here we show only the projected limits on BBDM from TXS 0506+056 at SK (blue) and the region for which the DM hypothesis for the 2017 IceCube neutrino from the same blazar holds (black). We overlay in red the spike depletion limits that we estimate according to Eq. (B.15). Solid (dashed) lines correspond to BMCI (BMCII). All other details are as in Fig. 4.12.

Appendix C

Results on the neutrino-nucleon interaction cross-sections

C.1 Form Factors of the ν-N Neutral Current Elastic Scattering Cross Section

A detailed derivation of the ν-N elastic scattering cross section can be found in, e.g., [505] (see also [506]). Here, for completeness, we only report the form of the factors A_N and C_N appearing in Eq. (4.54) of the main text in terms of the momentum transfer Q^2. These are given in terms of the weak neutral current form factors by [505, 506]

$$A_N(Q^2) = \frac{Q^2}{m_N^2}\left\{\left(1+\frac{Q^2}{4m_N^2}\right)\left(G_{\rm A}^{ZN}(Q^2)\right)^2 - \left(1-\frac{Q^2}{4m_N^2}\right)\left[\left(F_1^{ZN}(Q^2)\right)^2 + \frac{Q^2}{4m_N^2}\left(F_2^{ZN}(Q^2)\right)^2\right]\right\} \tag{C.1}$$

$$C_N(Q^2) = \frac{1}{4}\left[\left(G_{\rm A}^{ZN}(Q^2)\right)^2 + \left(F_1^{ZN}(Q^2)\right)^2 + \frac{Q^2}{4m_N^2}\left(F_2^{ZN}(Q^2)\right)^2\right] \tag{C.2}$$

where $F_{1,2}^{ZN}(Q^2) \simeq \pm(1/2)[F_{1,2}^{p}(Q^2) - F_{1,2}^{n}(Q^2)] - 2s_{\rm W}^2 F_{1,2}^{N}(Q^2)$, with F_1^N and F_2^N being respectively the Dirac and Pauli electromagnetic form factors for the nucleon $N = n, p$, with the $+\,(-)$ sign for $p\,(n)$, $s_{\rm W}^2 \simeq 0.229$ [536] the sine squared of the Weinberg angle, $G_{\rm A}^{Zp}(Q^2) \simeq (1/2)G_{\rm A}(Q^2)$ and $G_{\rm A}^{Zn}(Q^2) \simeq -(1/2)G_{\rm A}(Q^2)$ and $G_{\rm A}(Q^2)$ the axial weak charged current form factor. We have neglected the contributions from the form factors related to strange and heavier quarks, as well as the pseudo-scalar contribution (which vanishes exactly in the case of massless neutrinos). It is useful to define also the electric and magnetic form factors respectively as [549, 550, 551]

$$G_{\rm E}^N(Q^2) \equiv F_1^N(Q^2) - \frac{Q^2}{4m_N^2}F_2^N(Q^2), \tag{C.3}$$

$$G_{\rm M}^N(Q^2) \equiv F_1^N(Q^2) + F_2^N(Q^2). \tag{C.4}$$

At zero momentum transfer, i.e. $Q^2 = 0$, we have $G_{\rm E}^p(0) = 1$, $G_{\rm E}^n(0) = 0$, $G_{\rm M}^p(0) = \mu_p/\mu_N$ and $G_{\rm M}^n(0) = \mu_n/\mu_N$, where μ_N is the nuclear magneton, while $\mu_p \simeq 2.79\mu_N$ and $\mu_n \simeq -1.91\mu_N$ are respectively the magnetic moments of the proton and of the neutron [536]. The Q^2-dependence of the electric, magnetic and axial form factors is often fitted experimentally against dipole expressions, namely $G_{\rm E,M}(Q^2) = G_{\rm E,M}(0)(1+Q^2/\Lambda^2_{\rm E,M})^{-2}$ with $\Lambda_{\rm E,M} \simeq 0.8\,$GeV, given in terms of the experimentally measured electric charge and magnetic radii of the proton $\left\langle r^2_{\rm E,M}\right\rangle^{1/2} = \sqrt{12}/\Lambda_{\rm E,M} \simeq 0.85\,$fm [552, 545], while $G_{\rm A}(Q^2) = G_{\rm A}(0)(1+Q^2/m_{\rm A}^2)^{-2}$ with $G_{\rm A}(0) \simeq 1.245$ and $m_{\rm A} \simeq 1.17\,$GeV, from measurements of the axial radius $\langle r^2_{\rm A}\rangle^{1/2} = \sqrt{12}/m_{\rm A} \simeq 0.582\,$fm [561].

C.2 Neutral Current Deep Inelastic Scattering Cross Section

If the centre-of-mass energy is sufficiently large, the interaction between a neutrino and a nucleon $N = p, n$ takes place with its constituents through DIS. In this section, we derive the NC DIS cross section assuming a parton model with quarks carrying a fraction ξ of the nucleon's momentum, and then average the results over the quark PDFs. The process is diagrammatically represented below using the Ti*k*Z-Feynamn package [445].

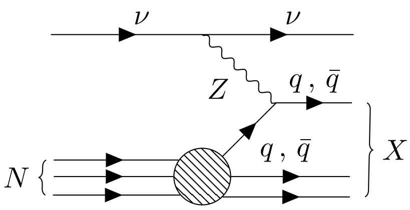

We fix the momenta of the incoming neutrino and quark respectively as $p_\nu = (E_\nu, \vec{p}_\nu)$ and $p_q = (E_q, \vec{p}_q)$. Analogously, for the outgoing neutrino and quarks we define $k_\nu = (E'_\nu, \vec{k}_\nu)$ and $k_q = (E'_q, \vec{k}_q)$, respectively. Furthermore, we neglect the quark masses. The DIS is typically studied in the frame of reference in which the nucleon is at rest $\vec{p}_N = 0$ (LAB), see, e.g., the comprehensive derivation in [505] and references therein (see also [554]). However, we are interested in the frame in which the relic neutrino is at rest instead. Our approach will be that of recovering the DIS cross section in the LAB frame and write it in terms of Lorentz invariants, so to render any change of reference frame immediate. It will prove useful to define also the initial nucleon momentum $p_N = p_q/\xi = (E_N, \vec{p}_N)$ and the 4-momentum transfer $q = p_\nu - k_\nu$. Keeping the same notation as in the main text, we denote the squared centre-of-mass energy and momentum transfer respectively as $s = (p_N + p_\nu)^2$ and $Q^2 = -q^2$. We also define the following Lorentz invariant quantities:

- ◇ *energy transfer*
$$\epsilon \equiv \frac{p_N \cdot q}{m_N}; \tag{C.5}$$
- ◇ *inelasticity*
$$y \equiv \frac{p_N \cdot q}{p_N \cdot p_\nu} = \frac{2\epsilon m_N}{s - m_N^2 - m_\nu^2}; \tag{C.6}$$
- ◇ *Bjorken scaling variable*
$$x \equiv \frac{Q^2}{2p_N \cdot q} = \frac{Q^2}{(s - m_N^2 - m_\nu^2)\, y}. \tag{C.7}$$

Moreover, we have the following set of relations:

$$Q^2 \overset{\text{LAB}}{=} -2m_\nu^2 + 2E_\nu E'_\nu - 2|\vec{p}_\nu||\vec{k}_\nu|\cos\theta, \tag{C.8}$$

$$E_\nu \overset{\text{LAB}}{=} \frac{s - m_N^2 - m_\nu^2}{2m_N}, \tag{C.9}$$

$$E'_\nu \overset{\text{LAB}}{=} E_\nu(1-y), \tag{C.10}$$

$$v_{\text{rel}} \overset{\text{LAB}}{=} |\vec{p}_\nu| m_N/(E_\nu E_N), \tag{C.11}$$

where θ is the scattering angle in the LAB frame and v_{rel} is the relative velocity between the neutrino and the nucleon. In particular, we have $\partial\cos\theta/\partial x = -m_N E_\nu y/(|\vec{p}_\nu||\vec{k}_\nu|)$ and $\partial E'_\nu/\partial y \overset{\text{LAB}}{=} -E_\nu$, so that:

$$\frac{4\pi}{4E_\nu E_N v_{\text{rel}}}\frac{d^3k_\nu}{(2\pi)^3 2E'_\nu} = \frac{y}{8\pi}\left[1 + \mathcal{O}\left(\frac{m_\nu m_N}{p_\nu\cdot p_N}\right)\right] dxdy. \tag{C.12}$$

The master formula for the DIS differential cross section can be written as [554]:

$$\begin{aligned} d\sigma_{\nu N}^{\text{DIS}} &= \frac{1}{4E_\nu E_N v_{\text{rel}}}\frac{d^3k_\nu}{(2\pi)^3 2E'_\nu}\sum_{a=q,\bar{q}}\int_0^1 d\xi f_a^N(\xi,Q^2)\frac{E_N}{E_a}\int\frac{d^3k_a}{(2\pi)^3 2E'_a}(2\pi)^4\delta^{(4)}(\xi p_N + q - k_a)|\overline{\mathcal{M}}|^2 \\ &\simeq \frac{G_F^2}{2\pi}\frac{y}{(1+Q^2/M_Z^2)^2}[p_\nu^\alpha k_\nu^\beta + p_\nu^\beta k_\nu^\alpha - g^{\alpha\beta}(k_\nu\cdot p_\nu) \pm i\varepsilon^{\alpha\beta\gamma\delta}p_{\nu,\gamma}k_{\nu,\delta}]\sum_{a=q,\bar{q}} F^a_{\alpha\beta}dxdy, \end{aligned} \tag{C.13}$$

where $+(-)$ applies to neutrinos (antineutrinos); $G_F \simeq 1.167\times 10^{-5}$ GeV $^{-2}$ is the Fermi weak coupling constant; $|\overline{\mathcal{M}}|^2$ is the squared Feynman amplitude of the neutrino-quark elastic scattering averaged over the initial quark spins; $g^{\alpha\beta} = \text{diag}(1,-1,-1,-1)$ is the Minkowski metric tensor; $\varepsilon^{\alpha\beta\gamma\delta}$ is the totally anti-symmetric tensor; $f^N_{q(\bar{q})}$ is the Lorentz scalar PDF for the (anti)quark q $(\bar{q})$ in the nucleon N and we have neglected neutrino masses in comparison with the energies and other mass scales involved. The hadronic tensor $F^a_{\alpha\beta}$ related to (anti)quark $a = q(\bar{q})$ is defined as

$$\begin{aligned} F^a_{\alpha\beta} = \frac{f_a^N(x,Q^2)}{4Q^2}\sum_{\text{spins}} &\langle a(xp_N)|J^a_\alpha|a(k_a)\rangle \\ &\times\langle a(k_a)|J^{a\dagger}_\beta|a(xp_N)\rangle, \end{aligned} \tag{C.14}$$

and the neutral quark current (multiplied by the numerator of the Z boson propagator and having factored out the electroweak coupling constant) as

$$J^q_\alpha = \left(g_{\alpha\beta} - \frac{q_\alpha q_\beta}{M_Z^2}\right)\bar{q}\gamma^\beta(g_V^q - g_A^q\gamma_5)q, \tag{C.15}$$

where γ^α are the ordinary Dirac gamma matrices, $\gamma^5 = (i/4!)\varepsilon_{\alpha\beta\gamma\delta}\gamma^\alpha\gamma^\beta\gamma^\gamma\gamma^\delta$ is the fifth gamma matrix, and the couplings are given by $g_V^{u,c,t} = 1/2 - (4/3)s^2_W$, $g_A^{u,c,t} = 1/2$, $g_V^{d,s,b} = -1/2 + (2/3)s^2_{\text{W}}$ and $g_A^{d,s,b} = -1/2$. We note that $F^a_{\alpha\beta}$ can only depend on the momenta p_N and q and thus decomposes into

$$\begin{aligned}F^a_{\alpha\beta} = &- g_{\alpha\beta} F^a_1 + \frac{p_{N\,\alpha} p_{N\,\beta}}{m_N^2} \frac{m_N}{\epsilon} F^a_2 - i\, \frac{\epsilon_{\alpha\beta\gamma\delta} p_N^\gamma q^\delta}{2m_N^2} \frac{m_N}{\epsilon} F^a_3 \\ &+ \frac{q^\alpha q^\beta}{m_N^2} F^a_4 + \frac{p_N^\alpha q^\beta + p_N^\beta q^\alpha}{2m_N^2} F^a_5 \\ &+ i\, \frac{p_N^\alpha q^\beta - p_N^\beta q^\alpha}{2m_N^2} F^a_6\,.\end{aligned} \tag{C.16}$$

With the adopted decomposition of $F^a_{\alpha\beta}$, the quantities F^a_1, F^a_2, F^a_3, F^a_4, F^a_5 and F^a_6 are dimensionless. As can be checked, the third line proportional to F^a_6 gives vanishing contributions when contracted with the combination of leptonic momenta appearing in the second line of Eq. (C.13). The same holds for the F^a_4 and F^a_5 contributions in the limit of vanishing neutrino masses. Thus, only the terms proportional to F^a_1, F^a_2 and F^a_3 are relevant in our calculation. We then get the following expressions for the F^a_1, F^a_2 and F^a_3 [505]:

$$F_1^{q(\bar{q})} = \frac{1}{2}[(g_V^q)^2 + (g_A^q)^2] f^N_{q(\bar{q})}(x, Q^2), \tag{C.17}$$

$$F_2^{q(\bar{q})} = 2x F_1^{q(\bar{q})} \tag{C.18}$$

$$F_3^{q(\bar{q})} = (-) 2 g_V^q g_A^q f^N_{q(\bar{q})}(x, Q^2). \tag{C.19}$$

Plugging the above expressions in Eq. (C.13), after contraction of the Lorentz indices, we arrive to [505, 506]:

$$\frac{d^2\sigma^{\rm DIS}_{\nu N}}{dx dy} \simeq \frac{G_F^2}{2\pi} \frac{Q^2}{[1+Q^2/M_Z^2]^2} \left[y F_1^{ZN}(x, Q^2) + \frac{1}{xy}\left(1 - y - \frac{m_N^2 x^2 y^2}{Q^2}\right) F_2^{ZN}(x, Q^2) \pm \left(1 - \frac{y}{2}\right) F_3^{ZN}(x, Q^2)\right], \tag{C.20}$$

where $+(-)$ for the scattering with (anti)neutrinos, while $F_1^{ZN} = \sum_{a=q,\bar{q}} F^a_1$, $F_2^{ZN} = \sum_{a=q,\bar{q}} F^a_2$ and $F_3^{ZN} = \sum_{a=q,\bar{q}} F^a_3$. Note that, in the above formula, Q^2 should be given in terms of x, y and s as $Q^2 = (s - m_N^2 - m_\nu^2)xy$. It can be further simplified if we consider the sum of neutrinos and antineutrinos contributions, $\sigma^{\rm DIS}_{(\nu+\bar{\nu})N} = \sigma^{\rm DIS}_{\nu N} + \sigma^{\rm DIS}_{\bar{\nu} N}$:

$$\begin{aligned}\frac{d^2\sigma^{\rm DIS}_{(\nu+\bar{\nu})N}}{dx dy} \simeq \sum_{a=q,\bar{q}} \frac{G_F^2}{2\pi} &\frac{Q^2[(g_V^a)^2 + (g_A^a)^2] f^N_a(x, Q^2)}{[1+Q^2/M_Z^2]^2} \\ &\times \left(y - 2 + \frac{2}{y} - \frac{2 m_N^2 x^2 y}{Q^2}\right).\end{aligned} \tag{C.21}$$

In the reference frame in which the neutrino is at rest, the variable x can be written as $x = (E_\nu - m_\nu)/(E_N y)$, from which we get $dx/dE_\nu = 1/(E_N y)$. Then, the DIS differential cross section that we need for the boosted neutrino flux calculation is given by:

$$\frac{d\sigma^{\rm DIS}_{(\nu+\bar{\nu})N}}{dE_\nu} = \frac{1}{E_N} \int_{y_{\rm min}}^{y_{\rm max}} \frac{dy}{y} \frac{d\sigma^{\rm DIS}_{(\nu+\bar{\nu})N}}{dx dy}, \tag{C.22}$$

which leads to the expression given in Eq. (4.55) of the main text, where, to keep a shorter notation, we have written $d\sigma^{\rm DIS}_{\nu N}$ in place of $d\sigma^{\rm DIS}_{(\nu+\bar{\nu})N}$. As already specified, to evaluate numerically the quark PDFs, we made use of the Python package `parton` and the "CT10" PDF set [449]. The quark PDFs in the considered library are given for $x \geq x_{\rm min} = 10^{-8}$ and in the range $Q^2_{\rm min} = 1.69\,{\rm GeV}^2 \leq Q^2 \leq Q^2_{\rm max} = 10^{10}\,{\rm GeV}^2$. This practically limits our ability to properly estimate the DIS cross section outside the energy range $Q^2_{\rm min}/(2m_\nu) \leq E_\nu - m_\nu \leq \min\{Q^2_{\rm max}/(2m_\nu), T_\nu^{\rm max}(T_N)\}$, where $T_\nu^{\rm max}(T_N)$ is the maximal kinetic energy the neutrino can have after an elastic scattering,

$$T_\nu^{\rm max}(T_N) = \frac{\left(T_N^2 + 2m_N T_N\right)}{T_N + (m_N + m_\nu)^2/(2m_\nu)}, \tag{C.23}$$

and $T_N \equiv E_N - m_N$ the initial kinetic energy of the incoming nucleon. As an indicative procedure to avoid unphysical discontinuities, we have extrapolated the DIS contribution for $Q^2 \leq Q^2_{\rm min}$ by assuming a linear scaling in Q^2. In practice, this does not affect any of our predictions for the range of E_ν of interest for the UHE neutrino telescopes considered in our study. Finally, we note that the inelasticity parameter lies between $y_{\rm min} = (E_\nu - m_\nu)/E_N$ and $y_{\rm max} = \min\{1, (E_\nu - m_\nu)/(E_N x_{\rm min})\} = 1$.

Bibliography

[1] M. Dichtl, J. Nava, S. Pascoli and F. Sala, *Baryogenesis and leptogenesis from supercooled confinement*, *JHEP* **02** (2024) 059 [2312.09282].

[2] A. G. De Marchi, A. Granelli, J. Nava and F. Sala, *Relic neutrino background from cosmic-ray reservoirs*, *Phys. Rev. D* **111** (2025) 023023 [2405.04568].

[3] A. G. De Marchi, A. Granelli, J. Nava and F. Sala, *Did IceCube discover Dark Matter around Blazars?*, 2412.07861.

[4] A. G. De Marchi, A. Granelli, J. Nava and F. Sala, *Diffuse astrophysical neutrinos from dark matter around blazars*, 2506.06416.

[5] A. G. De Marchi, A. Granelli, F. Sala and J. Nava, *Boosted dark matter versus dark matter-induced neutrinos from single and stacked blazars*, 2507.12278.

[6] A. Musumeci, J. Nava, S. Pascoli and F. Sala, *Nanohertz gravitational waves from the baryon dark matter coincidence*, arXiv:25xx.xxxxx.

[7] P. Escribano, M. Hirsch, J. Nava and A. Vicente, *Observable flavor violation from spontaneous lepton number breaking*, *JHEP* **01** (2022) 098 [2108.01101].

[8] V. De Romeri, J. Nava, M. Puerta and A. Vicente, *Dark matter in the scotogenic model with spontaneous lepton number violation*, *Phys. Rev. D* **107** (2023) 095019 [2210.07706].

[9] NEON collaboration, *New Constraints on Axionlike Particles with the NEON Detector at a Nuclear Reactor*, *Phys. Rev. Lett.* **134** (2025) 201002 [2406.06117].

[10] P. A. M. Dirac, *The quantum theory of the electron*, *Proc. Roy. Soc. Lond. A* **117** (1928) 610.

[11] C. D. Anderson, *The Positive Electron*, *Phys. Rev.* **43** (1933) 491.

[12] G. Steigman, *Observational tests of antimatter cosmologies*, *Ann. Rev. Astron. Astrophys.* **14** (1976) 339.

[13] G. Steigman, *When Clusters Collide: Constraints On Antimatter On The Largest Scales*, *JCAP* **10** (2008) 001 [0808.1122].

[14] Planck collaboration, *Planck 2018 results. VI. Cosmological parameters*, *Astronomy & Astrophysics* **641** (2020) A6 [1807.06209].

[15] B. D. Fields, K. A. Olive, T.-H. Yeh and C. Young, *Big-Bang Nucleosynthesis after Planck*, *JCAP* **03** (2020) 010 [1912.01132].

[16] E. W. Kolb and M. S. Turner, *The Early Universe*, vol. 69. Taylor and Francis, 5, 2019, 10.1201/9780429492860.

[17] A. H. Guth, *The Inflationary Universe: A Possible Solution to the Horizon and Flatness Problems*, *Phys. Rev. D* **23** (1981) 347.

[18] A. D. Sakharov, *Violation of CP Invariance, C asymmetry, and baryon asymmetry of the universe*, *Pisma Zh. Eksp. Teor. Fiz.* **5** (1967) 32.

[19] A. Riotto and M. Trodden, *Recent progress in baryogenesis*, *Ann. Rev. Nucl. Part. Sci.* **49** (1999) 35 [hep-ph/9901362].

[20] G. 't Hooft, *Symmetry Breaking Through Bell-Jackiw Anomalies*, *Phys. Rev. Lett.* **37** (1976) 8.

[21] S. R. Coleman and E. J. Weinberg, *Radiative Corrections as the Origin of Spontaneous Symmetry Breaking*, *Phys. Rev. D* **7** (1973) 1888.

[22] M. Trodden, *Electroweak baryogenesis*, *Rev. Mod. Phys.* **71** (1999) 1463 [hep-ph/9803479].

[23] V. A. Kuzmin, V. A. Rubakov and M. E. Shaposhnikov, *On the Anomalous Electroweak Baryon Number Nonconservation in the Early Universe*, *Phys. Lett. B* **155** (1985) 36.

[24] M. D'Onofrio, K. Rummukainen and A. Tranberg, *Sphaleron Rate in the Minimal Standard Model*, *Phys. Rev. Lett.* **113** (2014) 141602 [1404.3565].

[25] G. D. Moore, C.-r. Hu and B. Muller, *Chern-Simons number diffusion with hard thermal loops*, *Phys. Rev. D* **58** (1998) 045001 [hep-ph/9710436].

[26] J. A. Harvey and M. S. Turner, *Cosmological baryon and lepton number in the presence of electroweak fermion number violation*, *Phys. Rev. D* **42** (1990) 3344.

[27] M. Kobayashi and T. Maskawa, *CP Violation in the Renormalizable Theory of Weak Interaction*, *Prog. Theor. Phys.* **49** (1973) 652.

[28] M. B. Gavela, P. Hernandez, J. Orloff, O. Pene and C. Quimbay, *Standard model CP violation and baryon asymmetry. Part 2: Finite temperature*, *Nucl. Phys. B* **430** (1994) 382 [hep-ph/9406289].

[29] M. B. Gavela, M. Lozano, J. Orloff and O. Pene, *Standard model CP violation and baryon asymmetry. Part 1: Zero temperature*, *Nucl. Phys. B* **430** (1994) 345 [hep-ph/9406288].

[30] C. Jarlskog, *Commutator of the Quark Mass Matrices in the Standard Electroweak Model and a Measure of Maximal CP Nonconservation*, *Phys. Rev. Lett.* **55** (1985) 1039.

[31] K. Kajantie, M. Laine, K. Rummukainen and M. E. Shaposhnikov, *Is there a hot electroweak phase transition at $m_H \gtrsim m_W$?*, *Phys. Rev. Lett.* **77** (1996) 2887 [hep-ph/9605288].

[32] K. Rummukainen, M. Tsypin, K. Kajantie, M. Laine and M. E. Shaposhnikov, *The Universality class of the electroweak theory*, *Nucl. Phys. B* **532** (1998) 283 [hep-lat/9805013].

[33] H. Georgi and S. L. Glashow, *Unity of All Elementary Particle Forces*, *Phys. Rev. Lett.* **32** (1974) 438.

[34] A. Y. Ignatiev, N. V. Krasnikov, V. A. Kuzmin and A. N. Tavkhelidze, *Universal CP Noninvariant Superweak Interaction and Baryon Asymmetry of the Universe*, *Phys. Lett. B* **76** (1978) 436.

[35] M. Yoshimura, *Unified Gauge Theories and the Baryon Number of the Universe*, *Phys. Rev. Lett.* **41** (1978) 281.

[36] Super-Kamiokande collaboration, *Search for proton decay via $p \to \nu K^+$ using 260 kiloton·year data of Super-Kamiokande*, *Phys. Rev. D* **90** (2014) 072005 [1408.1195].

[37] B. A. Bassett, S. Tsujikawa and D. Wands, *Inflation dynamics and reheating*, *Rev. Mod. Phys.* **78** (2006) 537 [astro-ph/0507632].

[38] A. Riotto, *Theories of baryogenesis*, in *ICTP Summer School in High-Energy Physics and Cosmology*, pp. 326–436, 7, 1998, hep-ph/9807454.

[39] I. Affleck and M. Dine, *A New Mechanism for Baryogenesis*, *Nucl. Phys. B* **249** (1985) 361.

[40] R. Allahverdi and A. Mazumdar, *A mini review on Affleck-Dine baryogenesis*, *New J. Phys.* **14** (2012) 125013.
[41] M. Fukugita and T. Yanagida, *Baryogenesis Without Grand Unification*, *Phys. Lett. B* **174** (1986) 45.
[42] P. Minkowski, *$\mu \to e\gamma$ at a Rate of One Out of 10^9 Muon Decays?*, *Phys. Lett. B* **67** (1977) 421.
[43] T. Yanagida, *Horizontal gauge symmetry and masses of neutrinos*, *Conf. Proc. C* **7902131** (1979) 95.
[44] S. Davidson and A. Ibarra, *A Lower bound on the right-handed neutrino mass from leptogenesis*, *Phys. Lett. B* **535** (2002) 25 [hep-ph/0202239].
[45] A. Pilaftsis and T. E. J. Underwood, *Resonant leptogenesis*, *Nucl. Phys. B* **692** (2004) 303 [hep-ph/0309342].
[46] S. Davidson, E. Nardi and Y. Nir, *Leptogenesis*, *Phys. Rept.* **466** (2008) 105 [0802.2962].
[47] W. Buchmuller, R. D. Peccei and T. Yanagida, *Leptogenesis as the origin of matter*, *Ann. Rev. Nucl. Part. Sci.* **55** (2005) 311 [hep-ph/0502169].
[48] A. G. Cohen, D. B. Kaplan and A. E. Nelson, *Progress in electroweak baryogenesis*, *Ann. Rev. Nucl. Part. Sci.* **43** (1993) 27 [hep-ph/9302210].
[49] ACME collaboration, *Order of Magnitude Smaller Limit on the Electric Dipole Moment of the Electron*, *Science* **343** (2014) 269 [1310.7534].
[50] J. M. No, *Large Gravitational Wave Background Signals in Electroweak Baryogenesis Scenarios*, *Phys. Rev. D* **84** (2011) 124025 [1103.2159].
[51] J. M. Cline, A. Friedlander, D.-M. He, K. Kainulainen, B. Laurent and D. Tucker-Smith, *Baryogenesis and gravity waves from a UV-completed electroweak phase transition*, *Phys. Rev. D* **103** (2021) 123529 [2102.12490].
[52] A. Falkowski and J. M. No, *Non-thermal Dark Matter Production from the Electroweak Phase Transition: Multi-TeV WIMPs and 'Baby-Zillas'*, *JHEP* **02** (2013) 034 [1211.5615].
[53] I. Baldes, Y. Gouttenoire and F. Sala, *Hot and heavy dark matter from a weak scale phase transition*, *SciPost Phys.* **14** (2023) 033 [2207.05096].
[54] A. Azatov, M. Vanvlasselaer and W. Yin, *Dark Matter production from relativistic bubble walls*, *JHEP* **03** (2021) 288 [2101.05721].
[55] H. Pagels and J. R. Primack, *Supersymmetry, Cosmology and New TeV Physics*, *Phys. Rev. Lett.* **48** (1982) 223.
[56] P. Sikivie, *Axion Cosmology*, *Lect. Notes Phys.* **741** (2008) 19 [astro-ph/0610440].
[57] G. Elor et al., *New Ideas in Baryogenesis: A Snowmass White Paper*, in *Snowmass 2021*, 3, 2022, 2203.05010.
[58] G. Elor, M. Escudero and A. Nelson, *Baryogenesis and Dark Matter from B Mesons*, *Phys. Rev. D* **99** (2019) 035031 [1810.00880].
[59] G. Elor and R. McGehee, *Making the Universe at 20 MeV*, *Phys. Rev. D* **103** (2021) 035005 [2011.06115].
[60] K. M. Zurek, *Asymmetric Dark Matter: Theories, Signatures, and Constraints*, *Physics Reports* **537** (2014) 91 [1308.0338].
[61] D. B. Kaplan, *A Single explanation for both the baryon and dark matter densities*, *Phys. Rev. Lett.* **68** (1992) 741.
[62] J. Shelton and K. M. Zurek, *Darkogenesis: A baryon asymmetry from the dark matter sector*, *Phys. Rev. D* **82** (2010) 123512 [1008.1997].

[63] T. Bringmann, J. M. Cline and J. M. Cornell, *Baryogenesis from neutron-dark matter oscillations*, *Phys. Rev. D* **99** (2019) 035024 [1810.08215].

[64] NANOGrav collaboration, *The NANOGrav 15 yr Data Set: Search for Signals from New Physics*, *Astrophys. J. Lett.* **951** (2023) L11 [2306.16219].

[65] W. Pauli, *Dear radioactive ladies and gentlemen*, *Phys. Today* **31N9** (1978) 27.

[66] C. L. Cowan, F. Reines, F. B. Harrison, H. W. Kruse and A. D. McGuire, *Detection of the free neutrino: A Confirmation*, *Science* **124** (1956) 103.

[67] R. Davis, Jr., D. S. Harmer and K. C. Hoffman, *Search for neutrinos from the sun*, *Phys. Rev. Lett.* **20** (1968) 1205.

[68] B. Pontecorvo, *Mesonium and anti-mesonium*, *Journal of Experimental and Theoretical Physics* **6** (1957) 429.

[69] B. Pontecorvo, *Inverse beta processes and nonconservation of lepton charge*, *Journal of Experimental and Theoretical Physics* **34** (1957) 247.

[70] Super-Kamiokande collaboration, *Evidence for oscillation of atmospheric neutrinos*, *Phys. Rev. Lett.* **81** (1998) 1562 [hep-ex/9807003].

[71] SNO collaboration, *Direct evidence for neutrino flavor transformation from neutral current interactions in the Sudbury Neutrino Observatory*, *Phys. Rev. Lett.* **89** (2002) 011301 [nucl-ex/0204008].

[72] KamLAND collaboration, *First results from KamLAND: Evidence for reactor anti-neutrino disappearance*, *Phys. Rev. Lett.* **90** (2003) 021802 [hep-ex/0212021].

[73] Z. Maki, M. Nakagawa and S. Sakata, *Remarks on the unified model of elementary particles*, *Progress of Theoretical Physics* **28** (1962) 870.

[74] Particle Data Group collaboration, *Review of particle physics*, *Phys. Rev. D* **110** (2024) 030001.

[75] KATRIN collaboration, *Direct neutrino-mass measurement based on 259 days of KATRIN data*, *Science* **388** (2025) adq9592 [2406.13516].

[76] DESI collaboration, *DESI 2024 VI: Cosmological Constraints from the Measurements of Baryon Acoustic Oscillations*, 2404.03002.

[77] JUNO collaboration, *JUNO physics and detector*, *Prog. Part. Nucl. Phys.* **123** (2022) 103927 [2104.02565].

[78] DUNE collaboration, *Long-Baseline Neutrino Facility (LBNF) and Deep Underground Neutrino Experiment (DUNE): Conceptual Design Report, Volume 2: The Physics Program for DUNE at LBNF*, 1512.06148.

[79] Hyper-Kamiokande collaboration, *Hyper-Kamiokande Design Report*, 1805.04163.

[80] Double Chooz collaboration, *Improved measurements of the neutrino mixing angle θ_{13} with the Double Chooz detector*, *JHEP* **10** (2014) 086 [1406.7763].

[81] KamLAND collaboration, *Constraints on θ_{13} from A Three-Flavor Oscillation Analysis of Reactor Antineutrinos at KamLAND*, *Phys. Rev. D* **83** (2011) 052002 [1009.4771].

[82] T2K collaboration, *Precise Measurement of the Neutrino Mixing Parameter θ_{23} from Muon Neutrino Disappearance in an Off-Axis Beam*, *Phys. Rev. Lett.* **112** (2014) 181801 [1403.1532].

[83] U. Rahaman, S. Razzaque and S. U. Sankar, *A Review of the Tension between the T2K and NOνA Appearance Data and Hints to New Physics*, *Universe* **8** (2022) 109 [2201.03250].

[84] P. B. Denton, J. Gehrlein and R. Pestes, *CP-Violating Neutrino Nonstandard Interactions in Long-Baseline-Accelerator Data*, *Phys. Rev. Lett.* **126** (2021) 051801 [2008.01110].

[85] I. Esteban, M. C. Gonzalez-Garcia, M. Maltoni, I. Martinez-Soler, J. a. P. Pinheiro and T. Schwetz, *NuFit-6.0: updated global analysis of three-flavor neutrino oscillations*, *JHEP* **12** (2024) 216 [2410.05380].

[86] J. Engel and J. Menéndez, *Status and Future of Nuclear Matrix Elements for Neutrinoless Double-Beta Decay: A Review*, *Rept. Prog. Phys.* **80** (2017) 046301 [1610.06548].

[87] C. Alexandrou, S. Bacchio, M. Constantinou, K. Hadjiyiannakou, K. Jansen and G. Koutsou, *Quark flavor decomposition of the nucleon axial form factors*, *Physical Review D* **104** (2021) .

[88] S. Stoica and M. Mirea, *New calculations for phase space factors involved in double-β decay*, *Phys. Rev. C* **88** (2013) 037303 [1307.0290].

[89] M. Agostini, G. Benato, J. A. Detwiler, J. Menéndez and F. Vissani, *Toward the discovery of matter creation with neutrinoless $\beta\beta$ decay*, *Rev. Mod. Phys.* **95** (2023) 025002 [2202.01787].

[90] S. Weinberg, *Baryon and Lepton Nonconserving Processes*, *Phys. Rev. Lett.* **43** (1979) 1566.

[91] E. Ma, *Pathways to naturally small neutrino masses*, *Phys. Rev. Lett.* **81** (1998) 1171 [hep-ph/9805219].

[92] J. Schechter and J. W. F. Valle, *Neutrino Masses in SU(2) x U(1) Theories*, *Phys. Rev. D* **22** (1980) 2227.

[93] M. Magg and C. Wetterich, *Neutrino Mass Problem and Gauge Hierarchy*, *Phys. Lett. B* **94** (1980) 61.

[94] R. Foot, H. Lew, X. G. He and G. C. Joshi, *Seesaw Neutrino Masses Induced by a Triplet of Leptons*, *Z. Phys. C* **44** (1989) 441.

[95] Y. Cai, J. Herrero-García, M. A. Schmidt, A. Vicente and R. R. Volkas, *From the trees to the forest: a review of radiative neutrino mass models*, *Front. in Phys.* **5** (2017) 63 [1706.08524].

[96] R. Primulando, J. Julio and P. Uttayarat, *Scalar phenomenology in type-II seesaw model*, *JHEP* **08** (2019) 024 [1903.02493].

[97] A. Atre, T. Han, S. Pascoli and B. Zhang, *The Search for Heavy Majorana Neutrinos*, *JHEP* **05** (2009) 030 [0901.3589].

[98] ATLAS collaboration, *Search for type-III seesaw heavy leptons in leptonic final states in pp collisions at $\sqrt{s} = 13$ TeV with the ATLAS detector*, *Eur. Phys. J. C* **82** (2022) 988 [2202.02039].

[99] A. Zee, *A Theory of Lepton Number Violation, Neutrino Majorana Mass, and Oscillation*, *Phys. Lett. B* **93** (1980) 389.

[100] A. Zee, *Quantum Numbers of Majorana Neutrino Masses*, *Nucl. Phys. B* **264** (1986) 99.

[101] K. S. Babu, *Model of 'Calculable' Majorana Neutrino Masses*, *Phys. Lett. B* **203** (1988) 132.

[102] E. Ma, *Verifiable radiative seesaw mechanism of neutrino mass and dark matter*, *Phys. Rev. D* **73** (2006) 077301 [hep-ph/0601225].

[103] V. C. Rubin and W. K. Ford, Jr., *Rotation of the Andromeda Nebula from a Spectroscopic Survey of Emission Regions*, *Astrophys. J.* **159** (1970) 379.

[104] F. Zwicky, *Die Rotverschiebung von extragalaktischen Nebeln*, *Helv. Phys. Acta* **6** (1933) 110.

[105] C. L. Sarazin, *X-ray emission from clusters of galaxies*, *Rev. Mod. Phys.* **58** (1986) 1.

[106] M. Bradac, S. W. Allen, T. Treu, H. Ebeling, R. Massey, R. G. Morris et al., *Revealing the properties of dark matter in the merging cluster MACSJ0025.4-1222*, *Astrophys. J.* **687** (2008) 959 [0806.2320].

[107] D. E. McLaughlin, *Evidence in virgo for the universal dark matter halo*, *Astrophys. J. Lett.* **512** (1999) L9 [astro-ph/9812242].

[108] D. Clowe, M. Bradac, A. H. Gonzalez, M. Markevitch, S. W. Randall, C. Jones et al., *A direct empirical proof of the existence of dark matter*, *Astrophys. J. Lett.* **648** (2006) L109 [astro-ph/0608407].

[109] K. G. Begeman, A. H. Broeils and R. H. Sanders, *Extended rotation curves of spiral galaxies: Dark haloes and modified dynamics*, *Mon. Not. Roy. Astron. Soc.* **249** (1991) 523.

[110] D. J. Fixsen, *The Temperature of the Cosmic Microwave Background*, *Astrophys. J.* **707** (2009) 916 [0911.1955].

[111] BOSS collaboration, *The clustering of galaxies in the completed SDSS-III Baryon Oscillation Spectroscopic Survey: cosmological analysis of the DR12 galaxy sample*, *Mon. Not. Roy. Astron. Soc.* **470** (2017) 2617 [1607.03155].

[112] eBOSS collaboration, *The SDSS-IV extended Baryon Oscillation Spectroscopic Survey: Overview and Early Data*, *Astron. J.* **151** (2016) 44 [1508.04473].

[113] M. Viel, G. D. Becker, J. S. Bolton and M. G. Haehnelt, *Warm dark matter as a solution to the small scale crisis: New constraints from high redshift Lyman-α forest data*, *Phys. Rev. D* **88** (2013) 043502 [1306.2314].

[114] S. Chabanier, M. Millea and N. Palanque-Delabrouille, *Matter power spectrum: from Lyα forest to CMB scales*, *Mon. Not. Roy. Astron. Soc.* **489** (2019) 2247 [1905.08103].

[115] M. Cirelli, A. Strumia and J. Zupan, *Dark Matter*, 2406.01705.

[116] M. W. Goodman and E. Witten, *Detectability of Certain Dark Matter Candidates*, *Phys. Rev. D* **31** (1985) 3059.

[117] DAMA, LIBRA collaboration, *New results from DAMA/LIBRA*, *Eur. Phys. J. C* **67** (2010) 39 [1002.1028].

[118] COSINE-100 collaboration, *Search for a Dark Matter-Induced Annual Modulation Signal in NaI(Tl) with the COSINE-100 Experiment*, *Phys. Rev. Lett.* **123** (2019) 031302 [1903.10098].

[119] XENON collaboration, *Search for Electronic Recoil Event Rate Modulation with 4 Years of XENON100 Data*, *Phys. Rev. Lett.* **118** (2017) 101101 [1701.00769].

[120] XENON collaboration, *WIMP Dark Matter Search using a 3.1 tonne $\times$ year Exposure of the XENONnT Experiment*, 2502.18005.

[121] LZ collaboration, *Dark Matter Search Results from 4.2 Tonne-Years of Exposure of the LUX-ZEPLIN (LZ) Experiment*, 2410.17036.

[122] PandaX-4T collaboration, *Dark Matter Search Results from the PandaX-4T Commissioning Run*, *Phys. Rev. Lett.* **127** (2021) 261802 [2107.13438].

[123] A. Migdal, *Ionizatsiya atomov pri yadernykh reaktsiyakh*, *Sov. Phys. JETP* **9** (1939) 1163.

[124] R. Essig et al., *Working Group Report: New Light Weakly Coupled Particles*, in *Snowmass 2013: Snowmass on the Mississippi*, 10, 2013, 1311.0029.

[125] C. A. J. O'Hare, *New Definition of the Neutrino Floor for Direct Dark Matter Searches*, *Phys. Rev. Lett.* **127** (2021) 251802 [2109.03116].

[126] T. Siegert, R. Diehl, G. Khachatryan, M. G. H. Krause, F. Guglielmetti, J. Greiner et al., *Gamma-ray spectroscopy of Positron Annihilation in the Milky Way*, *Astron. Astrophys.* **586** (2016) A84 [1512.00325].

[127] C. Boehm, D. Hooper, J. Silk, M. Casse and J. Paul, *MeV dark matter: Has it been detected?*, *Phys. Rev. Lett.* **92** (2004) 101301 [astro-ph/0309686].

[128] P. De la Torre Luque, S. Balaji, M. Fairbairn, F. Sala and J. Silk, *511 keV Galactic Photons from a Dark Matter Spike*, 2410.16379.

[129] S. Das, M. R. Krumholz, R. M. Crocker, T. Siegert and L. Eisenberger, *Relaxation of Energy Constraints for Positrons Generating the Galactic Annihilation Signal*, 2506.00847.

[130] P. De la Torre Luque, S. Balaji and J. Koechler, *Importance of Cosmic-Ray Propagation on Sub-GeV Dark Matter Constraints*, *Astrophys. J.* **968** (2024) 46 [2311.04979].

[131] G. M. Fuller, A. Kusenko, D. Radice and V. Takhistov, *Positrons and 511 keV Radiation as Tracers of Recent Binary Neutron Star Mergers*, *Phys. Rev. Lett.* **122** (2019) 121101 [1811.00133].

[132] N. Prantzos et al., *The 511 keV emission from positron annihilation in the Galaxy*, *Rev. Mod. Phys.* **83** (2011) 1001 [1009.4620].

[133] S. Murgia, *The Fermi–LAT Galactic Center Excess: Evidence of Annihilating Dark Matter?*, *Ann. Rev. Nucl. Part. Sci.* **70** (2020) 455.

[134] L. Goodenough and D. Hooper, *Possible Evidence For Dark Matter Annihilation In The Inner Milky Way From The Fermi Gamma Ray Space Telescope*, 0910.2998.

[135] Fermi-LAT collaboration, *The Fermi Galactic Center GeV Excess and Implications for Dark Matter*, *Astrophys. J.* **840** (2017) 43 [1704.03910].

[136] O. Macias, C. Gordon, R. M. Crocker, B. Coleman, D. Paterson, S. Horiuchi et al., *Galactic bulge preferred over dark matter for the Galactic centre gamma-ray excess*, *Nature Astron.* **2** (2018) 387 [1611.06644].

[137] ANTARES collaboration, *Limits on Dark Matter Annihilation in the Sun using the ANTARES Neutrino Telescope*, *Phys. Lett. B* **759** (2016) 69 [1603.02228].

[138] IceCube collaboration, *Search for annihilating dark matter in the Sun with 3 years of IceCube data*, *Eur. Phys. J. C* **77** (2017) 146 [1612.05949].

[139] Super-Kamiokande collaboration, *Indirect search for dark matter from the Galactic Center and halo with the Super-Kamiokande detector*, *Phys. Rev. D* **102** (2020) 072002 [2005.05109].

[140] PAMELA collaboration, *An anomalous positron abundance in cosmic rays with energies 1.5-100 GeV*, *Nature* **458** (2009) 607 [0810.4995].

[141] A. Cuoco, M. Krämer and M. Korsmeier, *Novel Dark Matter Constraints from Antiprotons in Light of AMS-02*, *Phys. Rev. Lett.* **118** (2017) 191102 [1610.03071].

[142] GAPS collaboration, *Antideuteron Sensitivity for the GAPS Experiment*, *Astropart. Phys.* **74** (2016) 6 [1506.02513].

[143] G. Jungman, M. Kamionkowski and K. Griest, *Supersymmetric dark matter*, *Phys. Rept.* **267** (1996) 195 [hep-ph/9506380].

[144] ATLAS collaboration, *Search for dark matter in events with missing transverse momentum and a Higgs boson decaying into two photons in pp collisions at $\sqrt{s}$ = 13 TeV with the ATLAS detector*, *JHEP* **10** (2021) 013 [2104.13240].

[145] T. R. Slatyer, *Energy Injection And Absorption In The Cosmic Dark Ages*, *Phys. Rev. D* **87** (2013) 123513 [1211.0283].

[146] S. Bianco, P. F. Depta, J. Frerick, T. Hambye, M. Hufnagel and K. Schmidt-Hoberg, *Photo- and Hadrodisintegration constraints on massive relics decaying into neutrinos*, 2505.01492.

[147] G. Steigman, *Primordial Nucleosynthesis in the Precision Cosmology Era*, Ann. Rev. Nucl. Part. Sci. **57** (2007) 463 [0712.1100].

[148] T. R. Slatyer, *Indirect dark matter signatures in the cosmic dark ages. I. Generalizing the bound on s-wave dark matter annihilation from Planck results*, Phys. Rev. D **93** (2016) 023527 [1506.03811].

[149] G. Steigman, B. Dasgupta and J. F. Beacom, *Precise Relic WIMP Abundance and its Impact on Searches for Dark Matter Annihilation*, Phys. Rev. D **86** (2012) 023506 [1204.3622].

[150] G. Steigman, *Neutrinos And Big Bang Nucleosynthesis*, Advances in High Energy Physics **2012** (2012) 268321 [1208.0032].

[151] SuperCDMS Collaboration, *Search for low-mass dark matter via bremsstrahlung radiation and the Migdal effect in SuperCDMS*, Phys. Rev. D **107** (2023) 112013 [2302.09115].

[152] Y. Hochberg, E. Kuflik, T. Volansky and J. G. Wacker, *Mechanism for Thermal Relic Dark Matter of Strongly Interacting Massive Particles*, Phys. Rev. Lett. **113** (2014) 171301 [1402.5143].

[153] S. Knapen, T. Lin and K. M. Zurek, *Light Dark Matter: Models and Constraints*, Phys. Rev. D **96** (2017) 115021 [1709.07882].

[154] CRESST collaboration, *First results from the CRESST-III low-mass dark matter program*, Phys. Rev. D **100** (2019) 102002 [1904.00498].

[155] DarkSide Collaboration, *Low-Mass Dark Matter Search with the DarkSide-50 Experiment*, Phys. Rev. Lett. **121** (2018) 081307 [1802.06994].

[156] NEWS-G collaboration, *Search for Light Dark Matter with NEWS-G at the Laboratoire Souterrain de Modane Using a Methane Target*, Phys. Rev. Lett. **134** (2025) 141002 [2407.12769].

[157] SENSEI Collaboration, *SENSEI: First Direct-Detection Results on sub-GeV Dark Matter from SENSEI at SNOLAB*, 2312.13342.

[158] S. Knapen, T. Lin, M. Pyle and K. M. Zurek, *Detection of Light Dark Matter With Optical Phonons in Polar Materials*, Phys. Lett. B **785** (2018) 386 [1712.06598].

[159] R. Essig, J. Pradler, M. Sholapurkar and T.-T. Yu, *Relation between the Migdal Effect and Dark Matter-Electron Scattering in Isolated Atoms and Semiconductors*, Phys. Rev. Lett. **124** (2020) 021801 [1908.10881].

[160] J. Xu et al., *Search for the Migdal effect in liquid xenon with keV-level nuclear recoils*, 2307.12952.

[161] R. Essig, J. Mardon and T. Volansky, *Direct Detection of Sub-GeV Dark Matter*, Phys. Rev. D **85** (2012) 076007 [1108.5383].

[162] S. Derenzo, R. Essig, A. Massari, A. Soto and T.-T. Yu, *Direct Detection of sub-GeV Dark Matter with Scintillating Targets*, Phys. Rev. D **96** (2017) 016026 [1607.01009].

[163] T. Bringmann and M. Pospelov, *Novel direct detection constraints on light dark matter*, Phys. Rev. Lett. **122** (2019) 171801 [1810.10543].

[164] Y. Ema, F. Sala and R. Sato, *Light Dark Matter at Neutrino Experiments*, Phys. Rev. Lett. **122** (2019) 181802 [1811.00520].

[165] Y. Ema, F. Sala and R. Sato, *Neutrino experiments probe hadrophilic light dark matter*, SciPost Phys. **10** (2021) 072 [2011.01939].

[166] J.-W. Wang, A. Granelli and P. Ullio, *Direct Detection Constraints on Blazar-Boosted Dark Matter*, *Phys. Rev. Lett.* **128** (2022) 221104 [2111.13644].
[167] G. Bertone and T. Tait, M. P., *A new era in the search for dark matter*, *Nature* **562** (2018) 51 [1810.01668].
[168] R. D. Peccei and H. R. Quinn, *CP Conservation in the Presence of Instantons*, *Phys. Rev. Lett.* **38** (1977) 1440.
[169] S. Dodelson and L. M. Widrow, *Sterile-neutrinos as dark matter*, *Phys. Rev. Lett.* **72** (1994) 17 [hep-ph/9303287].
[170] A. M. Green and B. J. Kavanagh, *Primordial Black Holes as a dark matter candidate*, *J. Phys. G* **48** (2021) 043001 [2007.10722].
[171] K. Fang, J. S. Gallagher and F. Halzen, *The TeV Diffuse Cosmic Neutrino Spectrum and the Nature of Astrophysical Neutrino Sources*, *Astrophys. J.* **933** (2022) 190 [2205.03740].
[172] C. A. Argüelles, F. Halzen and N. Kurahashi, *From the Dawn of Neutrino Astronomy to A New View of the Extreme Universe*, 2405.17623.
[173] E. Vitagliano, I. Tamborra and G. Raffelt, *Grand Unified Neutrino Spectrum at Earth: Sources and Spectral Components*, *Rev. Mod. Phys.* **92** (2020) 45006 [1910.11878].
[174] PTOLEMY collaboration, *Neutrino physics with the PTOLEMY project: active neutrino properties and the light sterile case*, *Journal of Cosmology and Astroparticle Physics* **07** (2019) 047 [1902.05508].
[175] Borexino Collaboration collaboration, *Experimental evidence of neutrinos produced in the cno fusion cycle in the sun*, *Nature* **587** (2020) 577–582.
[176] T. Araki et al., *Experimental investigation of geologically produced antineutrinos with KamLAND*, *Nature* **436** (2005) 499.
[177] Borexino collaboration, *Observation of Geo-Neutrinos*, *Phys. Lett. B* **687** (2010) 299 [1003.0284].
[178] J. F. Beacom, *The Diffuse Supernova Neutrino Background*, *Ann. Rev. Nucl. Part. Sci.* **60** (2010) 439 [1004.3311].
[179] M. Harada, *Review of diffuse SN neutrino background*, 2024. 10.5281/zenodo.12726429.
[180] JUNO collaboration, *Prospects for detecting the diffuse supernova neutrino background with JUNO*, *JCAP* **10** (2022) 033 [2205.08830].
[181] Super-Kamiokande collaboration, *Diffuse supernova neutrino background search at Super-Kamiokande*, *Phys. Rev. D* **104** (2021) 122002 [2109.11174].
[182] K. Møller, A. M. Suliga, I. Tamborra and P. B. Denton, *Measuring the supernova unknowns at the next-generation neutrino telescopes through the diffuse neutrino background*, *JCAP* **05** (2018) 066 [1804.03157].
[183] IceCube collaboration, *Evidence for High-Energy Extraterrestrial Neutrinos at the IceCube Detector*, *Science* **342** (2013) 1242856 [1311.5238].
[184] IceCube, Fermi-LAT, MAGIC, AGILE, ASAS-SN, HAWC, H.E.S.S., INTEGRAL, Kanata, Kiso, Kapteyn, Liverpool Telescope, Subaru, Swift NuSTAR, VERITAS, VLA/17B-403 collaboration, *Multimessenger observations of a flaring blazar coincident with high-energy neutrino IceCube-170922A*, *Science* **361** (2018) eaat1378 [1807.08816].
[185] IceCube collaboration, *Constraints on Ultrahigh-Energy Cosmic-Ray Sources from a Search for Neutrinos above 10 PeV with IceCube*, *Phys. Rev. Lett.* **117** (2016) 241101 [1607.05886].

[186] K. Fang and K. Murase, *Linking High-Energy Cosmic Particles by Black Hole Jets Embedded in Large-Scale Structures*, *Nature Physics* **14** (2018) 396 [1704.00015].

[187] IceCube collaboration, *First observation of PeV-energy neutrinos with IceCube*, *Phys. Rev. Lett.* **111** (2013) 021103 [1304.5356].

[188] (IceCube Collaboration)*, IceCube collaboration, *All-flavor constraints on nonstandard neutrino interactions and generalized matter potential with three years of IceCube DeepCore data*, *Phys. Rev. D* **104** (2021) 072006 [2106.07755].

[189] IceCube collaboration, *Searches for Sterile Neutrinos with the IceCube Detector*, *Phys. Rev. Lett.* **117** (2016) 071801 [1605.01990].

[190] IceCube collaboration, *Search for quantum gravity using astrophysical neutrino flavour with IceCube*, *Nature Phys.* **18** (2022) 1287 [2111.04654].

[191] IceCube-Gen2 collaboration, *IceCube-Gen2: the window to the extreme Universe*, *Journal of Physics G: Nuclear and Particle Physics* **48** (2021) 060501 [2008.04323].

[192] KM3NeT collaboration, *Letter of intent for KM3NeT 2.0*, *J. Phys. G* **43** (2016) 084001 [1601.07459].

[193] KM3NeT collaboration, *Observation of an ultra-high-energy cosmic neutrino with KM3NeT*, *Nature* **638** (2025) 376.

[194] S. W. Li, P. Machado, D. Naredo-Tuero and T. Schwemberger, *Clash of the Titans: ultra-high energy KM3NeT event versus IceCube data*, 2502.04508.

[195] ANITA collaboration, *Constraints on the ultrahigh-energy cosmic neutrino flux from the fourth flight of ANITA*, *Physical Review D* **99** (2019) 122001 [1902.04005].

[196] Baikal-GVD collaboration, *Baikal-GVD: status and prospects*, *EPJ Web Conf.* **191** (2018) 01006 [1808.10353].

[197] RNO-G collaboration, *Design and Sensitivity of the Radio Neutrino Observatory in Greenland (RNO-G)*, *Journal of Instrumentation* **16** (2021) P03025 [2010.12279].

[198] GRAND collaboration, *The Giant Radio Array for Neutrino Detection (GRAND): Science and Design*, *Science China Physics, Mechanics & Astronomy* **63** (2020) 219501 [1810.09994].

[199] P-ONE collaboration, *The Pacific Ocean Neutrino Experiment*, *Nature Astron.* **4** (2020) 913 [2005.09493].

[200] TRIDENT collaboration, *A multi-cubic-kilometre neutrino telescope in the western Pacific Ocean*, *Nature Astron.* **7** (2023) 1497 [2207.04519].

[201] C. M. Urry and P. Padovani, *Unified schemes for radio-loud active galactic nuclei*, *Publ. Astron. Soc. Pac.* **107** (1995) 803 [astro-ph/9506063].

[202] P. Padovani et al., *Active galactic nuclei: what's in a name?*, *Astron. Astrophys. Rev.* **25** (2017) 2 [1707.07134].

[203] N. Bennert, H. Falcke, H. Schulz, A. S. Wilson and B. J. Wills, *Size and structure of the narrow-line region of quasars*, *Astrophys. J. Lett.* **574** (2002) L105 [astro-ph/0206334].

[204] M. Cerruti, *Leptonic and Hadronic Radiative Processes in Supermassive-Black-Hole Jets*, *Galaxies* **8** (2020) 72 [2012.13302].

[205] P. Giommi, P. Padovani, G. Polenta, S. Turriziani, V. D'Elia and S. Piranomonte, *A simplified view of blazars: clearing the fog around long-standing selection effects*, *Mon. Not. Roy. Astron. Soc.* **420** (2012) 2899 [1110.4706].

[206] K. Murase, D. Guetta and M. Ahlers, *Hidden Cosmic-Ray Accelerators as an Origin of TeV-PeV Cosmic Neutrinos*, *Phys. Rev. Lett.* **116** (2016) 071101 [1509.00805].

[207] A. Keivani et al., *A Multimessenger Picture of the Flaring Blazar TXS 0506+056: implications for High-Energy Neutrino Emission and Cosmic Ray Acceleration*, *Astrophys. J.* **864** (2018) 84 [1807.04537].

[208] M. Cerruti, A. Zech, C. Boisson, G. Emery, S. Inoue and J. P. Lenain, *Leptohadronic single-zone models for the electromagnetic and neutrino emission of TXS 0506+056*, *Mon. Not. Roy. Astron. Soc.* **483** (2019) L12 [1807.04335].

[209] R.-Y. Liu, K. Wang, R. Xue, A. M. Taylor, X.-Y. Wang, Z. Li et al., *Hadronuclear interpretation of a high-energy neutrino event coincident with a blazar flare*, *Phys. Rev. D* **99** (2019) 063008 [1807.05113].

[210] C. Righi, F. Tavecchio and S. Inoue, *Neutrino emission from BL Lac objects: the role of radiatively inefficient accretion flows*, *Mon. Not. Roy. Astron. Soc.* **483** (2019) L127 [1807.10506].

[211] IceCube collaboration, *Neutrino emission from the direction of the blazar TXS 0506+056 prior to the IceCube-170922A alert*, *Science* **361** (2018) 147 [1807.08794].

[212] S. Gabici, C. Evoli, D. Gaggero, P. Lipari, P. Mertsch, E. Orlando et al., *The origin of Galactic cosmic rays: challenges to the standard paradigm*, *International Journal of Modern Physics D* **28** (2019) 1930022 [1903.11584].

[213] J. Becker Tjus and L. Merten, *Closing in on the origin of Galactic cosmic rays using multimessenger information*, *Physics Reports* **872** (2020) 1 [2002.00964].

[214] X.-J. Lv, X.-J. Bi, K. Fang, Y.-Q. Guo, H.-H. He, L.-L. Ma et al., *Precise measurement of the cosmic-ray spectrum and $\langle \ln A \rangle$ by LHAASO – connecting the Galactic to the extragalactic components*, 2403.11832.

[215] Pierre Auger collaboration, *Constraining the sources of ultra-high-energy cosmic rays across and above the ankle with the spectrum and composition data measured at the Pierre Auger Observatory*, *Journal of Cosmology and Astroparticle Physics* **05** (2023) 024 [2211.02857].

[216] J. Heinze, A. Fedynitch, D. Boncioli and W. Winter, *A new view on Auger data and cosmogenic neutrinos in light of different nuclear disintegration and air-shower models*, *Astrophys. J.* **873** (2019) 88 [1901.03338].

[217] K. Greisen, *End to the cosmic ray spectrum?*, *Physical Review Letters* **16** (1966) 748.

[218] G. Brunetti and T. W. Jones, *Cosmic rays in galaxy clusters and their nonthermal emission*, *International Journal of Modern Physics D* **23** (2014) 1430007 [1401.7519].

[219] A. M. Hillas, *The Origin of Ultrahigh-Energy Cosmic Rays*, *Ann. Rev. Astron. Astrophys.* **22** (1984) 425.

[220] R. Abbasi et al., *Improved Characterization of the Astrophysical Muon–neutrino Flux with 9.5 Years of IceCube Data*, *Astrophys. J.* **928** (2022) 50 [2111.10299].

[221] S. Buson et al., *Beginning a Journey Across the Universe: The Discovery of Extragalactic Neutrino Factories*, *Astrophys. J. Lett.* **933** (2022) L43 [2207.06314].

[222] S. Buson, A. Tramacere, L. Oswald, E. Barbano, G. F. de Clairfontaine, L. Pfeiffer et al., *Extragalactic neutrino factories*, 2305.11263.

[223] C. Bellenghi, P. Padovani, E. Resconi and P. Giommi, *Correlating High-energy IceCube Neutrinos with 5BZCAT Blazars and RFC Sources*, *Astrophys. J. Lett.* **955** (2023) L32 [2309.03115].

[224] IceCube collaboration, *Search for Correlations of High-energy Neutrinos Detected in IceCube with Radio-bright AGN and Gamma-Ray Emission from Blazars*, *Astrophys. J.* **954** (2023) 75 [2304.12675].

[225] IceCube collaboration, *Constraining High-energy Neutrino Emission from Supernovae with IceCube*, *Astrophys. J. Lett.* **949** (2023) L12 [2303.03316].

[226] R. Abbasi et al., *Searches for Neutrinos from Gamma-Ray Bursts Using the IceCube Neutrino Observatory*, *Astrophys. J.* **939** (2022) 116 [2205.11410].

[227] A. Ambrosone, M. Chianese, D. F. G. Fiorillo, A. Marinelli, G. Miele and O. Pisanti, *Starburst galaxies strike back: a multi-messenger analysis with Fermi-LAT and IceCube data*, *Mon. Not. Roy. Astron. Soc.* **503** (2021) 4032 [2011.02483].

[228] B. Zhou, M. Kamionkowski and Y.-f. Liang, *Search for High-Energy Neutrino Emission from Radio-Bright AGN*, *Phys. Rev. D* **103** (2021) 123018 [2103.12813].

[229] Pierre Auger collaboration, *Probing the origin of ultra-high-energy cosmic rays with neutrinos in the EeV energy range using the Pierre Auger Observatory*, *Journal of Cosmology and Astroparticle Physics* **10** (2019) 022 [1906.07422].

[230] ARA collaboration, *Constraints on the diffuse flux of ultrahigh energy neutrinos from four years of Askaryan Radio Array data in two stations*, *Phys. Rev. D* **102** (2020) 043021 [1912.00987].

[231] A. Anker et al., *A search for cosmogenic neutrinos with the ARIANNA test bed using 4.5 years of data*, *JCAP* **03** (2020) 053 [1909.00840].

[232] IceCube collaboration, *Differential limit on the extremely-high-energy cosmic neutrino flux in the presence of astrophysical background from nine years of IceCube data*, *Phys. Rev. D* **98** (2018) 062003 [1807.01820].

[233] S. Wissel et al., *Prospects for high-elevation radio detection of >100 PeV tau neutrinos*, *JCAP* **11** (2020) 065 [2004.12718].

[234] A. Romero-Wolf et al., *An Andean Deep-Valley Detector for High-Energy Tau Neutrinos*, in *Latin American Strategy Forum for Research Infrastructure*, 2, 2020, 2002.06475.

[235] A. M. Brown, M. Bagheri, M. Doro, E. Gazda, D. Kieda, C. Lin et al., *Trinity: An Imaging Air Cherenkov Telescope to Search for Ultra-High-Energy Neutrinos*, in *37th International Cosmic Ray Conference*, 9, 2021, 2109.03125.

[236] S. Prohira et al., *Observation of Radar Echoes From High-Energy Particle Cascades*, *Phys. Rev. Lett.* **124** (2020) 091101 [1910.12830].

[237] POEMMA collaboration, *The POEMMA (Probe of Extreme Multi-Messenger Astrophysics) observatory*, *JCAP* **06** (2021) 007 [2012.07945].

[238] RNO-G collaboration, *Multimessenger Potential of the Radio Neutrino Observatory in Greenland*, *Proceedings of Science* **ICRC2023** (2023) 1485 [2308.07224].

[239] PUEO collaboration, *The Payload for Ultrahigh Energy Observations (PUEO): a white paper*, *Journal of Instrumentation* **16** (2021) P08035 [2010.02892].

[240] M. Ackermann et al., *High-energy and ultra-high-energy neutrinos: A Snowmass white paper*, *JHEAp* **36** (2022) 55 [2203.08096].

[241] LIGO Scientific, Virgo collaboration, *GW150914: The Advanced LIGO Detectors in the Era of First Discoveries*, *Phys. Rev. Lett.* **116** (2016) 131103 [1602.03838].

[242] A. H. Nitz, S. Kumar, Y.-F. Wang, S. Kastha, S. Wu, M. Schäfer et al., *4-OGC: Catalog of Gravitational Waves from Compact Binary Mergers*, *Astrophys. J.* **946** (2023) 59 [2112.06878].

[243] C. Caprini and D. G. Figueroa, *Cosmological Backgrounds of Gravitational Waves*, *Class. Quant. Grav.* **35** (2018) 163001 [1801.04268].

[244] NANOGrav collaboration, *The NANOGrav 15 yr Data Set: Evidence for a Gravitational-wave Background*, *Astrophys. J. Lett.* **951** (2023) L8 [2306.16213].

[245] EPTA, InPTA: collaboration, *The second data release from the European Pulsar Timing Array - III. Search for gravitational wave signals*, *Astron. Astrophys.* **678** (2023) A50 [2306.16214].

[246] D. J. Reardon et al., *Search for an Isotropic Gravitational-wave Background with the Parkes Pulsar Timing Array*, *Astrophys. J. Lett.* **951** (2023) L6 [2306.16215].
[247] R. Xue, R.-Y. Liu, M. Petropoulou, F. Oikonomou, Z.-R. Wang, K. Wang et al., *A two-zone model for blazar emission: implications for TXS 0506+056 and the neutrino event IceCube-170922A*, 1908.10190.
[248] M. Maggiore, *Gravitational Waves. Vol. 1: Theory and Experiments*. Oxford University Press, 2007, 10.1093/acprof:oso/9780198570745.001.0001.
[249] E. S. Phinney, *A Practical theorem on gravitational wave backgrounds*, astro-ph/0108028.
[250] P. A. Rosado, *Gravitational wave background from binary systems*, *Phys. Rev. D* **84** (2011) 084004 [1106.5795].
[251] E. Thrane and J. D. Romano, *Sensitivity curves for searches for gravitational-wave backgrounds*, *Phys. Rev. D* **88** (2013) 124032 [1310.5300].
[252] T. Robson, N. J. Cornish and C. Liu, *The construction and use of LISA sensitivity curves*, *Class. Quant. Grav.* **36** (2019) 105011 [1803.01944].
[253] A. J. Farmer and E. S. Phinney, *The gravitational wave background from cosmological compact binaries*, *Mon. Not. Roy. Astron. Soc.* **346** (2003) 1197 [astro-ph/0304393].
[254] KAGRA, Virgo, LIGO Scientific collaboration, *Upper limits on the isotropic gravitational-wave background from Advanced LIGO and Advanced Virgo's third observing run*, *Phys. Rev. D* **104** (2021) 022004 [2101.12130].
[255] M. Branchesi et al., *Science with the Einstein Telescope: a comparison of different designs*, *JCAP* **07** (2023) 068 [2303.15923].
[256] C. Caprini, D. G. Figueroa, R. Flauger, G. Nardini, M. Peloso, M. Pieroni et al., *Reconstructing the spectral shape of a stochastic gravitational wave background with LISA*, *JCAP* **11** (2019) 017 [1906.09244].
[257] S. Kawamura et al., *Current status of space gravitational wave antenna DECIGO and B-DECIGO*, *PTEP* **2021** (2021) 05A105 [2006.13545].
[258] K. Aggarwal et al., *The NANOGrav 11-Year Data Set: Limits on Gravitational Waves from Individual Supermassive Black Hole Binaries*, *Astrophys. J.* **880** (2019) 2 [1812.11585].
[259] Planck collaboration, *Planck 2018 results. X. Constraints on inflation*, *Astron. Astrophys.* **641** (2020) A10 [1807.06211].
[260] T. W. B. Kibble, *Topology of Cosmic Domains and Strings*, *J. Phys. A* **9** (1976) 1387.
[261] L. Brunelli, M. Cicoli and F. G. Pedro, *Growth of cosmic strings beyond kination*, *JCAP* **07** (2025) 010 [2503.11293].
[262] J. J. Blanco-Pillado and K. D. Olum, *Stochastic gravitational wave background from smoothed cosmic string loops*, *Phys. Rev. D* **96** (2017) 104046 [1709.02693].
[263] J. J. Blanco-Pillado, K. D. Olum and X. Siemens, *New limits on cosmic strings from gravitational wave observation*, *Phys. Lett. B* **778** (2018) 392 [1709.02434].
[264] R. Easther, J. T. Giblin, Jr. and E. A. Lim, *Gravitational Wave Production At The End Of Inflation*, *Phys. Rev. Lett.* **99** (2007) 221301 [astro-ph/0612294].
[265] M. C. Begelman, R. D. Blandford and M. J. Rees, *Massive black hole binaries in active galactic nuclei*, *Nature* **287** (1980) 307.
[266] M. Milosavljevic and D. Merritt, *Long term evolution of massive black hole binaries*, *Astrophys. J.* **596** (2003) 860 [astro-ph/0212459].
[267] M. W. Winkler and K. Freese, *Origin of the stochastic gravitational wave background: First-order phase transition versus black hole mergers*, *Phys. Rev. D* **111** (2025) 083509 [2401.13729].

[268] T. Bringmann, P. F. Depta, T. Konstandin, K. Schmidt-Hoberg and C. Tasillo, *Does NANOGrav observe a dark sector phase transition?*, 2306.09411.

[269] F. Costa, J. Hoefken Zink, M. Lucente, S. Pascoli and S. Rosauro-Alcaraz, *Supercooled dark scalar phase transitions explanation of NANOGrav data*, Phys. Lett. B **868** (2025) 139634 [2501.15649].

[270] LISA collaboration, *Laser Interferometer Space Antenna*, 1702.00786.

[271] M. Punturo et al., *The Einstein Telescope: A third-generation gravitational wave observatory*, Class. Quant. Grav. **27** (2010) 194002.

[272] LIGO Scientific collaboration, *Exploring the Sensitivity of Next Generation Gravitational Wave Detectors*, Class. Quant. Grav. **34** (2017) 044001 [1607.08697].

[273] Y. Aoki, G. Endrodi, Z. Fodor, S. D. Katz and K. K. Szabo, *The Order of the quantum chromodynamics transition predicted by the standard model of particle physics*, Nature **443** (2006) 675 [hep-lat/0611014].

[274] M. E. Shaposhnikov, *Possible Appearance of the Baryon Asymmetry of the Universe in an Electroweak Theory*, JETP Lett. **44** (1986) 465.

[275] T. Hambye, A. Strumia and D. Teresi, *Super-cool Dark Matter*, JHEP **08** (2018) 188 [1805.01473].

[276] M. B. Hindmarsh, M. Lüben, J. Lumma and M. Pauly, *Phase transitions in the early universe*, SciPost Phys. Lect. Notes **24** (2021) 1 [2008.09136].

[277] S. W. Hawking, I. G. Moss and J. M. Stewart, *Bubble Collisions in the Very Early Universe*, Phys. Rev. D **26** (1982) 2681.

[278] H. Kodama, M. Sasaki and K. Sato, *Abundance of Primordial Holes Produced by Cosmological First Order Phase Transition*, Prog. Theor. Phys. **68** (1982) 1979.

[279] M. J. Baker, M. Breitbach, J. Kopp and L. Mittnacht, *Primordial black holes from first-order cosmological phase transitions*, Phys. Lett. B **868** (2025) 139625 [2105.07481].

[280] Y. Gouttenoire, G. Servant and P. Simakachorn, *Beyond the Standard Models with Cosmic Strings*, JCAP **07** (2020) 032 [1912.02569].

[281] T. Vachaspati, *Magnetic fields from cosmological phase transitions*, Phys. Lett. B **265** (1991) 258.

[282] R. Jinno, H. Seong, M. Takimoto and C. M. Um, *Gravitational waves from first-order phase transitions: Ultra-supercooled transitions and the fate of relativistic shocks*, JCAP **10** (2019) 033 [1905.00899].

[283] M. Lewicki, P. Toczek and V. Vaskonen, *Primordial black holes from strong first-order phase transitions*, JHEP **09** (2023) 092 [2305.04924].

[284] S. R. Coleman, *The Fate of the False Vacuum. 1. Semiclassical Theory*, Phys. Rev. D **15** (1977) 2929.

[285] A. D. Linde, *Decay of the False Vacuum at Finite Temperature*, Nucl. Phys. B **216** (1983) 421.

[286] Y. Gouttenoire, *Beyond the Standard Model Cocktail*, 2207.01633.

[287] J. R. Espinosa, T. Konstandin, J. M. No and G. Servant, *Energy Budget of Cosmological First-order Phase Transitions*, JCAP **06** (2010) 028 [1004.4187].

[288] J. Ellis, M. Lewicki, J. M. No and V. Vaskonen, *Gravitational wave energy budget in strongly supercooled phase transitions*, JCAP **06** (2019) 024 [1903.09642].

[289] K. Enqvist, J. Ignatius, K. Kajantie and K. Rummukainen, *Nucleation and bubble growth in a first order cosmological electroweak phase transition*, Phys. Rev. D **45** (1992) 3415.

[290] D. Bodeker and G. D. Moore, *Can electroweak bubble walls run away?*, *JCAP* **05** (2009) 009 [0903.4099].

[291] D. Bodeker and G. D. Moore, *Electroweak Bubble Wall Speed Limit*, *JCAP* **05** (2017) 025 [1703.08215].

[292] Y. Gouttenoire, R. Jinno and F. Sala, *Friction pressure on relativistic bubble walls*, *JHEP* **05** (2022) 004 [2112.07686].

[293] J. Ellis, M. Lewicki and J. M. No, *On the Maximal Strength of a First-Order Electroweak Phase Transition and its Gravitational Wave Signal*, *JCAP* **04** (2019) 003 [1809.08242].

[294] W.-Y. Ai, X. Nagels and M. Vanvlasselaer, *Criterion for ultra-fast bubble walls: the impact of hydrodynamic obstruction*, *JCAP* **03** (2024) 037 [2401.05911].

[295] I. Baldes, M. Dichtl, Y. Gouttenoire and F. Sala, *Particle shells from relativistic bubble walls*, *JHEP* **07** (2024) 231 [2403.05615].

[296] S. J. Huber and T. Konstandin, *Gravitational Wave Production by Collisions: More Bubbles*, *JCAP* **09** (2008) 022 [0806.1828].

[297] C. Caprini, R. Durrer, T. Konstandin and G. Servant, *General Properties of the Gravitational Wave Spectrum from Phase Transitions*, *Phys. Rev. D* **79** (2009) 083519 [0901.1661].

[298] C. Caprini et al., *Science with the space-based interferometer eLISA. II: Gravitational waves from cosmological phase transitions*, *JCAP* **04** (2016) 001 [1512.06239].

[299] D. Cutting, M. Hindmarsh and D. J. Weir, *Vorticity, kinetic energy, and suppressed gravitational wave production in strong first order phase transitions*, *Phys. Rev. Lett.* **125** (2020) 021302 [1906.00480].

[300] D. Cutting, E. G. Escartin, M. Hindmarsh and D. J. Weir, *Gravitational waves from vacuum first order phase transitions II: from thin to thick walls*, *Phys. Rev. D* **103** (2021) 023531 [2005.13537].

[301] T. Konstandin, *Gravitational radiation from a bulk flow model*, *JCAP* **03** (2018) 047 [1712.06869].

[302] C. Caprini et al., *Detecting gravitational waves from cosmological phase transitions with LISA: an update*, *JCAP* **03** (2020) 024 [1910.13125].

[303] M. Hindmarsh, S. J. Huber, K. Rummukainen and D. J. Weir, *Numerical simulations of acoustically generated gravitational waves at a first order phase transition*, *Phys. Rev. D* **92** (2015) 123009 [1504.03291].

[304] E. Witten, *Cosmic Separation of Phases*, *Phys. Rev.* **D30** (1984) 272.

[305] C. J. Hogan, *Gravitational radiation from cosmological phase transitions*, *Mon. Not. Roy. Astron. Soc.* **218** (1986) 629.

[306] J. Antoniadis et al., *The second data release from the European Pulsar Timing Array: V. Implications for massive black holes, dark matter and the early Universe*, 2306.16227.

[307] Y. Gouttenoire, *First-order Phase Transition interpretation of PTA signal produces solar-mass Black Holes*, 2307.04239.

[308] LISA Cosmology Working Group collaboration, *Cosmology with the Laser Interferometer Space Antenna*, 2204.05434.

[309] I. Baldes, Y. Gouttenoire and F. Sala, *String Fragmentation in Supercooled Confinement and Implications for Dark Matter*, *JHEP* **04** (2021) 278 [2007.08440].

[310] I. Baldes, M. Dichtl, Y. Gouttenoire and F. Sala, *Bubbletrons*, 2306.15555.

[311] J. Liu, L. Bian, R.-G. Cai, Z.-K. Guo and S.-J. Wang, *Primordial Black Hole Production during First-Order Phase Transitions*, *Phys. Rev. D* **105** (2022) L021303 [2106.05637].

[312] K. Hashino, S. Kanemura and T. Takahashi, *Primordial black holes as a probe of strongly first-order electroweak phase transition*, *Phys. Lett. B* **833** (2022) 137261 [2111.13099].

[313] Y. Gouttenoire and T. Volansky, *Primordial Black Holes from Supercooled Phase Transitions*, 2305.04942.

[314] A. Katz and A. Riotto, *Baryogenesis and Gravitational Waves from Runaway Bubble Collisions*, *JCAP* **1611** (2016) 011 [1608.00583].

[315] A. Azatov, M. Vanvlasselaer and W. Yin, *Baryogenesis via Relativistic Bubble Walls*, *JHEP* **10** (2021) 043 [2106.14913].

[316] I. Baldes, S. Blasi, A. Mariotti, A. Sevrin and K. Turbang, *Baryogenesis via relativistic bubble expansion*, *Phys. Rev. D* **104** (2021) 115029 [2106.15602].

[317] P. Huang and K.-P. Xie, *Leptogenesis triggered by a first-order phase transition*, *JHEP* **09** (2022) 052 [2206.04691].

[318] E. J. Chun, T. P. Dutka, T. H. Jung, X. Nagels and M. Vanvlasselaer, *Bubble-assisted leptogenesis*, *JHEP* **09** (2023) 164 [2305.10759].

[319] E. Witten, *Cosmological Consequences of a Light Higgs Boson*, *Nucl. Phys. B* **177** (1981) 477.

[320] N. Levi, T. Opferkuch and D. Redigolo, *The supercooling window at weak and strong coupling*, *JHEP* **02** (2023) 125 [2212.08085].

[321] E. Gildener and S. Weinberg, *Symmetry Breaking and Scalar Bosons*, *Phys. Rev. D* **13** (1976) 3333.

[322] P. Creminelli, A. Nicolis and R. Rattazzi, *Holography and the electroweak phase transition*, *JHEP* **03** (2002) 051 [hep-th/0107141].

[323] L. Randall and G. Servant, *Gravitational waves from warped spacetime*, *JHEP* **05** (2007) 054 [hep-ph/0607158].

[324] G. Nardini, M. Quiros and A. Wulzer, *A Confining Strong First-Order Electroweak Phase Transition*, *JHEP* **09** (2007) 077 [0706.3388].

[325] T. Konstandin and G. Servant, *Cosmological Consequences of Nearly Conformal Dynamics at the TeV scale*, *JCAP* **1112** (2011) 009 [1104.4791].

[326] I. Baldes, Y. Gouttenoire, F. Sala and G. Servant, *Supercool composite Dark Matter beyond 100 TeV*, *JHEP* **07** (2022) 084 [2110.13926].

[327] S. Iso, P. D. Serpico and K. Shimada, *QCD-Electroweak First-Order Phase Transition in a Supercooled Universe*, *Phys. Rev. Lett.* **119** (2017) 141301 [1704.04955].

[328] B. von Harling and G. Servant, *QCD-induced Electroweak Phase Transition*, *JHEP* **01** (2018) 159 [1711.11554].

[329] T. Appelquist and Y. Bai, *A Light Dilaton in Walking Gauge Theories*, *Phys. Rev. D* **82** (2010) 071701 [1006.4375].

[330] B. Bellazzini, C. Csaki, J. Hubisz, J. Serra and J. Terning, *A Higgslike Dilaton*, *Eur. Phys. J. C* **73** (2013) 2333 [1209.3299].

[331] F. Coradeschi, P. Lodone, D. Pappadopulo, R. Rattazzi and L. Vitale, *A naturally light dilaton*, *JHEP* **11** (2013) 057 [1306.4601].

[332] Z. Chacko, R. K. Mishra and D. Stolarski, *Dynamics of a Stabilized Radion and Duality*, *JHEP* **09** (2013) 121 [1304.1795].

[333] E. Megias and O. Pujolas, *Naturally light dilatons from nearly marginal deformations*, *JHEP* **08** (2014) 081 [1401.4998].

[334] T. Konstandin and J. M. No, *Hydrodynamic obstruction to bubble expansion*, *JCAP* **02** (2011) 008 [1011.3735].
[335] B. Laurent and J. M. Cline, *First principles determination of bubble wall velocity*, *Phys. Rev. D* **106** (2022) 023501 [2204.13120].
[336] I. Baldes and M. O. Olea-Romacho, *Primordial black holes as dark matter: Interferometric tests of phase transition origin*, 2307.11639.
[337] I. Baldes, M. Dichtl, Y. Gouttenoire and F. Sala, *Particle Shells from Relativistic Bubble Walls*, 231X.XXXXX.
[338] S. Bruggisser, B. Von Harling, O. Matsedonskyi and G. Servant, *Baryon Asymmetry from a Composite Higgs Boson*, *Phys. Rev. Lett.* **121** (2018) 131801 [1803.08546].
[339] S. Bruggisser, B. von Harling, O. Matsedonskyi and G. Servant, *Status of electroweak baryogenesis in minimal composite Higgs*, *JHEP* **08** (2023) 012 [2212.11953].
[340] S. Y. Khlebnikov and M. E. Shaposhnikov, *The Statistical Theory of Anomalous Fermion Number Nonconservation*, *Nucl. Phys. B* **308** (1988) 885.
[341] R. Durrer and C. Caprini, *Primordial magnetic fields and causality*, *JCAP* **11** (2003) 010 [astro-ph/0305059].
[342] NANOGrav collaboration, *The NANOGrav 12.5 yr Data Set: Search for an Isotropic Stochastic Gravitational-wave Background*, *Astrophys. J. Lett.* **905** (2020) L34 [2009.04496].
[343] B. Goncharov et al., *On the Evidence for a Common-spectrum Process in the Search for the Nanohertz Gravitational-wave Background with the Parkes Pulsar Timing Array*, *Astrophys. J. Lett.* **917** (2021) L19 [2107.12112].
[344] EPTA collaboration, *Common-red-signal analysis with 24-yr high-precision timing of the European Pulsar Timing Array: inferences in the stochastic gravitational-wave background search*, *Mon. Not. Roy. Astron. Soc.* **508** (2021) 4970 [2110.13184].
[345] J. Antoniadis et al., *The International Pulsar Timing Array second data release: Search for an isotropic gravitational wave background*, *Mon. Not. Roy. Astron. Soc.* **510** (2022) 4873 [2201.03980].
[346] NANOGrav collaboration, *Searching for Gravitational Waves from Cosmological Phase Transitions with the NANOGrav 12.5-Year Dataset*, *Phys. Rev. Lett.* **127** (2021) 251302 [2104.13930].
[347] R. E. Cutkosky, *Singularities and Discontinuities of Feynman Amplitudes*, *Journal of Mathematical Physics* **1** (1960) 429.
[348] ALEPH, DELPHI, L3, OPAL, SLD, LEP Electroweak Working Group, SLD Electroweak Group, SLD Heavy Flavour Group collaboration, *Precision electroweak measurements on the Z resonance*, *Phys. Rept.* **427** (2006) 257 [hep-ex/0509008].
[349] ALEPH collaboration, *Search for supersymmetric particles with R parity violating decays in e^+e^- collisions at $\sqrt{s}$ up to 209-GeV*, *Eur. Phys. J. C* **31** (2003) 1 [hep-ex/0210014].
[350] CDF collaboration, *Search for Pair Production of Strongly Interacting Particles Decaying to Pairs of Jets in $p\bar{p}$ Collisions at $\sqrt{s} = 1.96$ TeV*, *Phys. Rev. Lett.* **111** (2013) 031802 [1303.2699].
[351] ATLAS collaboration, *A search for pair-produced resonances in four-jet final states at $\sqrt{s} = 13$ TeV with the ATLAS detector*, *Eur. Phys. J. C* **78** (2018) 250 [1710.07171].
[352] CMS collaboration, *Search for resonant and nonresonant production of pairs of dijet resonances in proton-proton collisions at $\sqrt{s} = 13$ TeV*, 2206.09997.

[353] C. Abel et al., *Measurement of the Permanent Electric Dipole Moment of the Neutron*, *Phys. Rev. Lett.* **124** (2020) 081803 [2001.11966].

[354] W. Bensalem and D. Stolarski, *Flavor and CP violation from a QCD-like hidden sector*, *JHEP* **02** (2022) 011 [2111.05515].

[355] S. M. Barr and A. Zee, *Electric Dipole Moment of the Electron and of the Neutron*, *Phys. Rev. Lett.* **65** (1990) 21.

[356] F. Sala, *A bound on the charm chromo-EDM and its implications*, *JHEP* **03** (2014) 061 [1312.2589].

[357] G. F. Giudice, B. Gripaios and R. Sundrum, *Flavourful Production at Hadron Colliders*, *JHEP* **08** (2011) 055 [1105.3161].

[358] M. Bona et al., *Unitarity Triangle global fits beyond the Standard Model: UTfit 2021 NP update*, *PoS* **EPS-HEP2021** (2022) 500.

[359] R. N. Mohapatra, *Mechanism for Understanding Small Neutrino Mass in Superstring Theories*, *Phys. Rev. Lett.* **56** (1986) 561.

[360] R. N. Mohapatra and J. W. F. Valle, *Neutrino Mass and Baryon Number Nonconservation in Superstring Models*, *Phys. Rev. D* **34** (1986) 1642.

[361] Z. Chacko, P. J. Fox, R. Harnik and Z. Liu, *Neutrino Masses from Low Scale Partial Compositeness*, *JHEP* **03** (2021) 112 [2012.01443].

[362] K. Agashe, P. Du, M. Ekhterachian, C. S. Fong, S. Hong and L. Vecchi, *Natural Seesaw and Leptogenesis from Hybrid of High-Scale Type I and TeV-Scale Inverse*, *JHEP* **04** (2019) 029 [1812.08204].

[363] L. Covi, E. Roulet and F. Vissani, *CP violating decays in leptogenesis scenarios*, *Phys. Lett. B* **384** (1996) 169 [hep-ph/9605319].

[364] F. F. Deppisch and A. Pilaftsis, *Lepton Flavour Violation and theta(13) in Minimal Resonant Leptogenesis*, *Phys. Rev. D* **83** (2011) 076007 [1012.1834].

[365] S. Blanchet, T. Hambye and F.-X. Josse-Michaux, *Reconciling leptogenesis with observable mu —> e gamma rates*, *JHEP* **04** (2010) 023 [0912.3153].

[366] H. Al Ali et al., *The muon Smasher's guide*, *Rept. Prog. Phys.* **85** (2022) 084201 [2103.14043].

[367] C. Aime et al., *Muon Collider Physics Summary*, 2203.07256.

[368] P. Li, Z. Liu and K.-F. Lyu, *Heavy neutral leptons at muon colliders*, *JHEP* **03** (2023) 231 [2301.07117].

[369] M. J. Dolan, T. P. Dutka and R. R. Volkas, *Dirac-Phase Thermal Leptogenesis in the extended Type-I Seesaw Model*, *JCAP* **06** (2018) 012 [1802.08373].

[370] B. Fornal and B. Grinstein, *Dark Matter Interpretation of the Neutron Decay Anomaly*, *Phys. Rev. Lett.* **120** (2018) 191801 [1801.01124].

[371] V. L. Eletsky and B. L. Ioffe, *On the thermal mass shift of nucleons*, *Phys. Lett. B* **401** (1997) 327 [hep-ph/9702388].

[372] N. Fettes, U.-G. Meissner and S. Steininger, *Pion - nucleon scattering in chiral perturbation theory. 1. Isospin symmetric case*, *Nucl. Phys. A* **640** (1998) 199 [hep-ph/9803266].

[373] J. Ruiz de Elvira, M. Hoferichter, B. Kubis and U.-G. Meißner, *Extracting the σ-term from low-energy pion-nucleon scattering*, *J. Phys. G* **45** (2018) 024001 [1706.01465].

[374] Z. Tang et al., *Search for the Neutron Decay $n \to X+\gamma$ where X is a dark matter particle*, *Phys. Rev. Lett.* **121** (2018) 022505 [1802.01595].

[375] J. M. Cline and J. M. Cornell, *Dark decay of the neutron*, *JHEP* **07** (2018) 081 [1803.04961].

[376] F. E. Wietfeldt, *The Neutron Lifetime*, in *8th International Workshop on the CKM Unitarity Triangle*, 11, 2014, 1411.3687.

[377] M. Quiros, *Finite temperature field theory and phase transitions*, in *ICTP Summer School in High-Energy Physics and Cosmology*, pp. 187–259, 1, 1999, hep-ph/9901312.

[378] M. Kierkla, A. Karam and B. Swiezewska, *Conformal model for gravitational waves and dark matter: a status update*, *JHEP* **03** (2023) 007 [2210.07075].

[379] M. Kierkla, B. Swiezewska, T. V. I. Tenkanen and J. van de Vis, *Gravitational waves from supercooled phase transitions: dimensional transmutation meets dimensional reduction*, *JHEP* **02** (2024) 234 [2312.12413].

[380] V. Guada, M. Nemevšek and M. Pintar, *FindBounce: Package for multi-field bounce actions*, *Comput. Phys. Commun.* **256** (2020) 107480 [2002.00881].

[381] D. McKeen, A. E. Nelson, S. Reddy and D. Zhou, *Neutron stars exclude light dark baryons*, *Phys. Rev. Lett.* **121** (2018) 061802 [1802.08244].

[382] S. Gandolfi, J. Carlson and S. Reddy, *The maximum mass and radius of neutron stars and the nuclear symmetry energy*, *Phys. Rev. C* **85** (2012) 032801 [1101.1921].

[383] D. Zhou, *Neutron Star Constraints on Neutron Dark Decays*, *Universe* **9** (2023) 484.

[384] D. McKeen, M. Pospelov and N. Raj, *Neutron Star Internal Heating Constraints on Mirror Matter*, *Phys. Rev. Lett.* **127** (2021) 061805 [2105.09951].

[385] S. Deng and L. Bian, *Constraints on new physics around the MeV scale with cosmological observations*, *Phys. Rev. D* **108** (2023) 063516 [2304.06576].

[386] P. Gondolo and J. Silk, *Dark matter annihilation at the galactic center*, *Phys. Rev. Lett.* **83** (1999) 1719 [astro-ph/9906391].

[387] M. Gorchtein, S. Profumo and L. Ubaldi, *Probing Dark Matter with AGN Jets*, *Phys. Rev. D* **82** (2010) 083514 [1008.2230].

[388] A. Granelli, P. Ullio and J.-W. Wang, *Blazar-boosted dark matter at Super-Kamiokande*, *JCAP* **07** (2022) 013 [2202.07598].

[389] R. Essig et al., *Snowmass2021 Cosmic Frontier: The landscape of low-threshold dark matter direct detection in the next decade*, in *Snowmass 2021*, 3, 2022, 2203.08297.

[390] PandaX collaboration, *Search for Light Dark Matter from the Atmosphere in PandaX-4T*, *Phys. Rev. Lett.* **131** (2023) 041001 [2301.03010].

[391] Super-Kamiokande collaboration, *Search for Cosmic-Ray Boosted Sub-GeV Dark Matter Using Recoil Protons at Super-Kamiokande*, *Phys. Rev. Lett.* **130** (2023) 031802 [2209.14968].

[392] J. Alvey, M. Campos, M. Fairbairn and T. You, *Detecting Light Dark Matter via Inelastic Cosmic Ray Collisions*, *Phys. Rev. Lett.* **123** (2019) 261802 [1905.05776].

[393] G. Cao, X. Geng, J. Wang and X. Yang, *Progress in multi-messenger observations and emission models of blazars*, *New Astron. Rev.* **98** (2024) 101693.

[394] S. Gao, A. Fedynitch, W. Winter and M. Pohl, *Modelling the coincident observation of a high-energy neutrino and a bright blazar flare*, *Nature Astron.* **3** (2019) 88 [1807.04275].

[395] M. Cerruti, A. Zech, C. Boisson, G. Emery, S. Inoue and J.-P. Lenain, *Erratum: Lepto-hadronic single-zone models for the electromagnetic and neutrino emission of TXS 0506+056*, *Mon. Not. R. Astron. Soc.: Letters* **502** (2021) L21.

[396] X. Rodrigues, V. S. Paliya, S. Garrappa, A. Omeliukh, A. Franckowiak and W. Winter, *Leptohadronic multi-messenger modeling of 324 gamma-ray blazars*, *Astron. Astrophys.* **681** (2024) A119 [2307.13024].

[397] K. Wang, R.-Y. Liu, Z. Li, X.-Y. Wang and Z.-G. Dai, *Jet Cloud–Star Interaction as an Interpretation of Neutrino Outburst from the Blazar TXS 0506+056*, Universe **9** (2023) 1 [1809.00601].

[398] S. Bhowmick, D. Ghosh and D. Sachdeva, *Blazar boosted dark matter — direct detection constraints on $\sigma_{e\chi}$: role of energy dependent cross sections*, JCAP **07** (2023) 039 [2301.00209].

[399] S. Jeesun, *Blazar boosted ALP and vector portal dark matter confronting light mediator searches*, Phys. Rev. D **111** (2025) 103022 [2501.11569].

[400] E. Massaro, A. Maselli, C. Leto, P. Marchegiani, M. Perri, P. Giommi et al., *The 5th edition of the Roma-BZCAT. A short presentation*, Astrophys. Space Sci. **357** (2015) 75 [1502.07755].

[401] Fermi-LAT collaboration, *Incremental Fermi Large Area Telescope Fourth Source Catalog*, Astrophys. J. Supp. **260** (2022) 53 [2201.11184].

[402] Fermi-LAT collaboration, *Fermi Large Area Telescope Fourth Source Catalog Data Release 4 (4FGL-DR4)*, 2307.12546.

[403] P. Giommi, P. Padovani and G. Polenta, *A simplified view of blazars: the gamma-ray case*, Mon. Not. Roy. Astron. Soc. **431** (2013) 1914 [1302.4331].

[404] P. Padovani, F. Oikonomou, M. Petropoulou, P. Giommi and E. Resconi, *TXS 0506+056, the first cosmic neutrino source, is not a BL Lac*, Mon. Not. Roy. Astron. Soc. **484** (2019) L104 [1901.06998].

[405] P. Padovani, P. Giommi, E. Resconi, T. Glauch, B. Arsioli, N. Sahakyan et al., *Dissecting the region around IceCube-170922A: the blazar TXS 0506+056 as the first cosmic neutrino source*, Mon. Not. Roy. Astron. Soc. **480** (2018) 192 [1807.04461].

[406] Fermi-LAT, ASAS-SN, IceCube collaboration, *Investigation of two Fermi-LAT gamma-ray blazars coincident with high-energy neutrinos detected by IceCube*, Astrophys. J. **880** (2019) 880:103 [1901.10806].

[407] MAGIC collaboration, *The blazar TXS 0506+056 associated with a high-energy neutrino: insights into extragalactic jets and cosmic ray acceleration*, Astrophys. J. Lett. **863** (2018) L10 [1807.04300].

[408] P. Banik and A. Bhadra, *Describing correlated observations of neutrinos and gamma-ray flares from the blazar TXS 0506+056 with a proton blazar model*, Phys. Rev. D **99** (2019) 103006 [1908.11849].

[409] P. Banik, A. Bhadra, M. Pandey and D. Majumdar, *Implications of a proton blazar inspired model on correlated observations of neutrinos with gamma-ray flaring blazars*, Phys. Rev. D **101** (2020) 063024 [1909.01993].

[410] G. Cao, C. Yang, J. Yang and J. Wang, *A self-consistent leptonic–hadronic interpretation of the electromagnetic and neutrino emissions from blazar TXS 0506+056*, Publ. Astron. Soc. Jap. **72** (2020) 20 [1912.07448].

[411] S. Das, N. Gupta and S. Razzaque, *Implications of multiwavelength spectrum on cosmic-ray acceleration in blazar TXS 0506+056*, Astron. Astrophys. **668** (2022) A146 [2208.00838].

[412] MAGIC, OVRO, Metsähovi collaboration, *Investigating the Blazar TXS 0506+056 through Sharp Multiwavelength Eyes During 2017–2019*, Astrophys. J. **927** (2022) 197 [2202.02600].

[413] M. Kadler et al., *Coincidence of a high-fluence blazar outburst with a PeV-energy neutrino event*, Nature Phys. **12** (2016) 807 [1602.02012].

[414] V. S. Paliya, M. Böttcher, A. Olmo-García, A. Domínguez, A. Gil de Paz, A. Franckowiak et al., *Multifrequency Observations of the Candidate Neutrino-emitting Blazar BZB J0955+3551*, *The Astrophysical Journal* **902** (2020) 29 [2003.06012].

[415] X. Rodrigues, S. Garrappa, S. Gao, V. S. Paliya, A. Franckowiak and W. Winter, *Multiwavelength and Neutrino Emission from Blazar PKS 1502 + 106*, *Astrophys. J.* **912** (2021) 54 [2009.04026].

[416] F. Oikonomou, M. Petropoulou, K. Murase, A. Tohuvavohu, G. Vasilopoulos, S. Buson et al., *Multi-messenger emission from the parsec-scale jet of the flat-spectrum radio quasar coincident with high-energy neutrino IceCube-190730A*, *JCAP* **10** (2021) 082 [2107.11437].

[417] N.-H. Liao, Z.-F. Sheng, N. Jiang, Y.-L. Chang, Y.-B. Wang, D.-L. Xu et al., *GB6 J2113+1121: A Multiwavelength Flaring γ-Ray Blazar Temporally and Spatially Coincident with the Neutrino Event IceCube-191001A*, *Astrophys. J. Lett.* **932** (2022) L25 [2202.03788].

[418] N. Sahakyan, P. Giommi, P. Padovani, M. Petropoulou, D. Bégué, B. Boccardi et al., *A multimessenger study of the blazar PKS 0735+178: a new major neutrino source candidate*, *Mon. Not. Roy. Astron. Soc.* **519** (2022) 1396 [2204.05060].

[419] X. Jiang, N.-H. Liao, Y.-B. Wang, R. Xue, N. Jiang and T.-G. Wang, *The Awakening of a Blazar at Redshift 2.7 Temporally Coincident with the Arrival of Cospatial Neutrino Event IceCube-201221A*, *The Astrophysical Journal Letters* **965** (2024) L2 [2401.12122].

[420] S. Ji and Z. Wang, *PKS 2254+074: A Blazar in Likely Association with the Neutrino Event IceCube-190619A*, 2410.14079.

[421] S. Ji, Z. Wang and D. Zheng, *PKS˜2332−017 and PMN J1916−1519: Candidate Blazar Counterparts to Two High-energy Neutrino Events*, 2411.01448.

[422] P. Giommi and P. Padovani, *Astrophysical Neutrinos and Blazars*, *Universe* **7** (2021) 492 [2112.06232].

[423] M. Boettcher, M. Fu, T. Govenor, Q. King and P. Roustazadeh, *Multiwavelength and Multimessenger Observations of Blazars and Theoretical Modeling: Blazars as Astrophysical Neutrino Sources*, *Acta Phys. Polon. Supp.* **15** (2022) 8 [2204.12242].

[424] IceCube collaboration, *Evidence for neutrino emission from the nearby active galaxy NGC 1068*, *Science* **378** (2022) 538 [2211.09972].

[425] IceCube collaboration, *Time-Integrated Neutrino Source Searches with 10 Years of IceCube Data*, *Phys. Rev. Lett.* **124** (2020) 051103 [1910.08488].

[426] S. Paiano, R. Falomo, A. Treves and R. Scarpa, *The redshift of the BL Lac object TXS 0506+056*, *Astrophys. J. Lett.* **854** (2018) L32 [1802.01939].

[427] D. Merritt, *Single and binary black holes and their influence on nuclear structure*, in *Carnegie Observatories Centennial Symposium. 1. Coevolution of Black Holes and Galaxies*, 1, 2003, astro-ph/0301257.

[428] L. Sadeghian, F. Ferrer and C. M. Will, *Dark matter distributions around massive black holes: A general relativistic analysis*, *Phys. Rev. D* **88** (2013) 063522 [1305.2619].

[429] J. F. Navarro, C. S. Frenk and S. D. M. White, *The Structure of cold dark matter halos*, *Astrophys. J.* **462** (1996) 563 [astro-ph/9508025].

[430] J. F. Navarro, C. S. Frenk and S. D. M. White, *A Universal density profile from hierarchical clustering*, *Astrophys. J.* **490** (1997) 493 [astro-ph/9611107].

[431] J. Kormendy and L. C. Ho, *Coevolution (Or Not) of Supermassive Black Holes and Host Galaxies*, *Ann. Rev. Astron. Astrophys.* **51** (2013) 511 [1304.7762].

[432] M. Labita, A. Treves, R. Falomo and M. Uslenghi, *The BH mass of nearby QSOs: a comparison of the bulge luminosity and virial methods*, *Monthly Notices of the Royal Astronomical Society* **373** (2006) 551 [astro-ph/0609185].

[433] Z. Pei, J. Fan, J. Yang, D. Huang and Z. Li, *The Estimation of Fundamental Physics Parameters for Fermi-LAT Blazars*, *Astrophys. J.* **925** (2022) 97 [2112.00530].

[434] J. M. Cline, S. Gao, F. Guo, Z. Lin, S. Liu, M. Puel et al., *Blazar Constraints on Neutrino-Dark Matter Scattering*, *Phys. Rev. Lett.* **130** (2023) 091402 [2209.02713].

[435] F. Ferrer, G. Herrera and A. Ibarra, *New constraints on the dark matter-neutrino and dark matter-photon scattering cross sections from TXS 0506+056*, *JCAP* **05** (2023) 057 [2209.06339].

[436] J. M. Cline and M. Puel, *NGC 1068 constraints on neutrino-dark matter scattering*, *JCAP* **06** (2023) 004 [2301.08756].

[437] G. Herrera and K. Murase, *Probing light dark matter through cosmic-ray cooling in active galactic nuclei*, *Phys. Rev. D* **110** (2024) L011701 [2307.09460].

[438] J.-W. Wang, *Blazar-Boosted Dark Matter: Novel Signatures via Elastic and Inelastic Scattering*, 2503.22105.

[439] S. L. Shapiro and J. Shelton, *Weak annihilation cusp inside the dark matter spike about a black hole*, *Phys. Rev. D* **93** (2016) 123510 [1606.01248].

[440] P. Ullio, H. Zhao and M. Kamionkowski, *A Dark matter spike at the galactic center?*, *Phys. Rev. D* **64** (2001) 043504 [astro-ph/0101481].

[441] D. Merritt, M. Milosavljevic, L. Verde and R. Jimenez, *Dark matter spikes and annihilation radiation from the galactic center*, *Phys. Rev. Lett.* **88** (2002) 191301 [astro-ph/0201376].

[442] O. Y. Gnedin and J. R. Primack, *Dark Matter Profile in the Galactic Center*, *Phys. Rev. Lett.* **93** (2004) 061302 [astro-ph/0308385].

[443] G. Bertone and D. Merritt, *Time-dependent models for dark matter at the Galactic Center*, *Phys. Rev. D* **72** (2005) 103502 [astro-ph/0501555].

[444] T. Abe, M. Fujiwara and J. Hisano, *Loop corrections to dark matter direct detection in a pseudoscalar mediator dark matter model*, *JHEP* **02** (2019) 028 [1810.01039].

[445] J. Ellis, *TikZ-Feynman: Feynman diagrams with TikZ*, *Comput. Phys. Commun.* **210** (2017) 103 [1601.05437].

[446] A. Alloul, N. D. Christensen, C. Degrande, C. Duhr and B. Fuks, *FeynRules 2.0 - A complete toolbox for tree-level phenomenology*, *Comput. Phys. Commun.* **185** (2014) 2250 [1310.1921].

[447] J. Alwall, R. Frederix, S. Frixione, V. Hirschi, F. Maltoni, O. Mattelaer et al., *The automated computation of tree-level and next-to-leading order differential cross sections, and their matching to parton shower simulations*, *JHEP* **07** (2014) 079 [1405.0301].

[448] C. Bierlich et al., *A comprehensive guide to the physics and usage of PYTHIA 8.3*, *SciPost Phys. Codeb.* **2022** (2022) 8 [2203.11601].

[449] H.-L. Lai, M. Guzzi, J. Huston, Z. Li, P. M. Nadolsky, J. Pumplin et al., *New parton distributions for collider physics*, *Physical Review D* **82** (2010) 074024 [1007.2241].

[450] Super-Kamiokande collaboration, *Search for Astronomical Neutrinos from Blazar TXS 0506+056 in Super-Kamiokande*, *Astrophys. J. Lett.* **887** (2019) L6 [1910.07680].

[451] M. Carrillo González and N. Toro, *Cosmology and signals of light pseudo-Dirac dark matter*, *JHEP* **04** (2022) 060 [2108.13422].
[452] A. Berlin, G. Krnjaic and E. Pinetti, *Reviving MeV-GeV indirect detection with inelastic dark matter*, *Phys. Rev. D* **110** (2024) 035015 [2311.00032].
[453] X. Rodrigues, S. Gao, A. Fedynitch, A. Palladino and W. Winter, *Leptohadronic Blazar Models Applied to the 2014–2015 Flare of TXS 0506+056*, *The Astrophysical Journal Letters* **874** (2019) L29 [1812.05939].
[454] A. Das, T. Herbermann, M. Sen and V. Takhistov, *Energy-dependent boosted dark matter from diffuse supernova neutrino background*, *JCAP* **07** (2024) 045 [2403.15367].
[455] C. Xia, Y.-H. Xu and Y.-F. Zhou, *Production and attenuation of cosmic-ray boosted dark matter*, *JCAP* **02** (2022) 028 [2111.05559].
[456] T. Emken and C. Kouvaris, *How blind are underground and surface detectors to strongly interacting Dark Matter?*, *Phys. Rev. D* **97** (2018) 115047 [1802.04764].
[457] DUNE collaboration, *The DUNE Far Detector Interim Design Report Volume 1: Physics, Technology and Strategies*, 1807.10334.
[458] KamLAND collaboration, *Measurement of the 8B Solar Neutrino Flux with the KamLAND Liquid Scintillator Detector*, *Phys. Rev. C* **84** (2011) 035804 [1106.0861].
[459] C. V. Cappiello and J. F. Beacom, *Strong New Limits on Light Dark Matter from Neutrino Experiments*, *Phys. Rev. D* **100** (2019) 103011 [1906.11283].
[460] B. Chauhan, B. Dasgupta and A. Dighe, *Large-energy single hits at JUNO from atmospheric neutrinos and dark matter*, *Phys. Rev. D* **105** (2022) 095035 [2111.14586].
[461] Borexino collaboration, *New limits on heavy sterile neutrino mixing in B8 decay obtained with the Borexino detector*, *Phys. Rev. D* **88** (2013) 072010 [1311.5347].
[462] M. Escudero, *Neutrino decoupling beyond the Standard Model: CMB constraints on the Dark Matter mass with a fast and precise $N_{\rm eff}$ evaluation*, *JCAP* **02** (2019) 007 [1812.05605].
[463] N. Sabti, J. Alvey, M. Escudero, M. Fairbairn and D. Blas, *Refined Bounds on MeV-scale Thermal Dark Sectors from BBN and the CMB*, *JCAP* **2020** (2020) 004 [1910.01649].
[464] M. L. Graesser, I. M. Shoemaker and L. Vecchi, *Asymmetric WIMP dark matter*, *JHEP* **10** (2011) 110 [1103.2771].
[465] I. Baldes and K. Petraki, *Asymmetric thermal-relic dark matter: Sommerfeld-enhanced freeze-out, annihilation signals and unitarity bounds*, *JCAP* **09** (2017) 028 [1703.00478].
[466] I. Baldes, M. Cirelli, P. Panci, K. Petraki, F. Sala and M. Taoso, *Asymmetric dark matter: residual annihilations and self-interactions*, *SciPost Phys.* **4** (2018) 041 [1712.07489].
[467] TESSERACT collaboration, *First Limits on Light Dark Matter Interactions in a Low Threshold Two Channel Athermal Phonon Detector from the TESSERACT Collaboration*, 2503.03683.
[468] XENON collaboration, *First Dark Matter Search with Nuclear Recoils from the XENONnT Experiment*, *Phys. Rev. Lett.* **131** (2023) 041003 [2303.14729].
[469] J. I. Collar, *Search for a nonrelativistic component in the spectrum of cosmic rays at Earth*, *Phys. Rev. D* **98** (2018) 023005 [1805.02646].
[470] PandaX collaboration, *Search for Dark-Matter–Nucleon Interactions with a Dark Mediator in PandaX-4T*, *Phys. Rev. Lett.* **131** (2023) 191002 [2308.01540].

[471] XENON collaboration, *Search for Light Dark Matter Interactions Enhanced by the Migdal Effect or Bremsstrahlung in XENON1T*, *Phys. Rev. Lett.* **123** (2019) 241803 [1907.12771].

[472] NA62 collaboration, *Measurement of the very rare $K^+ \to \pi^+ \nu \overline{\nu}$ decay*, *JHEP* **06** (2021) 093 [2103.15389].

[473] P. Cox, M. J. Dolan and J. Wood, *New Limits on Light Dark Matter-Nucleon Scattering*, 2408.12144.

[474] ATLAS collaboration, *Search for new phenomena in events with two opposite-charge leptons, jets and missing transverse momentum in pp collisions at $\sqrt{\mathrm{s}} = 13$ TeV with the ATLAS detector*, *JHEP* **04** (2021) 165 [2102.01444].

[475] ATLAS collaboration, *Constraints on simplified dark matter models involving an s-channel mediator with the ATLAS detector in pp collisions at $\sqrt{s} = 13$ TeV*, *Eur. Phys. J. C* **84** (2024) 1102 [2404.15930].

[476] CMS collaboration, *Search for new particles in events with energetic jets and large missing transverse momentum in proton-proton collisions at $\sqrt{s} = 13$ TeV*, *JHEP* **11** (2021) 153 [2107.13021].

[477] I. M. Shoemaker and L. Vecchi, *Unitarity and Monojet Bounds on Models for DAMA, CoGeNT, and CRESST-II*, *Phys. Rev. D* **86** (2012) 015023 [1112.5457].

[478] Y. Kahn, G. Krnjaic, S. Mishra-Sharma and T. M. P. Tait, *Light Weakly Coupled Axial Forces: Models, Constraints, and Projections*, *JHEP* **05** (2017) 002 [1609.09072].

[479] S. Gori, S. Knapen, T. Lin, P. Munbodh and B. Suter, *Spin-Dependent Scattering of Sub-GeV Dark Matter: Models and Constraints*, 2506.11191.

[480] J. Lesgourgues, G. Mangano, G. Miele and S. Pastor, *Neutrino Cosmology*. Cambridge University Press, 2, 2013.

[481] M. Bauer and J. D. Shergold, *Limits on the cosmic neutrino background*, *Journal of Cosmology and Astroparticle Physics* **01** (2023) 003 [2207.12413].

[482] A. Apponi et al., *Implementation and optimization of the PTOLEMY transverse drift electromagnetic filter*, *Journal of Instrumentation* **17** (2022) P05021 [2108.10388].

[483] Y. Cheipesh, V. Cheianov and A. Boyarsky, *Navigating the pitfalls of relic neutrino detection*, *Physical Review D* **104** (2021) 116004 [2101.10069].

[484] PTOLEMY collaboration, *Heisenberg's uncertainty principle in the PTOLEMY project: A theory update*, *Physical Review D* **106** (2022) 053002 [2203.11228].

[485] M. Aker et al., *New constraint on the local relic neutrino background overdensity with the first katrin data runs*, *Physical Review Letters* **129** (2022) .

[486] Y.-D. Tsai, J. Eby, J. Arakawa, D. Farnocchia and M. S. Safronova, *OSIRIS-REx constraints on local dark matter and cosmic neutrino profiles*, *Journal of Cosmology and Astroparticle Physics* **02** (2024) 029 [2210.03749].

[487] A. Ringwald and Y. Y. Y. Wong, *Gravitational clustering of relic neutrinos and implications for their detection*, *Journal of Cosmology and Astroparticle Physics* **12** (2004) 005 [hep-ph/0408241].

[488] D. Fargion, B. Mele and A. Salis, *Ultrahigh-energy neutrino scattering onto relic light neutrinos in galactic halo as a possible source of highest energy extragalactic cosmic rays*, *The Astrophysical Journal* **517** (1999) 725 [astro-ph/9710029].

[489] T. J. Weiler, *Cosmic ray neutrino annihilation on relic neutrinos revisited: A Mechanism for generating air showers above the Greisen-Zatsepin-Kuzmin cutoff*, *Astroparticle Physics* **11** (1999) 303 [hep-ph/9710431].

[490] J. Franklin, I. Martinez-Soler, Y. F. Perez-Gonzalez and J. Turner, *Constraints on the Cosmic Neutrino Background from NGC 1068*, 2404.02202.

[491] B. Eberle, A. Ringwald, L. Song and T. J. Weiler, *Relic neutrino absorption spectroscopy*, *Physical Review D* **70** (2004) 023007 [hep-ph/0401203].

[492] V. Brdar, P. S. B. Dev, R. Plestid and A. Soni, *A new probe of relic neutrino clustering using cosmogenic neutrinos*, *Physics Letters B* **833** (2022) 137358 [2207.02860].

[493] T. Hara and H. Sato, *Scattering of the Cosmic Neutrinos by High Energy Cosmic Rays*, *Progress of Theoretical Physics* **64** (1980) 1089.

[494] T. Hara and H. Sato, *Elastic and Inelastic Scattering of the Relic Neutrinos by High-energy Cosmic Rays*, *Progress of Theoretical Physics* **65** (1981) 477.

[495] M. Císcar-Monsalvatje, G. Herrera and I. M. Shoemaker, *Upper Limits on the Cosmic Neutrino Background from Cosmic Rays*, *Physical Review D* **10** (2024) 110 [2402.00985].

[496] Telescope Array collaboration, *Mass composition of ultrahigh-energy cosmic rays with the Telescope Array Surface Detector data*, *Physical Review D* **99** (2019) 022002 [1808.03680].

[497] K. Bondarenko, A. Boyarsky, J. Pradler and A. Sokolenko, *Best-case scenarios for neutrino capture experiments*, *Journal of Cosmology and Astroparticle Physics* **10** (2023) 026 [2306.12366].

[498] A. Y. Smirnov and X.-J. Xu, *Neutrino bound states and bound systems*, *Journal of High Energy Physics* **08** (2022) 170 [2201.00939].

[499] H. J. Volk, F. A. Aharonian and D. Breitschwerdt, *The nonthermal energy content and gamma-ray emission of starburst galaxies and clusters of galaxies*, *Space Science Reviews* **75** (1996) 279.

[500] V. S. Berezinsky, P. Blasi and V. S. Ptuskin, *Clusters of Galaxies as a Storage Room for Cosmic Rays*, *The Astrophysical Journal* **487** (1997) 529 [astro-ph/9609048].

[501] K. Murase, S. Inoue and S. Nagataki, *Cosmic Rays Above the Second Knee from Clusters of Galaxies and Associated High-Energy Neutrino Emission*, *The Astrophysical Journal* **689** (2008) L105 [0805.0104].

[502] K. Kotera, D. Allard, K. Murase, J. Aoi, Y. Dubois, T. Pierog et al., *Propagation of ultrahigh energy nuclei in clusters of galaxies: resulting composition and secondary emissions*, *The Astrophysical Journal* **707** (2009) 370 [0907.2433].

[503] K. Murase and J. F. Beacom, *Galaxy Clusters as Reservoirs of Heavy Dark Matter and High-Energy Cosmic Rays: Constraints from Neutrino Observations*, *Journal of Cosmology and Astroparticle Physics* **02** (2013) 028 [1209.0225].

[504] A. Condorelli, J. Biteau and R. Adam, *Impact of Galaxy Clusters on the Propagation of Ultrahigh-energy Cosmic Rays*, *The Astrophysical Journal* **957** (2023) 80 [2309.04380].

[505] C. Giunti and C. W. Kim, *Fundamentals of Neutrino Physics and Astrophysics*. Oxford University Press, Oxford, UK, 2007.

[506] J. A. Formaggio and G. P. Zeller, *From eV to EeV: Neutrino Cross Sections Across Energy Scales*, *Rev. Mod. Phys.* **84** (2012) 1307 [1305.7513].

[507] D. Z. Freedman, D. N. Schramm and D. L. Tubbs, *The Weak Neutral Current and Its Effects in Stellar Collapse*, *Annual Review of Nuclear and Particle Science* **27** (1977) 167.

[508] R. P. Feynman, M. Kislinger and F. Ravndal, *Current matrix elements from a relativistic quark model*, *Physical Review D* **3** (1971) 2706.

[509] D. Rein and L. M. Sehgal, *Neutrino Excitation of Baryon Resonances and Single Pion Production*, Annals of Physics **133** (1981) 79.

[510] S. Thoudam, J. P. Rachen, A. van Vliet, A. Achterberg, S. Buitink, H. Falcke et al., *Cosmic-ray energy spectrum and composition up to the ankle: the case for a second Galactic component*, Astronomy & Astrophysics **595** (2016) A33 [1605.03111].

[511] R. Alves Batista et al., *Open Questions in Cosmic-Ray Research at Ultrahigh Energies*, Frontiers in Astronomy and Space Sciences **6** (2019) 23 [1903.06714].

[512] Pierre Auger collaboration, *Cosmic-ray anisotropies in right ascension measured by the Pierre Auger Observatory*, The Astrophysical Journal **891** (2020) 142 [2002.06172].

[513] A. Coleman et al., *Ultra high energy cosmic rays The intersection of the Cosmic and Energy Frontiers*, Astroparticle Physics **149** (2023) 102819 [2205.05845].

[514] HiRes collaboration, *A Study of the composition of ultrahigh energy cosmic rays using the High Resolution Fly's Eye*, The Astrophysical Journal **622** (2005) 910 [astro-ph/0407622].

[515] R. Aloisio, V. Berezinsky and P. Blasi, *Ultra high energy cosmic rays: implications of Auger data for source spectra and chemical composition*, Journal of Cosmology and Astroparticle Physics **10** (2014) 020 [1312.7459].

[516] R. U. Abbasi et al., *Study of Ultra-High Energy Cosmic Ray composition using Telescope Array's Middle Drum detector and surface array in hybrid mode*, Astroparticle Physics **64** (2015) 49 [1408.1726].

[517] Telescope Array collaboration, *The Cosmic-Ray Composition between 2 PeV and 2 EeV Observed with the TALE Detector in Monocular Mode*, The Astrophysical Journal **909** (2021) 178 [2012.10372].

[518] Pierre Auger collaboration, *Constraining models for the origin of ultra-high-energy cosmic rays with a novel combined analysis of arrival directions, spectrum, and composition data measured at the Pierre Auger Observatory*, Journal of Cosmology and Astroparticle Physics **01** (2024) 022 [2305.16693].

[519] G. Guo, Y.-L. S. Tsai, M.-R. Wu and Q. Yuan, *Elastic and Inelastic Scattering of Cosmic-Rays on Sub-GeV Dark Matter*, Phys. Rev. D **102** (2020) 103004 [2008.12137].

[520] CDEX collaboration, *Constraints on sub-GeV dark matter boosted by cosmic rays from the CDEX-10 experiment at the China Jinping Underground Laboratory*, Physical Review D **106** (2022) 052008 [2201.01704].

[521] T. Wibig and A. W. Wolfendale, *Heavy Cosmic Ray Nuclei from Extragalactic Sources above 'The Ankle'*, The Open Astronomy Journal **2** (2009) 95 [0712.3403].

[522] A. M. Taylor, M. Ahlers and F. A. Aharonian, *The need for a local source of UHE CR nuclei*, Physical Review D **84** (2011) 105007 [1107.2055].

[523] S. Mollerach and E. Roulet, *Ultrahigh energy cosmic rays from a nearby extragalactic source in the diffusive regime*, Physical Review D **99** (2019) 103010 [1903.05722].

[524] R. G. Lang, A. M. Taylor, M. Ahlers and V. de Souza, *Revisiting the distance to the nearest ultrahigh energy cosmic ray source: Effects of extragalactic magnetic fields*, Physical Review D **102** (2020) 063012 [2005.14275].

[525] P. Plotko, A. van Vliet, X. Rodrigues and W. Winter, *Differences between the Pierre Auger Observatory and Telescope Array Spectra: Systematic Effects or Indication of a Local Source of Ultra-high-energy Cosmic Rays?*, The Astrophysical Journal **953** (2023) 129 [2208.12274].

[526] IceCube collaboration, *Characteristics of the diffuse astrophysical electron and tau neutrino flux with six years of IceCube high energy cascade data*, *Physical Review Letters* **125** (2020) 121104 [2001.09520].

[527] IceCube collaboration, *Detection of a particle shower at the Glashow resonance with IceCube*, *Nature* **591** (2021) 220 [2110.15051].

[528] IceCube collaboration, *The IceCube high-energy starting event sample: Description and flux characterization with 7.5 years of data*, *Physical Review D* **104** (2021) 022002 [2011.03545].

[529] R. Abbasi et al., *Characterization of the Astrophysical Diffuse Neutrino Flux using Starting Track Events in IceCube*, *Physical Review D* **110** (2024) 022001 [2402.18026].

[530] KM3NeT collaboration, *Differential Sensitivity of the KM3NeT/ARCA detector to a diffuse neutrino flux and to point-like source emission: exploring the case of the Starburst Galaxies*, *Astroparticle Physics* **162** (2024) 102990 [2402.09088].

[531] IceCube-Gen2 collaboration, *Sensitivity studies for the IceCube-Gen2 radio array*, *Proceedings of Science* **ICRC2021** (2021) 1183 [2107.08910].

[532] Pierre Auger collaboration, *Features of the Energy Spectrum of Cosmic Rays above 2.5×10^{18} eV Using the Pierre Auger Observatory*, *Physical Review Letters* **125** (2020) 121106 [2008.06488].

[533] I. Esteban, M. C. Gonzalez-Garcia, M. Maltoni, T. Schwetz and A. Zhou, *The fate of hints: updated global analysis of three-flavor neutrino oscillations*, *Journal of High Energy Physics* **09** (2020) 178 [2007.14792].

[534] KATRIN collaboration, *Direct neutrino-mass measurement with sub-electronvolt sensitivity*, *Nature Physics* **18** (2022) 160 [2105.08533].

[535] J. F. Navarro, C. S. Frenk and S. D. M. White, *A universal density profile from hierarchical clustering*, *The Astrophysical Journal* **490** (1997) 493–508.

[536] Particle Data Group collaboration, *Review of Particle Physics*, *Progress of Theoretical and Experimental Physics* **2022** (2022) 083C01.

[537] A. Palladino and F. Vissani, *The natural parameterization of cosmic neutrino oscillations*, *The European Physical Journal C* **75** (2015) 433 [1504.05238].

[538] M. Bustamante, J. F. Beacom and W. Winter, *Theoretically palatable flavor combinations of astrophysical neutrinos*, *Physical Review Letters* **115** (2015) 161302 [1506.02645].

[539] IceCube collaboration, *Flavor Ratio of Astrophysical Neutrinos above 35 TeV in IceCube*, *Physical Review Letters* **114** (2015) 171102 [1502.03376].

[540] A. Palladino, *The flavor composition of astrophysical neutrinos after 8 years of IceCube: an indication of neutron decay scenario?*, *The European Physical Journal C* **79** (2019) 500 [1902.08630].

[541] A. Coleman, O. Ericsson, M. Bustamante and C. Glaser, *The flavor composition of ultra-high-energy cosmic neutrinos: measurement forecasts for in-ice radio-based EeV neutrino telescopes*, 2402.02432.

[542] Z. Chacko, P. Du and M. Geller, *Detecting a Secondary Cosmic Neutrino Background from Majoron Decays in Neutrino Capture Experiments*, *Phys. Rev. D* **100** (2019) 015050 [1812.11154].

[543] D. McKeen, *Cosmic neutrino background search experiments as decaying dark matter detectors*, *Phys. Rev. D* **100** (2019) 015028 [1812.08178].

[544] S. J. Dong, J. F. Lagae and K. F. Liu, *Pi N sigma term, anti-s s in nucleon, and scalar form-factor: A Lattice study*, *Phys. Rev. D* **54** (1996) 5496 [hep-ph/9602259].

[545] H. Gao and M. Vanderhaeghen, *The proton charge radius*, *Reviews of Modern Physics* **94** (2022) 015002 [2105.00571].

[546] M. Hoferichter, J. R. de Elvira, B. Kubis and U.-G. Meißner, *On the role of isospin violation in the pion–nucleon σ-term*, *Phys. Lett. B* **843** (2023) 138001 [2305.07045].

[547] C. Alexandrou, S. Bacchio, M. Constantinou, J. Finkenrath, R. Frezzotti, B. Kostrzewa et al., *Nucleon axial and pseudoscalar form factors using twisted-mass fermion ensembles at the physical point*, 2309.05774.

[548] S. Bilenky and S. Mikhov, *Basics of introduction to Feynman diagrams and electroweak interactions physics*. Editions Frontieres, France, 1994.

[549] F. J. Ernst, R. G. Sachs and K. C. Wali, *Electromagnetic form factors of the nucleon*, *Physical Review* **119** (1960) 1105.

[550] L. N. Hand, D. G. Miller and R. Wilson, *Electric and magnetic form factors of the nucleon*, *Reviews of Modern Physics* **35** (1963) 335.

[551] C. F. Perdrisat, V. Punjabi and M. Vanderhaeghen, *Nucleon Electromagnetic Form Factors*, *Progress in Particle and Nuclear Physics* **59** (2007) 694 [hep-ph/0612014].

[552] J. M. Alarcón, D. W. Higinbotham and C. Weiss, *Precise determination of the proton magnetic radius from electron scattering data*, *Physical Review C* **102** (2020) 035203 [2002.05167].

[553] M. R. Schindler, T. Fuchs, J. Gegelia and S. Scherer, *Axial, induced pseudoscalar, and pion-nucleon form factors in manifestly lorentz-invariant chiral perturbation theory*, *Physical Review C* **75** (2007) .

[554] M. E. Peskin and D. V. Schroeder, *An Introduction to quantum field theory*. Addison-Wesley, Reading, USA, 1995.

[555] N. I. Shakura and R. A. Sunyaev, *Black holes in binary systems. Observational appearance*, *Astron. Astrophys.* **24** (1973) 337.

[556] B. Betancourt Kamenetskaia, M. Fujiwara, A. Ibarra and T. Toma, *Dark matter spikes with strongly self-interacting particles*, 2506.12642.

[557] D. N. Spergel and P. J. Steinhardt, *Observational evidence for selfinteracting cold dark matter*, *Phys. Rev. Lett.* **84** (2000) 3760 [astro-ph/9909386].

[558] S. Ando, K. Hayashi, S. Horigome, M. Ibe and S. Shirai, *Stringent Constraints on Self-Interacting Dark Matter Using Milky-Way Satellite Galaxies Kinematics*, 2503.13650.

[559] K. E. Andrade, J. Fuson, S. Gad-Nasr, D. Kong, Q. Minor, M. G. Roberts et al., *A stringent upper limit on dark matter self-interaction cross-section from cluster strong lensing*, *Mon. Not. Roy. Astron. Soc.* **510** (2021) 54 [2012.06611].

[560] S. L. Shapiro and V. Paschalidis, *Self-interacting dark matter cusps around massive black holes*, *Phys. Rev. D* **89** (2014) 023506 [1402.0005].

[561] Extended Twisted Mass collaboration, *Nucleon axial and pseudoscalar form factors using twisted-mass fermion ensembles at the physical point*, *Physical Review D* **109** (2024) 034503 [2309.05774].